Design of simulation platform joigning site specific radio propagation and human mobility for localization applications

Nicolas Amiot

ANNÉE 2013

THÈSE / UNIVERSITÉ DE RENNES 1
sous le sceau de l'Université Européenne de Bretagne

pour le grade de

DOCTEUR DE L'UNIVERSITÉ DE RENNES 1

Mention : Traitement du signal et Télécommunications

Ecole doctorale (MATISSE)

présentée par

Nicolas AMIOT

Préparée à l'unité de recherche IETR- UMR CNRS 6164
(Institut d'Electronique et de Télécommunication de Rennes)
(groupe Propagation Localisation)

Design of a Simulation Platform Joining Site Specific Radio Propagation and Human Mobility for Localization Applications

Thèse soutenue à Rennes

le 2 Décembre 2013

devant le jury composé de :

Laurent CLAVIER
Professeur, Télécom Lille / rapporteur

Rodolphe VAUZELLE
Professeur, Université de Poitiers / rapporteur

Benoît DENIS
Ingénieur Docteur, CEA-Leti / *examinateur*

Emanuel RADOI
Professeur, Université de Bretagne Occidentale / examinateur

Bernard UGUEN
Professeur, Université de Rennes 1 / directeur de thèse

Mohamed LAARAIEDH
Enseignant Chercheur, SupCom Tunis / co-directeur de thèse

PH.D Thesis

Design of a Simulation Platform Joining Site Specific Radio Propagation and Human Mobility for Localization Applications

Nicolas AMIOT

December 2013

Nicolas AMIOT

Design of a Simulation Platform Joining Site Specific Radio Propagation and Human Mobility for Localization Applications

This Ph.D. thesis was defended December 2, 2013, at University of Rennes 1.

Assessment Committee:

Prof. Laurent CLAVIER, TELECOM-LILLE, Lille, France
Prof. Rodolphe VAUZELLE, XLIM-SIC, Poitiers, France
Ph.D. Ing. Benoît DENIS, CEA LETI, Grenoble, France
Prof. Emanuel RADOI, LEST, Brest, France

Supervisors:

Prof. Bernard UGUEN, IETR-UR1, Rennes, France
Ph.D. Mohamed LAARAIEDH, SupCom, Tunis

To Jean, Emilie and my parents.

Acknowledgments

First of all, I would like to thank my thesis supervisor, Professor Bernard Uguen, for his unfailing patience, attentiveness and availability over the last three years. I should in fact thank him for all the knowledge he handed down to me for almost a decade, first as a professor when I was still an engineering student, and then as a colleague when he hired me as a research engineer. Therefore, I thank him infinitely for having enlightened my view of electronics in particular and science in general.

I would also like to thank Mohamed Laaraiedh, my colleague and joint supervisor, for his help during the five years we shared the same office. I would hereby like to pay tribute to his professionalism and rigor which I witnessed from the beginning of his thesis until today. A few months ago, he found a new job in which I wish him all the best. I would also like to spare a kind thought for his wife and daughter who was born during our years of collaboration.

In the course of this thesis, Professor Troels Pedersen from the University of Aalborg, Denmark, was invited to spend a month at the laboratory in the framework of the European FP7 Where2 project. I would like to thank him infinitely for all the help he provided, the interest he showed and the time he devoted to me during this period. His mathematical rigor combined with his knowledge has deeply contributed to transform my work methods and the way I handle scientific issues.

In the laboratory, I would like to thank Stéphane Avrillon who has always been attentive and available. I would like to thank Noëlle Le Ber, secretary of the department, and pay tribute to her professionalism, rigor but also her devotion and humanity. I would also like to spare a kind thought for all my thesis colleagues with whom I share or have shared my office: Meriem, Ronan, Erwan, Roxana, Papa Moussa, Lei, and who have put up with me for all these years.

On a more personal level, I would like to start by thanking my friends for their moral support and for all the good times we have spent together. I would like to start with those who live far away and who I cannot see as often as I would like. I thank José for having been a faithful friend for 15 years, as well as his partner Charlotte for their warm welcome and all the good times shared together. I also thank Nico and Marion who are finally enjoying life in Bordeaux; I appreciate their support, good mood and all the fun we have had together. I would also like to thank those who are closer by and who I should nevertheless see more often. Thanks to Adrien and Louise, Pierre and Véra, Serge and Aurélie, for all the memories from when we were at engineering school and all the parties in Rennes full of music, juggling and badminton.

Last but not least, I would like to thank my partner Emilie, who encourages, supports and puts up with me, and gives me the strength I need to achieve such work. I thank her for giving me all the love and attention I need that is what gives me the strength, courage and will to succeed. And of course, our happiness would not be complete without our son Jean who has been lighting up our lives for the past year and a half. I would not be whole without them by my side. Finally, I would like to thank my parents for always giving me their support and love.

Contents

Chapter 1

Introduction

The wireless world has never been facing so many challenges. Among the most important is to find the best solutions to conciliate the two antagonist constraints of facing the exponential growth of data throughput demand and the necessity, on a global scale, to reduce the associated energy consumption. For addressing those challenges, wireless networks are to become more adaptive, more self aware of environment and of available spectral resources, more optimized, more self learning capable, in a word more cognitive. In that trend, in the wireless context, key enabling features which facilitate proaction are the localization and positioning functions.

This information of position which was originally an asset for the end user, is about to become an asset for the TelCo operator using the location information both for continuing offering added value services for the end user but especially for optimizing its network in term of throughput and energy. For instance, the knowledge of the position of the user devices allows to focus the energy of the communication to the receiver (beamforming) or to efficiently distribute the spectrum resource between the different devices.

The efficient use of the position in the communication field has been studied in European cooperative project as for example the FP7 WHERE1 (2007-2010) and FP7 WHERE2 (2010-2013). From these studies and from many others, it appears that the possibilities offered by the localization can question the initial centralized network organization. That organization existing from the beginning of mobile network to the incipient 4G network could move to a distributed organization. Indeed, distributed networks are motivated both by the localization capabilities and by the multiplication of the number of standards available on a single device.

Presuming that the future radio networks will be both distributed and heterogeneous and that localization will be a key allowing these evolutions, it is mandatory to update the existing algorithms to be compliant with the upcoming progress. So the simulation question arises.

One of the challenge engendered by those evolutions is to provide simulation tools able to validate such complex scenarios. This challenge requires multiple achievements: First, assuming an increase of both frequency and bandwidth of the standards, a sim-

ulator should be able to simulate ultra large band technologies to be compliant with most of the upcoming evolutions. Second, the wireless capability is generally linked to mobile radio devices. In terms of simulation, it means that the mobility has to be taken into account. However, from the simulation point of view, the mobility gathers two challenges: Creating a realistic agent mobility to be able to produce correct observables; Integrating the simulation mobility as a parameter of the global simulation. Third, in distributed network the constant quality of service is essentially ensured by the capability of the node to communicate with each other. If this communication is a cornerstone, mechanisms to realize it are still an open question. From this observation, it is required from the simulator to consider all possible options offered by such networks.

The main purpose of this thesis is to present a generic platform which aims to address those questions, ranging from the basics of physics of propagation toward the behavioral analysis of cooperative agents living in a realistic indoor environment, going through a proposed localization algorithm based on interval analysis methods. This thesis is an attempt to build 3 bridges between propagation and mobility, mobility and algorithms, algorithms and propagation, in the purpose of proposing new tools design with the localization function in mind but which could be suitable for wider uses in heterogeneous network context.

This work has strongly been driven by the commitment of cooperative projects. At first the FP7 WHERE1 project then the FP7 WHERE2 project and more recently the ANR CORMORAN project. The long term goal overtakes largely the short time scale of a thesis and a large part of the work borrow much to precedent work on the same field.

Document Overview

This work describes a simulation platform with three distinct layers i.e site-specific channel simulation, indoor localization, and multi-agent simulation. The document organization reflects the platform structure and is divided into four main chapters. Chapters 2, 3 and 4 address each a specific point of the platform (propagation, localization, mobility). Each one of these chapters is self consistent and provides a dedicated state of the art, a presentation of a specific formalism and an evaluation of the described method. The chapter 5 is an attempt to illustrates the potentiality of the tools introduced and presented before. It provides illustrations and comparison on various scenarios either purely based on simulation or also taking advantage of measurements data.

The chapter 2 is dedicated to the presentation of an indoor site specific radio propagation simulator based on graph-aided ray tracing. After a short state of the art on the different methods used to model the propagation channel, an history and an overview of the existing RT tools is provided. After considering that non pre-existing tools are convenient enough to correctly address the problem of the dynamic localization in the UWB context, a brief reminder on the propagation channel properties is proposed.

Then, the description of the proposed RT tool start. This description first proposes an original graph description of the environment. From that graph description, rays are built using among other the concept of signature (which is very innovative and convenient for incremental RT). Once the rays have been obtained, a second part focuses on the evaluation of the channel from those rays. This part introduces a new vectorized approach using Multi Dimensional Array (MDA) which has required to introduce a specific notation. The propagation and transmission channel are thus expressed using this notation. Finally, taking advantage of the vectorized approach, the process of a site specific multi-wall model is described. As a validation, a comparison of the interaction coefficients evaluation is performed with a pre-existing approach.

The chapter 3 is focused on the indoor heterogeneous localization algorithms. It starts with an overview of the both location strategies in wireless networks, and the available observables. Then, two types of algorithms are detailed: algebraic based algorithms and geometric based algorithms. After a short introduction mentioning the advantages of using a geometric based algorithm, the Robust Geometric Positioning Algorithm (RGPA) is proposed. The different steps of this algorithm are detailled in that part. Then, the method is validated using Monte Carlo simulations and compared to Maximum Likelihood (ML) and Weighted Least Square (WLS) approaches. Using the property of the geometric processing of producing multi-modal solutions , an heterogeneous location method based on hypothesis testing is then introduced. The method helps to resolve the ambiguity appearing when the number of radio observables is insufficient to obtain a unique position estimation, by using the power information to take a decision. The method is finally evaluated with Monte Carlo simulations and with a canonical message passing problem.

The chapter 4 addresses several problems of the dynamic platform, including the mobility, the network organization and the inter-nodes communication. The chapter starts with a state of the art on mobility models and dynamic radio simulators. Then, a simulation of agent mobility at 2 scale is described: At large scale, the agent mobility simulation uses the graph description for managing the destination of agents into an environment; At small scale, the movement of the agents to their destinations is managed by a virtual force method based on the *steering behaviors*. Once this mobility is described, the chapter focuses on the network relationships between the agents. Notably, the previously mentioned multi-wall approach is used to evaluate the Location Dependent Parameters (LDPs) simulated between the agents. Then, a basic communication protocol between the agents of the dynamic platform is introduced. Finally, the last section 4.6 is dedicated to the use of the dynamic platform to produce realistic simulations. A first dynamic scenario involving a single agent is run and LDPs and Channel Impulse Response (CIR) are produced using the site specific muti-wall and the RT tool. A second dynamic scenario is run with 2 agents moving into a synthetic environment. Those simulations demonstrate the importznce of the implemented communication protocol to achieve cooperative localization.

The chapter 5, is focused on the exploitation of the FP7 WHERE2 measurement campaign to validate the proposed algorithms. First, the measurement campaign is described including the used technology and the scenario specifications. Thereafter,

the channel parameters are extracted from the scenario to feed the location algorithms. The measured LDPs of all the points of the measurement campaign are compared to those obtained with multi-wall simulations. Then, the CIRs obtained with the RT tool are compared to the measurements for few points. Finally the localization algorithms are evaluated. First the performances of the RGPA algorithm are compared to a ML approach on the whole data set, then the method based on a hypothesis testing is applied on a specific situation using real measurements.

In addition to these four main chapters, the introduction, and the conclusion, an appendix is provided at the end of the dissertation. This appendix describes the Multi Dimensional Array (MDA) computation rules used to compute the vectorized channel.

Chapter 2

Deterministic Propagation Modeling: A Vectorized Graph-Based Approach

2.1 Introduction

In a context where the number of wireless devices and the bit rate of the emerging network continuously increase, the knowledge of the propagation channel needs to be more precise to manage properly the available radio resources. In the same time, research on the future networks reveals that the localization information could become highly valuable for optimizing the infrastructure. Considering those aspects, it appears that dedicated simulation tools have to emerge in order to take into consideration both propagation and localization aspects.

Concerning the propagation channel predicting tools, two options are generally envisaged, either based on statistical or on deterministic approaches. In localization context, deterministic tools are generally preferred due to capability to provide site specific observables required for evaluation purposes.

Section 2.2 provides first a brief summary on their utilization of RT tool for radio channel modeling. In particular, the existing tools are discussed in regard of the specific needs of the localization problem. General considerations on the propagation channel are reminded and mathematical models and their main required parameters are detailed.

In order to address the indoor localization problem in mobility, this chapter proposes the description of a novel RT tool intensively based on graph data structures described in section 2.3. The very reduction of the computation time in the dynamic context is addressed with the help of two proposed evolutions. The first evolution lies in the determination of rays themselves by using a pre-calculated objects called ray signatures in section 2.4. During the ray determination phase, some signatures can be reused when moving from a position to another. Signatures are precursors of rays which are spatially persistent. After describing the procedure to obtain rays from signature in section 2.5, the second evolution lies on the vectorization of the calculation of the field along the

rays. Section 2.6 describes the proposed vectorized approach which enables an efficient evaluation for UWB simulations. A compact mathematical formalism based on Multi Dimensional Array Multi Dimensional Array (MDA) is introduced for that purpose.

Taking advantage of that vectorized formalism, a site specific multi wall implementation is introduced in section 2.7. This approach is much simpler and thus faster than the full ray tracing however it gives access to valuable information for localization algorithms. That section ends on a comparison of the interaction coefficients evaluation to a pre-existing approach as a validation of the computation.

2.2 Context Overview : Ray-Tracing, UWB and Propagation

This section proposes a panorama of the pre-existing simulation tools, methods and knowledge about the propagation channel. A state of the art of RT tools is provided. Pointing the lack of simulator dedicated to the localization, and aware of the requirement of such simulator a quick reminder of the UWB technology is provided. Finally generalities on the deterministic channel model are provided.

2.2.1 Modeling the Propagation Channel in Regard of the Current Needs

The UHF band goes from 300MHz to 3GHz. In this band still lives today most of the used wireless standards. In the early hours of the development of those standards there has been a huge effort for predicting the wave propagation properties, which is a key factor for good design of a wireless link or network. First approaches have been to conduct measurement campaigns, but from the very early time it has been very important to get also accurate simulations from dedicated electromagnetic tools.

Sometimes, engineers need models which capture the main features of a channel for designing a system and sometimes engineers need to be specific and want to predict actual values of received quantities (received power, BER, PER, capacity, SINR, ...) on a given site with given properties. That is the reason why, one encounters :

- *statistical models*, which are most of the time specifically defined when a new standard has to be designed for some purpose
- *site-specific methods*, which are most of the time dedicated to the operator needs for coverage information for actual tuning of an operated network.

Statistical models are built from measurement campaigns where a post processing allows to extract the main characteristics of the propagation channel. Those models are generally used to evaluate the performances in terms of bit rate or error probability on a given scenario. Statistical models are very convenient because the same set of parameters is adapted for a large number of similar situations. However, in indoor situation, the channel is highly dependent on the environment, and can present very different behavior from one place to another e.g. inside a room and in a corridor. Moreover the problem of indoor localization requires to obtain site specific observables

which includes this channel variability.

Hence, for localization purposes, site specific method are generally preferred. Site specific methods are also known as deterministic methods by opposition to statistical methods. Deterministic methods are based on the propagation properties of electromagnetic waves. Depending on sought purpose, three approaches are generally considered:

- Finite Difference Time Domain (FDTD) approaches
- Method of Moments (MoM)
- The rays based approaches

The FDTD technique is an exact method. It is based on a discretization of the Maxwell's equations using central-difference approximations to the space and time partial derivatives. The resulting electric field vector components are solved for a given volume and a given instant of time. The process uses the previous electromagnetic field estimation time instant $(t-1)$ for computing a new estimation at time instant t. Despite of its higher accuracy, the method requires a powerful computation to provide results in the propagation context. Thus, the initial solving method proposed in [1] is generally coupled to other approaches to reduce the computation time [2]. For now, the exact resolution of Maxwell equation is not widely used in the propagation context mostly because the actual limitations comes more from the uncertainty of the ground truth description environment than from the accuracy of the method itself. However, this makes sense in lower band but when it comes to address frequency above UHF, asymptotic methods are very much suited and should be used for a long time still.

To cope with this computational complexity, the MoM approach [3] can be envisaged. This method requires calculating only boundary values, rather than values throughout the space. This approach is especially convenient for problems when the studied environment is in the order of magnitude of the wavelength. This approach is generally used with ray based approaches either as a validation [4] or for hybrid approaches [5].

The ray based method, are based on Geometrical Optics (GO) and Uniform Theory of Diffraction (UTD). The GO considers that an electromagnetic wave can be assimilated to a ray. This ray interacts with different element of the environment by being reflected, refracted or diffracted. The UTD allows to circumvent the discontinuities of the GO with uniform diffraction coefficient [6]. Those contributions are especially important in NLOS urban outdoor situations.

Unlike the previous method, the ray based methods cannot be used for low frequencies (typically below 100 MHz) and when interacting objects in the environment are smaller in regard of the considered wavelength. Hopefully, those two conditions becomes less restrictive considering the increase of used frequency in communication standards.

Ray determination methods are generally divided in 2 subgroups: Ray-Tracing (RT) and ray launching.

- The ray launching consists in launching rays from the transmitter and find those who reach a predefined vicinity of the receiver.
- The RT consists in tracing rays from the receiver to the transmitter. Exploring the full combinatory can be highly time consumming

2.2.1.1 Advent of Ray-Tracing (RT) Tools

The ray tracing tools have been widely used for radio coverage in urban environment during the explosive growth of the cellular telecommunication industry, [7],[8], [9], [10], [11], [12]. One important milestone for using RT tool for indoor propagation is probably in 1994, where the first comparison between ray tracing simulation and indoor measurements were reported [13]. Due to fairly accurate comparison with actual measurements, the method provoked a high interest and especially in that period of the increase of radio communication and especially in a context of cellular telecommunication emergence. At the end of the 90's, the method continued to be improved, notably in France with seminal works especially concerning the implementation of recent advance in the Uniform Theory of Diffraction [10] which was a corner stone of those emerging deterministic models. At that time the theory of diffraction was also widely used in stealth studies for Radar Cross Section reduction.

Using those improvements, the RT supports the comparison with an exact method as MoM [14]. Although RT were already much faster than exact methods, their speed has been increased significantly in 1999 by considering the pre-calculation of visibility relations [12]. That preprocessing allows to gain a 10^3 factor on a normal RT, and thus enables the possibility to address more complex scenario as complete city coverage or indoor coverage.

The same year, the complete RT coverage of Munich, Germany is compared against several measured datasets and thus demonstrated that ray-based simulation offers a high fidelity approach for RF prediction [15]. In the 2k's, the demand of cellular telecommunication still quickly increases and requires the carrier operator to quickly develop their networks. For that purpose, commercial RT tools appears during this period such as Volcano [16] , WinProp [17] Wireless Insite [18], or SigInt [19].

2.2.1.2 Current Trends in RT

To support the ongoing evolution of cellular networks in heterogeneous configurations (3G, 4G, LTE, broadcasting networks,...), it is necessary to adapt the tools for predicting the coverage and associated application services. This has been done all along the two decades of this story. During this 2 decades, both the networks and applications have evolved. Globally the networks have increased in terms of frequency and bandwidth in order to provide large bit rates. However, the number of networks has also increased to be more specific in regards of the requirements of the users. And in parallel, the users have developed new needs relative to the networks possibilities.

From those specific needs, localization is a particularly interesting application. As we will see later (Section 3.2), localization in upcoming networks would still be a requirement, a need for the user and a need for the infrastructure itself.

Paradoxically, along the 20 years of development, RT tools have mostly remained tools for predicting the propagation. The under exploitation of RT tools for testing indoor localization algorithms has recently been noticed in [20]. Nevertheless, RT tools required to be updated in order to address the upcoming problematic of e.g. localization or cooperation. One needs to predict more and more high level indicators out of the RT

tools [21]. At the convergence of the specific need of the localization and to the trend of increasing frequency in networks, appears the UWB technology.

Originally reserved to the military use, the UWB bandwidth has been declared unlicensed to use by the FCC on 14th February 2002 [22] for a band from 3.1GHz to 10.6GHz. This release of spectrum have had a huge impact of the scientific community, with the perspective of such a huge spectrum opportunities for short range communication both for low and high data rate. But that technology was quickly turned from communication application to localization applications, thanks to the achievable centimeter accuracy in ranging [23].

In addition to that interesting accuracy, UWB technology provides other valuable information on the propagation channel as reflected signal paths [24, 25]. Although most tools using such a large bandwidth are based on exact methods [26], only few RT tools take in consideration that technology. For that purpose, more details on the specificities of the UWB signal are proposed in subsection 2.2.2.

Another underlying aspect of the localization problem, is the mobility of the nodes. Taking into account the mobility of the node in a RT tool is generally a complex task. Hence, the movement of the nodes requires to recompute at each time step a new CIR to be able to estimate correct LDPs. Despite the reciprocity of the propagation channel allows to compute only one time the CIR between to two devices, the computation time becomes a bottleneck when problems with a large number of nodes are considered. The complexity of the problem does not fit with the classical ray-launching/ ray-tracing approach which is both not quick enough and not flexible enough to address that kind of problems. To cope with that issue, a solution is to envisage an incremental RT tools to avoid restarting the ray computation from the beginning for each position [27].

Finally, the problem which is faced in this thesis is the following : How a RT tool has to be designed to take into consideration a localization problem based on UWB technology ? In other words: How can we provide a fast and accurate CIR and/or LDP for a large bandwidth?

2.2.2 Specificities of the Ultra Wide Band (UWB) Technology

Among other, the previous section has presented a quick overview of the available RT tools dedicated for localization purposes. It appeared that the UWB technology presents several assets for localization purposes, that are going to be presented in this subsection.

2.2.2.1 Generalities on Ultra Wide Band (UWB)

An UWB signal is defined as a signal with a fractional bandwidth B:

$$B = \frac{f_h - f_l}{(f_h + f_l)/2} > 0.2 \tag{2.1}$$

with f_h and f_l are respectively the high frequency and low frequency of the considered band defined at -10 dB. This also corresponds to any signal with a bandwidth greater

or equal to 500 MHz. Recalling that the channel capacity C of a SISO system in AWGN condition is related to its bandwidth W and SNR as :

$$C = W\log_2(1 + SNR) \tag{2.2}$$

$$SNR = \frac{P_r}{N_0 W} \tag{2.3}$$

Where P_r is the received power and N_0 the noise power spectral density, it clearly appears that UWB technology can potentially offers very high data rate. It can also offer high time resolution and significant range at low data rate. This last property makes UWB a key technology for ranging applications. Naturally, the transmitted power has to be regulated in order not to interfere existing legitimate systems. And it is then understandable that the SNR will be a fast decreasing function of range. In 2002, The FCC unlicensed the UWB for 3 types of application : vehicle radar, imaging and monitoring (medical imaging, imaging through obstacles), and communication system. In USA, the original FCC emission mask given in Figure 2.1a. In Europe, to prevent interferences with preexisting standards, the ETSI group in charge of this regulation has imposed more restrictive conditions on the UWB emission mask, as it can be seen on Figure 2.1b .

When following the imposed regulation, the UWB theoretically has the advantage to present a very low power density spectrum, which allowsits coexistence with other system ensuring very low interferences. Moreover, the use of a large band has the advantage to limit the fast fading effects in environment generating high number of multi-paths (e.g. indoor environment). Indeed, wave cancellation effects can be resolved as long as reception is especially designed to take advantage of those multi-path (rake receiver). Another interesting property of UWB signals is their good material penetration capabilities especially in the lowest part of the spectrum.

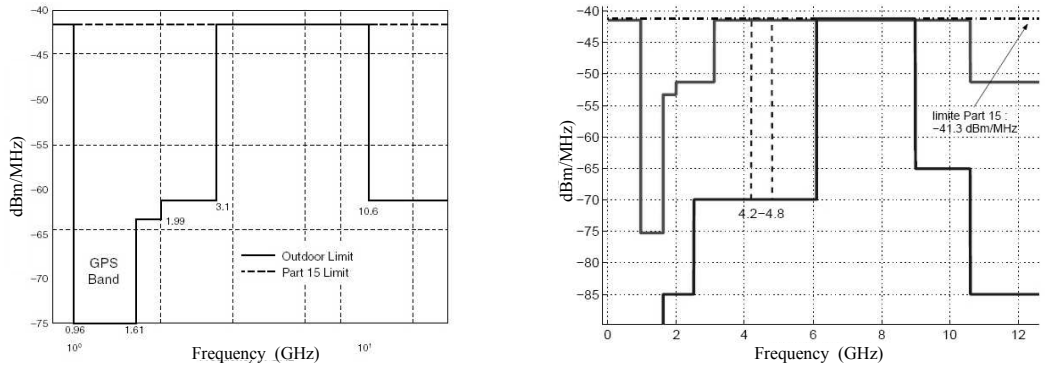

(a) FCC mask (b) ETSI mask

Fig. 2.1: UWB telecommunication emission mask for (a) USA and (b) Europe

2.2.2.2 Ultra Wide Band (UWB) Impulse Radio or Multi-Band : Different Applications

Since 2006 and the dissolution of the IEEE 802.15.3a standardization group, two main types of UWB technologies are differentiated:

1. Multi-band UWB where signals are emitted on multiple frequency carriers with bandwidth > 500 MHz.
2. The Impulse Response Ultra Wide Band (IR-UWB) which corresponds to short impulse emission (in the 1 ns order of magnitude) with or without a central carrier frequency.

The Multi-band UWB technology is generally envisaged for high rate and short range applications, taking advantage of the high capacity properties of the UWB signals. Although some marginal commercial application with e.g. the Wireless-USB the use of UWB for communication has never really convinced. The dissolution of first the IEEE 802.15.3a standardization group, and second the WiMedia Alliance, has limited the development of the UWB technology for communication, which nowadays is more concerned by the emerging 60 GHz technologies.

The IR-UWB technology, is generally used for localization purpose. Indeed, because the UWB ensures to generate small impulsions in time domain, it allows to appreciate delays with a high precision at the reception. First used by the military for radar application at 24 GHz the localization capability are offered to a larger public from the IEEE 802.15 standardizations. One example of this standard is the 802.15.4a [28], which is an amendment of the low data rate 802.15.4 (ZigBee) standard. The 802.15.4a has the advantage to offer a very low consumption and allows to connect a large number of wireless equipments for a limited cost [29]. Based on this standard, commercial companies have proposed improvement : this is especially the case of BeSpoon which recently achieves the world record of range measurement [30]. Decawave [31] provides also an embedded chip enabling an accurate position estimation. Another emerging 802.15 standard is the 802.15.6 especially dedicated in application with very low latency. This standard is especially dedicated for Wireless Body Area Networks (BAN) applications [32].

In spite of their differences, those standards obviously rely on electromagnetic waves as a support of the information exchange. In the following, some important aspects on the propagation channel are reminded.

2.2.3 Generalities on the Propagation channel

This section recalled some basics about how electromagnetic waves propagate and how they interact with the environment.

2.2.3.1 Modeling the transmission channel

The propagation channel is the space where the electromagnetic waves are propagated. The transmission channel includes everything between the transmitted signal and received signal including antennas and RF components of both transmitter an receivers.

The transmission channel can be seen as a time dependent linear filter transforming an applied input electric signal to another one, delayed, attenuated and or distorted.

Classically, according to Bello [33], it exists 4 equivalent representations of the transmission channel represented in Figure 2.2

- Time-variant transfer function $h(\tau, t)$
  which directly represent the channel impulse response of the channel. The outgoing signal $y(t)$ is obtained from the ongoing signal $x(t)$ using :

$$y(t) = \int_{-\infty}^{+\infty} x(t-\tau)h(\tau - t)d\tau \tag{2.4}$$

  where $h(\tau, t)$ is the channel impulse response of the channel at time t for a past event at τ.
- frequency variant transfer function $T(f, \nu)$
  Assuming that $X(f)$ and $Y(f)$ are the Fourier transform of $x(t)$ and $y(t)$ respectively, it is possible to write :

$$Y(t) = \int_{-\infty}^{+\infty} X(f-\nu)T(f,\nu)d\nu \tag{2.5}$$

  where $T(f, \nu)$ can be obtained from the Fourier transform on both t and τ as well as :

$$T(f,\nu) = \int_{-\infty}^{+\infty}\int_{-\infty}^{+\infty} h(t,\tau)e^{-j2\pi f\tau}e^{-j2\pi\nu t}d\tau dt \tag{2.6}$$

- Time frequency function $H(f, t)$
  This function allows to express the frequency response of the channel as a function of time. Hence, the outgoing time signal $y(t)$ can be expressed from the incoming frequency signal $X(f)$.

$$y(t) = \int_{-\infty}^{+\infty} X(f)H(f,t)e^{j2\pi ft}df \tag{2.7}$$

  Where $H(f, t)$ can be expressed with :

$$H(f,t) = \int_{-\infty}^{+\infty} h(\tau,t)e^{-j2\pi f\tau} = \int_{-\infty}^{+\infty} T(f,\nu)e^{j2\pi\nu t}d\nu \tag{2.8}$$

- Delay-Doppler function $S(\tau, \nu)$
  This function allow to express variation of the channel as a function of the Doppler. Assuming that expression :

$$y(t) = \int_{-\infty}^{+\infty} x(t-\tau)\left(\int_{-\infty}^{+\infty} S(\tau,\nu)e^{j2\pi\nu t}d\nu\right)d\tau \tag{2.9}$$

  which express that each part of the received signal is a delayed version of the emitted signal, it is possible to write :

$$S(\tau,\nu) = \int_{-\infty}^{+\infty} h(\tau,t)e^{-j2\pi\nu t}dt = \int_{-\infty}^{+\infty} T(f,\nu)e^{j2\pi f\tau}df \tag{2.10}$$

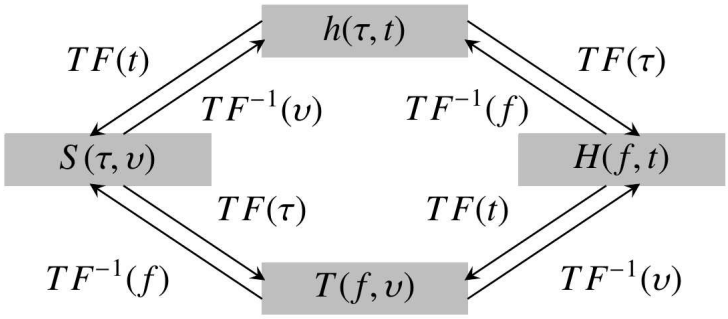

Fig. 2.2: Bello functions describing the propagation channel and connection there between.

In case any mobility is neglected the channel is said static, it is then possible to remove dependencies with time and Doppler frequency, the 4 equations can be reduced to only the channel impulse response $h(\tau)$ and the transfer function of the channel $H(f)$.

2.2.3.2 The Propagation Losses

In free space, the received power P_r at distance d can be expressed using the Friis formula [34]:

$$P_r = P_t G_r G_t \left(\frac{\lambda}{4\pi d}\right)^2 \tag{2.11}$$

where P_t is the transmitted power, G_r and G_t are the antenna gain of the receiver and the transmitter, and λ is the wavelength. At this point, it is possible to define the path loss in free space as the ratio between the transmit and the received power, neglecting the two antennas. This path loss L is usually expressed in dB with :

$$L_{dB} = -20\log_{10}\left(\frac{\lambda}{4\pi d}\right) \tag{2.12}$$

Practically, this equation is generally expressed relatively to a reference distance d_0 as :

$$\bar{L} = L_0 + 10 n_p \log_{10}\left(\frac{d}{d_0}\right) \tag{2.13}$$

with :

$$L_0 = 20\log_{10}\left(\frac{4\pi d_0}{\lambda}\right) \tag{2.14}$$

and n_p is called the path loss exponent. $n_p = 2$ for a free space situation.

For non free space propagation channel, the influence of the environment is taken into consideration by introducing a path loss exponent parameter n_p, and the possible

obstacles producing reflection, scattering, and diffraction [35, 34] are modeled with a Gaussian random variable, X_{sh}, with a standard deviation σ_{sh}. The random variable X_{sh} models the shadowing:

$$L = L_0 + 10 n_p \log_{10}\left(\frac{d}{d_0}\right) + X_{sh} \tag{2.15}$$

This formula expressed a relation between distance and propagation losses, it can be exploited for relating received power to distance for RSS ranging.

2.2.3.3 Modeling the Multipaths

In some circumstances, the transmitter and the receiver can be in direct visibility. This situation is called a Line of Sight (LOS) situation. However, it exists a large number of situations where the receiver and the transmitter are in Non Line of Sight (NLOS). This situation generally appends when obstacles are inserted between both ends of the transmission channel. The received signal is then a sum of echoes attenuated and delayed in time (and shifted in phase for baseband signal representation).

As represented in Figure 2.3, three main phenomena dictates how waves are propagated off obstacles:

- **Reflection (specular or diffuse) and Refraction**
  This phenomena happens when the wave arrives at the interface of 2 materials, as long as the irregularity of the materials are smaller in regard of the wavelength. In case where the material is completely reflecting, the entire incoming energy of the wave is reflected on the interface. This phenomena is called specular reflection. In case where the material is not completely reflecting, a part of the energy of the incoming wave is reflected whereas another part is refracted into the material. The proportion of reflected and refracted energy is directly related to the properties of the materials. If the irregularity of the materials are not negligible, the reflection is diffuse, which means that the energy is dispersed in multiple directions.
- **Transmission**
  As long has the obstacles have a finite thickness, the refracted part of an incoming waves can fully goes through the obstacle. In that case, when the refracted part goes out from the obstacle a second refraction appears. Such a multiple refraction phenomena ending by crossing a material is called a transmission.
- **Diffraction**
  Diffraction happens when a wave encounters the edge of an obstacle, large in regard of the considered wavelength. According to the Huygens principle, the diffraction point radiates energy in all the directions of space.

All those interactions create multi-path in the channel. Hence, it is usual to write the static channel impulse response $h(\tau)$ as a sum of those different paths as:

$$h(\tau) = \sum_{k=0}^{K-1} \alpha_k \delta(\tau - \tau_k) \tag{2.16}$$

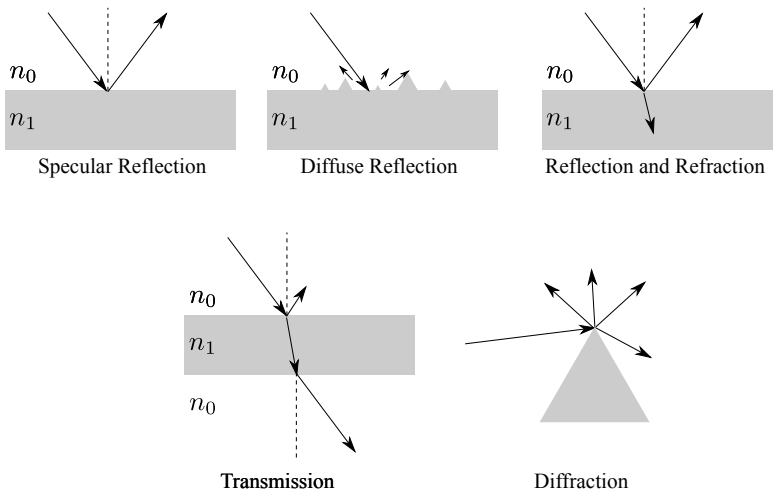

Fig. 2.3: Main propagation phenomena

where α_k and τ_k are the amplitude and the delay of a given path k, and δ refers to the Dirac delta distribution.

2.2.3.4 Effect on the Channel

Typically, the influence of the different phenomena related to the multi-paths has an influence on the received signal. Two perturbations can be observed due to those phenomenas:

- The *slow shadowing effect*:
  It corresponds to slow time variations of the received signal, due to the actual position of the obstacles between the transmitter and the receiver. This activity is generally modeled by a Gaussian random variable.
- The *fast shadowing effect*, also known as *fading*:
  It corresponds to fast time variation of the received signal due to the constructive and destructive waves process. Those activities are generally modeled respectively by a Rayleigh or a Rice law, depending whether a predominant path can be identified or not.

2.2.4 Specificities of the UWB Propagation Channel

Due to its large bandwidth, the UWB propagation channel presents some particularities which have to be taken into account to build a realistic model. The main UWB parameters and the used statistical models are reminded in the following.

2.2.4.1 Parameters for Characterization

According to Hashemi [36] and Forester [37], the parameters to be taken into account for an UWB channel model are :

- The multi-path delay spread
  which are generally summarized by :
  - τ_m : the mean delay to reach the receiver,
  - τ_{RMS} : the standard deviation around the mean delay,
  - τ_{max}: the delay of the last path.
- The number of multi-path components (MPC) achievable by the channel
  This number is calculated from the maximal attenuation threshold, determined from the strongest path.
- The multi-path energy amount
  The number of multi-paths required to get a certain level of energy.
- The multi-path amplitude fading distribution
  Required for extracting the path-loss exponent and the standard deviation parameters.

2.2.4.2 Statistical Models

It has been seen previously, that in case of indoor propagation, a large number of multi-paths appears. From the CIR, it means that the original emitted signal is attenuated and spread in time. However, it appears that the model given in (2.16) does not take into consideration the fact that the different multi-path constituting the CIR arrive by clusters. From that observation Saleh and Valenzuela [38], have proposed a CIR model, which has been updated for UWB in the 802.15.3 and 802.15.4.a standard. Using this model, the channel impulse response $h(\tau)$ can be written:

$$h(\tau) = A \sum_{l=0}^{L} \sum_{k=0}^{K} \alpha_{k,l} \delta(\tau - T_l - \tau_{k,l}) \tag{2.17}$$

where :

- A is a log-normal random amplitude value,
- L and K designate the number of components per clusters and the number of observable clusters respectively,
- T_l is the delay related to the lth cluster,
- $\tau_{k,l}$ is the delay of the kth component of the lth cluster,
- $\alpha_{k,l}$ is a weight coefficient of the kth component of the lth cluster.

The cluster delay and path delay distributions of a given cluster l reads respectively:

$$p(T_l|T_{l-1}) = \Lambda e^{-\Lambda(T_l - T_{l-1})} \text{ for } l \geq 1 \tag{2.18}$$

$$p(\tau_{k,l}|\tau_{k-1,l}) = \lambda e^{-\lambda(\tau_{k,l} - \tau_{k-1,l})} \tag{2.19}$$

with Λ and λ are the apparition rates of the clusters and to a component into a given cluster respectively.

As well, the weight coefficient can be written :

$$\alpha_{k,l} = p_{k,l} \epsilon_l \beta_{k,l} \tag{2.20}$$

where

- $p_{k,l}$ is the polarity of the signal
- ϵ_l and $\beta_{k,l}$ parameterizing the fading of a given component k in cluster l where:

$$\log_{10}(\epsilon_l \beta_{k,l}) \propto \mathcal{N}(v_{k,l}, \sigma_1 + \sigma_2) \tag{2.21}$$

$$v_{k,l} = \frac{10ln(\Omega_0) - 10T_l/\Gamma - 10\tau_{k,l}/\gamma}{ln(10)} - \frac{(\sigma_1^2 + \sigma_2^2)\ln(10)}{20} \tag{2.22}$$

$$E[|\epsilon_l \beta_{k,l}|] = \Omega_0 e^{-T_l/\Gamma} e^{-\tau_{k,l}/\gamma} \tag{2.23}$$

σ_1 and σ_2 are the standard deviation of the log-normal power attenuation respectively per cluster and by path into a cluster. Ω_0 is the energy of the first path of a given cluster. Γ and γ are the attenuation of the cluster or of the path of a given cluster. All those variable can be observed on Figure 2.4

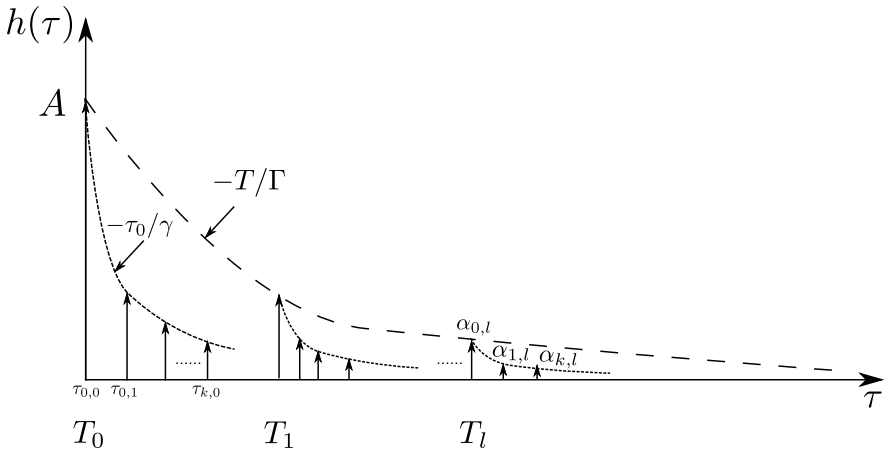

Fig. 2.4: Typical channel impulse response behavior with multiple clusters.

The 802.15.4a model has brought some modifications to this model, in order be more accurate on the apparition frequency of the clusters and the paths. In particular,

- the distribution of the paths' time-of-arrival per cluster $p(\tau_{k,l}|\tau_{k-1,l})$ is now modeled by 2 Poisson's law parametrized by λ_1 and λ_2 and a parameter μ:

$$\begin{aligned} p(\tau_{k,l}|\tau_{k-1,l}) =& \mu\lambda_1 e^{-\lambda_1(\tau_{k,l}-\tau_{k-1,l})} \\ &+ (\mu-1)\lambda_2 e^{-\lambda_2(\tau_{k,l}-\tau_{k-1,l})} \text{ for } k \geq 1 \end{aligned} \tag{2.24}$$

- The amplitude of component per cluster depends on the situation LOS :

$$E[|\alpha_{k,l}|^2] = \Omega_l \frac{1}{\gamma_l((1-\nu)\lambda_1 + \nu\lambda_2 + 1)} e^{-\tau_{k,l}/\gamma_l} \tag{2.25}$$

- or NLOS situation with :

$$E[|\alpha_{k,l}|^2] = 1 + \chi e^{-\tau_{k,l}/\gamma_r} e^{-\tau_{k,l}/\gamma_d} \frac{\gamma_r + \gamma_d}{\gamma_d} \frac{\Omega_l}{\gamma_r + \gamma_d(1-\chi)} \tag{2.26}$$

where Ω_l is the power into the lth cluster,γ_l an intra-cluster decrease factor, χ a parameter describing the attenuation of first component and γ_r and γ_d, 2 indicator on the power decrease speed into a cluster.

2.2.5 Deterministic Model of the Propagation Channel

This section starts with some basics theory on the electromagnetic wave propagation. Then, assuming an UWB propagation channel, assumptions of the GO model and interaction coefficients are reminded.

2.2.5.1 Maxwell's Equations

Any monochromatic electromagnetic wave with a pulsation ω is made of an electric field $\mathbf{E}(\mathbf{s},\omega)$ and a magnetic Field $\mathbf{H}(\mathbf{s},\omega)$, for a given observation point defined by the vector $\mathbf{s}$. Assuming that both field propagate into an inhomogeneous environment with a given permitivity $\epsilon(\mathbf{s})$ and and a permeability $\mu(\mathbf{s})$, the four Maxwell's equations are:

$$\nabla \times \mathbf{E}(\mathbf{s},\omega) + j\omega\mu(\mathbf{s})\mathbf{H}(\mathbf{s},\omega) = \vec{0} \tag{2.27}$$

$$\nabla \times \mathbf{H}(\mathbf{s},\omega) - j\omega\epsilon(\mathbf{s})\mathbf{E}(\mathbf{s},\omega) = \vec{0} \tag{2.28}$$

$$\nabla \left[\epsilon(\mathbf{s})\mathbf{E}(\mathbf{s},\omega)\right] = \vec{0} \tag{2.29}$$

$$\nabla \left[\mu(\mathbf{s})\mathbf{H}(\mathbf{s},\omega)\right] = \vec{0} \tag{2.30}$$

In the following, the simplified case of a homogeneous dielectric environment is considered. As a consequence, both the permitivity and the permeability are position independent which leads to the simplification $\epsilon(\mathbf{s}) = \epsilon$ and $\mu(\mathbf{s}) = \mu$

Using that simplification, Maxwell's equations can be re-written as the vectorized Helmholtz equation :

$$\nabla\mathbf{U}(\mathbf{s},\omega) + k^2\mathbf{U}(\mathbf{s},\omega) = 0 \tag{2.31}$$

where $\mathbf{U}(\mathbf{s},\omega)$ represents either the electric or magnetic field, k is the propagation environment wavenumber, which can be written :

$$k = \omega\sqrt{\epsilon\mu} = \frac{2\pi}{\lambda} = \frac{2\pi}{\lambda_0}\sqrt{\epsilon_r\mu_r} \tag{2.32}$$

with

- λ and λ_0 the wave length in the propagation environment and in the vacuum respectively,
- ϵ_r and μ_r the relative environment permitivity and permeability defined with:

$$\epsilon_r = \epsilon'_r - j60\sigma\lambda \tag{2.33}$$

$$\mu = \mu' - j\mu''_r \tag{2.34}$$

- σ the environment conductivity

Using both the Maxwell equations and Helmholtz equation, the following properties on the electromagnetic waves can be written :

- Assuming an homogeneous propagation environment, the energy propagate along a straight line orthogonal to the wave front. Wave fronts are plane, spherical or cylindrical surfaces where the amplitude and/or phase are constants. A set of ray is a Sheaf or a tube, using 2 caustic segments (AB and CD on Figure 2.5)

- The energy carried by a ray is continuous in for each point of time and space, both in amplitude and phase
- Rays are compliant with the Fermat principle, which establishes that the path taken between two points by a ray is the path that can be traversed in the least time. In a homogeneous environment, this corresponds to the fact that electromagnetic waves propagate in a straight line.

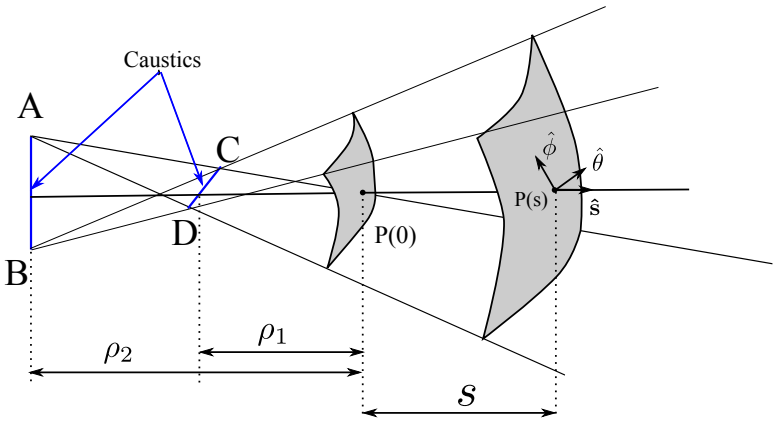

Fig. 2.5: Sheaf, cautics and local basis

2.2.5.2 Field Locality Principle

It always exists a scale where the wave can be considered locally plane. This approximation allows to generalize the principle of plane waves to all electromagnetic waves. This is known as the principle of locality of electromagnetic waves. Both electric and magnetic waves are perpendicular to the propagation direction $\mathbf{s}$. Thus, the electric field vector belongs to a plane which is perpendicular to the propagation direction. The trihedron $(\mathbf{E}, \mathbf{H}, \mathbf{s})$ is orthonormal, direct and leads to:

$$\mathbf{E} = \sqrt{\frac{\mu}{\epsilon}}(\mathbf{H} \times \mathbf{s}) \tag{2.35}$$

Thus, it is possible to limit the study to the electric field $\mathbf{E}$, expressed in the local basis $\mathbf{B} = (\mathbf{s}, \hat{\boldsymbol{\theta}}, \hat{\boldsymbol{\phi}})$ dependent of the propagation direction (2.5).

2.2.5.3 Field Expression using Geometrical Optics (GO)

The development of the electric field in GO formalism results from the works of Luneberg and Kline on the Maxwell's equations:

$$\mathbf{E}(s) = A(s, \rho_1, \rho_2)\mathbf{E}(0)e^{-jk\psi(s)} \tag{2.36}$$

$$\mathbf{E}(s) = \begin{bmatrix} 0 \\ E_{\parallel}(s) \\ E_{\perp}(s) \end{bmatrix}_B = A(s, \rho_1, \rho_2) \begin{bmatrix} 0 \\ E_{\parallel}(0) \\ E_{\perp}(0) \end{bmatrix}_B e^{-jk\psi(s)} \tag{2.37}$$

where

- $A(s, \rho_1, \rho_2)$ is the amplitude ratio between $\mathbf{E}(s)$ and $\mathbf{E}(0)$, as known as the divergence factor :

$$A(s, \rho_1, \rho_2) = \sqrt{\frac{\rho_1 \rho_2}{(\rho_1 + s)(\rho_2 + s)}} \tag{2.38}$$

- s is the distance between $P(0)$ and $P(s)$ (Figure 2.5)
- $\psi(s) = s$ is a phase function for a given observation point $P(s)$
- ρ_1 and ρ_2 are the two principals radius of curvature of the wave front, measured on the ray, from the reference central point $P(0)$. This point corresponds to the position of the source or to an interaction point between the wave and the surface.

Because, following the plane wave assumption, the electric field is assumed orthogonal to the propagation direction $\hat{\mathbf{s}}$, the field component along the axis $\hat{\mathbf{s}}$ is equal to zero. The field is then expressed in a basis $\mathbf{B}$ depending only on the parallel and perpendicular components orthogonal to the direction of propagation:

$$\mathbf{E}(s) = \begin{bmatrix} E_{\parallel}(s) \\ E_{\perp}(s) \end{bmatrix}_B = A(s, \rho_1, \rho_2) \begin{bmatrix} E_{\parallel}(0) \\ E_{\perp}(0) \end{bmatrix}_B e^{-jks} \tag{2.39}$$

The two radius of curvature ρ_1 and ρ_2 are modified all along the ray trajectory. Hence, each time the ray encountered an obstacle along its trajectory, those radius of curvatures have to be updated. Depending on the obstacle encountered by the ray, one of the interaction described in subsection 2.2.3.3 can occur.

2.2.5.4 Interaction Coefficients

The evolution of the electric field value, depends on the type of interactions encountered during propagation. This section describe the weighting coefficients of the electric field depending of the interaction type.

Reflection Coefficient

On Figure 2.6, are presented a reflection and refraction phenomena. The interface point on the dielectric material surface is called Q. The angles θ^i,θ^r and θ^t designate the incidence angle, the reflection angle and the refraction angle respectively. Those angles are defined in regard of the tangent plan normal $\hat{\mathbf{n}}$. The reflected field evaluated in P_R, at distance s^r of the reflection point Q can be written :

$$\begin{bmatrix} E^r_{\parallel}(s^r) \\ E^r_{\perp}(s^r) \end{bmatrix}_{B^r} = \sqrt{\frac{\rho^r_1}{\rho^r_1 + s^r} \frac{\rho^r_2}{\rho^r_2 + s^r}} \begin{bmatrix} R_{\parallel} & 0 \\ 0 & R_{\perp} \end{bmatrix} \begin{bmatrix} E^i_{\parallel}(s^i) \\ E^i_{\perp}(s^i) \end{bmatrix}_{B^i} e^{-jks^r} \tag{2.40}$$

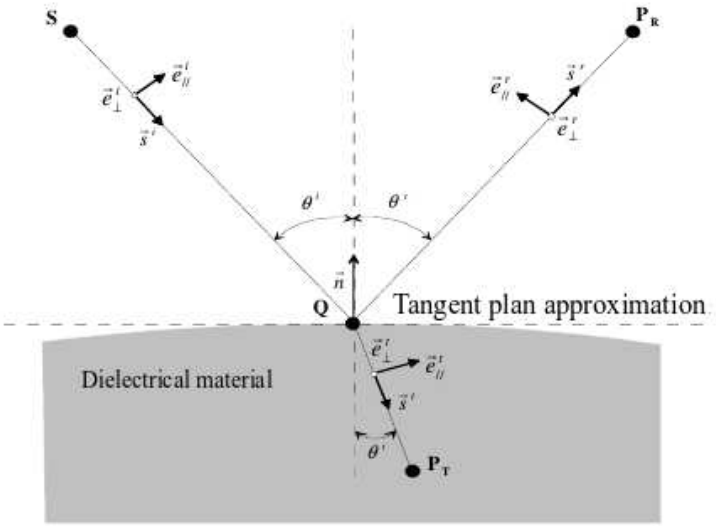

Fig. 2.6: Reflexion and refraction basis

where ρ_1^r and ρ_2^r are the principal radius of curvature of the reflected wave front at the reference point and $B^r = (\mathbf{s}^r, \mathbf{e}_{\parallel}^r, \mathbf{e}_{\perp}^r)$ a local direct reflected base. In case the surface is plane, $\rho_1^r = \rho_1^i$ and $\rho_2^r = \rho_2^i$.

Considering that the surface is unlimited and has a permitivity ϵ_r, it is possible to write the soft reflection coefficient $R_{\parallel}$ and the hard reflection coefficient $R_{\perp}$, in the case where $\theta^i = \theta^r$, with:

$$R_{\parallel} = \frac{\epsilon_r \cos\theta^i - \sqrt{\epsilon_r - \sin^2\theta^i}}{\epsilon_r \cos\theta^i + \sqrt{\epsilon_r - \sin^2\theta^i}} \tag{2.41}$$

$$R_{\perp} = \frac{\cos\theta^i - \sqrt{\epsilon_r - \sin^2\theta^i}}{\cos\theta^i + \sqrt{\epsilon_r - \sin^2\theta^i}} \tag{2.42}$$

It may be noticed that in case the surface is perfectly conducting, the reflection coefficient don't depend on the wavelength anymore and are equal to :

$$R_{\parallel} = +1 \tag{2.43}$$

$$R_{\perp} = -1 \tag{2.44}$$

$$\tag{2.45}$$

Transmission Coefficient

Similarly the transmitted field can be written :

$$\begin{bmatrix} E_{\parallel}^t(s^t) \\ E_{\perp}^t(s^t) \end{bmatrix}_{B^t} = \sqrt{\frac{\rho_1^t}{\rho_1^t + s^t}\frac{\rho_2^t}{\rho_2^t + s^t}} \begin{bmatrix} T_{\parallel} & 0 \\ 0 & T_{\perp} \end{bmatrix} \begin{bmatrix} E_{\parallel}^i(s^i) \\ E_{\perp}^i(s^i) \end{bmatrix}_{B^i} e^{-jks^t} \tag{2.46}$$

where ρ_1^t and ρ_2^t are the principals radius of curvature of the wave front transmitted to the reference point and $B^t = (\mathbf{s}^t, \mathbf{e}_\parallel^t, \mathbf{e}_\perp^t)$ a local direct transmitted base. In a case where the surface is plane, $\rho_1^r = \rho_1^i$ and $\rho_2^r = \rho_2^i$. If the interface is plane, the expression of the radius of curvature can be written [10]:

$$\rho_1^t = \rho_1^i \alpha^{-1} \tag{2.47}$$

$$\rho_2^t = \rho_2^i \alpha^{-1} \gamma^{-2} \tag{2.48}$$

with :

$$\alpha = \frac{1}{\sqrt{\epsilon_r}} \tag{2.49}$$

and

$$\gamma = \frac{\cos\theta^i}{\cos\theta^t} \tag{2.50}$$

In case of indoor propagation, walls are constituted of different layers of different materials. Such a stack is called a slab. Then, the reflection and refraction effects are repeated at each interface with a new material.

Thus, the transmission parameter is a complex function which depends on the type and the number of stacked material into the slab. At each different interface constituting the slab, a reflection refraction phenomena appears. According to [39], it is possible to write the components of the outgoing electric field as a sum of the electric fields outgoing from each materials. This particular point is treated in section 2.6.3.

2.3 Layout's Graphs Description

The previous section has presented a state of the art on propagation toolsand some considerations on the propagation channel models especially on the UWB technology. With this section begins the description of a dedicated RT tool for localization. In particular, this section focuses on the graph based environment description.

2.3.1 Graphs Notation

From the graph theory, a graph is a connected set of nodes. Graphs can be oriented or non oriented. In the sequel, we will refer to graph also as a specific high level data structure. In that case, those graph data structures embed specific dictionaries associated with nodes or edges, to store the relevant piece of information related to their nature.

Throughout the manuscript, the introduced graphs will be indexed with a letter x related to their name.

The following notations for graph description are used :

A graph indexed x from its name is noted $\mathcal{G}_x(\mathcal{V}_x, \mathcal{E}_x)$ where $\mathcal{V}_x$ and $\mathcal{E}_x$ are respectively the set of nodes and the set of edges of the graph $\mathcal{G}_x$.

For a graph $\mathcal{G}_x(\mathcal{V}_x, \mathcal{E}_x)$ having N nodes and E edges,

$$\mathcal{V}_x = \{v_x^0, \ldots, v_x^{N-1}\} \tag{2.51}$$

$$\mathcal{E}_x = \{e_x^0, \ldots, e_x^{E-1}\} \tag{2.52}$$

where for an oriented graph

$$e_x^k = (\text{tail}(e_x^k), \text{head}(e_x^k)) \in \mathcal{V}_x \times \mathcal{V}_x$$

2.3.2 The Graphs for Layout Description

This section introduce the 4 graphs required:

- gor layout description
  - the graph of structure $\mathcal{G}_s(\mathcal{V}_s, \mathcal{E}_s)$, (non oriented)
  - the topological graph $\mathcal{G}_t(\mathcal{V}_t, \mathcal{E}_t)$, (non oriented)
- gor signatures determination
  - the graph of visibility $\mathcal{G}_v(\mathcal{V}_s, \mathcal{E}_v)$, (non oriented)
  - the graph of interactions $\mathcal{G}_i(\mathcal{V}_i, \mathcal{E}_i)$, (**oriented**)

2.3.2.1 $\mathcal{G}_s(\mathcal{V}_s, \mathcal{E}_s)$ the graph of structure

The Graph $\mathcal{G}_s$, is used to describe the simulaton environement. It is the first graph to be defined. This graph is directly obtained from a node list and edge list. This graph is being modified all along the layout editing phase which is done with a dedicated built-in editor. It can also be generated from proper conversion from other existing format as XML open street map format (.osm) [40]. All the other graphs are derived from processing on its nodes and edges.

In the indoor case, a layout is generally a building floor plan. Each segment describing the layout outlines is associated to a node of $\mathcal{G}_s$. As well, the two points bounding each segments are also associated to two nodes of $\mathcal{G}_s$. Conventionally, nodes of $\mathcal{G}_s$ associated to segments are denoted with a positive integer, whereas nodes associated to points are denoted with a negative integer. By construction all nodes with a positive index (segments) are linked to two nodes with negative indexes (points). Note that the inverse is not true, a point can be connected to more that two segments.

Figure 2.7 shows an example of the generated graph of structure $\mathcal{G}_s$.

Positive nodes of $\mathcal{G}_s$ have attached a meta-data dictionary containing the information listed below which is useful either for further mechanical or electromagnetic processing:

- a list of the connected points indexes (a.k.a. the nodes of $\mathcal{G}_s$ with a negative index),
- the name of the slab associated to the segment,
- a position,
- a height value,
- a normal vector associated to segment,
- a boolean transition indicator.

The list of connected points is directly deduced from the graph connectivity. The slab's name is specified during the layout edition.

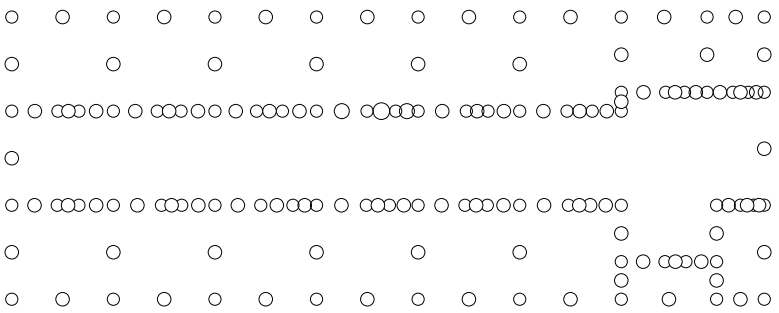

Fig. 2.7: example of Graph of structure $\mathcal{G}_s$. White dots represent segments (nodes with positive index) and hatched dots represents points (nodes with a negative index) of the layout.

A slab is a stack of different constitutive materials of different thickness. This description requires the knowledge of all slab elements with their electromagnetic properties. The slab description is developped in section 2.6.4.

The position is given as a vector in $\mathbb{R}^3$. The height and elevation values allow to address situations where a segment is made with different slabs at different heights. The list of cycle numbers contains all cycles . At most, a node can be surrounded by two cycles. This information is filled once the topological graph $\mathcal{G}_t$ has been built. More information about $\mathcal{G}_t$ and cycles is provided in 2.3.2.2. The signed normal vector is used to determine the orientation of the segment. The transition indicator indicates if the segment can mechanically be crossed (by an agent).

In this connection, transition indicator is very useful for describing air walls. Air walls are virtual partition which affect neither mechanic nor electromagnetic computation. That abstraction has been introduced to reduce complexity during higher-level graph computation.

2.3.2.2 The Graph of Topology $\mathcal{G}_t$

The topological graph $\mathcal{G}_t$ aims to abstract the structural graph $\mathcal{G}_s$ to cycles representation.

A graph cycle is a closed path starting and finishing at the same node, where nodes and edges of that path can be only used once.

Cycles are convenient to obtain a high-level structure information of the layout in order to increase the processing speed and derive other useful graphs. For the problem at hand, $\mathcal{G}_t$ is built from $\mathcal{G}_s$ nodes in respect of three rules :

1. all cycles have to be disjoint, which means none cycle must be included into another.
2. all nodes of $\mathcal{G}_s$ with a negative index has to be used for building cycles
3. Each of those nodes can only be used for building two cycles at most.
4. each node of $\mathcal{G}_s$ with a positive index can link 2 cycles at most.

The first step to build $\mathcal{G}_t$ is to obtain a cycle basis from the decomposition of $\mathcal{G}_s$. Because $\mathcal{G}_s$ is an undirected graph it can be defined as a cycle space. It exists a set of

linearly independent cycles named basis cycles, which can represent $\mathcal{G}_s$ [41].

The basis cycle decomposition is performed by using a specific algorithm described in [42]. Algorithm 1 describes the building process of $\mathcal{G}_t$.

Algorithm 1 building topological Graph $\mathcal{G}_t$

Require: $\mathcal{G}_s$
$C = \text{cycle\_basis}(\mathcal{G}_s)$
$\mathcal{G}_t = \text{Graph}(C)$
$\mathcal{G}_t = \text{remove\_included\_cycles}(\mathcal{G}_t)$
$\mathcal{G}_t = \text{decompose}(\mathcal{G}_t)$

Definition 1 (Adjacent Cycles) *Two cycles are adjacent if they share at least one segment. Cycles which are only connected through a single point are not considered adjacent and though are not connected*

As shown in Figure 2.8, nodes of the resulting $\mathcal{G}_t$ graph represent cycles. By construction, edges connect adjacent cycles.

Fig. 2.8: An example of topological Graph $\mathcal{G}_t$. Nodes of this graphs are cycles. Edges of this graph connect adjacent cycles

Both $\mathcal{G}_s$ and $\mathcal{G}_t$ are required for a precise description and organization of a layout. They are also mandatory to build higher level graphs relative to propagation.

2.3.3 Graphs for Helping Determination of Signatures

In addition to structural and topological information, propagation-specific graph must be built to perform a GO/UTD based ray-tracing.

2.3.3.1 Graph of Visibility $\mathcal{G}_v$

The graph of visibility $\mathcal{G}_v$ is used to describe the optical visibility between points and segments of a layout.

The nodes of $\mathcal{G}_v$ are the same as those of $\mathcal{G}_s$. The edges of $\mathcal{G}_v$ connect nodes related through an "optical" visibility relationship. Those visibility relations might concern two segments, a point and a segment or two points.

Depending on the geometry, some points are candidate for becoming diffraction points. A simple rule for determining a diffracting point exploits the sign and the degree of the node.

Definition 2 (Diffracting Node) *A diffracting node ν_s is such that*

$$(\nu_s < 0) \ \textbf{\textit{and}} \ (degree(\nu_s) \leq 2)$$

where degree of a node designate the number of edges incident to the vertex

Algorithm 2, describes the different steps of building $\mathcal{G}_v$. This is a divide and conquer approach. The graph of visibility for each cycle of the layout is obtained independently and composed in a loop to obtained the overall graph. One variant has been implemented where we do not compose graph but keep each graph of visibility separated in a dictionary indexed by the cycle number.

An example of the resulting graph processed by this algorithm is shown in Figure 2.9.

Algorithm 2 build Graph of visibility $\mathcal{G}_v$

Require: $\mathcal{G}_s$, $\mathcal{G}_t$
  $\mathcal{G}_v$ = Graph() ▷ Instantiate a void graph
  for *cycle* **in** $\mathcal{G}_t$ **do**
    $\mathcal{G}_v(cycle)$ = buildGv($\mathcal{G}_s, cycle$) ▷ build $\mathcal{G}_v$ for *cycle*
    $\mathcal{G}_v$ = compose($\mathcal{G}_v, \mathcal{G}_v(cycle)$)
  end for
  Return($\mathcal{G}_v$)

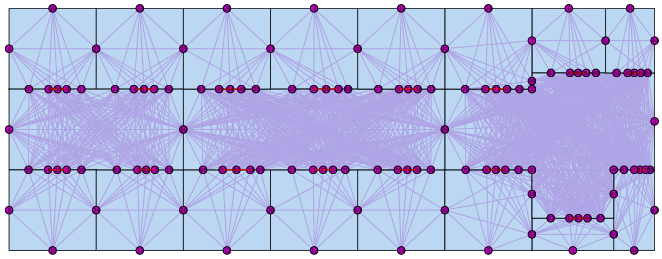

Fig. 2.9: Graph of Visibility $\mathcal{G}_v$

One important requirement for future development in 2.4.2 is to retrieve the type of interaction. Here, one difficulty is to make the distinction between reflection and transmission. The proposed manner to solve this problem is to introduce a new graph derived from $\mathcal{G}_v$ which makes clear for each segment what is the involved type of interaction.

2.3.3.2 Graph of Interactions G_i

The graph of interactions $\mathcal{G}_i$ is derived from the $\mathcal{G}_v$. The graph of interactions $\mathcal{G}_i$ is a directed graph which gathers all the possible interactions between nodes $\mathcal{V}_s$ of a given cycle of $\mathcal{G}_t$.

Practically, a single interaction on a segment of $\mathcal{G}_v$ can potentially generate up to 4 interactions in $\mathcal{G}_i$: The reflection from a side of the interaction, and/or the reflection from the other side, and/or the transmission in one way and/or the transmission in the other way. Figure 2.10 shows these distinctions.

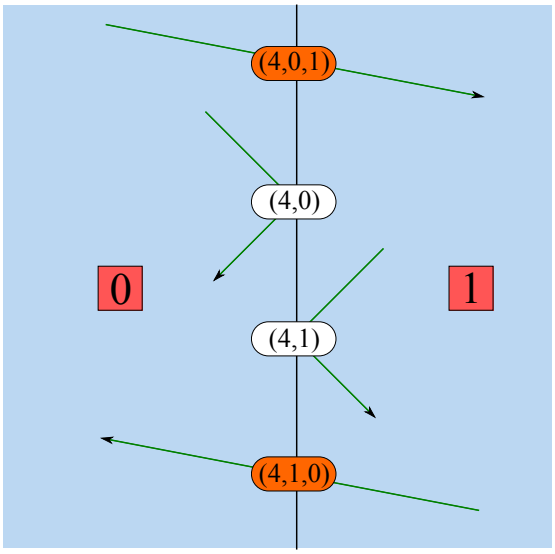

Fig. 2.10: The 4 potential types of interactions on a given material

Three types of electromagnetic interactions are to be considered: the transmission (T), the reflection (R), and the diffraction (D). According to the notation defined in 2.3.1:

- (v_s^i, v_t^k) is a reflection on a segment $v_s^i > 0$ and cycle v_t^k
- (v_s^i, v_t^k, v_t^l) is a transmission across segment $v_s^i > 0$ and from cycles v_t^k to cycle v_t^l.
- (v_s^j) is a diffraction on node $v_s^j < 0$

Algorithm 3 describes how is created $\mathcal{G}_i$ from $\mathcal{G}_v$. The resulting graph is shown in Figure 2.11.

Nodes of $\mathcal{G}_i$ consists of heterogeneous interactions tuples. Hence written, it can be observed that the node names of $\mathcal{G}_i$ are tuples which contain information about:

- the index of involved segments or points from the $\mathcal{G}_s$ nodes,
- a type of interaction reflexion or diffraction depending on the number of elements in tuple.

That specific description would be very convenient in the new section, for the Signature description.

Algorithm 3 Build graph of interactions $\mathcal{G}_i$

Require: $\mathcal{G}_s$, $\mathcal{G}_t$, $\mathcal{G}_v$
▷ Build $\mathcal{G}_i$ nodes
for n **in** nodes($\mathcal{G}_v$) **do** ▷ Loop on $\mathcal{G}_v$ nodes
if $n < 0$ **then** ▷ If node is a point
$\mathcal{G}_i$.add_node.((n)) ▷ add diffraction node
else ▷ if node is a segment
cy$_0$,cy$_1$=get_cycles($\mathcal{G}_s, n$)
$\mathcal{G}_i$.add_nodes.$((n, cy_0, cy_1), (n, cy_1, cy_0))$ ▷ 2 transmissions
$\mathcal{G}_i$.add_nodes.$((n, cy_0), (n, cy_0)))$ ▷ 2 reflections
end if
end for

▷ Build $\mathcal{G}_i$ edges
for $inter_1$ in $nodes(\mathcal{G}_i)$ **do**
$linter$ = visi2inter($\mathcal{G}_v, inter_1$) ▷ find nodes of $\mathcal{G}_i$ in visibility, from nodes of $\mathcal{G}_v$
for $inter_2$**in** $linter$ **do**
if ($inter_2$ is Reflection) **or** ($inter_2$ is Diffraction) **then**
$\mathcal{G}_i$.add_edge $((inter_1, inter_2))$
else if $inter_2$ is Transmission **and** $inter_1$is Transmission **then**
$\mathcal{G}_i.add\_edge((inter_1, inter_2))$
end if
end for
end for

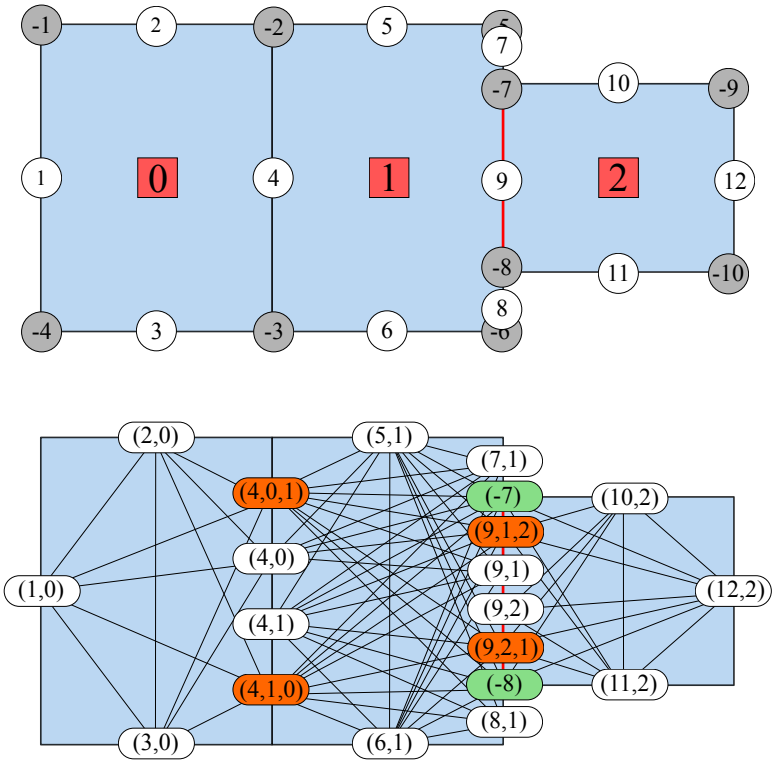

Fig. 2.11: The graph on the top combines several graphs : segments nodes (positive number in white dots) and points nodes (negative numbers in grey dots) are from $\mathcal{G}_s$ and the cycle number (number in red square) are from $\mathcal{G}_t$. The graph below is the associated graph of interaction $\mathcal{G}_i$. The nodes corresponding to reflection, transmission and diffraction are colored in white, orange and green respectively. Segment 4 corresponds to different type of interactions : $(4, 0)$ reflection toward cycle 0, $(4, 1)$ reflection toward cycle 1, $(4, 0, 1)$ transmission from cycle 0 to 1, and $(4, 1, 0)$ transmission from cycle 1 to 0

2.4 From Graphs to Ray Signatures

In the following is introduced the new concept of ray signature. First the motivations behind that concept and the definition of signatures are given. Thereafter, the method to obtain those signatures from the previous graph description is detailed.

2.4.1 Motivation of the Introduction of Ray Signature

The propagation channel parameters are time varying due to the motion of the extremities of the radio link or the motion of humans or objects evolving in the propagation environment. In spite of those movements, path persistency has been defined in [43] as the evolution of a particular path of the CIR which exhibits a differential change of a given feature in accordance with its differential motion. Considering a RT approach, such differential change into the CIR, should be related to something observable into the rays, or more precisely into their related lists of interaction points. It appears that they are related by the **nature** of the involved slabs and the **type** of interactions on those slabs.

Based on this observation, it can be defined a ray-signature (or a signature) as an individual contributor of the stationary part of the CIR. By extension, the stationary part of the CIR is obtained by aggregating all the signatures.

Hence defined, it can be observed that a signature is not hardly related to a transmitter or a receiver position and can be the same for a small (or in some cases large) position change. This means that it can be used for generating a whole set of rays between two different regions. The use of graph for modeling stochastic channel has also been introduced and developed in [44] to describe the channel reverberation inside a room. This study has shown that the reverberating part of the CIR inside a reverberating volume can be explained and reproduced with high fidelity by using a graph description. Inspired by this representation, it is proposed in the following to take advantage of a graph description for building site specific signatures.

2.4.2 Obtaining the Signatures from $\mathcal{G}_i$

The concept of signature is introduced to build 2D rays. A 2D ray $\tilde{\mathbf{r}}$, as defined in Def. 3, is obtained in $(O, \hat{\mathbf{x}}, \hat{\mathbf{y}})$ and the tilde notation indicates that their components are given with only 2 dimensions. Hence, a 2D ray $\tilde{\mathbf{r}}$ is a sequence of interactions points $\tilde{\mathbf{p}}_l$ defined in $(O, \hat{\mathbf{x}}, \hat{\mathbf{y}})$.

Definition 3 (2D rays) *2D rays are 2D poly-lines whose each segment is delimited by interaction or termination points in* $(O, \hat{\mathbf{x}}, \hat{\mathbf{y}})$. *A 2D ray* $\mathbf{r}$ *with* L_h *interaction points is an ordered list of* $L_h + 2$ *points, assuming that 2 points* $\tilde{\mathbf{p}}_{-1}$ *and* $\tilde{\mathbf{p}}_{L_h}$ *representing either the transmitter or the receiver are added in first and last position respectively. Thus, a 2D ray can can be written:*

$$\tilde{\mathbf{r}} = [\tilde{\mathbf{p}}_{-1}, \tilde{\mathbf{p}}_0, \ldots, \tilde{\mathbf{p}}_{L_h-1}, \tilde{\mathbf{p}}_{L_h}] \tag{2.53}$$

As defined in Def. 4, a signature is the association of 2 ordered sequences : the nature of the support (slab) and the type of the interactions. The nodes of $\mathcal{G}_i$, as described in section 2.3.3.2, contain information about the cycles involved in the interaction, the nature of the interaction, the associated index corresponding to a slab. Those two last information can be advantageously used to build a signature.

Definition 4 (Ray Signature) *A ray signature* $\mathbf{s} = \mathcal{S}(\tilde{\mathbf{r}})$ *of a 2D ray* $\tilde{\mathbf{r}}$ *with* L_h *interactions is the association of two ordered sequence of length* L_h*. A first sequence provides the nature of the slab and a second sequence provides the associated type of interaction among (R,T,D). Signatures can be obtained either from determination of paths in the oriented graph* $\mathcal{G}_i$ *or derived from an existing ray. Thus, a signature can be written:*

$$\mathbf{s} = \begin{bmatrix} n_0 & \dots & n_l & \dots & n_{L_h-1} \\ t_0 & \dots & t_l & \dots & t_{L_h-1} \end{bmatrix} \tag{2.54}$$

Obtaining a signature from a sequence of nodes of $\mathcal{G}_i$ is a 2 steps process:

- determining two subsets of nodes $\mathcal{V}_i^{\tilde{\mathbf{p}}_{-1}}$ and $\mathcal{V}_i^{\tilde{\mathbf{p}}_{L_h}}$ from $\mathcal{G}_i$ which are in direct visibility of $\tilde{\mathbf{p}}_{-1}$ and $\tilde{\mathbf{p}}_{L_h}$ respectively.
- finding all simple paths (paths with no repeated nodes) between any distinct pair of interactions $(\mathcal{V}_i^{\mathbf{p}_{-1}}, \mathcal{V}_i^{\mathbf{p}_L})$.

Those return paths are ordered sequences of nodes $\mathcal{G}_i$, which can be easily transformed into signatures. Algorithm 4 describes that procedure.

Algorithm 4 Determination of signatures

Require: $\tilde{\mathbf{p}}_{-1}$,$\tilde{\mathbf{p}}_{L_h}$
Require: $\mathcal{G}_i$
  $\mathbf{S} = [\,]$ ▷ Initialize an empty list
  $\mathcal{V}_i^{\tilde{\mathbf{p}}_{-1}} \leftarrow$ get-visible-interactions$(\mathcal{G}_i, \tilde{\mathbf{p}}_{-1})$
  $\mathcal{V}_i^{\tilde{\mathbf{p}}_{L_h}} \leftarrow$ get-visible-interactions$(\mathcal{G}_i, \tilde{\mathbf{p}}_{L_h})$
  for *it in* $\mathcal{V}_i^{\tilde{\mathbf{p}}_{-1}}$ **do**
    for *ir in* $\mathcal{V}_i^{\tilde{\mathbf{p}}_{L_h}}$ **do**
      S.append(all-simple-paths$(\mathcal{G}_i, \tilde{\mathbf{p}}_{-1}, \tilde{\mathbf{p}}_{L_h})$)
    end for
  end for
  $\mathbf{s}$ = reshape-to-signature(**S**)

2.5 Getting Rays out of Signatures

This section describes the 2 steps to obtain a 3D ray from a signature. First a 2D ray is obtained from a signature. Second, the 2D ray is extended with multiple floor/ceil reflections to create a 3D ray.

2.5.1 Getting 2D Rays out of Signatures

The determination of a 2D ray in the plane $(O, \hat{\mathbf{x}}, \hat{\mathbf{y}})$ from its signature is a 3 steps process.

- The first step consists in extracting the tail and head position of interaction segments from the signature.
- The second step consists in calculating intermediate points from one termination (T or R) in following the sequence of interactions of the signature.
- The third step consists in calculating valid interaction points on segments with the help of previously found intermediate points.

2.5.1.1 Phase 1 : Extraction of Interactions Points Segments

Out of the signature obtained from algorithm 4, it is possible to get the segment or point number n_l and from graph $\mathcal{G}_s$ the associated terminations ($\mathbf{a}_l$ and $\mathbf{b}_l$) defined with :

$$\mathbf{a}_l = [x_{a_l}, y_{a_l}]^T, \tag{2.55}$$
$$\mathbf{b}_l = [x_{b_l}, y_{b_l}]^T, \tag{2.56}$$

In case the interaction is a diffraction tail and head points, for shape uniformity, a point is represented as a segment of length 0 whith the two terminations having the same coordinates $\mathbf{g}_l = (\mathbf{a}_l, \mathbf{a}_l)$.

Hence, from the whole signature $\mathbf{s}$, 2 ordered lists of tail and head point coordinates $\tilde{\mathbf{p}}_a$ and $\tilde{\mathbf{p}}_b$ are extracted:

$$\tilde{\mathbf{p}}_a = [\mathbf{a}_0, ..., \mathbf{a}_{L_h-1}] \tag{2.57}$$
$$\tilde{\mathbf{p}}_b = [\mathbf{b}_0, ..., \mathbf{b}_{L_h-1}] \tag{2.58}$$

2.5.1.2 Phase 2 : Determination of The Sequence of Intermediate Points

The sequence of intermediate points is determined from the knowledge of the transmitter (or receiver) position $\tilde{\mathbf{p}}_{-1} = [x_{-1}, y_{-1}]^T$, the sequence of interactions segments obtained in phase 1 and also very importantly the type of interaction because the computation of intermediate points depends on the nature of the interaction as follow:

- (R) : the image of the current point w.r.t the segment,
- (T) : the current point itself
- (D) : the diffraction (interaction) point itself

The sequence of intermediate points is written as a $(2 \times L_h)$ vector:

$$\mathbf{m} = [\mathbf{m}_0, ..., \mathbf{m}_{L_h-1}]$$

with :

$$\mathbf{m}_l = [x_l, y_l]^T$$

$\mathbf{m}_0$ position depends on the type of the first interaction as:

– (R) : $\mathbf{m}_0 = \mathbf{K}_0\tilde{\mathbf{p}}_{-1} + \mathbf{v}_0$
– (T) : $\mathbf{m}_0 = \tilde{\mathbf{p}}_{-1}$
– (D) : $\mathbf{m}_0 = \mathbf{a}_0$

and generally, $\mathbf{m}_k$ position depends on the type of the l^{th} interaction:

– (R) : $\mathbf{m}_l = \mathbf{K}_l\mathbf{m}_{l-1} + \mathbf{v}_l$
– (T) : $\mathbf{m}_l = \mathbf{m}_{l-1}$
– (D) : $\mathbf{m}_l = \mathbf{a}_l$

where $\mathbf{K}_l$ is a reflection matrix defined as:

$$\mathbf{K}_l = \begin{bmatrix} a_l & -b_l \\ -b_l & -a_l \end{bmatrix} \tag{2.59}$$

and $\mathbf{v}_l$ is a translation vector defined as :

$$\mathbf{v}_l = [c_l, d_l]^T \tag{2.60}$$

with

$$a_l = \frac{(x_{a_l}-x_{b_l})^2-(y_{a_l}-y_{b_l})^2}{(x_{a_l}-x_{b_l})^2+(y_{a_l}-y_{b_l})^2} \tag{2.61}$$

$$b_l = \frac{2(x_{b_l}-x_{a_l})(y_{a_l}-y_{b_l})}{(x_{a_l}-x_{b_l})^2+(y_{a_l}-y_{b_l})^2} \tag{2.62}$$

$$c_l = 2\frac{x_{a_l}(y_{a_l}-y_{b_l})^2+y_{a_l}(x_{b_l}-x_{a_l})(y_{a_l}-y_{b_l})}{(x_{a_l}-x_{b_l})^2+(y_{a_l}-y_{b_l})^2} \tag{2.63}$$

$$d_l = 2\frac{x_{a_l}(y_{a_l}-y_{b_l})(x_{b_l}-x_{a_l})+y_{a_l}(x_{b_l}-x_{a_l})^2}{(x_{a_l}-x_{b_l})^2+(y_{a_l}-y_{b_l})^2} \tag{2.64}$$

The coordinates of all intermediates points are obtained by solving the following linear system:

$$\mathbf{A}\mathbf{m} = \mathbf{y} \tag{2.65}$$

$$\mathbf{A} = \begin{bmatrix} \mathbf{I}_2 & & & \\ \{-\mathbf{K}_1|-\mathbf{I}_2|\mathbf{O}_2\} & \mathbf{I}_2 & & \\ & \ddots & \ddots & \\ & & \{-\mathbf{K}_{L_h-1}|-\mathbf{I}_2|\mathbf{O}_2\} & \mathbf{I}_2 \end{bmatrix} \tag{2.66}$$

$$\mathbf{y} = \begin{bmatrix} \{\mathbf{K}_0\tilde{\mathbf{p}}_{-1} + \mathbf{v_0}|\tilde{\mathbf{p}}_{-1}|\mathbf{a}_0\} \\ \{\mathbf{v_1}|\mathbf{z}_2|\mathbf{d}_1\} \\ \vdots \\ \{\mathbf{v}_{L_h-1}|\mathbf{z}_2|\mathbf{d}_{L_h-1}\} \end{bmatrix} \tag{2.67}$$

where $\mathbf{I}_2$ and $\mathbf{O}_2$ are respectively the identity matrix and the null matrix of dimension 2, $\mathbf{z}_2$ is 2×1 zero column vector. The notation $\{R|T|D\}$ stands for the possible matrix entries depending on the interaction type.

Figure 2.12 shows an example of two intermediate points from a signature involving 2 reflections.

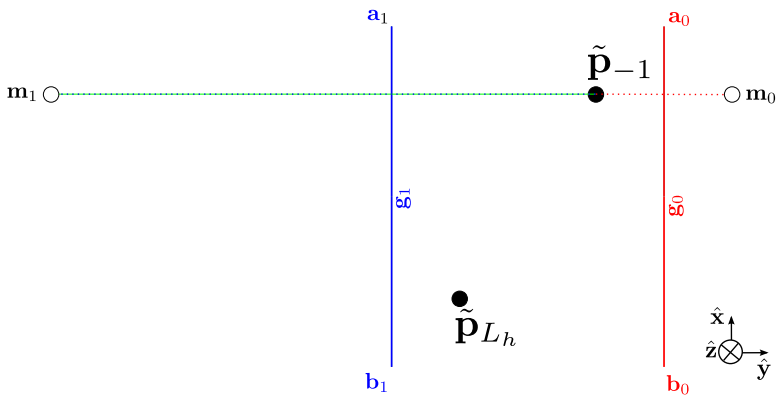

Fig. 2.12: Determination of intermediate points $\mathbf{m}_0$ and $\mathbf{m}_1$ from the Transmitter $\tilde{\mathbf{p}}_{-1}$ position. $\mathbf{m}_0$ is the image of $\tilde{\mathbf{p}}_{-1}$ through $\mathbf{g}_0$, the segment delimited by point $\mathbf{a}_0$ and $\mathbf{b}_0$. $\mathbf{m}_1$ is the image of $\mathbf{m}_0$ through $\mathbf{g}_1$, the segment delimited by point $\mathbf{a}_1$ and $\mathbf{b}_1$.

2.5.1.3 Phase 3 : Computing the Interaction Points from Positions of Intermediate Points

Let is define the l^{th} interaction point along a 2D ray as $\tilde{\mathbf{p}}_l = [x_l^{'}, y_l^{'}]^T$. Each such point is obtained from the intersection of 2 segments: the *interaction segment* $\mathbf{s}_l$ and the *ray segment* joining $\mathbf{m}_l$ and $\mathbf{m}_{l-1}$. In case the two segments would not intersecting each other, the ray would be rejected.

In order to test the existence of this intersection, a parametrization vector $\mathbf{\Gamma}_l = [\alpha_l, \beta_l]^T$ is introduced. Hence, the unknown of the equation system becomes a (4×1) column vector is $\mathbf{x}_l^{'} = \left[\tilde{\mathbf{p}}_l^T, \mathbf{\Gamma}_l^T\right]^T$.

The interaction points are found starting from the receiver $\tilde{\mathbf{p}}_{L_h} = [x_{L_h}, y_{L_h}]^T$. From the receiver and joining the last intermediate point $\mathbf{m}_{L_h-1}$, it can be written:

$$\tilde{\mathbf{p}}_0 + \alpha_0(\tilde{\mathbf{p}}_{L_h} - \mathbf{m}_{L_h-1}) = \tilde{\mathbf{p}}_{L_h} \tag{2.68}$$

$$\tilde{\mathbf{p}}_0 + \beta_0(\mathbf{a}_{L_h-1} - \mathbf{b}_{L_h-1}) = \mathbf{a}_{L_h-1} \tag{2.69}$$

The position of the first interaction point is found by solving this linear system

$$\mathbf{W}_0 \mathbf{x}_0^{'} = \mathbf{y}_0^{'} \tag{2.70}$$

with :

$$\mathbf{W}_0 = \begin{bmatrix} \mathbf{I}_2 & \tilde{\mathbf{p}}_{L_h} - \mathbf{m}_{L_h-1} & \mathbf{0}_{2\times 1} \\ \mathbf{I}_2 & \mathbf{0}_{2\times 1} & \mathbf{a}_{L_h-1} - \mathbf{b}_{L_h-1} \end{bmatrix} \tag{2.71}$$

$$\mathbf{y}_0^{'} = \left[\tilde{\mathbf{p}}_{L_h}^T, \mathbf{a}_{L_h-1}^T\right]^T \tag{2.72}$$

The next interaction point $\tilde{\mathbf{p}}_l$ is determined identically taking advantage of the knowledge of point $\tilde{\mathbf{p}}_{l-1}$:

$$\tilde{\mathbf{p}}_l + \alpha_l(\tilde{\mathbf{p}}_{l-1} - \mathbf{m}_{L_h-(l+1)}) = \tilde{\mathbf{p}}_{l-1} \tag{2.73}$$

$$\tilde{\mathbf{p}}_l + \beta_l(\mathbf{a}_{L_h-(l+1)} - \mathbf{b}_{L_h-(l+1)}) = \mathbf{a}_{L_h-(l+1)} \tag{2.74}$$

$$\tag{2.75}$$

$$\mathbf{W}_l \mathbf{x}_l^{'} = \mathbf{y}_l^{'} \tag{2.76}$$

with :

$$\mathbf{W}_l = \begin{bmatrix} \mathbf{I}_2 & \mathbf{p}_{l-1} - \mathbf{m}_{L_h-(l+1)} & \mathbf{0}_{2\times 1} \\ \mathbf{I}_2 & \mathbf{0}_{2\times 1} & \mathbf{a}_{L_h-(l+1)} - \mathbf{b}_{L_h-(l+1)} \end{bmatrix} \tag{2.77}$$

$$\mathbf{y}_l^{'} = \left[\tilde{\mathbf{p}}_{l-1}^T, \mathbf{a}_{L_h-(l+1)}^T\right]^T \tag{2.78}$$

The parametrization of the signature segment plays a very important role, if $0 < \beta_l, \alpha_l < 1$ the interaction point $\tilde{\mathbf{p}}_l$ is valid and the calculation can proceed otherwise the interaction point does not intersect the segment and the signature is rejected for the current receiver. Once the computation process has been done, as illustrated on Figure 2.13, all the interaction points $\tilde{\mathbf{p}}_l$ are determined which means that the 2D $\tilde{\mathbf{r}}$ is known.

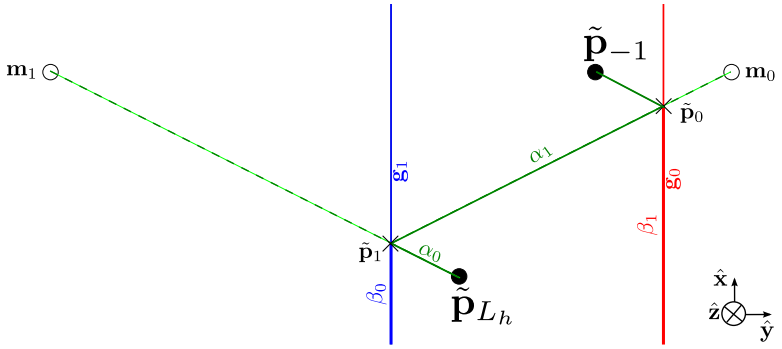

Fig. 2.13: Determination of 2 interaction points $\tilde{\mathbf{p}}_0$ and $\tilde{\mathbf{p}}_1$. $\tilde{\mathbf{p}}_0$ is the intersection point of the segment $[\mathbf{r}, \mathbf{m}_1]$ and $\mathbf{g}_1$. $\tilde{\mathbf{p}}_1$ is the intersection point of the segment $\left[\mathbf{p}_0^{\parallel}, \mathbf{m}_0\right]$ and $\mathbf{s}_0$. β_0 and β_1 are length parameters on $\mathbf{g}_0$ and $\mathbf{g}_1$ respectively. α_0 and α_1 are length parameters on segments $[\mathbf{r}, \mathbf{m}_1]$ and $[\tilde{\mathbf{p}}_0, \mathbf{m}_0]$ respectively.

2.5.2 Deriving 3D Rays from 2D Rays

The transformation of 2D rays in 3D rays is based on an elevation of 2D rays. Lets consider the 3D ray represented in 2.14a. From the previous computation, the obtained 2D ray is a projection in $(O, \hat{\mathbf{x}}, \hat{\mathbf{y}})$ of the 3D ray as shown in Figure 2.14b. As it can be observed, a 3D ray is composed of:

- the computed interaction points from the 2D rays where the z component is missing

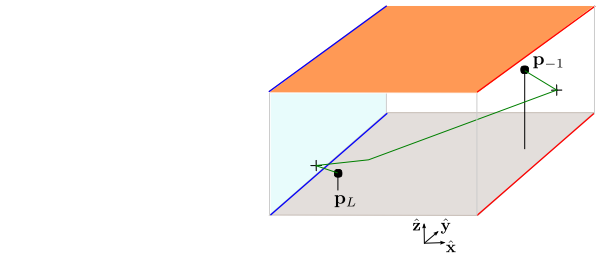

(a) 3d vizualization

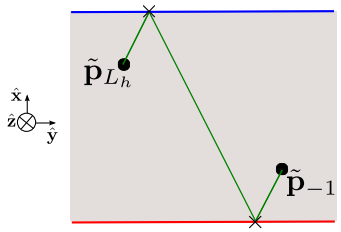

(b) projection in $(O, \hat{\mathbf{x}}, \hat{\mathbf{y}})$

(c) elevation of interactions points along the ray axis $\hat{\mathbf{s}}$

Fig. 2.14: 3 Representations in different axis of a same ray.

– new interaction points due to ceil and/or floor reflection where x and y components are missing (assuming the elevation of the ceil is known).

The 3D transformation consists in 2 steps :

1. Determining the relative positions of ceil/or floor interactions on the ray.
2. Determining the position of all the interactions points (including the new coming ceil/floor interactions) in $(O, \hat{\mathbf{x}}, \hat{\mathbf{y}}, \hat{\mathbf{z}})$.

The relative position of ceil/floor interactions uses a representation presented in Figure 2.14c. That representation shows the elevation of interaction points as a function of the length of the ray. In the figure, the poly-line representing the ray in $(O, \hat{\mathbf{x}}, \hat{\mathbf{y}})$ has been unwrapped and used as the horizontal axis thus denoted the $\hat{\mathbf{s}}$ axis. The positions of the interactions are thus relative to their positions on the ray. The introduction of those representations is required to determine the ceil/floor interactions in subsection 2.5.2.1, and is used to determine all the positions of interactions in section 2.5.2.2.

2.5.2.1 Finding the Relative Positions of Ceil/Floor Interactions Points

The search of relative position of interaction points consists in finding where the rays reflect on the floor and/or the ceil. As mentioned previously, the search of those relative positions is performed in frame $(O, \hat{\mathbf{z}}, \hat{\mathbf{s}})$, the unfolded plan along the ray trajectory. However, it is possible to write both the transmitter and receiver positions in that plan denoted $\mathbf{a}$ and $\mathbf{b}$ respectively defined with :

$$\mathbf{a} = [0, z_{-1}]^T \tag{2.79}$$

$$\mathbf{b} = [(s, z_L]^T \tag{2.80}$$

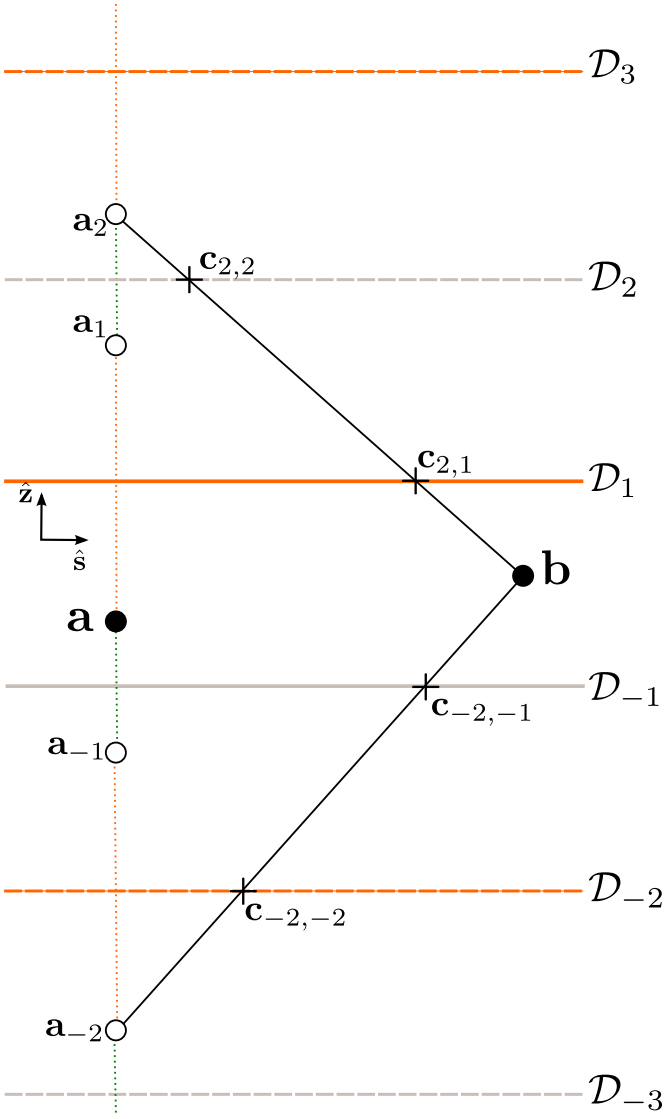

Fig. 2.15: Finding the intersection between the reflection lines $\mathcal{D}_m$ and segments from the images of $\mathbf{a}$ and $\mathbf{b}$, for $L_e = 2$.

where s denotes the length of the ray, which can be written :

$$s = \sum_{l=0}^{l=L} ||\mathbf{p}_l - \mathbf{p}_{l-1}|| \tag{2.81}$$

The *image* method is used to find those reflections. This method consists in finding an ordered set of L_e relative position of interactions points $\tilde{\mathbf{q}}$. Theoretically, that number of successive reflections on the floor and on the ceil L_e can be infinite. In practice, this is a parameter of the simulation.

For that purpose, let's define two lines $\mathcal{D}_{-1}$ and $\mathcal{D}_1$ representing the floor and the ceil respectively. By denoting $\mathcal{D}_{m-2}|\mathcal{D}_{m-1}$ the reflection of $\mathcal{D}_{m-2}$ by $\mathcal{D}_{m-1}$, each *image lines* $\mathcal{D}_m$ can be build with:

$$\mathcal{D}_m = \begin{cases} \mathcal{D}_{m-2}|\mathcal{D}_{m-1} & for\ m \in]2, L_e] \\ \mathcal{D}_{m+2}|\mathcal{D}_{m+1} & for\ m \in [-L_e, 2[\\ \mathcal{D}_{m-3}|\mathcal{D}_{m-1} & for\ m = 2 \\ \mathcal{D}_{m+3}|\mathcal{D}_{m+1} & for\ m = -2 \end{cases} \tag{2.82}$$

Similarly, it is possible to define the *images points* of $\mathbf{a}$ through reflection lines $\mathcal{D}_m$ with :

$$\mathbf{a}_{m'} = \begin{cases} \mathbf{a}_{m'-1}|\mathcal{D}_{m'} & if\ m' \in]0, ..., L_e] \\ \mathbf{a}_{m'+1}|\mathcal{D}_{m'+1} & if\ m' \in [-L_e, ..., 0[\end{cases} \tag{2.83}$$

where $\mathbf{a}_m|\mathcal{D}_m$ denote the reflection of $\mathbf{a}_m$ through the image line $\mathcal{D}_m$.

As illustrated on Figure 2.15, the *intersection points* $\mathbf{c}_{m',m}$ can be build as the intersection between each segment limited by $\mathbf{a}_{m'}$ and $\mathbf{b}$ and each reflection line $\mathcal{D}_m$:

$$\mathbf{c}_{m',m} = [\mathbf{a}_{m'}, \mathbf{b}] \cap \mathcal{D}_m \tag{2.84}$$

The orthogonal projection $\mathcal{P}$ is applied on the intersection points either on $\mathcal{D}_{-1}$ or $\mathcal{D}_1$ depending on the sign of m':

$$\mathbf{c}^{\perp}_{m',m} = \begin{cases} \mathcal{P}(\mathbf{c}_{m',m}, \mathcal{D}_1) & if\ \{2m'+1; m' \in \mathbb{N}\ | k \in 2\mathbb{Z}^-\} \\ \mathcal{P}(\mathbf{c}_{m',m}, \mathcal{D}_{-1}) & if\ \{2m'+1; m' \in \mathbb{Z}^-\ | k \in 2\mathbb{N}\} \end{cases} \tag{2.85}$$

Note that points already on $\mathcal{D}_1$ or $\mathcal{D}_{-1}$ coincide with their projection.

As depicted in Figure 2.16 those orthogonally projected points are relative interactions points positions up to an ordering process. Assuming always the same convention where the tilde describes a list of vectors of 2 components, it is possible to write the ordered sequence $\tilde{\mathbf{q}}_{m',c}$ of interactions points in $(O, \hat{\mathbf{z}}, \hat{\mathbf{s}})$ with:

$$\tilde{\mathbf{q}}_{m',c} = [\mathbf{a}, \mathbf{c}^{\perp}_{m',c}, \mathbf{c}^{\perp}_{m',2c} ..., \mathbf{c}^{\perp}_{m',(m'-1)c}, \mathbf{b}] \tag{2.86}$$

where m' is the number of wished reflection and $c = \{-1, 1\}$ a value to choose a set which end with a cell interaction or a floor interaction. For a given number of reflections $m' = L_e$ with a length $L_e + 2$, 2 possible sequences are generated.

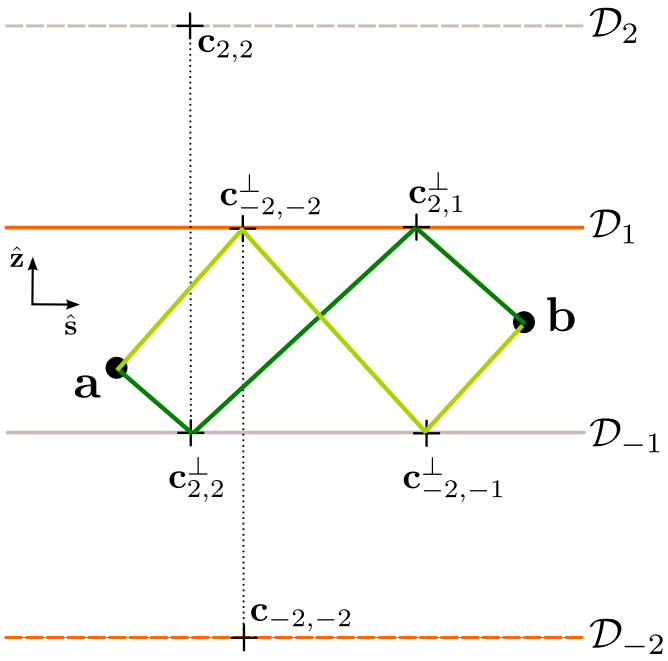

Fig. 2.16: 2 ordered sequences of $\tilde{\mathbf{q}}_{m',c}$ with $m^{'} = 2$. The darker green poly-line is obtained with $c = 1$, whereas the lighter green poly-line is obtained with $c = -1$

The method allows to generate 2 set of points, which allows to generate 2 different rays where the position floor/ceil interactions are switched. All the possible set of points until a given number of interactions L_e can be obtained by considering all the combinations of $m^{'} = 1, \ldots, L_e$ and $c = \{-1, 1\}$.

The aim of this section is to explain how a 3D ray is built. Then, only a single sequence is considered and is written $\tilde{\mathbf{q}}$, relaxing the lower script dependencies for the ease of the reader.

2.5.2.2 Obtaining a 3D ray

A 3D ray can be obtained by using jointly the list of ceil/floor interaction $\tilde{\mathbf{q}}$ and the the list of interaction points a.k.a. the 2D ray $\tilde{\mathbf{r}}$. As mentioned before, those 2 lists have not been obtained in the same plan, and thus cannot be used together unchanged. Let's denote Π a function which parameterizes the element of a sequence in regard of its bounds. Hence, it is possible to write two parametrized sequences $\Pi(\tilde{\mathbf{r}})$ and $\Pi(\tilde{\mathbf{q}})$ as :

$$\Pi(\tilde{\mathbf{r}}) = [0, \alpha_0, \ldots, \alpha_{L_{h-1}}, 1] \tag{2.87}$$

$$\Pi(\tilde{\mathbf{q}}) = [0, \beta_0, \ldots, \beta_{L_{e-1}}, 1] \tag{2.88}$$

with $\alpha_j \in]0, ..., 1[$ and $\beta_k \in]0, ..., 1[$.

If the two sequences $\tilde{\mathbf{r}}$ and $\tilde{\mathbf{q}}$ are defined in 2 different planes, their extrema points refer to the same points $\mathbf{p}_{-1}$ and $\mathbf{p}_L$. It is remarkable that, due to geometric properties

(Thales formula), the 2 parametrizations (2.87) and (2.88), are consistent together. As a consequence, it is possible to gather and sort those 2 parametrizations in order to create a global ordered parametrization sequence $\Pi(\mathbf{r})$:

$$\Pi(\mathbf{r}) = sort\left(\Pi(\tilde{\mathbf{r}}) \cup \Pi(\tilde{\mathbf{q}})\right) \tag{2.89}$$

where *sort* is a function ordering the elements from the lowest to the highest value. $\Pi(\mathbf{r})$ is an ordered sequence containing values of both $\Pi(\tilde{\mathbf{r}})$ and $\Pi(\tilde{\mathbf{q}})$. Consequently, each element π_l of $\Pi(\mathbf{r})$ corresponds either to an element α_j or an element β_k depending on the sort operation. It thus can be written:

$$\Pi(\mathbf{r}) = [0, ..., \pi_l, ..., 1] \tag{2.90}$$

where the number of element of $\Pi(\mathbf{r})$ is $L_e + L_h + 2$.

Hence, $\Pi(\mathbf{r})$ is the parametrization of a 3D ray $\mathbf{r}$ which can be written:

$$\mathbf{r} = [\mathbf{p}_{-1}, ..., \mathbf{p}_l, ..., \mathbf{p}_L] \tag{2.91}$$

with $\mathbf{p}_l = [x_l, y_l, z_l]^T$. Consequently, to each $\mathbf{p}_l$ corresponds either:

- an element of $\tilde{\mathbf{r}}$ where the z_l component is unknown,
- or to an element of $\tilde{\mathbf{q}}$ where x_l and y_l components are unknown.

The following procedure consists in determining those missing component values of $\mathbf{p}_l$ elements. Using the parametrization $\Pi(\mathbf{r})$, it is possible to determine for $\mathbf{r}$:

- the missing x_l and y_l coordinates of ceil/floor interactions points obtained in section 2.5.2.1
- the missing z_l coordinate of interactions points from the 2D ray obtained in section 2.5.1.3

Determination of missing x_l and y_l values

As it has been seen, the missing x_l and y_l values only correspond to p_l elements obtained from $\tilde{\mathbf{q}}$. The method consists in successively find the missing x_l and y_l values along the 3D ray starting from index $l = -1$. By construction, each element π_l corresponding to an element from $\Pi(\tilde{\mathbf{q}})$, is always surrounded by 2 elements π_{-1} and π_{l+n} both corresponding to elements from $\Pi(\tilde{\mathbf{r}})$ ($l + n$ designates the index of the next element from $\Pi(\tilde{\mathbf{p}})$). Then, it is possible to obtain x_l and y_l with the help of a new parametrization of π_l on π_{-1} and π_{l+n} :

$$x_l = x_{l-1} + K(x_{l+n} - x_l) \tag{2.92}$$

$$y_l = y_{l-1} + K(y_{l+n} - y_l) \tag{2.93}$$

with

$$K = \frac{\pi_l - \pi_{l-1}}{\pi_{l+n} - \pi_{l-1}} \tag{2.94}$$

Using (2.92) and (2.93), the x_l and y_l components of all p_l elements can be determined.

In the example provided in Figure 2.17 the coordinates x_1 and y_1 of the floor interaction point p_1 has to be determined. Both coordinates (x_0, y_0) and (x_2, y_2) of points p_0 and p_2 respectively are known from the previous 2D ray computation. The bottom line represents the parametrization of $\tilde{\mathbf{r}}$. At each interaction position $\tilde{\mathbf{p}}_l$ corresponds a parameter π_l. It is thus possible to parametrize π_1 with the help of π_0 and π_2. That parametrization directly give the value of K in equation (2.94). Hence, both positions x_1 and y_1 are obtained by resolving (2.92) and (2.93) respectively. In that situation the unknown coordinate positions are directly surrounded by known positions which means $n = 1$ for the two equations.

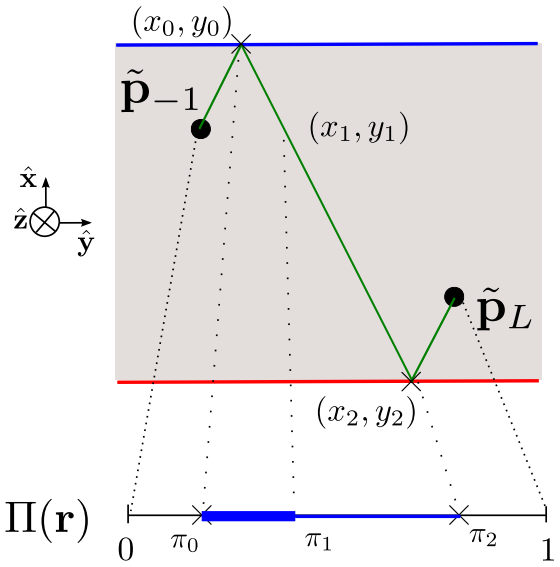

Fig. 2.17: Illustration of the determination of coordinates x and y of a ceil/floor interaction using parametrization.

Determination of missing z_l values

Similarly, the missing z_l values of p_l elements which have been obtained from $\tilde{\mathbf{r}}$ can be determined using the same procedure. This time, the considered π_l elements corresponds to an element from $\Pi(\tilde{\mathbf{r}})$. Then, it is possible to parametrize π_l on π_{-1} and π_{l+n}, both corresponding to elements from $\Pi(\tilde{\mathbf{q}})$ and the obtain:

$$z_l = z_{l-1} + K(z_{l+n} - z_l) \tag{2.95}$$

At the end of these both computations, all the components of each element of the 3D ray $\mathbf{r}$ are known.

2.5.2.3 3D Rays Extended

The calculation of a 3D ray allows to know the position of the interactions points into $(O, \hat{\mathbf{x}}, \hat{\mathbf{y}}, \hat{\mathbf{z}})$. However, for the field evaluation, the type of interaction, the type of

slab, and the incident and output wave planes has to be known. The purpose of this section is to describe the different methods to obtain those information, and determine a notation to store them for a more than a single ray.

Notation Extension Precision

According to (2.90), a 3D ray is an ordered set of interaction points. Practically, the raytracing aims to generate a large number of rays, constituted of different interaction points. Until that section, and for the ease of the reader, the notation has not took into consideration that diversity. The previous notation can now be extended to manage r rays. Thus, a 3D ray r can be written :

$$\mathbf{r}_r = [\mathbf{p}_{r,0}, ..., \mathbf{p}_{r,L}] \tag{2.96}$$

where $\mathbf{p}_{r,l}$ is the interaction position l of ray r.

Interaction Type and Slab

For interactions points obtained directly from the signatures (a.k.a. interactions points found in $(O, \hat{\mathbf{x}}, \hat{\mathbf{y}})$), information about their interactions type $(R|T|D)$ and their associated slab has been conserved. For the remaining interactions points obtained from the reflection on the floor/ceil, it is also possible to associate an interaction type (R) and a slab (ceil or floor).

Hence each interaction l of a given ray r can be stored both into a slab matrix :

$$\mathbf{M}_r = [M_{r,0}, \ldots, M_{r,l}, \ldots, M_{r,L-1}]. \tag{2.97}$$

and a type matrix:

$$\mathbf{N}_r = [N_{r,0}, \ldots, N_{r,l}, \ldots, N_{r,L-1}], \tag{2.98}$$

Practically, each interaction of $N_{r,l}$ match a number such as $R = 1$, $T = 2$, and $D = 3$, and is associated to a slab element $M_{r,l}$ defined in (2.104).

Defining Bases of Incoming and Outgoing Plane Waves

Each ray r is a succession of segments bounded by interaction points $\mathbf{p}_{r,l}$ and $\mathbf{p}_{r,l+1}$ with $l = -1, \ldots, L$ (where index -1 and L correspond to the position of the transmission antenna and the reception antenna respectively). To the l^{th} interaction is associated the normal vector $\hat{\mathbf{n}}_{r,l}$ of layout segment involved (if R or T). This normal vector information is stored in $\mathcal{G}_s$.

$\hat{\mathbf{s}}_{l-1}$ and $\hat{\mathbf{s}}_l$ are two unitary vectors along the ray constructed from segments $[\mathbf{p}_{r,l-1}, \mathbf{p}_{r,l}]$ and $[\mathbf{p}_{r,l}, \mathbf{p}_{r,l+1}]$ respectively. An incoming and outcoming plane wave are so defined for an interaction l of a given ray r as depicted in Figure 2.18:

- the incident plane is given by $\left(\hat{\mathbf{e}}_{r,l}^{i,\perp}, \hat{\mathbf{e}}_{r,l}^{i,\parallel}\right)$, arriving on $\mathbf{p}_{r,l}$ transverse to $\hat{\mathbf{s}}_{r,l-1}$
- the output plane is given by $\left(\hat{\mathbf{e}}_{r,l}^{o,\perp}, \hat{\mathbf{e}}_{r,l}^{o,\parallel}\right)$ departing from $\mathbf{p}_{r,l}$ transverse to $\hat{\mathbf{s}}_{r,l}$

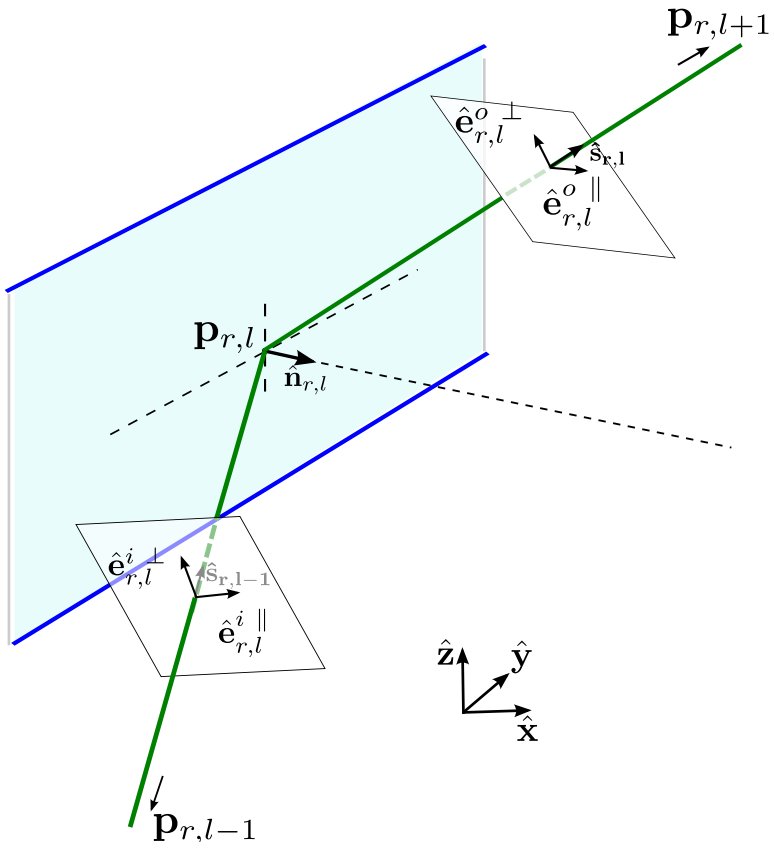

Fig. 2.18: input wave plane and output wave plane on interaction l

where $\hat{\mathbf{e}}_{r,l}^{i,\perp}$ and $\hat{\mathbf{e}}_{r,l}^{i,\parallel}$ are two basis vectors of the incident wave plane and $\hat{\mathbf{e}}_{r,l}^{o,\perp}$ and $\hat{\mathbf{e}}_{r,l}^{o,\parallel}$ are two basis vectors of the output wave plane. Both vectors have dimensions (3×1)

Similarly, to the type and the material stack , it is possible to build the matrix $\mathbf{B}_r^i$ gathering all the incident plane bases defined by :

$$\mathbf{B}_r^i = \left[\hat{\mathbf{e}}_{r,-1}^{i,\perp}, \hat{\mathbf{e}}_{r,-1}^{i,\parallel}, \ldots, \hat{\mathbf{e}}_{r,L-1}^{i,\perp}, \hat{\mathbf{e}}_{r,L-1}^{i,\parallel}\right] \tag{2.99}$$

with dimension $(3 \times 2L)$.

It is also possible to build the matrix $\mathbf{B}_r^o$ gathering all the output plane bases defined by :

$$\mathbf{B}_r^o = \left[\hat{\mathbf{e}}_{r,0}^{o,\perp}, \hat{\mathbf{e}}_{r,0}^{o,\parallel}, \ldots, \hat{\mathbf{e}}_{r,L}^{o,\perp}, \hat{\mathbf{e}}_{r,L}^{o,\parallel}\right] \tag{2.100}$$

with dimension $(3 \times 2L)$

For a later use , it is also convenient to store separately the incidence angle of of the ray on each interaction. This can be easily obtained using the scalar product between $\hat{\mathbf{s}}_{r,l}$ and $\hat{\mathbf{n}}_{r,l}$. Then, it is possible to define an incidence angle matrix $\boldsymbol{\theta}_r$:

$$\boldsymbol{\theta}_r = [\theta_{r,0}, ..., \theta_{r,L-1}] \tag{2.101}$$

with

$$\boldsymbol{\theta}_{r,l} = \arccos(\hat{\mathbf{n}}_{r,l}, \hat{\mathbf{s}}_{r,l}) \tag{2.102}$$

As shown in Figure 2.19, $\mathbf{B}_r^i$ matrix gathered all interactions from the transmitter $\mathbf{p}_{r,-1}$ to the last interaction $\mathbf{p}_{r,L-1}$ whereas $\mathbf{B}_r^o$ matrix gathered all interactions from the first interaction $\mathbf{p}_{r,0}$ to the receiver $\mathbf{p}_{r,L}$.

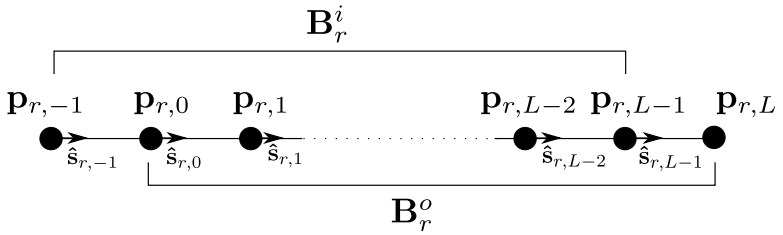

Fig. 2.19: interactions involved by $\mathbf{B}_r^i$ and $\mathbf{B}_r^o$.

In addition, considering that the transmitter and receiver antennas orientations in $(O, \hat{\mathbf{x}}, \hat{\mathbf{y}}, \hat{\mathbf{z}})$ can be modeled by two transformation matrices $\mathbf{T}_{-1}$ and $\mathbf{T}_L$ respectively, it is possible to define $\hat{\mathbf{s}}_{r,-1}^{\ell}$ and $\hat{\mathbf{s}}_{r,L}^{\ell}$ the direction of departure vector and direction of arrival vector expressed into the local bases of both antennas with :

$$\hat{\mathbf{s}}_{r,-1}^{\ell} = \mathbf{T}_{-1}\hat{\mathbf{s}}_{r,-1} \text{ and } \hat{\mathbf{s}}_{r,L}^{\ell} = \mathbf{T}_L\hat{\mathbf{s}}_{r,L} \tag{2.103}$$

As a consequence the 2 local bases associated to the transmitter and receiver antennas are defined by:

- $\mathbf{B}_{r,-1}^{\ell}$ the basis of the plane transverse to $\hat{\mathbf{s}}_{r,-1}^{\ell}$
- $\mathbf{B}_{r,L}^{\ell}$ the basis of the plane transverse to $\hat{\mathbf{s}}_{r,L}^{\ell}$

2.6 Computation of the Transmission Channel

This section describes the different steps to evaluate the transmission channel from the rays. In this section a vectorized approach is described. For that purpose, the section starts with a description of the MDA concept. Consequently to this description, a specific data organization, where rays sharing the same number of interactions are stored into a same data bloc, is proposed. Thereafter the description of the interaction coefficient evaluation from the slabs is described. With the help of that description, the computation work flows to evaluate all the interactions of a given bloc of rays is detailed. Once all the interaction have been evaluated, the propagation channel and the transmission channel can be computed.

2.6.1 Multi Dimensional Array (MDA)

The concept of MDA as been introduced in [45], as an extension of the matrix notation for dimensions higher than 2. Hence, all the operations that can be done using matrices have their equivalent for MDAs. MDAs are very convenient structures because they can be directly assimilated to ''numpy ndarrays'' objects from the Python 'numpy' library [46].

For the problem at hand, operations have to be performed on Multi Dimensional Array (MDA) until 5 dimensions (a.k.a axes). Those dimensions are namely :

- frequency (f),
- rays (r),
- interactions (l),
- polarization 1 (p),
- polarization 2 (q).

Hence written, it appears that a frequency axis naturally appears in the MDA notation, allowing to deal with a large number of frequencies required when dealing with UWB signals. Using that frequency axis allows to calculate quantity of interest vectorially at once for all frequencies, thus avoiding high level time consuming looping.

By convention, each axis is designated by a letter in relation with its nature. For example : f for frequency, r for ray, l for interaction, p and q for both polarizations. This constraint is desirable for clarity purpose, i.e for giving a direct information about which axis is associated with each quantity. All notations and operation conventions on MDAs used in the following are described in Annexe A.

2.6.2 Choosing a Vectorized Data Organization

Similarly to matrices requiring that the number of column elements is the same for each row, MDAs require to respect a constant number elements on each axis. For the problem at hand, the generated rays have different number of interactions which means that they cannot directly be stored into MDAs. A possible solution to avoid that problem is to classify rays by their constitutive number of interactions.

A 3D ray is an ordered list of L_n interactions. Thus, each ray with the same number of interactions L_n is stored into an interaction block $\mathbf{L}_n$. Once all rays have been

computed using the method described in 2.4, it is possible to determine a sequence $(\mathbf{L}_0, .., \mathbf{L}_n, ., \mathbf{L}_{N_i-1})$ of N_i blocks of rays. The block $\mathbf{L}_n$ is a block containing R_n rays of L_n interactions.

Figure 2.20 shows an example of that data organization for 2 3D rays.

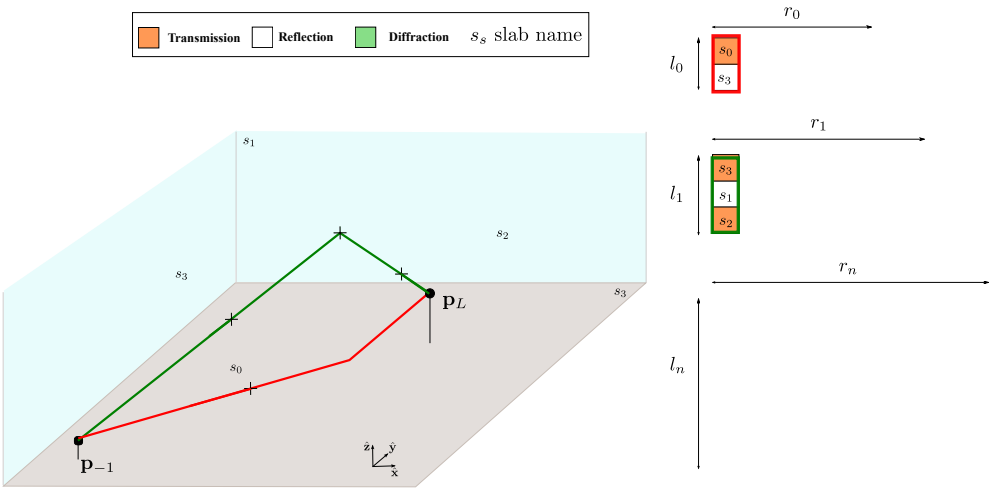

Fig. 2.20: Example of data organization for 2 rays : The red ray has 2 interactions which are stored into the $\mathbf{L}_n$ block 0.The green ray has 3 interactions which are stored into the $\mathbf{L}_n$ block 1. Others data into the $\mathbf{L}_n$ block designate others rays not represented on the figure.

2.6.3 Expression of Slab's Interactions

The following describes the method to evaluate the transmission coefficients for a specific slab.

2.6.3.1 Slab expression

As mentioned previously, the layout constitution is described with the help of objects call slabs. A slab $\mathbf{s}_s$ is defined as an ordered list of S constitutive materials $\mathbf{c}_s$ each with their associated thickness l_s:

$$\mathbf{s}_s = \begin{bmatrix} \mathbf{c}_0 & \dots & \mathbf{c}_{S-1} \\ l_0 & \dots & l_{S-1} \end{bmatrix} \tag{2.104}$$

Each material $\mathbf{c}_c$ has its specific parameters as : the relative permittivity ϵ_c, the relative permeability μ_c, conductivity σ_c. Their indice of refraction is deduced from

$$n_c = \sqrt{\frac{\epsilon_c}{\mu_c}}. \tag{2.105}$$

According to [39], the transverse reflection coefficients at the material $c+1$ considering a incidence angle θ_c on material c is defined with :

$$\rho_c^{\perp} = \frac{n_{c-1}^{\perp} - n_c^{\perp}}{n_{c-1}^{\perp} + n_c^{\perp}} \tag{2.106}$$

$$\rho_c^{\parallel} = \frac{-(n_{c-1}^{\parallel} - n_c^{\parallel})}{n_{c-1}^{\parallel} + n_c^{\parallel}} \tag{2.107}$$

with

$$n_c^{\perp} = \frac{n_c}{\cos\theta_c} \tag{2.108}$$

$$n_c^{\parallel} = n_c \cos\theta_c \tag{2.109}$$

2.6.3.2 Equivalent Material

Each material deviates the field of a specific angle. This output angle becomes the new input angle of the next material and so on. It is thus possible to write the interface matrices $\mathbf{c}_c^{\parallel}$ and $\mathbf{c}_c^{\perp}$ of a material c for transverse and parallel polarization respectively with:

$$\mathbf{c}_c^{\parallel} = \frac{1}{1+\rho_{c+1}^{\parallel}} \begin{bmatrix} e^{j\delta_c} & \rho_c^{\parallel} e^{-j\delta_c} \\ \rho_c^{\parallel} e^{j\delta_c} & e^{-j\delta_c} \end{bmatrix} \tag{2.110}$$

$$\mathbf{c}_c^{\perp} = \frac{1}{1+\rho_{c+1}^{\perp}} \begin{bmatrix} e^{j\delta_c} & \rho_c^{\perp} e^{-j\delta_c} \\ \rho_c^{\perp} e^{j\delta_c} & e^{-j\delta_c} \end{bmatrix} \tag{2.111}$$

with

$$\delta_c = \frac{2\pi f}{c} l_c n_{c+1} \cos\theta_c$$

.

2.6.3.3 MDA Slab Evaluation

Considering equation (2.110) and (2.111), it can be observed, that interface matrices depend on both the incidence angle and the frequency. The slab needs to be evaluated for several interactions. If those interactions have to be evaluated for the same frequency range, it is not the case for the incidence angle which is different for each interaction. Due to that difference of nature, the two quantities cannot be used in the same manner. For that reason, in the MDA extensions of $\mathbf{c}_c^{\perp}$ and $\mathbf{c}_c^{\parallel}$ treat the frequency as a new axis f and the incidence angle a as a parameter. In addition, to enable the process of several interactions in the same time, it is required to create an interaction axis l. That, interaction axis would be related to the parameter a (at each interaction correspond a specific incidence angle). Finally, MDA extension of $\mathbf{c}_c^{\parallel}$ and $\mathbf{c}_c^{\perp}$ can be respectively written :

- ${}_{c,a}\mathbf{c}_{f,l,p,q}^{\parallel}$
- ${}_{c,a}\mathbf{c}_{f,l,p,q}^{\perp}$

Thus written, it is possible to evaluate the slab interface MDAs for each polarization ${}_{s,a}\mathbf{s}^{\parallel}_{f,l,p,q}$ and ${}_{s,a}\mathbf{s}^{\perp}_{f,l,p,q}$ of slab s, defined as the product of all their constitutive materials:

$$ {}_{s,a}\mathbf{s}^{\parallel}_{f,l,p,q} = \prod_{u=c_s-1}^{0} {}_{c=u,a}\mathbf{c}^{\parallel}_{f,l,p,q} \tag{2.112} $$

$$ {}_{s,a}\mathbf{s}^{\perp}_{f,l,p,q} = \prod_{u=c_s-1}^{0} {}_{c=u,a}\mathbf{c}^{\perp}_{f,l,p,q} \tag{2.113} $$

2.6.3.4 Transmission and Reflection Coefficients

From the slab evaluation MDAs, it is possible to deduce either transmission or reflection coefficients for all the interactions.

For that purpose two MDAs ${}_{s,a}\mathbf{X}_{f,l,p}$ and ${}_{s,a}\mathbf{Y}_{f,l,q}$, based on equations (2.112) and (2.113) are introduced:

$$ {}_{s,a}\mathbf{X}_{f,l,p} = \begin{bmatrix} 1/({}_{s,a}\mathbf{s}^{\perp}_{f,l,p[0],q[0]}) \\ 1/({}_{s,a}\mathbf{s}^{\parallel}_{f,l,p[0],q[0]}) \end{bmatrix} \tag{2.114} $$

$$ {}_{s,a}\mathbf{Y}_{f,l,q} = \begin{bmatrix} {}_{s,a}\mathbf{s}^{\perp}_{f,l,p[0],q[1]} \\ {}_{s,a}\mathbf{s}^{\parallel}_{f,l,p[0],q[1]} \end{bmatrix} \tag{2.115} $$

Regarding the notation adopted in 2.5.2.3 for $(R|T|D)$, the coefficient MDAs ${}_{i=1,s,a}\mathbf{A}_{f,l,p,q}$ and ${}_{i=2,s,a}\mathbf{A}_{f,l,p,q}$ corresponding to a reflection and a transmission respectively, can be written :

$$ {}_{i=1,s,a}\mathbf{A}_{f,l,p,q} = \mathbf{I}^{p,q}_{\star\star} \odot \left({}_{s}\mathbf{X}^{p,\underline{1}}_{f,l} \; {}_{s}\mathbf{Y}^{q,\underline{1}}_{f,l} \right) \tag{2.116} $$

$$ {}_{i=2,s,a}\mathbf{A}_{f,l,p,q} = \mathbf{I}^{p,q}_{\star\star} \odot {}_{s,a}\mathbf{X}^{p,1}_{f,l} \tag{2.117} $$

where $\mathbf{I}_{p,q}$ is an identity MDA whose zeros are used to mask the anti-diagonal terms of the product in (2.116) and (2.117), defined by:

$$ \mathbf{I}_{p,q} = \begin{bmatrix} 1 & 0 \\ 0 & 1 \end{bmatrix} \tag{2.118} $$

2.6.4 Evaluation of Interactions

This part describes the different steps to evaluate all the interactions of a given interaction block $\mathbf{L}_n$, with the help of MDA description. For that purpose, a first part details the procedure to build a MDA from the meta ray information obtained in 2.5.2.3. In particular, the extension to MDA of the bases and interactions matrices is explained. Then, the different reshaping operations allowing the vectorized evaluation of the interaction MDA is detailed. Once that evaluation performed, the invert reshaping operations are applied for the upcoming channel estimation.

2.6.4.1 Multi Dimensional Array (MDA) storage

The upcoming vectorized computation of all the interactions first requires that the bases, slab and interactions matrices be converted into MDA

Bases MDA

The expression of bases matrices $\mathbf{B}_r^i$ and $\mathbf{B}_r^o$ has been obtained for a single ray in 2.5.2.3. Those matrices have a dimension $(3\times 2L)$, where L is the number of interactions of the ray. According to the data organization described in subsection 2.6.2, each ray with L_n interactions belongs to a $\mathbf{L}_n$ block. Then in order to turn the base matrices into MDAs, the same organization has to be chosen. Both base MDAs can thus be written for a $\mathbf{L}_n$ block :

- ${}^{i}_{n}\mathbf{B}_{r,lp,x}$
- ${}^{o}_{n}\mathbf{B}_{r,lp,x}$

where the axes r, x and lp represents the ray axis, space axis, and lp the concatenation of both interaction and polarization respectively with $\dim(r) = R_n$, $\dim(x) = 3$ and $\dim(lp) = 2L_n$. Indeed, the axis lp denoted the fact that all the basis vectors of all interactions have been stacked into the same axis. It is possible to differentiate those two axis using the reshape operation as defined in A.3.4:

$$ {}^{i}_{n}\mathbf{B}_{r,l,p,x} = \underset{(r,l,p,x)}{\text{reshape}}\left({}^{i}_{n}\mathbf{B}_{r,lp,x}\right) \tag{2.119} $$

$$ {}^{o}_{n}\mathbf{B}_{r,l,p,x} = \underset{(r,l,p,x)}{\text{reshape}}\left({}^{o}_{n}\mathbf{B}_{r,lp,x}\right) \tag{2.120} $$

The two axes l and p represent the interaction and polarization axis respectively, with $\dim(l) = L_n$ and $\dim(p) = 2$.

Assuming the convention that the first and last interaction of each rays are assimilated to the transmitter and the receiver respectively, it is thus possible to define an unitary MDA ${}_n\mathbf{B}_{r,l,p,q}$ linking two successive bases matrices with:

$$ {}_n\mathbf{B}_{r,l,p,q} = {}^{o}_{n}\mathbf{B}^{x,p}_{r,l}\ {}^{i}_{n}\mathbf{B}^{x,p}_{r,l} \tag{2.121} $$

As well, the 2 local bases matrices of the antennas $\mathbf{B}^{\ell}_{-1}$ and $\mathbf{B}^{\ell}_{L_n}$ can be rewritten into two MDAs: ${}^{\ell}\mathbf{B}_{l[-1],x,p}$ and ${}^{\ell}\mathbf{B}_{l[L_n],x,p}$ respectively. It goes the same for $\mathbf{T}_{-1}$ and $\mathbf{T}_{L_n}$, becoming $\mathbf{T}_{l[-1],x}$ and $\mathbf{T}_{l[L_n],x}$ respectively.

Creating an Interactions MDAs

From a given ray, different types of meta information can be obtained. Indeed, it has been shown that those meta information are stored into an interaction type matrix $\mathbf{N}_r$, a slab matrix $\mathbf{M}_r$ and an incidence angle matrix $\boldsymbol{\theta}_r$. Those matrices return respectively the whole interaction type, the interactions material, and the incidence angle for all interactions of a given ray. Similarly to bases matrices, it is possible to create 3 associated MDAs for a given $\mathbf{L}_n$ block : ${}_n\mathbf{N}_{r,l}$, ${}_n\mathbf{M}_{r,l}$ and ${}_n\boldsymbol{\theta}_{r,l}$.

By construction, ${}_n\mathbf{N}_{r,l}$, ${}_n\mathbf{M}_{r,l}$ and ${}_n\boldsymbol{\theta}_{r,l}$ are 3 MDAs referring to the same block, the same rays and the same interactions. The information of those 4 MDAs can thus be integrated into a single interaction MDA defined by :

$$ {}_{n,i,s,a}\mathbf{A}_{r,l} \tag{2.122}$$

where i, s, and a parameters indicate the type of interaction, the used slab and the incident angle on interaction l of ray r in block n respectively. The parameters i, s, and a are respectively carried by ${}_n\mathbf{N}_{r,l}$, ${}_n\mathbf{M}_{r,l}$ and ${}_n\boldsymbol{\theta}_{r,l}$.

2.6.4.2 Reshaping and Classifying MDAs

In order to exploit the vectorized format of the MDAs, each interaction of a same type and involving the same slab are calculated efficiently as a block. This evaluation requires to split the global MDA into several smaller MDAs. Practically, it consists in selecting as much MDAs as they are slabs and interaction types. To achieve that classification, 2 steps are required. First data of ${}_{n,i,s,a}\mathbf{A}_{r,l}$ are reorganized, second the classification is applied. In terms of computation speed, both steps are quick, they only rely on a memory readdressing process.

The data reorganization of ${}_{n,i,s,a}\mathbf{A}_{r,l}$ consists in reshaping the MDA by joining the ray axis and the interaction axis.

$$ {}_{n,i,s,a}\mathbf{A}_{rl} = \underset{(rl)}{\text{reshape}}({}_{n,i,s,a}\mathbf{A}_{r,l}) \tag{2.123}$$

where rl is $dim(rl) = R_n L_n$

and to concatenate all the blocks n along the rl axis:

$$ {}_{i,s,a}\mathbf{A}_{rl} = \overset{\Big|^{N-1}}{\underset{\Big|_{n=0}}{rl}} {}_{n,i,s,a}\mathbf{A}_{rl} \tag{2.124}$$

where rl is $dim(rl) = \sum_{n=0}^{N-1} R_n L_n$.

Assuming the convention that addressing an interaction corresponding to a specific slab or a specific interaction type, requires specifying parameter s or i respectively. Considering that the interaction MDA involves 3 different type of interactions and S type of different slabs, it is possible to read ${}_{i,s,a}\mathbf{A}_{rl}$ from equation 2.124 as:

$$ {}_{i,s,a}\mathbf{A}_{rl} = \bigcup_{u=1}^{3} \bigcup_{v=s_0}^{s_{S-1}} {}_{i=u,s=v,a}\mathbf{A}_{rl} \tag{2.125}$$

Those reshaping and classification operations on the interaction MDA are represented on Figure 2.21

2.6.4.3 Evaluation of Interactions

From that point it exists several small MDAs organized by slab s and interaction type i. Thus organized, each one of those MDA can be evaluated with the help of

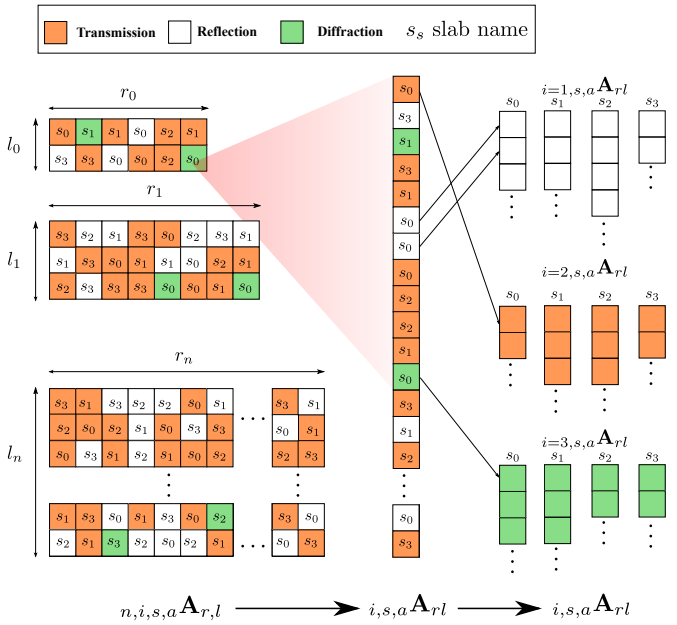

Fig. 2.21: Operations on the interaction MDA. Starting from the MDA organized in $\mathbf{L}_n$ block, the concatenation and reshape operation and the dispatching into several MDA depending on the interaction type and involved slab.

the equations (2.116) and (2.117). The evaluation process aims to return reflection, transmission or diffraction coefficient for a given frequency range f. The resulting MDAs is thus under the form :

$$_{i,s}\mathbf{A}_{f,nrl,p,q} \tag{2.126}$$

2.6.4.4 Reshaping Interactions

Once the slab evaluation has been performed, the original block organization of the rays has to be retrieved, for the upcoming channel evaluation. As it appears on Figure 2.22, those reshaping operations are close to those described in 2.6.4.2.

At this point, there is as much evaluated interaction MDAs as slab and type of interaction. The first step is to gather all those interaction MDAs into a single one, with the help of the union operator:

$$\mathbf{A}_{f,rl,p,q} = \bigcup_{i,s} {}_{i,s}\mathbf{A}_{f,rl,p,q} \tag{2.127}$$

Now, the complete evaluated interaction MDA can be reshaped to its original shape. This can be made in two steps: First by recreating blocks of interaction with

$$_{n}\mathbf{A}_{f,rl,p,q} = {}^{-1}{}_{rl}^{|N}(\mathbf{A}_{f,rl,p,q}). \tag{2.128}$$

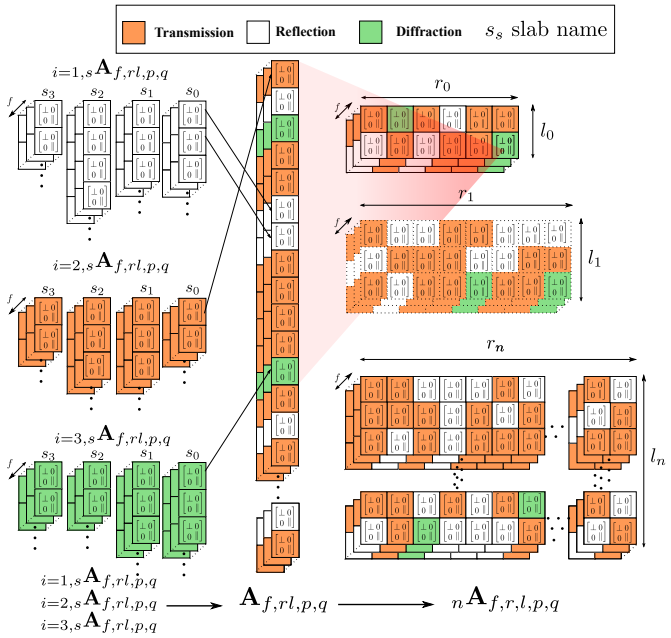

Fig. 2.22: Operations on the evaluated interaction MDA. The evaluated MDA is reshaped to obtain the original oragnization in $\mathbf{L}_n block$.

Second, by reshaping each block with the original a ray and interaction axis:

$$ {}_n\mathbf{A}_{f,r,l,p,q} = \underset{(f,r,l,p,q)}{reshape}({}_n\mathbf{A}_{f,rl,p,q}). \tag{2.129}$$

2.6.5 The Propagation Channel and Transmission Channel

The knowledge of all the evaluated interactions, allows to write the expression of the propagation channel. From that point, the scalar ray transfer function of the transmission channel can be derived, by adding the antenna descriptions. Then the complete vectorized expression of the transmission channel is obtained.

2.6.5.1 The Propagation Channel

The proposed expression of the propagation channel (channel without antennas) is updated from [47] to take into account the MDA notation and thus perform a computation for a large range of frequencies simultaneously. The tilde notation is used to highlight that the expression only assumes the attenuation and polarization. Delays will be reintroduced during the computation of the transmission channel (channel including antennas). Using (2.121) and (2.129), the propagation channel ${}^{ab}_{n}\tilde{\mathbf{C}}_{f,r,p,q}$ between 2

points a and b can be written as the following MDA product:

$$ {}^{ab}_{n}\tilde{\mathbf{C}}_{f,r,p,q} = {}_{n}\mathbf{B}^{p,q}_{\star,r,l[L_n]} \left[\prod_{u=l_{n-1}}^{0} {}_{n}\mathbf{A}^{p,q}_{f,r,l[u]} \; {}_{n}\mathbf{B}^{p,q}_{\star,r,l[u]} \right] \tag{2.130} $$

Once the product on all the interactions has been processed, the MDA ${}^{ab}_{n}\tilde{\mathbf{C}}_{f,r,p,q}$ does not depend on the number of interactions. As a consequence, all ${}^{ab}_{n}\tilde{\mathbf{C}}_{f,r,p,q}$ MDA from each block n can be stacked on a single MDA ${}^{ab}\tilde{\mathbf{C}}_{f,r,p,q}$ along the r axis:

$$ {}^{ab}\tilde{\mathbf{C}}_{f,r,p,q} = \left[{}^{ab}_{0}\tilde{\mathbf{C}}_{f,r,p,q}, .., \overset{|}{r}, ..., \; {}^{ab}_{N-1}\tilde{\mathbf{C}}_{f,r,p,q} \right] \tag{2.131} $$

$$ {}^{ab}\tilde{\mathbf{C}}_{f,r,p,q} = \overset{|}{r}_{n=0}^{N-1} \; {}^{ab}_{n}\tilde{\mathbf{C}}_{f,r,p,q} \tag{2.132} $$

where the dimension of axis r is now $dim(r) = \sum_{n=0}^{N} n \times R_n$. All those steps are illustrated in Figure 2.23.

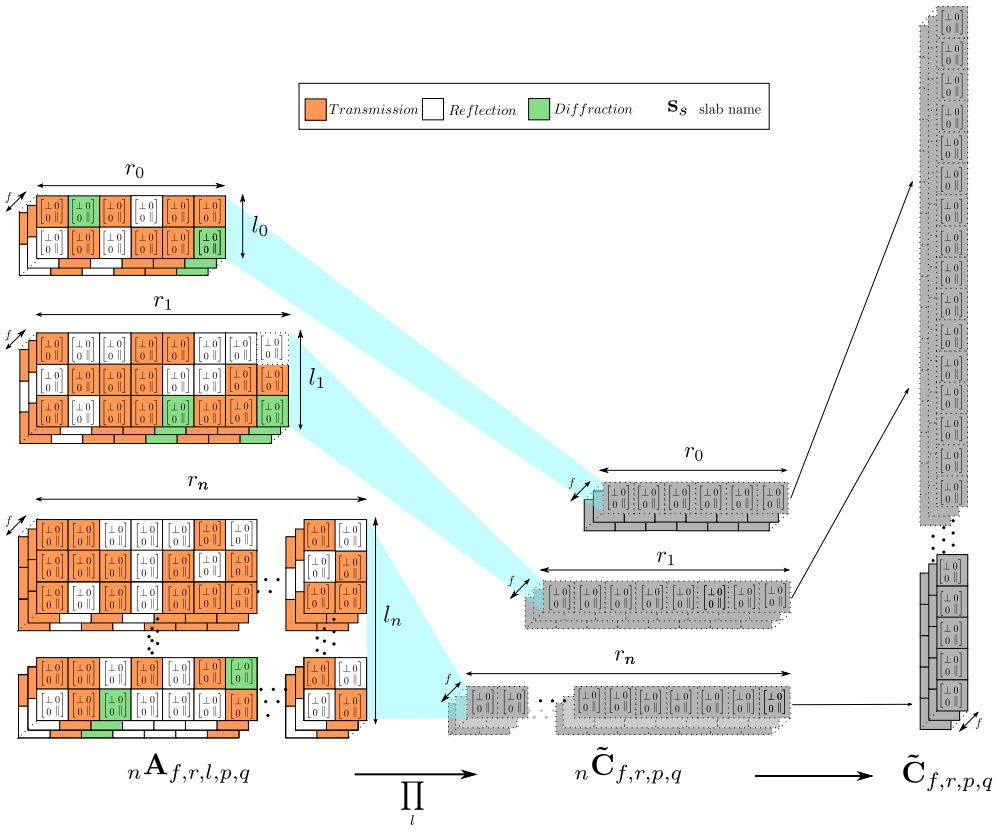

Fig. 2.23: Diagram showing how to obtain the propagation channel ${}^{ab\ell}\tilde{\mathbf{C}}_{f,r,p,q}$ for all the frequency range from the interactions MDAs classified by $\mathbf{L}_n$ blocks.

Finally, it can be observed that this expression of the propagation channel does not depend on the antenna orientations. By defining the local basis transformation ${}^{a\ell}\mathbf{B}_{p,q}$ and ${}^{b\ell}\mathbf{B}_{p,q}$ of the transmitter and receiver respectively with :

$$ {}^{a\ell}\mathbf{B}_{p,q} = {}^{\ell}\mathbf{B}^{\underline{x},p}_{l[-1]} \left(\mathbf{T}^{x,\underline{p}}_{l[-1]}\mathbf{B}^{\underline{p},q}_{l[-1]}\right)^{\underline{x},q}_{l[-1]}, \tag{2.133} $$

$$ {}^{b\ell}\mathbf{B}_{p,q} = {}^{\ell}\mathbf{B}^{\underline{x},p}_{l[L_n]} \left(\mathbf{T}^{x,\underline{p}}_{l[L_n]}\mathbf{B}^{\underline{p},q}_{l[L_n]}\right)^{\underline{x},q}_{l[L_n]}, \tag{2.134} $$

It is possible to express the propagation channel in the antennas local bases ${}^{ab\ell}\tilde{\mathbf{C}}_{f,r,p,q}$ with:

$$ {}^{ab\ell}\tilde{\mathbf{C}}_{f,r,p,q} = {}^{b\ell}\mathbf{B}^{p,\underline{q}}_{\star,\star}\left({}^{ab}\tilde{\mathbf{C}}^{p,\underline{q}}_{f,r}\ {}^{a\ell}\mathbf{B}^{\underline{p},q}_{\star,\star}\right)^{\underline{p},q}_{f,r} \tag{2.135} $$

2.6.5.2 The Scalar Ray Transfer Function

With the help of the propagation channel expression (2.135), it is possible to relate the two MDAs of received incoming field ${}^{b\ell}\mathbf{E}_{f,r,p}$ to the transmitted outgoing field ${}^{a\ell}\mathbf{E}_{f,r,p}$, where ℓ denotes that the field is expressed in the antennas local coordinate systems

$$ {}^{b\ell}\mathbf{E}_{f,r,p} = {}^{ab\ell}\tilde{\mathbf{C}}^{p,\underline{q}}_{f,r}\ {}^{a\ell}\mathbf{E}^{\underline{p},1}_{f,r} \tag{2.136} $$

Then, to determine the transmitted outgoing field, it is possible to define two quantities for the receiver and the transmitter:

$$ {}^{a}\mathbf{F}_{f,r,p} = \sqrt{{}^{a}G_{f,\star,p}}\ {}^{a}\mathbf{U}_{f,r,p} \tag{2.137} $$

$$ {}^{b}\mathbf{F}_{f,r,p} = \sqrt{{}^{b}G_{f,\star,p}}\ {}^{b}\mathbf{U}_{f,r,p} \tag{2.138} $$

where ${}^{a}G_{f,p}$ and ${}^{b}G_{f,p}$ are the gain of the antenna a and b respectively in a given direction ${}^{a}\hat{\mathbf{s}}_r$, ${}^{b}\hat{\mathbf{s}}_r$. The MDAs ${}^{a}\mathbf{U}_{f,r,p}$ and ${}^{b}\mathbf{U}_{f,r,p}$ give the polarization state of the emitter and transmitter antenna respectively. Note that for computational efficiency purpose, antennas would take advantage of the spherical harmonic description as proposed in [48]. ${}^{a}\mathbf{U}_{f,r,p}$ is expressed in the local basis ${}^{\ell}\mathbf{B}_{r,l[L_n],x,p}$ or ${}^{\ell}\mathbf{B}_{r,l[-1],x,p}$ depending on if it refers to the associated with the antenna of transmitter of receiver respectively. The emitted electric field ${}^{a\ell}\mathbf{E}_{f,r,p}$ can be obtained with

$$ {}^{a\ell}\mathbf{E}_{f,r,p} = \sqrt{\frac{2Z_0}{4\pi}}\left(1 - {}^{a}\mathbf{S}^{\underline{1},\underline{1}}_{f}\right){}^{a}\mathbf{F}^{\underline{1},p}_{f} \tag{2.139} $$

where Z_0 is the free space impedance and ${}^{a}\mathbf{S}_f$ is the scattering parameter characterizing the mismatching of the antenna a. It is thus possible to write the ray transfer function as:

$$ {}^{ab}\tilde{\mathbf{H}}_{f,r} = \frac{-jc}{\sqrt{4\pi}\sqrt{2Z_0}\mathbf{f}_{f,\star}}\left(1 - {}^{b}\mathbf{S}_{f,\star}\right){}^{b}\mathbf{F}^{\underline{p},1}_{f,r}\ {}^{b\ell}\mathbf{E}^{\underline{p},1}_{f,r} \tag{2.140} $$

where ${}^{b}S_f$ is the scattering parameter of the antenna b. Finally, by defining :

$$ {}^{ab}\boldsymbol{\gamma}_f = \frac{-jc}{4\pi \mathbf{f}_f}\big(1 - {}^{b}\mathbf{S}_f^{\underline{1},\underline{1}}\big)\big(1 - {}^{a}\mathbf{S}_f^{\underline{1},1}\big) \tag{2.141} $$

$$ {}^{ab}\boldsymbol{\alpha}_{f,r} = {}^{b}\mathbf{F}_{f,r}^{\underline{p},1}\ ({}^{ab\ell}\tilde{\mathbf{C}}_{f,r}^{p,\underline{q}}\ {}^{a}\mathbf{F}_{f,r}^{\underline{p},1})_{f,r}^{\underline{p},1} \tag{2.142} $$

then, equations (2.140), (2.139) and (2.136) yield:

$$ {}^{ab}\tilde{\mathbf{H}}_{f,r} = {}^{ab}\boldsymbol{\gamma}_{f,\star}\ {}^{ab}\boldsymbol{\alpha}_{f,r} \tag{2.143} $$

It may noticed that ${}^{ab}\boldsymbol{\gamma}_f$ only depends on the scattering parameters of antennas at both extremities.

2.6.5.3 The Complete Transmission Channel

The overall channel transfer function is derived from the summation of contributions coming from each ray, and by reintroducing the proper phase term:

$$ {}^{ab}\mathbf{H}_f = {}^{ab}\tilde{\mathbf{H}}_f^r exp(-2j\pi \mathbf{f}_{f,\star}\boldsymbol{\tau}_\star^r) \tag{2.144} $$

$$ {}^{ab}\mathbf{H}_f = {}^{ab}\boldsymbol{\gamma}_f\ {}^{ab}\boldsymbol{\alpha}_f^r exp(-2j\pi \mathbf{f}_f\boldsymbol{\tau}_\star^r) \tag{2.145} $$

If the roles of antennas are switched, the transfer function of the transmission channel becomes :

$$ {}^{ba}\mathbf{H}_f = {}^{ba}\boldsymbol{\gamma}_f\ {}^{ba}\boldsymbol{\alpha}_f^r exp(-2j\pi \mathbf{f}_f\boldsymbol{\tau}_\star^r) \tag{2.146} $$

with

$$ {}^{ba}\boldsymbol{\gamma}_f = {}^{ab}\boldsymbol{\gamma}_f \tag{2.147} $$

$$ {}^{ba}\boldsymbol{\alpha}_{f,r} = {}^{ab}\boldsymbol{\alpha}_{f,r} \tag{2.148} $$

We have indeed:

$$ {}^{ba}\boldsymbol{\alpha}_{f,r} = {}^{a}\mathbf{F}_{f,r}^{\underline{p},1}\ ({}^{ba\ell}\tilde{\mathbf{C}}_{f,r,}^{p,\underline{q}}\ {}^{b}\mathbf{F}_{f,r}^{\underline{p}})_{f,r}^{\underline{p},1} \tag{2.149} $$

$$ = {}^{b}\mathbf{F}_{f,r}^{\underline{p},1}\ ({}^{ab\ell}\tilde{\mathbf{C}}_{f,r,}^{\underline{p},q}\ {}^{a}\mathbf{F}_{f,r}^{\underline{p}})_{f,r}^{\underline{q},1} \tag{2.150} $$

Knowing that the MDA $\mathbf{A}_{f,r,l,p,q}$ is symmetric ($\mathbf{A}_{f,r,l,p,q} = \mathbf{A}_{f,r,l,q,p}$), the transpose of ${}^{ab}\tilde{\mathbf{C}}_{f,r,p,q}$ in (2.130) yield the equality:

$$ {}^{ba}\tilde{\mathbf{C}}_{f,r,p,q} = {}^{ab}\ \tilde{\mathbf{C}}_{f,r,q,p} \tag{2.151} $$

$$ \text{and } {}^{ba\ell}\tilde{\mathbf{C}}_{f,r,p,q} = {}^{ab\ell}\ \tilde{\mathbf{C}}_{f,r,q,p} \tag{2.152} $$

which proves the second equality in (2.148). Thus the channel reciprocity is verified:

$$ {}^{ba}\mathbf{H}_{f,r,p,q} = {}^{ab}\ \mathbf{H}_{f,r,p,q} \tag{2.153} $$

2.7 Site Specific Multi-wall Model

As seen in previous section, the use of the RT allows to compute the complete channel impulse response of a given layout. From that computation, it is thus possible to extract observables and construct LDPs required for feeding localization algorithms, using e.g.the method described in [49].

One of the main point enabling the vectorized approach of the RT is the description of the slabs using MDAs. Indeed, a such description allows the evaluation of interaction coefficients for several interactions and a large range of frequencies simultaneously. The idea behind that specific multi-wall description is to take advantage of the vectorized description, not for evaluating the coefficients on large number of rays obtained from the graphs, but only on the direct path between the transmitter and receiver and considering only the transmission coefficients.

First, a short overview of the most common Multi-wall models in order to highlight the differences with the proposed model is presented. Thereafter, both the method to determine the power losses and a specific process to evaluate the delay between the transmitter and the receiver are described. Finally, the computation of the interaction coefficients is illustrated with slabs and materials described in a pre-existing work.

2.7.1 Existing Multi-wall models

Multi-wall approaches are statistical methods which consists in evaluating the energy losses on the direct path between two agents. The evaluation of the losses can be made with different models:

- a Motley Keenan Model
- a COST 231 / 259 Model
- a Multi Wall and Floor (MWF)

With the help of a path loss shadowing model, the multi-wall approaches aims to predict the losses by adding some realism with the introduction of floor plan information. The Motley Keenan model [50], the losses are estimated on a direct path between a transmitter and a receiver. The total losses are estimated by adding to the free space losses a loss term due to the obstacles (walls, doors,...). COST 231 models [15], which adds an empirical correction term to the Motley Keenan model to take into consideration the wall type and adds multi floor considerations. COST 259 models [51] introduce a non linear correction factor to the COST 231 model as a function of the number of crossed walls. and Finally MWF model [52] adds to COSTs models the differentiation of both the losses introduced by the wall to the losses introduced by the ceil or the floor. The common between all those models is to require a precise description of the environment, to exactly know the type of material crossed by the direct path and exploiting a stochastic information in order to evaluate the losses.

2.7.2 Losses Estimations

Unlike the existing models, the proposed multi-wall approach exploits the precise knowledge of both the environment from the graph description (in section 2.3.2) and

the deterministic slab description (in section 2.6.3) to estimate the losses. The different steps describing the losses evaluation is given by algorithm 5. As a first step, the graphs are used to determine an ordered set of segments crossed by the direct path between the receiver and the transmitter. From that set of intersected segments, it is possible to obtain both the corresponding ordered set of incidence angles $\boldsymbol{\theta} = [\theta_0, \ldots, \theta_{L_i-1}]$ and the ordered set of intersected slabs $\mathbf{M} = [M_0, \ldots, M_{L_i-1}]$, where L_i is the number of intersected segments. Hence, using the transmission MDA equation (2.116) with both the set of incidence angles $\boldsymbol{\theta}$ and the set of intersected slabs $\mathbf{M}$, it is possible to evaluate the equivalent transmission MDA ${}^{e}\mathbf{A}_{f,p,q}$ for the L_i intersected segments with:

$$ {}^{e}\mathbf{A}_{f,p,q} = \prod_{l=L_i-1}^{0} {}_{i=1,s=M_l,a=\theta_l}\mathbf{A}_{f,l,p,q} \tag{2.154} $$

The losses MDA on the direct path $\mathbf{P}_{f,p,q}$ can thus be obtained for both polarization and for all desired frequencies with :

$$ \mathbf{P}_{f,p,q} = -20\log_{10} \mid {}^{e}\mathbf{A}_{f,p,q} \mid \tag{2.155} $$

Algorithm 5 Compute Losses using the Multi-Wall model

Require: $\mathbf{t}, \mathbf{r}, \mathcal{G}_s$

▷ get list of segments intersected by the direct path between $\mathbf{t}, \mathbf{r}$ and the associated list of incidence angle, la and ls

$\boldsymbol{\theta}, \mathbf{S} = \text{segonlink}(\mathbf{t}, \mathbf{r}, \mathcal{G}_s)$

▷ Find the list of materials $\mathbf{M}$ corresponding to the segments $\mathbf{S}$

$\mathbf{M} = \text{seg2mat}(\mathbf{S})$

▷ Evaluate the transmission parameters parallel and orthogonal for all the crossed materials for a given frequency range $\mathbf{f}$

$\mathbf{P}_o, \mathbf{P}_p = \text{eval}(\boldsymbol{\theta}, \mathbf{M}, \mathbf{f})$

▷ The losses are obtained for both polarization

$Lo = -20\log_{10} sum(\mathbf{P}_o)$

$L_p = -20\log_{10} sum(\mathbf{P}_p)$

2.7.3 Excess Delay Estimation

By construction, the equivalent transmission MDA given in (2.154) is filled with complex values. Hence, the transmission MDA intrinsically contains information about the excess delay τ_e introduced by crossing all the slabs. From this information, it is possible to compute the value of the global delay τ observed by the receiver, which takes into account that excess delay. The global delay τ can be directly obtained by summing the excess delay τ_e and the delay corresponding to the time spend in free space propagation

Practically, the delay associated to the free space propagation is not easily accessible, so the delay associated to the distance between the transmitter and the receiver τ_{LOS} is preferably used. However, the use of τ_{LOS} requires some considerations.

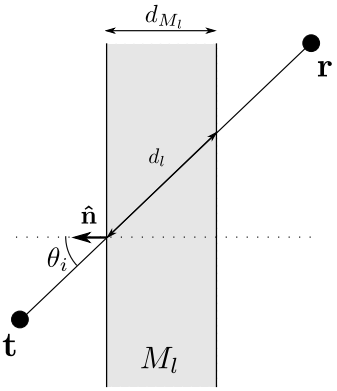

Fig. 2.24: Direct ray trajectory through the material, neglecting the refraction inside the material.

On minimal example of Figure 2.24, it can be observed that a difference exists between the delay of the direct path τ_{LOS} and the delay of the free space. This difference is the delay τ_M introduced by the time spend to crossing the slab. This delay is associated to the distance d_l an can be computed with:

$$d_l = d_{M_l} \cos(\theta_l) \tag{2.156}$$

where M_l and θ_l are the slab thickness and the incidence angle of the lth interaction.

Hence, at each interaction (a.k.a. each slab crossed) corresponds an excess distance. Then, it is possible to define a MDA $\mathbf{d}_l$ containing the excess distances introduced by all the slabs on the direct path. Using that MDA, the delay τ_M can be directly compensated during the equivalent transmission MDA computation. The compensated equivalent transmission MDA ${}^c\mathbf{A}_{f,p,q}$ can thus be written:

$${}^c\mathbf{A}_{f,p,q} = \prod_{l=L_i-1}^{0} {}_{i=1,s=M_l,a=\theta_l} \mathbf{A}^{l,\underline{1}}_{f,p,q} \ \exp^{(j\mathbf{d}^{\underline{l},1}_{\star,\star,\star})} \tag{2.157}$$

The associated compensated excess delay $\tau_c(f,p)$ for a given frequency f and a given polarization p can be obtained from ${}^c\mathbf{A}_{f,p,q}$ with:

$$\tau_c(f,p) = \begin{cases} \arg(\ {}^c\mathbf{A}_{f[f],p[0],q[0]}\ ), & \text{for an orthogonal polarization} \\ \arg(\ {}^c\mathbf{A}_{f[f],p[1],q[1]}\ ), & \text{for an parallel polarization} \end{cases} \tag{2.158}$$

Finally, the global delay $\tau(F,P)$ depends on the frequency and polarization and is obtained with:

$$\tau(f,p) = \tau_{LOS} + \tau_c(f,p) \tag{2.159}$$

It may be noticed that the model assumes a propagation of the ray along a straight line inside the slab, neglecting the refraction effects causing a different ray output position. As a consequence, an error in the computed LDPs values is introduced which is as

high as the material is thick or absorbent. The method also shares the same limitations than any multi-wall model: Because the power and delay information are only obtained from the direct path, the computed LDPs cannot fit with real ones in case of deep NLOS situation (where the LOS is not observable). However, the simulated results compared to measurements in section 5.3.1 will prove the interest of the method.

2.7.4 Evaluation of the Reflection and Transmission Coefficients

The evaluation of the transmission and reflection coefficients is a main part of both the RT and the site specific multi-wall approaches. It insures the correct estimation of the LDPs. For that purpose, this part proposes to illustrate and validate the slab evaluation with an example borrowed from a pre existing work [53]. This example considers a slab composed of a single homogeneous material for 3 different thicknesses: 5cm, 10cm and 15cm. The slab material has a permitivity $\epsilon_r = 3$ and a conductivity $\sigma = 0.06S/m$. The frequency is chosen at 4 GHz.

The evolution of the reflection coefficient in parallel and orthogonal polarization as a function of the incidence angle is shown in Figure 2.25a and 2.25b respectively. The same representation is adopted for the transmission coefficient presented in Figure 2.26a and 2.26b. Those results are consistent with the results presented in [53].

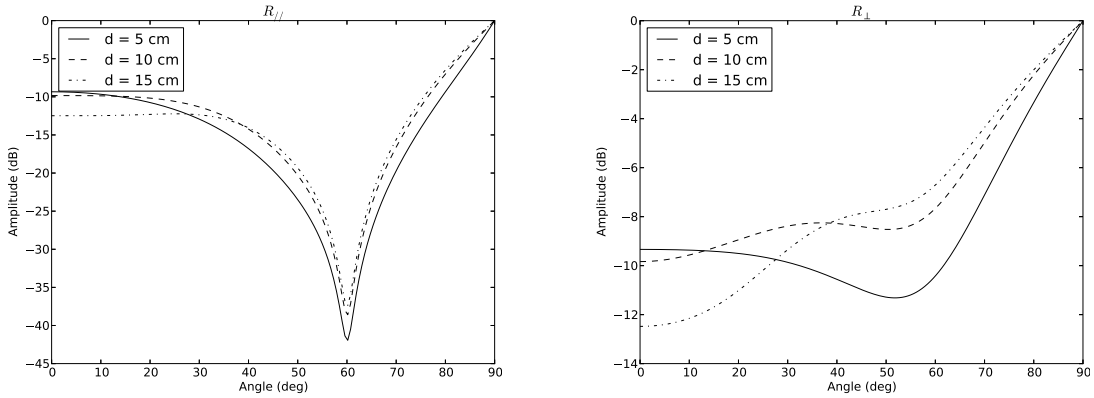

(a) Parallel polarization (b) Orthogonal polarization

Fig. 2.25: Module of reflection coefficients as a function of the incidence angle for a (a) parallel polarization and an (b) orthogonal polarization with $\epsilon_r = 3$,$\sigma = 0.06S/m$ and $f = 4$ GHz .

As an example, the modulus and phase of the reflection coefficient have been studied between 2 GHz and 16 GHz considering a material with complex permitivity, which can be written with (2.33): $\epsilon = \epsilon' + j\epsilon''$. The validation has been performed with a material of 5 cm for $\epsilon' = 2, 3, 4$ and $\epsilon'' = 0.04, 0.1$. Figures 2.27a and 2.27c show the modulus and phase respectively for a real part $\epsilon' = 0.03$. For that value, the propagation delay is 0.57 ns which is complaint to the oscillations of 1.73 GHz observable in 2.27a. Figures 2.27b and 2.27d show the modulus and phase respectively for a real part $\epsilon'' = 2$

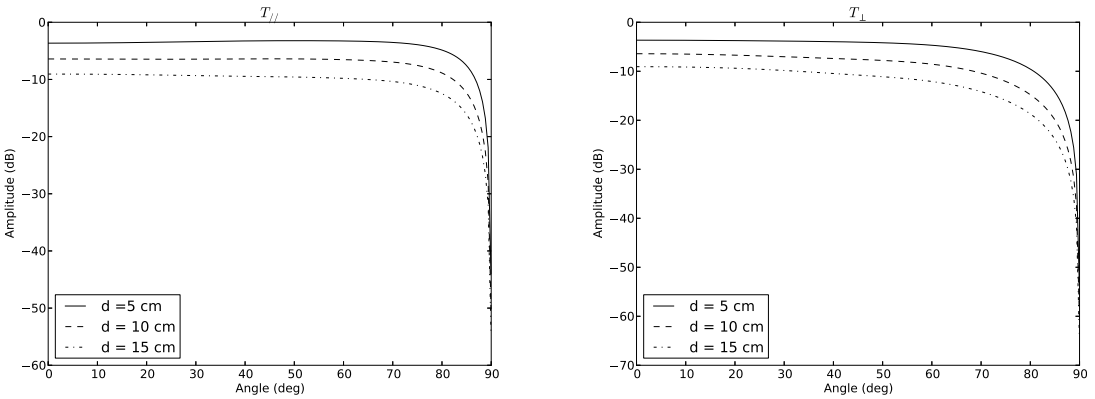

(a) Parallel polarization (b) Orthogonal polarization

Fig. 2.26: Module of transmission coefficients as a function of the incidence angle for a (a) parallel polarization and an (b) orthogonal polarization with $\epsilon_r = 3$,$\sigma = 0.06S/m$ and $f = 4$ GHz .

2.8 Conclusion

After a brief state of the art on the existing RT tools and some mathematical elements on the propagation channel, this chapter has presented a graph based RT technique. A first part has been focused on the description of the environment using graphs. Then it has been shown how that graph based description could also be advantageously be used for describing the electromagnetic interactions. In particular it has been shown how this description could be advantageously used for developing an incremental RT, by introducing the new concept of ray signature. A second part has shown how 3D rays can be extracted from that graph description using images and projections methods in different plans, and how structural element can be extracted from the graph for the upcoming evaluation. In a third part, an original vectorized organization of the data combined to a new formalism based on MDA, has been introduced. This formalism allows in a first time a fast evaluation of all the interactions from all the simulated rays, and the complete estimation of the propagation channel for a large number of frequency in the same time. Using the same formalism, the propagation channel is also evaluated. Then, a site specific multi-wall approach has been presented. This approach takes advantage of the MDA evaluation of the slabs, to quickly provide LDPs of a given direct path, by taking into account the realistic description of slabs. Finally, the slab computation has been compared to an existing model.

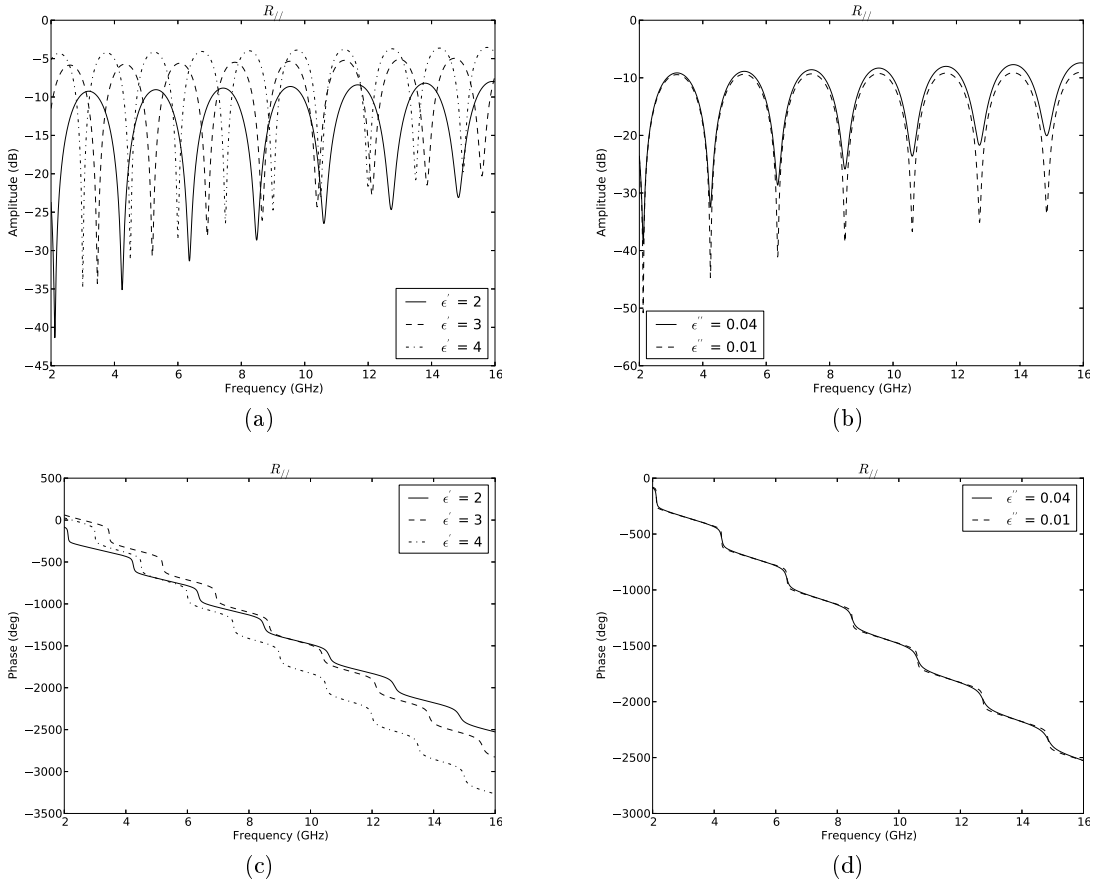

Fig. 2.27: Reflection coefficients in parallel polarization for complex permitivity coefficient. The influence of the real part with a fixed imaginary part $\epsilon'' = 0.03$ is shown in (a) modulus and (c) phase. The influence of the imaginary part with a fixed real part $\epsilon' = 2$ is shown in (b) modulus and (d) phase

Chapter 3

Indoor Localization: Robust and Heterogeneous Approaches

3.1 Introduction

During the last 10 years, the localization information has mainly benefit to end users of wireless networks. However, both the increase of bit rate requests and the need to reduce energy consumption have developed new problematics in wireless networks that the position information could help to resolve. Indeed, most of the envisaged schemes of wireless networks organization (distributed, cooperative, self-organized, ...) take advantage of that position information to improve their efficiency. Consequently, it is mandatory to develop the localization algorithms taking into account the specificities of such networks. This chapter presents two heterogeneous localization techniques based on one hand on interval analysis and on the other hand on a hypothesis testing. Prior to algorithms description, a state of the art on the localization strategies and the existing techniques is provided in section 3.2.

The second section 3.3 presents Robust Geometric Positioning Algorithm (RGPA), an original geometric based method for heterogeneous localization. The method is based on interval analysis approaches to perform the position estimation. The different processing steps are described from the geometric description of the LDPs to the position estimation. Finally, the algorithm is compared to existing methods using simulations.

Using possibilities offered by this geometric approach, the last section 3.4 provides an original algorithm based on hypothesis testing. The method proposes to maintain the position estimation accuracy achievable using range observables and prevent its degradation by power observables. For that purpose, the power observables are only used to decide between the 2 ambiguous positions created by range observables. That method is evaluated in simulation using a Monte Carlo approach and tested on a canonical cooperative localization problem.

3.2 State of the Art on Localization Techniques

This section proposes an overview of the localization techniques including the different uses of the position information and the main methods allowing its estimation. A first part describes how the knowledge the position information can benefit both to a end user and to the network. A second part explains how to obtain the position information, notably by describing the exploitable observables of a wireless network, and by identifying their different exploitation strategies. The 2 last parts detail 2 different types of algorithms based on an algebraic approach and on a geometric approach.

3.2.1 Applications of Localization

With both the new ability to obtain a precise position on mobile devices and the increasing powerful of those devices [54], new services are being created. The emergence of those services is now possible because all actors of the communication link are available: the end user has a smart device able to provide a position information with the help of specific applications, the communication network is able to connect mobile devices to infrastructure and finally the provider managing the infrastructure is able to collect the necessary data for getting the location information.

The use of this localization information potentially benefits both to the end user and to the provider. From the end user point of view, the position information has several applications. One of those that immediately comes in mind is the navigation and tracking application. Navigation consists in providing directions to user to a target. The best known example of this technology is probably the terminal rental based on global navigation satellite system (GNSS). The best known systems are Galileo, GPS and GLONASS in Europe, USA and Russia respectively. Tracking allows to follow the movement of the user into an environment. The convergence of navigation and tracking helps providing a transfer service located as in Google Maps Navigation. The position information can also be used as part of the geo-localized information. Hence, information about the region, city or business environment can be updated or displayed according to the current position of the user. By extension, this information may also be referred to an ad and offer discounts at a nearby shop. However, the position information can also be used for emergency services. Thus, in the USA, the mobile operators automatically locate the position of a cell phone calling an emergency service [55].

From the infrastructure and network side, the location information are generally used to enhance the quality of the network [56]:

- to predict changes in the environment and thus adapt signal synchronization,
- to predict the evolution of the channel using the movement history,
- to adapt transmission aspects as the antenna orientation (beamforming) or transmission parameters (modulation type, bit rate,...) to the relative position of a mobile terminal.

However those information can also be used, neither by the end user itself, nor by the infrastructure but by a third actor interested in collecting information [57]. This can be

the case in environmental monitoring where the position information linked to sensors allows to create a map distribution and thus explain the causes of different phenomenas.

If it has been shown that obtaining the localization has an interest for many applications from end user to infrastructure, the different methods to obtain that position information remains to be determined.

3.2.2 Obtaining a Position from the Radio Observables

By definition, a blind node is a wireless radio device with an unknown position whereas an anchor node is a radio device knowing its position in the 2 or 3-dimensional Euclidean space. The localization consists into obtaining the position of the blind node with the help of several anchor nodes. At the top level, the localization process can be seen as a two steps process:

1. Firstly, the blind node obtains radio observables from the anchor nodes either from the estimation or from the measurement of signal metrics.
2. Secondly, a location algorithm gather all that observables and try to estimate the blind node position.

Each one of the observables represent a Location Dependent Parameter (LDP) which can be seen as a constraint since it constraints the possible positions of the blind node.

In a case where those LDPs are measured without any errors, gathering of all the LDP would define a region inside of which the blind node stands. If there is enough Location Dependent Parameter (LDP), that region degenerates into a single point which is the blind node position.

However, in real application each LDPs is observed with an additive error term. An error term may have several causes depending on the observed LDP (desynchronization , shadowing, ...). For that purpose it is required to build location algorithms able to take into account those perturbations. Those error terms are taken into consideration as a realization of a random variable. The statistical properties of those random variables becomes thus an input of the location algorithm. Hence, it can be took into consideration the observed LDPs with a correct a priori on their inaccuracies.

3.2.3 Fingerprinting Based Method

Finger printing based method aims to provide a blind node position estimation by comparing an actual measurement of LDPs values with a set of LDPs values from a database with a known position. The blind node position is estimated by finding in the database, the set of LDPs which closely match the observed LDPs [58].

Practically, prior to be able to estimate a position, fingerprinting methods require an off-line phase, where a set LDP collected from different anchors nodes for different positions are stored into a database. Once that collection of LDPs has been obtained, the fingerprinting can be turned into an online phase enabling the position estimation. Different strategies can be used to minimize the distance between the LDPs observation vector and the database [59, 60].

If the fingerprinting methods potentially give an accurate position estimation [61], they obviously have some drawbacks: First, they are complicated to establish, because a long measurement campaign is required to sample a large number of predefine positions in the area where they'll be used. Secondly, the database requires a large amount of space in order to store the information, and in the same time, that information has to be accessible very fast in order to reduce the latency in the position estimation. Finally, they are not flexible, because any modification in the anchor positions or structural modification in the building would modify the LDP values and thus requires a reconstruction of the database.

3.2.4 Range Based Method

Contrary to the fingerprinting based methods, the range based methods propose to directly use the LDP observables to perform a position estimation. The three most used LDPs for feeding range based location algorithms [62] will be detailed in the following.

3.2.4.1 Received Signal Strength (RSS) Indicator

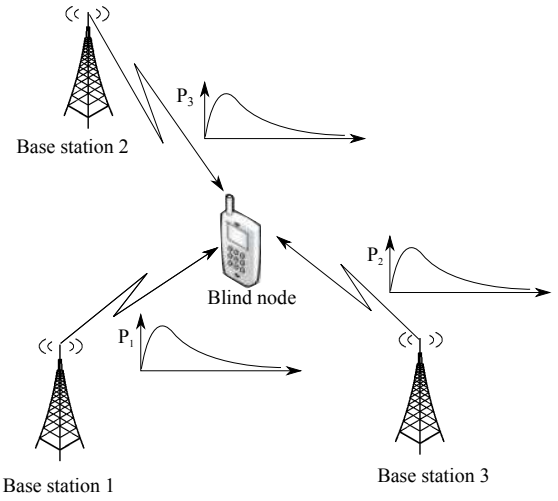

Fig. 3.1: Example of localization based on RSS.

The RSS indicator observables give an indication of the received power from a radio device to another. The RSS observables can be used to perform a positioning assuming an underlying path loss model, as shown in Figure 3.1. That path loss model allows to make an association between the power attenuation and a distance. Assuming that are known: the position of the emitter, its emitted power and the parameters of the pathloss model, each RSS observable delimits a circle region in 2D (resp a spherical region in 3D). The blind node position is estimated at the intersection of those regions. One of the advantages of the RSS observable, is it can be observed without neither extra inter node communication nor complex estimation processes.

3.2.4.2 Time of Arrival (ToA)

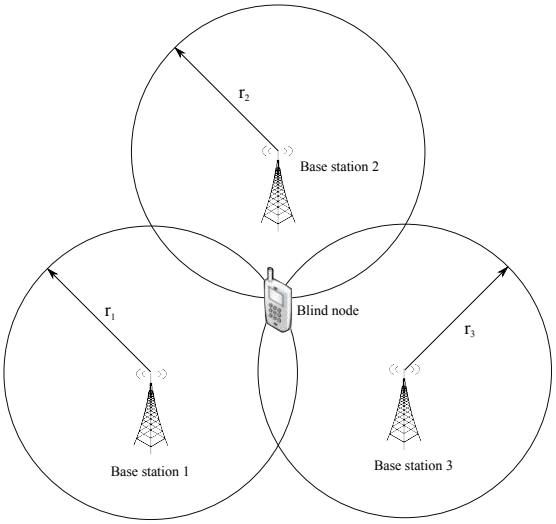

Fig. 3.2: Example of localization based on ToA.

The ToA observables gives information of the time spend to the signal to be propagated between the blind node and an anchor. Assuming that signals propagates at the speed of light ($c \approx 3 \times 10^8$m/s), it is possible to determine an associated range between the blind node and the anchor. As it can be see on Figure 3.2, such an observable delimits a constraint shaped as a circle in 2D (or a sphere in 3D) centered on anchor with a radius equal to the range. ToA location based algorithm gathered several ToAs constraints and try to find the intersection of all the circles (or spheres).

Practically two main methods exist to obtain that observable: The one-way ranging and the two-way ranging. In one-way ranging, the ToA is obtained by measuring the time elapsed between a transmitted signal and its reception. That technique requires the synchronization of both radio devices at each end of the communication channel. In a two-way ranging method, a device d_0 transmit a signal s_0 to another device d_1, and the device d_1 returns another signal s_1 to d_0. Inside that second signal s_1 is embedded the time elapsed between the reception of s_0 and the emission of s_1. Using that method, no more synchronization are required between the two devices. As a drawback, it doubles the number of required communications, which can be problematic in terms of overhead in networks with a high nodes density.

Several causes may degrade the ToAs observables accuracy:

- In case of of one-way ranging, the accuracy of the measurement relies on the accuracy of the synchronization of the nodes.
- As it has been seen in 2.2.3.3, the propagation channel presents multi-paths, which means that for a single emitted signal, several delayed and attenuated versions are received by the transmitter. Additive and destructive phenomena can appear on the received signal and in particular on the first path which is the solely related to the actual range.

– In case of NLOS situation, the direct path is blocked, then the distance is estimated with another path. As a consequence the observable will be biased.

3.2.4.3 Time Difference of Arrival (TDoA)

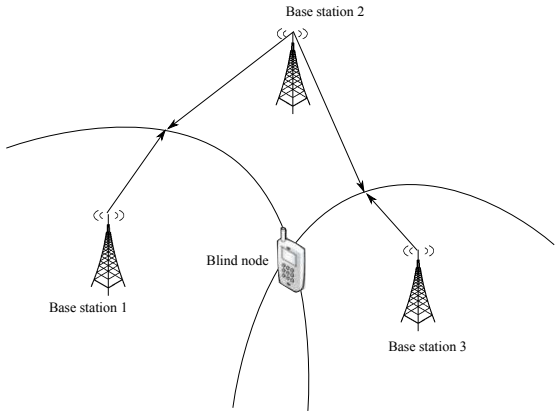

Fig. 3.3: Example of localization based on TDoA.

The TDoA based method uses the difference of ToA of signals between several transmitter to position the blind node. As shown on Figure 3.3, the region of the Euclidean space drawn by that observable lie on a hyperbola in 2D (resp. an hyperboloid in 3D). Localization algorithms based on TDoAs use several of those observables to estimate the position as the intersection point of those hyperbolas. One of the advantage of TDoA observable on ToA is it requires less synchronized nodes. Two major drawbacks can be noted:

– The TDoA based location algorithms are more sensitives to the noise
– Due to the noise, the hyperbolas intersection can degenerates in several regions leading to a non convex problem, which are quite hard to approximate with a classical estimator.

3.2.4.4 Strategies to Improve the Localization

Because the radio observables are not necessarily reliable due to different perturbations of the environment, it is required to elaborate mechanisms to obtain the best position estimation whatever their qualities. For that purpose, different strategies (which can advantageously be combined) are considered. Those strategies are based either on a selection of the more appropriate LDP depending on the considered situation, or on the network organization and the capability to exchange information between the different nodes.

Heterogeneous Localization

Heterogeneous localization consists in obtaining observables from different sources usable for localization purpose. For radio observables, it means obtaining a given type of LDP from different type of Radio Access Technologys (RATs). The multiplication of the observables is particularly interesting, in a context where the trend is to an increase of both the number of devices and the number of RATs embedded [63]. Viewed in the light of localization, that increase of observables helps localization either bring new observables to solve an under-dimensioned problem or to increase the position accuracy by adding redundancy.

Hybrid Localization

Another solution to increase the number of observables feeding the localization algorithm is to use different type of LDP from a given RAT [64]. Similarly to the heterogeneous localization, the hybrid localization allows to multiply the number of observables to increase the accuracy of the position estimation.

Distributed Network

Opposed to the centralized scheme, where the infrastructure estimate the position with the information from the nodes of the network [65], the distributed network delegates the position estimation to the nodes in regard to their available observables [66]. Hence, the available information is embedded in the mobile device, which consequently reduce the load of the infrastructure by limiting the number communication and conserving the localization accuracy [67].

Cooperation

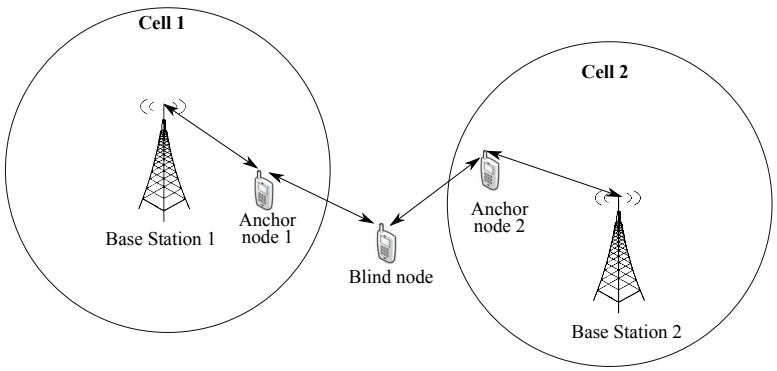

Fig. 3.4: The blind node obtains LDPs observables even being outside of cell 1 and cell 2.

Pending to the distributed network is the notion of cooperation. Cooperation designates the ability of nodes to exchange information without requesting the infrastructure

[68]. As shown in Figure 3.4, nodes communicate with each other to get the information required to estimate their position. Two main approaches are envisaged to enable node cooperation: Multi-hop and message passing.

The Multi-hop approaches supposes that a small part of the nodes of a network have access to their precise positions (with the help of a GPS for instance) [69]. The other nodes only have relative information between them, such as inter-node distances obtained from RSS or ToA. The gathered LDP information from all the nodes and the precise information of some allow to obtain an accurate position estimation of each nodes.

Message passing approach is an anchor less approach based on graphical models as factor graphs [70]. The nodes of the network only know their initial position. They update their marginal distributions of positions using their local a priori and the help of their neighbors [71]. Instead of simply exchanging LDPs for refining their position estimation, the whole Power Density Function (PDF) or a belief function is exchanged between nodes.

3.2.5 Algorithms based on Algebraic Method

If all localization algorithms are fed with LDPs, it exists different processing schemes to obtain a position. Here are presented the 2 most commons algebraic based processing methods, and the Cramer-Rao Lower Bound (CRLB) which indicates the theoretical achievable accuracy in regard of the observables variances.

3.2.5.1 Weighted Least Square (WLS) Estimator

A least square problem is an optimization problem where the unknown is part of the sum of squares of terms. Assuming that $\mathbf{a}$ and $\mathbf{b}$ are a parameter vector and an observation vector respectively and $\mathbf{X}$ the optimization variable, the least square problem can be formalized as :

$$\min_{\mathbf{X}} \quad f_0(\mathbf{X}) = \sum_{i=1}^{n} (\mathbf{a}_i^T \mathbf{X} - b_i)^2 \tag{3.1}$$

Assuming some linearization, the analytic solution $\hat{\mathbf{X}}$ can be written [72]:

$$\hat{\mathbf{X}} = (\mathbf{A}^T \mathbf{A})^{-1} \mathbf{A}^T \mathbf{b} \tag{3.2}$$

The weighted least square is similar to least square problem, except that a weighted factor on the observation vector is added to . Thus, (3.1) yields:

$$\min_{\mathbf{X}} \quad f_0(\mathbf{X}) = \sum_{i=1}^{n} w_i (\mathbf{a}_i^T \mathbf{X} - b_i)^2 \tag{3.3}$$

where w_i is the weight of observable i. Usually, in localization problem, the considered weights are the variance of each element of the observation vector. By defining $\mathbf{C} =$

$diag(w_0, ..., w_i)$, it is possible to rewrite 3.2 in order to fit with the WLS problem:

$$\hat{\mathbf{X}} = (\mathbf{A}^T\mathbf{C}^{-1}\mathbf{A})^{-1}\mathbf{A}^T\mathbf{C}^{-1}\mathbf{b} \tag{3.4}$$

The main advantage of the WLS approach is its simplicity and its relative low computational cost [73]. However, the resolution method relies on a linearization procedure and a matrix inversion, which can be tricky in case matrix is ill-conditioned. To address that particular problem, some enhancements have been proposed in [74]. Despite of this solution, least squares methods only fit with linear problem. In localization problem context, and especially in indoor, that hypothesis of linearity cannot be guaranteed. For that purpose, Maximum Likelihood (ML) methods are generally preferred.

3.2.5.2 Maximum Likelihood (ML) Estimator

Assuming that an observation vector $\mathbf{b}$ of the true position $\mathbf{X}$ of a blind node is distributed with the following density $p(\mathbf{b}|\mathbf{X})$, it is possible to define the associated likelihood:

$$\mathbf{f}(\mathbf{X}, \mathbf{b}) = p(\mathbf{b} \mid \mathbf{X}) \tag{3.5}$$

The maximum likelihood estimator aims to find a value of $\mathbf{X}$, which maximize $\mathbf{f}(\mathbf{X}, \mathbf{b})$. For a localization purpose, it means that the estimated position $\hat{\mathbf{X}}$ is obtained for :

$$\hat{\mathbf{X}} = \max_{\mathbf{X}} \mathbf{f}(\mathbf{X}, \mathbf{b}) \tag{3.6}$$

That research of maximum on the whole likelihood function can be time consuming. Practically, that searching is generally computed with an iterative procedure as expectation-maximization algorithm [75]. However, the effectiveness of this iterative method is limited to convex likelihood functions. In case of non convexity, a local extrema can be proposed as the solution of the estimation problem. Convex optimization techniques can also be used [73], but their computation time have to be added to the ML estimation.

3.2.5.3 Cramer-Rao Lower Bound (CRLB)

In estimation theory and statistics, the Cramer-Rao Lower Bound (CRLB) designates the lower bound on the variance of estimators of a deterministic parameter. Practically, it states that the variance of any unbiased estimator of a variable $\mathbf{X}$ is at least as high as the inverse of the Fisher information $\mathbf{J}(\mathbf{X})$. Regarding that the efficiency of an unbiased estimator is measured on its capacity to reach its lower bound, any solution achieving that bound would be designated as efficient. The Fisher information is a way of measuring the amount of information of $\mathbf{X}$. The Fisher information is equal to the variance of partial derivative, with respect to the unknown parameter, of the logarithm of the likelihood function [76]. The CRLB can thus be defined as the trace of the inverse of the Fisher information matrix:

$$CRLB(\mathbf{X}) = \text{trace}\left[\mathbf{J}((\mathbf{X}))^{-1}\right] \tag{3.7}$$

3.2.6 Algorithms based on Interval Analysis Methods

Interval analysis approach also uses LDPs to obtain the position, but its processing differs from algebraic methods. Indeed, this approach proposes to represent a random variable x using an interval denoted $[x]$ containing the support function of its PDF. Hence, in case of a zero mean Gaussian random variable q with a given standard deviation σ_q, it is possible to define a confidence interval $[I_q]$ with:

$$[I_q] = [q - 3\sigma_q, q + 3\sigma_q] \tag{3.8}$$

where the 3 factor ensures a 99% confidence interval for q.

The use of such an expression present some advantages (especially in the context of localization):

- It allows to describe the behavior of a random variable in a very compact form, using only the two boundaries of the interval,
- It allows to perform simple computation on intervals either than working with complex expressions of PDF,
- It can handle non linear problems,
- That simplification enables parallelization of interval processing.

Obviously that representation losses information in regards of the complete PDF. In particular, the corresponding probability value of a given realization cannot be known, and only the limits of the excursion of the random value remained. Another problem in case of large outliers, some inconsistence can appear and the interval could not guarantee containing the solution.

3.2.6.1 Interval Analysis Method For Localization

Interval analysis theory has been developed both by Moore [77] and by Hansen and its team [78]. It has taken 25 years and the creation of the interval analysis journal (now known as Reliable computing) for this method emerges from confidentiality of its original laboratory.

Interval analysis is broadly used for very different kind of applications from modeling of beams in particles accelerators [79], calculation of insurances problems [80] through robotic problems [81].

Robotic is probably the field where interval analysis has been the most considered for parameters estimation [82] and especially for robot localization [83, 84].

The problem of localization is very well suited for being addressed by interval analysis approaches. As it has been seen before, the uncertainty of the observables leads to a position estimation with a given accuracy. This is e.g. the case in GNSS navigation, where the actual position of the user is generally depicted as a circle centered on the estimated position, and where the radius represents the position uncertainty. Instead of giving a unique position, localization based on interval analysis returns the uncertainty interval, which is more "fair" in terms of actual knowledge of the position from the algorithm vision.

One other advantage for localization is its ability to easily merge observables of very different natures. For instance, interval analysis has been used in an advanced GPS approach where inertial sensors were used in addition the GNSS observables to compensate the urban canyon effect [85, 86].

After having being tested with TDoA observables for radar applications [87], the interval analysis has been more recently introduced in Mobile Ad-hoc sensor NETworks (MANET) for tracking nodes positions. The method has proved its interest compared to a particle filtering approach [88]. Consequently, the management of outliers observables has been added to increase its robustness of positioning [89]. For the particular case of indoor localization, interval analysis has not been widely explored, except in [90], where RSS observables where used to perform the position estimation in a building. Despite of the capacity to merge different type of observables, which is an advantage in both heterogeneous networks and hybrid data fusion scenarios, it is noticeable that interval analysis methods are still not well considered for localization in radio communications context.

All the different examples of position estimation based on interval analysis presented in this section rely on one of both existing methods to solve an interval analysis problem:

- the contraction based methods
- the bisection based methods

3.2.6.2 Contraction based methods

Contraction based methods consist in iteratively reducing (contracting) the interval of the solution in regard of both the known accuracy of the input parameter and their corresponding type of constraints. Practically, it means that the interval of a variable depends on the intervals of the other variables involved in the same constraint. Lets suppose a minimal example with 3 variables a, b and c supposed to lie in 3 intervals $[a] = [20, 30]$, $[b] = [-15, 25]$ and $[c] \in [-50, 10]$ respectively. Assuming that they are linked by the relation $c = a + b$, it is possible to use the interval analysis and its dedicated mathematical rules described in [91] to compute:

$$[c] = [a] + [b] = [20, 30] + [-15, 25] = [5, 55] \tag{3.9}$$

Using the prior information on $[c]$, it is possible to update the interval of c:

$$[c] = [c] \cap [5, 55] = [-50, 10] \cap [5, 55] = [5, 10] \tag{3.10}$$

The interval where c lies has been contracted. Another aspect of the contraction based method, is the constraint propagation of the results. It means that the contraction on interval c may also have consequences of intervals a and b. Continuing the same example, the contraction of $[c]$ can also helps to contract $[b]$:

$$[b] = ([c] - [a]) \cap [b] \tag{3.11}$$
$$= ([5, 10] - [20, 30]) \cap [b] \tag{3.12}$$
$$= ([-25, -10)] \cap [-15, 25] \tag{3.13}$$
$$= [-15, -10] \tag{3.14}$$

but not $[a]$ in this example:

$$[a] = ([c] - [b]) \cap [a] \tag{3.15}$$
$$= ([5, 10] - [-15, 25]) \cap [a] \tag{3.16}$$
$$= ([-20, 35)] \cap [20, 30] \tag{3.17}$$
$$= [20, 30] \tag{3.18}$$

More complexes problems with more variables and non linear equations, that constraint propagation process can be repeated to find an optimal interval for each parameters. That contraction method can be very efficient in terms of speed and accuracy in localization problems. However, it requires specific hardware implementation in order to correctly manage the intervals arithmetic.

3.2.6.3 Bisection based methods

Unlike contraction based methods, bisection based methods do not depend on interval arithmetic but on a recursive process [92]. Bisection based methods consists in spliting the parameter intervals in two equal intervals and checking the validity of this 2 intervals in regards of the constraints. Intervals which are not valid are removed whereas the others are candidate for a further bisection iteration. More details of that bisection method is provided in section 3.3.2.4. From the low level implementation point of view, bisection methods are very convenient because they only involved very basic operations. Indeed the decision on the validity is done with a simple comparison between the boundaries of an interval and the constraint. For that reason, bisection has been preferred in the Robust Geometric Positioning Algorithm (RGPA) presented in the next section.

In addition, it also exists interval analysis resolution method using joint contraction and bisection. One of the most famous is the SIVIA algorithm described in [93]. The simultaneous use of those method has proved its efficiency, but won't be considered in this work for the implementation reason mentioned before.

3.3 Description of the Robust Geometric Positioning Algorithm (RGPA)

The proposed RGPA, as any other range based localization methods, uses radio observables to estimate a position. Instead of using directly the values of the observables,

the RGPA converts them into geometrical shapes and search their intersection in the Euclidean space to resolve the positioning problem.

In the following, the description of the constraints associated with the 3 most used radio observables is provided in 3.3.1. Then the complete processing of the RGPA algorithm is described in 3.3.2. Finally, the method is evaluated and compared to a ML approach in simulation.

3.3.1 Constraints and Geometrical Constraints Definitions

Assuming a given model for radio observables, it is possible to obtain a mathematical expression which links the receiver and transmitter positions. That mathematical expression is used as a constraint of the problem (Def. 5).

Definition 5 (Constraint) *A constraint is a mathematical expression which restricts the space of possible solutions for a given variable.*

Associated to each constraint, it exists a geometrical constraint (Def. 6), which delimits a region of space. All points of the plan belonging to this region satisfy the constraint.

Definition 6 (Geometrical Constraint) *A geometrical constraint is the expression of a constraint into the Euclidean space.*

In the following, 3 types of LDPs are considered to build the constraints: the ranges, the difference of ranges and the received powers.

3.3.1.1 Range Constraint

A range observable r evaluated between an anchor at position $\mathbf{a} = [x_a, y_a, z_a]$ and the blind node at position $\mathbf{b} = [x_b, y_b, z_b]$ can be written:

$$r = \|\mathbf{a} - \mathbf{b}\| + \delta_r, \tag{3.19}$$

where δ_r is an additional range error.

3.3.1.2 Difference of Ranges Constraint

A difference of ranges Δ from two anchors at positions $\mathbf{a}$, $\mathbf{a}'$ can be written:

$$\Delta = \|\mathbf{a} - \mathbf{b}\| - \|\mathbf{a}' - \mathbf{b}\| + \delta_\Delta, \tag{3.20}$$

where δ_Δ is an additional difference of ranges error.

3.3.1.3 Power Constraint

A log received power observable can be modeled with a standard path loss model :

$$P(d) = P_0 - 10n_p \log_{10}(d) + X, \tag{3.21}$$

where P_0 is the power received at 1 meter, n_p is the path loss exponent and X a error realization. Thus, according to [94], the distance d associated to P between an anchor at position $\mathbf{a}$ and the blind node at position $\mathbf{b}$ can be estimated with:

$$d = \exp(M - S^2) + \delta_P \tag{3.22}$$

with

$$M = \frac{\log(10)(P_0 - P)}{10n_p} \tag{3.23}$$

$$S = -\frac{\log(10)\sigma_X}{10n_p} \tag{3.24}$$

where σ_X^2 is the variance of the received power observation perturbation. The additional δ_P estimated distance error can be computed with :

$$\delta_P = \sqrt{(1 - \exp(-S^2))\,(\exp(2M - 2S^2))} \tag{3.25}$$

Practically, the log received power information can be obtained from the received signal strength indicators.

3.3.1.4 Confidence Interval Determination

It has been seen that the values of the mathematical constraints all depend on the observation of an error term. Assuming a given probability model for that error, it is possible to bound each constraint with a confidence intervals (Def. 7).

Definition 7 (Confidence Interval) *The confidence interval of a given constraint is a bounded interval inside which, any value satisfies the constraint.*

Hence, assuming that the probability models chosen for δ_r, δ_Δ and δ_P are zero mean Gaussian with σ_r^2, σ_Δ^2 and σ_P^2 their variances respectively, it is possible to build $[I_r]$, $[I_\Delta]$ and $[I_P]$, the constraint interval of the range, of the difference of ranges constraint and of the power constraint respectively as:

$$[I_r] = [r - \gamma\sigma_r, r + \gamma\sigma_r] \tag{3.26}$$

$$[I_\Delta] = [\Delta - \gamma\sigma_\Delta, \Delta + \gamma\sigma_\Delta] \tag{3.27}$$

$$[I_P] = [P(d) - \gamma\sigma_P, P(d) + \gamma\sigma_P] \tag{3.28}$$

$$\tag{3.29}$$

with γ, an adjustment factor. Without prior information, $\gamma = 3$ to ensure a 99% confidence interval for each the constraint.

As a consequence,

- the geometric constraint from a range constraint is shaped as an annulus in two dimensions (2D) or a shell in three dimensions (3D), with center **a**.
- the geometric constraint from a TDoA is shaped as the region between two hyperbolas in 2D or two hyperboloids in 3D.
- the geometric constraint from a power constraint is shaped as an annulus in two dimensions (2D) or a shell in three dimensions (3D), with center **a**.

3.3.2 Geometric Algorithm Description

From the description of the confidence interval associated to radio observables, it is possible to build the geometric positioning algorithm. Similarly to the algebraic problem, where the estimation of the position can be assimilated to the resolution of a system of constraints, the geometric resolution consists in finding the region delimited by the intersection of the geometrical constraints and then estimate a position in that region. RGPA proposes to achieve the position estimation problem in 5 steps, detailed in the following and summarized in table 3.1.

Table 3.1: The Proposed Geometric Method: Algorithm Description

1. Build the constraints (Figure 3.5),
2. Box the constraints (Figure 3.6),
3. Merge the constraints to obtain a merged box (Figure 3.7),
4. Approximate the merged box with a Kd-Tree algorithm to obtain an approximated region (Figure 3.8),
5. Estimate the position from the approximated region (Figure 3.11).

3.3.2.1 Build the Constraints

The first step in RGPA computing is to convert the radio observables to constraints. Each radio observable desired to be used to perform the localization is associated to a certain constraint type as described in 3.3.1. Assuming the knowledge of the model parameters, it is possible to determine the confidence interval for those constraints. Figure 3.5 represents the geometric constraints build from their constraints for an example of localization scenario with 4 anchors where:

- 2 anchors provide a TDoA observable,
- 1 anchor provides a ToA observable,
- 1 anchor provides a RSS observable.

3.3.2.2 Box the Constraints

Instead of precisely bounding the intersection region of all the constraints, which can be a time consuming task, it is first preferred to find the enclosing box of that region. For that purpose, each constraint interval is projected on each axis in order to

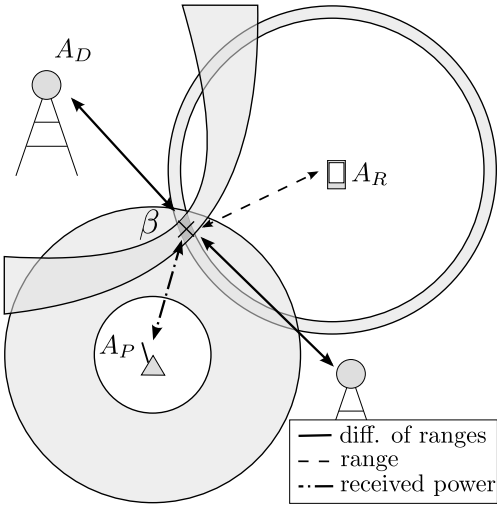

Fig. 3.5: The three constraints are built thanks to three different types of radio observables.

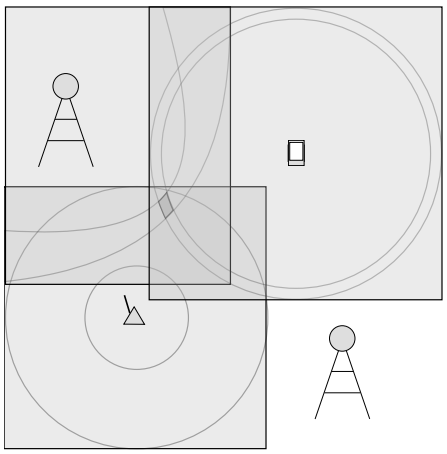

Fig. 3.6: The three constraints are boxed.

obtain a constraint box B (as defined in Def. 8). As a consequence, it is possible to define a geometric box from a constraint box (Def. 9), as represented in Figure 3.6.

Definition 8 (Box) *Given an axis dimension k set at $k = 2$ for a 2D problem, and defining $proj_k([I])$ as the projection of the interval $[I]$ on axis k. a box B can be defined with [91]:*

$$B = [\mathbf{I}] = [I_1] \times [I_2] \times \ldots \times [I_k], \tag{3.30}$$

$$with\, [I_k] = proj_k([I]),$$

Hence written, it can be observed that a box gathers as much interval as the given dimension k.

Definition 9 (Geometric Box) *A geometric box is the expression of a constraint box into the Euclidean space.*

3.3.2.3 Smart Merge of the Constraints

For the efficiency of the next computation step, the merged box resulting from the constraint boxes intersection has to be the smallest as possible. Therefore, a smart merge process is proposed to optimize the size of the merged box.

First, that operation requires to search the merged box B_m from all the constraints boxes B_n with :

$$B_m = \bigcap_{n}^{N} B_n \tag{3.31}$$

where n is the number of considered boxes.

From that point, two situations can be considered

- either B_m exists, which means that there is room to reduce the size of the merged box,
- or B_m does not exists, which means the all the boxes are not intersecting.

In both cases, it is required to update the constraint boxes either to reduce or to make exist B_m. Consequently, a modification of all the constraint boxes has to be applied:

- either all the constraint boxes are reduced, to reduce the size of B_m,
- or all the constraint boxes are embossed, to make appear B_m.

Practically, the size of the constraint boxes can be changed by modifying the value of their adjustment factor γ. The process is repeated until γ has reached a limit value. The smart merge is detailed in algorithm 6 and illustrated by Figure 3.7.

3.3.2.4 Approximate the Merged Box

The approximation of the merged box is performed using a bisection method. As observable in Figure 3.8, this is a recursive procedure consisting in recursively splitting the merged box to approximate the real shape created by the intersection of all geometrical constraints. That procedure requires 3 steps :

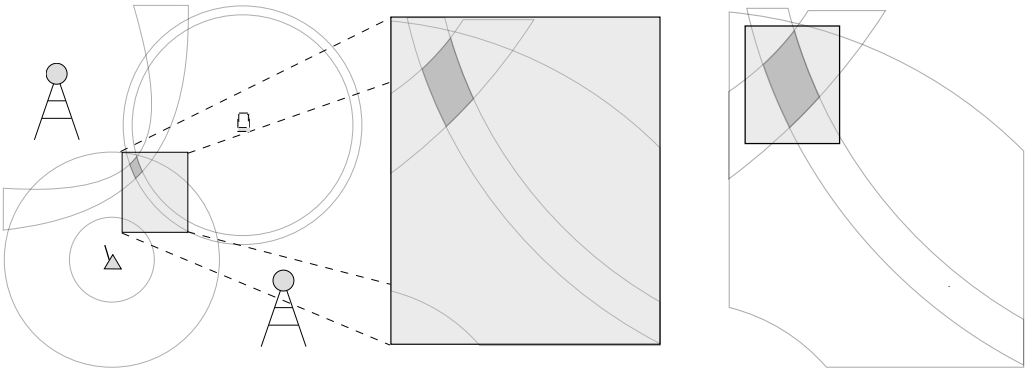

(a) Simple merge (b) Smart merge

Fig. 3.7: Illustration of the merging step, the grey area represents the merged box. (a) The result of the simple merge of the three geometrical boxes of the constraints. (b) result of the smart merge once the three geometrical boxes of the constraints have been resized, the merged box is smaller.

Algorithm 6 Smart Merge Algorithm

γ=3 ▷ to ensure a 99% confidence interval
while $\alpha > \alpha_{min}$ **or** $\gamma == \gamma_{min}$ **do**
  for n **in** N **do**
    B_n =update-size(B_n, γ) ▷ update boxes sizes
  end for
  $B_m = \bigcap_{n}^{N} B_n$ ▷ compute the box intersection of all constraints
  if $B_m == \emptyset$ **then**
    $\gamma = \gamma + \alpha$ ▷ increasing the confidence interval
    $\alpha = \alpha * 2$
  else
    $\gamma = \gamma - \alpha$ ▷ reducing the confidence interval
    $\alpha = \alpha/2$
  end if
end while

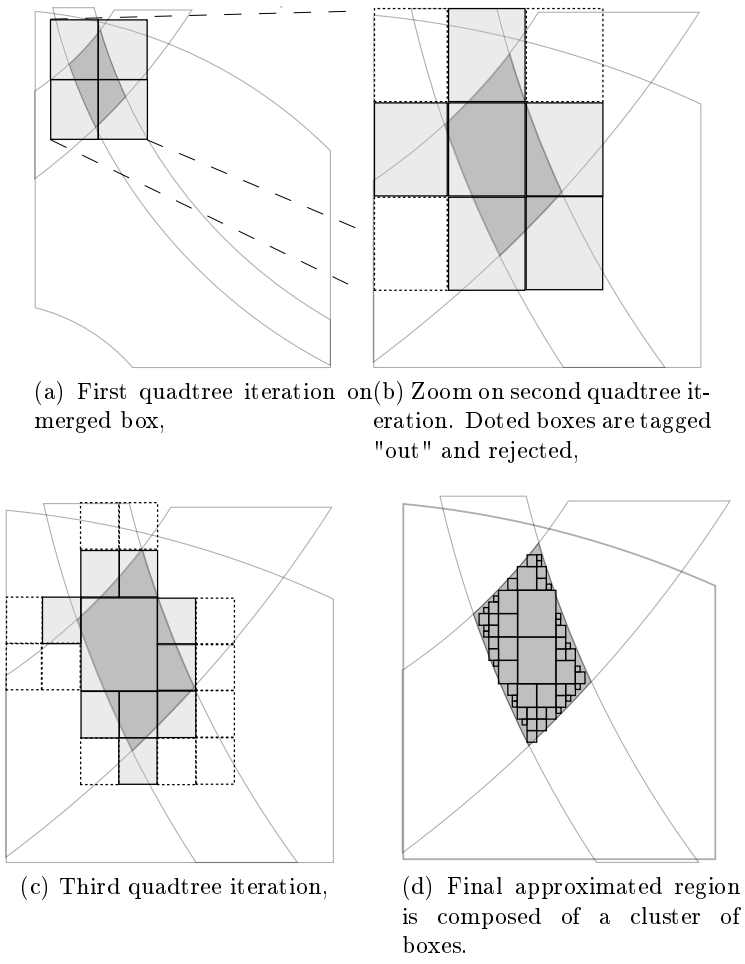

(a) First quadtree iteration on merged box,

(b) Zoom on second quadtree iteration. Doted boxes are tagged "out" and rejected,

(c) Third quadtree iteration,

(d) Final approximated region is composed of a cluster of boxes.

Fig. 3.8: The quadtree approximation to determine the enclosed and ambiguous boxes.

1. Applying a Kd-Tree algorithm [95] (a.k.a. quadtree algorithm in 2D, or octree algorithm in 3D) on the merged box.
2. Testing the resulting boxes one by one with each constraints,
3. Determining boxes to keep and restart the process on them.

Kd-Tree Algorithm

Kd-Tree Algorithm is a partitioning algorithm which splits a single object into several complementary ones. For the problem at hand, the algorithm is performed on the merged box. From the merged box, the Kd-Tree algorithm returns 2^k sets of boxes $\{B\}$, where k is the space dimension. Practically, for each dimension of a box, its interval is split into two complementary intervals.

Test the Boxes

Once the 2^k boxes have been obtained, they have to be tested in regard of all the constraints. Each box is tested one by one with each constraints to determine if:

- The box is an enclosed box (Def.10),
- The box is ambiguous (Def.11),
- The box is out (Def.12).

Definition 10 (Enclosed Box) *A box is said enclosed if the nearest vertex **and** the furtherest vertex from the center of a geometrical constraint are **inside** the confidence interval of the constraint.*

Definition 11 (Ambiguous Box) *A box is said Ambiguous if the nearest vertex **or** the furtherest vertex from the center of a geometrical constraint are **inside** the confidence interval of the constraint.*

Definition 12 (Out Box) *A box is said Out if the nearest vertex **and** the furtherest vertex from the center of a geometrical constraint are **outside** of the confidence interval of the constraint.*

In the example presented in Figure 3.9, the box number 1 is tagged as an "enclosed box"; the boxes number 2, 5 and 6 are tagged as "ambiguous boxes"; the boxes number 3 and 4 are tagged as "out boxes".

An exact solution to test the belonging of a box to a geometrical constraint would require verifying the belonging of each vertex of the box to the confidence interval of the constraint. In regard of the number of boxes to test, a non exact alternative method is proposed. This alternative method consists in testing only 2 vertexes of the box: the nearest vertex from the center of the geometrical constraint and the furthest one.

The example presented in Figure 3.10 illustrates that method. Lets define a constraint obtained from a range observable c located in O and perturbed with zero mean Gaussian with σ_c its variance. Its resulting confidence interval I_c can be written :

$$[I_c] = [c - \sigma_c, c + \sigma_c] \tag{3.32}$$

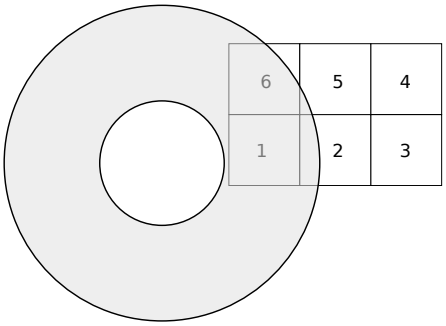

Fig. 3.9: Example representing a geometrical constraint and 6 boxes. Depending of their relative position to the confidence interval, the boxes will be tagged enclosed, ambiguous or out.

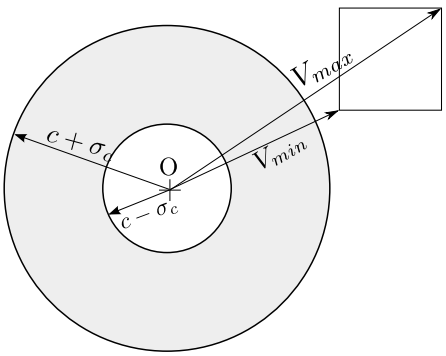

Fig. 3.10: Geometrical constraint and a box. The distances $c - \sigma_c$ and $c + \sigma_c$ are the distances limited by the confidence interval of the constraint. The distances V_{min} and V_{max} are the distance from the constraint center O, to the closer vertex of the box and the further vertex of the box respectively.

Then it is possible to define V_{min} and V_{max} the distance from the geometrical constraint center to the nearest vertex of the box and the further of the box respectively. Hence, for a given box and a given constraint, four hypotheses have to be tested :

$$\begin{cases} h_0 : V_{min} < c - \sigma_c \\ h_1 : V_{min} < c + \sigma_c \\ h_2 : V_{max} < c - \sigma_c \\ h_3 : V_{max} < c + \sigma_c \end{cases} \tag{3.33}$$

Practically those four hypotheses return boolean values which are set True or False regarding the values of D_{min}, D_{max}, c and σ_c. Then, it is possible to determine 2 logic indicator functions $\mathcal{L}_e(B_n)$ and $\mathcal{L}_a(B_n)$ returning a True logic value if a box B_n is enclosed or ambiguous respectively. Assuming some logic simplifications those indicators can be written:

$$\mathcal{L}_e(B_n) = \bar{h}_0 h_1 \bar{h}_2 h_3 \tag{3.34}$$

$$\mathcal{L}_a(B_n) = \bar{h}_0 \bar{h}_1 h_3 + h_1 \bar{h}_2 \bar{h}_3 + h_0 h_1 \bar{h}_2 \tag{3.35}$$

Decision and Novel Iteration

Using the results of the indicator functions, the enclosed boxes are stored, and the ambiguous boxes are candidate for a new Kd-Tree iteration. All the other boxes are rejected. The whole process is repeated until μ_e sets of enclosed boxes $\{B_e\}$ are obtained, whereupon the process is stopped. If no enclosed boxes are obtained, the process stops on a given number μ_a sets of ambiguous boxes $\{B_a\}$. Algorithm 7 describes the complete procedure of the implemented Kd-Tree algorithm.

3.3.2.5 Estimating the Position

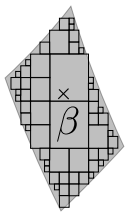

(a) Example of Position Estimation in the approximated region

(b) Screenshot from demonstrator of the approximated region.

Fig. 3.11: Estimation of the position (a) on the illustrated example , (b) using the implemented algorithm: green ball is the true position, the black ball is the estimated position, blue and red boxes are enclosed and ambiguous boxes respectively.

Figure 3.11 illustrates the position estimation step. That step only consists in estimating the true position from the center of mass of the set of enclosing boxes $\{B_e\}$

Algorithm 7 interval approximation by boxes

▷ initialization of the set of ambiguous boxes with the merged box B_m
$\{B_a\} = \{B_m\}$
▷ initialization of the set of enclosed boxes
$\{B_e\} = \{\}$
while $\text{card}(\{B_e\}) \leq \mu_e$ **or** $(\text{card}(\{B_e\}) + \text{card}(\{B_a\})) \leq \mu_a$ **do**
  for b **in** $\{B_a\}$ **do**
    $\{Q\} = \text{KdTree}(b)$ ▷ On each ambiguous box a Kd-Tree is applied
    for q **in** $\{Q\}$ **do**
      if $\mathcal{L}_e(q) == \text{True}$ **then** ▷ Test enclosure
        $\{B_e\} = \{B_e\} + q$
      else if $\mathcal{L}_a(q) == \text{True}$ **then** ▷ Test ambiguity
        $\{B_a\} = \{B_a\} + q$
      end if
    end for
  end for
end while

(or $\{B_a\}$ if $\{B_e\} = \emptyset$). Figure 3.11b is a screenshot where the enclosing boxes, ambiguous boxes, true and estimated blind node positions are displayed using the algorithm visualization tool.

Note that in cases where the set of enclosing boxes $\{B_e\}$ are disjoints, the position estimate could take advantage of an advanced estimation procedure based on hypothesis testing method as described in 3.4.

3.3.3 Evaluation of the Robust Geometric Positioning Algorithm (RGPA)

This section evaluates the positioning performances of the proposed RGPA, and compares it against algebraic methods.

3.3.3.1 Simulation Scenario

The scenario presented in Figure 3.12 has been used in [73] to evaluate hybrid and heterogeneous ML and WLS based methods. For that reason this scenario is used to provide a comparison between the proposed RGPA method and those algebraic ones. In this scenario, the blind node estimates its position β with the help of anchors providing three types of radio observables. The anchors at positions $\{A_P\}$ provide received power observations $\{P\}$, the anchors at positions $\{A_D\}$ provide difference of ranges observations $\{\Delta\}$ and the anchors at positions $\{A_R\}$ provide range observations $\{r\}$. These three types of anchors are drawn on the edges of three different squares, thus:

- $\{A_P\} \in \mathcal{H}_P$,
- $\{A_D\} \in \mathcal{H}_D$,
- $\{A_R\} \in \mathcal{H}_R$,

Table 3.2: Parameters settings

Parameter	Value	
$\mathcal{H}_P$	$[-1,1]\times[-1,1]$	km^2
$\mathcal{H}_D$	$[-100,100]\times[-100,100]$	m^2
$\mathcal{H}_R$	$[-10,10]\times[-10,10]$	m^2
σ_r	2.97	m
σ_Δ	3.55	m
σ_X	4.34	dB
n_p	2.64	
P_0	-40	dB

with $\mathcal{H}_R \subset \mathcal{H}_D \subset \mathcal{H}_P$. The blind node is assumed to search its position in $\mathcal{H}_R$.

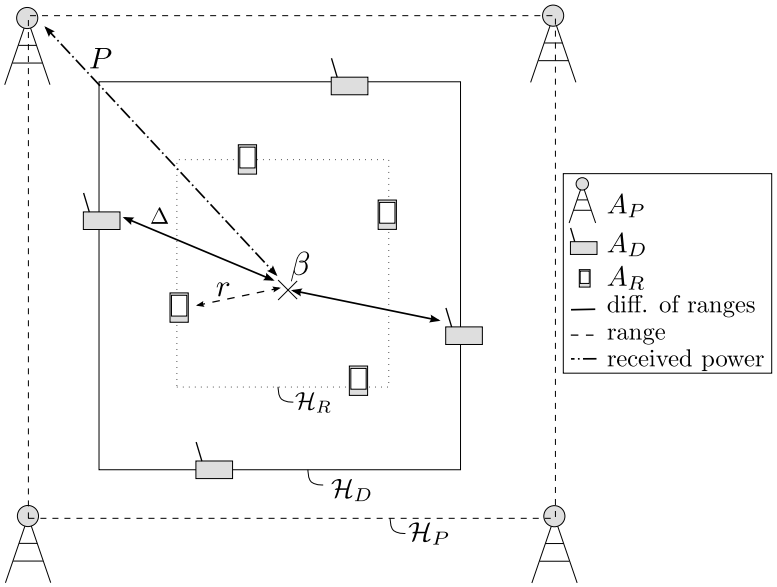

Fig. 3.12: A blind node at position β receives range observations $\{r\}$ from anchors at positions $\{A_R\}$, difference of ranges observations $\{\Delta\}$ from anchors at positions $\{A_D\}$ and received power observations $\{P\}$ from anchors at positions $\{A_P\}$.

The performance of the proposed geometric method is compared to a ML approximation and to the Cramer-Rao lower bound (CRLB) via Monte Carlo simulation based on the scenario described in Figure 3.12. The ML approximation uses a Nelder-Mead simplex optimizer initialized with a weighted least square solution (ML-WLS) [96]. Multidimensional likelihood functions corresponding to the given scenarios are described in [73]. The perturbation of the observation of the range constraint, the difference of range constraint and the power constraint are supposed zero mean Gaussian, with their respective variances σ_r^2, σ_Δ^2 and σ_P^2. The parameter settings in Table 3.2 have been chosen compliant with the WHERE1 measurement campaign [97].

3.3.3.2 Comparison of Performances

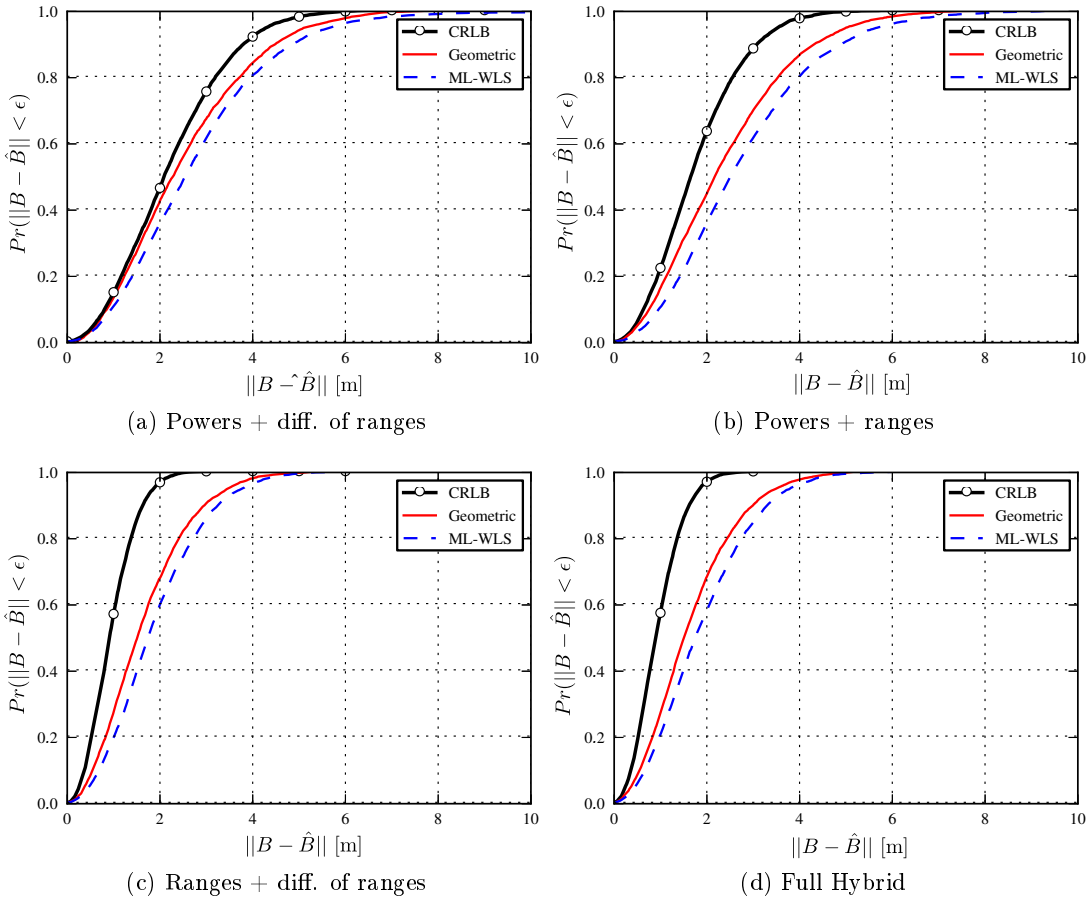

(a) Powers + diff. of ranges (b) Powers + ranges

(c) Ranges + diff. of ranges (d) Full Hybrid

Fig. 3.13: CDFs of positioning error using the proposed geometric method, ML-WLS, and CRLB applied on hybrid positioning technique.

The three algorithms are compared in terms of cumulative density function (CDF), root mean square error (RMSE) and computation speed for the hybrid cases for four hybrid configurations:

- Powers + difference of ranges, using 4 received powers and 3 difference of ranges observables (Figure 3.13a),
- Powers + ranges, using 4 received powers and 4 ranges observables (Figure 3.13b),
- Ranges + difference of ranges, using 4 ranges and 3 difference of ranges observables (Figure 3.13c),
- Full hybrid, using 4 received powers, 4 ranges and 3 difference of ranges observables (Figure 3.13d).

The non-hybrid cases using a unique type of observation (only range, difference of ranges, or received power) are not considered here. From the empirical CDF shown in

Figure 3.13 (a-d) it appears that the proposed geometric method prevails on ML-WLS. That increase of accuracy of positioning is especially significant on Figure 3.13a and Figure 3.13b. Those two cases using received power observables allow a gain between 0.5mand 1 m for all blind nodes. Other cases based only on time based observables as shown in Figure 3.13c, or using all type of observables as shown in Figure 3.13d, also show a better accuracy in terms of position estimation. Those results are confirmed by the RMSE values shown in Table 3.3. The most significant improvement is observed for the hybrid scheme mixing powers and ranges. In average, the proposed geometric method ensures a 30 cm increase of positioning accuracy for blind nodes drawn in a 20×20 m^2 room.

Obviously these improvements come out at the cost of extra computation complexity. In spite of providing a complete complexity study, Figure 3.14 shows some preliminary results based on an average of computation speed for each method. On those histograms, it can be observed that the proposed method is generally slower than the ML-WLS excepted when the received power observables and range observables are used. It also shows that the difference of ranges constraint is the worst in term of speed. A further investigation would be to improve the speed of the difference of ranges constraint. Moreover, the comparison between both methods is unfair, because the ML-WLS numerical optimization is based on an optimized compiled Fortran code, whereas the proposed geometric method is based on a non fully optimized interpreted code in Python. Considering that difference of implementation, a geometrical method as fast as the ML-WLS could be feasible. Moreover, the geometrical method is highly parallel and involves only elementary operations and could probably be very efficiently implemented in dedicated hardware.

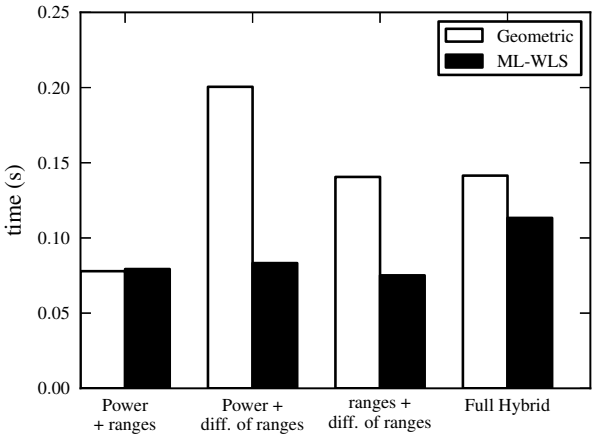

Fig. 3.14: Speed computation comparison between the proposed geometric method and a ML-WLS using a numerical optimizer.

Table 3.3: RMSE vs Method

Hybrid mode	Geometric (m)	ML-WLS (m)	CRLB (m)
Power + diff. of ranges	2.46	2.91	2.23
Power + ranges	2.51	2.81	1.78
Ranges + diff. of ranges	1.68	1.93	0.96
Full Hybrid	1.65	1.92	0.95

3.4 Heterogeneous Localization Using Hypothesis Testing

One of the advantages of the proposed RGPA algorithm is its capacity to always delimit a region of space containing the sought position. Hence, in situation where the number of observables is not sufficient to obtain the exact position of a node, RGPA is able to limit one or several region of space potentially containing the node. That property is used in this section to describe an original heterogeneous localization algorithm.

3.4.1 Description of the Problem

The considered scenario is illustrated in Figure 3.15. The position B of a blind node is estimated from the two noisy range observations r_1, r_2 provided by the range nodes at known positions R_1 and R_2,

$$r_i = \|R_i - B\| + \delta_i, \qquad i = 1, 2, \tag{3.36}$$

where δ_i is the error in the range estimate. Given a probability model for δ_i, it is possible to determine a confidence interval for the range estimate r_i, which as shown in Figure 3.15, yields a confidence region shaped as an annulus with center R_i. The ambiguity problem occurs when the intersection of two confidence annuli splits into two disconnected subsets $\mathscr{C}_1$ and $\mathscr{C}_2$ with centroids C_1 and C_2, respectively. The two subsets and their centroids can be obtained using the RGPA method described in 3.3.

To provide an unambiguous position estimate, additional information is required. It is assumed that additional observations $\{P_k\}$ of the log power are available from the helping nodes at positions $\{H_k\}$. The log power observation P_k is modeled as a distance dependent mean $\mu(d_k)$ distorted by an additive error term X_k, i.e.,

$$P_k = \mu(d_k) + X_k, \tag{3.37}$$

with $d_k = \|B - H_k\|$. It is assumed that the joint probability density function (pdf) of $X_1, \ldots, X_K$ are known. The log power observations are gathered into a vector $\mathbf{P} = [P_1, \ldots, P_K]$. Practically, the log power information can be obtained from the received signal strength indicators.

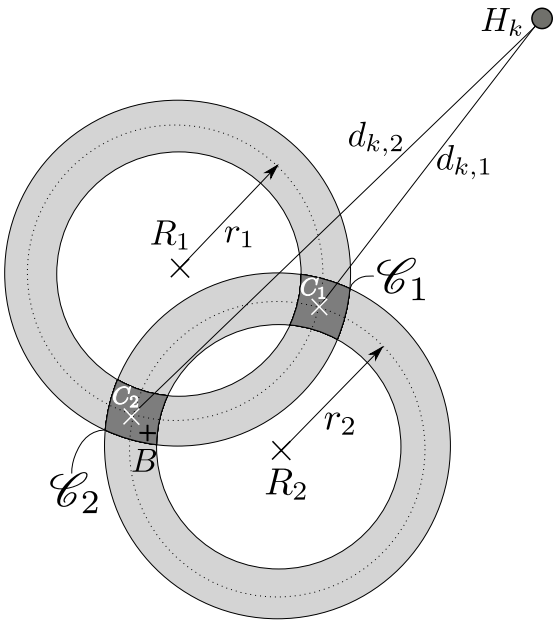

Fig. 3.15: The blind node at position B receives two range estimates r_1 and r_2 from ranging nodes at position R_1 and R_2 respectively. Errors in range estimates are modeled by two confidence annuli centered at R_1 and R_2, respectively. The intersection of annuli are the two shaded regions $\mathscr{C}_1$ and $\mathscr{C}_2$, with their centroids C_1 and C_2 respectively. In addition, the blind node achieves a log power observation from each helping node at position H_k. The distance from H_k to C_i is denoted by $d_{k,i}$.

3.4.2 Proposed Decision Rule

The conditional pdf is approximated for the power observation conditioned by the position of the blind node as:

$$f_{\mathbf{P}|B,r_1,r_2}(\mathbf{p}) \approx \begin{cases} f_{\mathbf{P}|\mathscr{C}_1,r_1,r_2}(\mathbf{p}), & B \in \mathscr{C}_1 \\ f_{\mathbf{P}|\mathscr{C}_2,r_1,r_2}(\mathbf{p}), & B \in \mathscr{C}_2 \\ 0, & \text{otherwise}, \end{cases} \tag{3.38}$$

with $\mathbf{p} \in \mathbb{R}^K$. In (3.38) the probability of the event $B \notin \mathscr{C}_1 \cup \mathscr{C}_2$ is neglected. This approximation is valid by appropriately choosing the regions $\mathscr{C}_1$ or $\mathscr{C}_2$. Since B is unknown, $f_{\mathbf{P}|B,r_1,r_2}(\mathbf{p})$ cannot be computed. However, if accurate range estimates are available, then B can be approximated by C_1 if $B \in \mathscr{C}_1$ or by C_2 if $B \in \mathscr{C}_2$, and thus:

$$d_k \approx \begin{cases} d_{k,1} = \|C_1 - H_k\|, & B \in \mathscr{C}_1 \\ d_{k,2} = \|C_2 - H_k\|, & B \in \mathscr{C}_2. \end{cases} \tag{3.39}$$

With the above approximations, the solution of the ambiguity problem can be phrased as a classical decision problem where λ is the likelihood ratio. The decision threshold γ can be defined to account with a priori information or costs [98]:

$$\lambda = \frac{f_{\mathbf{P}|\mathscr{C}_1,r_1,r_2}(\mathbf{p})}{f_{\mathbf{P}|\mathscr{C}_2,r_1,r_2}(\mathbf{p})} \underset{\mathscr{C}_1}{\overset{\mathscr{C}_2}{\lessgtr}} \gamma. \tag{3.40}$$

The ML decision rule is obtained for $\gamma = 1$.

3.4.3 Special Case: Uncorrelated Gaussian Log Power Errors

In the special case where $X_1, \ldots, X_K$ are independent Gaussian random variables with zero mean and variances $\sigma_1^2, \ldots, \sigma_K^2$, yields for B in $\mathscr{C}_i$:

$$f_{\mathbf{P}|\mathscr{C}_i,r_1,r_2}(\mathbf{p}) = \prod_{k=1}^{K} \frac{1}{\sqrt{2\pi}\sigma_k} \exp\left(-\frac{(p_k - \mu_{k,i})^2}{2\sigma_k^2}\right), \; i = 1, 2, \tag{3.41}$$

with $\mu_{k,i} = \mu(d_{k,i})$. Hence, the log likelihood ratio $\Lambda = \ln \lambda$ reads:

$$\Lambda = \sum_{k=1}^{K} \left[\frac{(p_k - \mu_{k,2})^2}{2\sigma_k^2} - \frac{(p_k - \mu_{k,1})^2}{2\sigma_k^2}\right] \tag{3.42}$$

The ML decision rule is obtained upon insertion of (3.42) into (3.40) with $\gamma = 1$:

$$\sum_{k=1}^{K} \frac{1}{2\sigma_k^2} \left[\mu_{k,2}^2 - \mu_{k,1}^2\right] \underset{\mathscr{C}_2}{\overset{\mathscr{C}_1}{\lessgtr}} \sum_{k=1}^{K} \frac{1}{\sigma_k} P_k(\mu_{k,1} - \mu_{k,2}). \tag{3.43}$$

It can be observed that for fixed centroids C_1 and C_2, the left hand terms are constants, while the right hand terms are a Gaussian random variable. Thus, the computation of error probability is well-known [98]. The evaluation of the performances of this particular method are given in section 3.4.4.

Table 3.4: Parameters settings

Parameter	Value	
$\mathcal{S}$	$[-20, 20] \times [-20, 20]$	m^2
$\mathcal{L}$	$[-80, 80] \times [-80, 80]$	m^2
σ_δ	0.9	m
σ_X	4	dB
n_p	3	
P_0	-40	dB

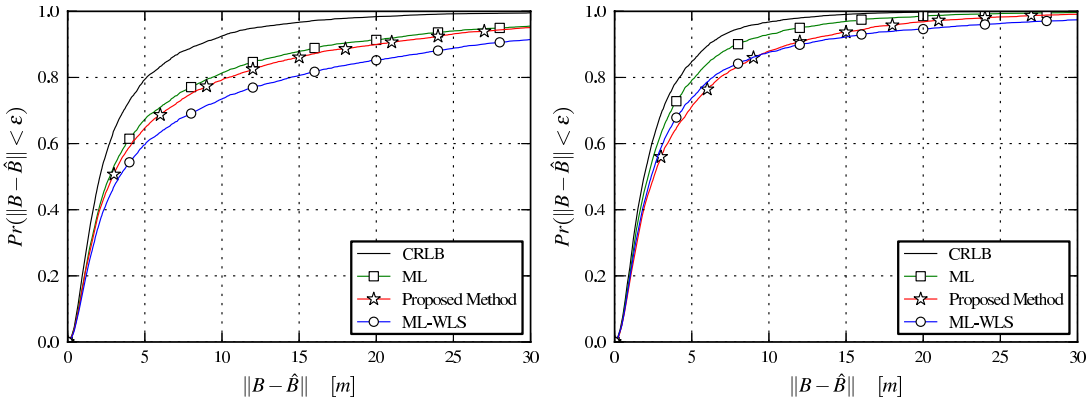

(a) Three helping nodes

(b) Ten helping nodes

Fig. 3.16: CDF comparison of the absolute positioning error between the Cramer Rao Lower Bound (CRLB) [99], the ML estimator (ML), the iterative ML estimator initialized with a weighted least squares solution (ML-WLS) and the proposed method with: (a) Three helping nodes nodes, and (b) Ten helping nodes.

3.4.4 Evaluation of Heterogeneous Localization using Hypothesis Testing

In this section the performance of the proposed method is compared to ML approaches via Monte Carlo simulations of the scenario described in Figure 3.15, and performances. A true ML estimator is considered relying on global optimization and an ML approximation (ML-WLS) in which a local optimizer is initialized with a weighted least squares solution [96], both introduced in Subsection 3.4.4.2.

3.4.4.1 Simulations Scenario

The performance of the proposed solution is assessed via Monte Carlo simulations. The special case described in Subsection 3.4.3 is considered for the setup given in Figure 3.15 with the parameters settings as in Table 3.4. The positions B, R_1, R_2 are drawn independently and uniformly on the area $\mathcal{S}$. The positions $\{H_k\}$ of the helping nodes are independently drawn according to an uniform distribution on the larger area $\mathcal{L}$. The

range errors δ_1 and δ_2 assumed to be independent zero mean Gaussian random variables with variance $\sigma^2_{\delta_i} = \sigma^2_\delta$. The mean of the received log power is modeled according to the standard path loss model $\mu(d_k)$:

$$\mu(d_k) = P_0 - 10n_p \log_{10}(d_k), \tag{3.44}$$

where P_0 is the power received at 1 meter and n_p is the path loss exponent. The variance σ^2_k is chosen equal to σ^2_X for all k. Values for P_0, n_p, σ^2_δ and σ^2_X are chosen according to the measurements reported in [97].

3.4.4.2 Maximum Likelihood Estimation

The ML estimator for the hybrid positioning problem reads $B \in \arg\max_z \Lambda_{\text{Hybrid}}(z)$, where $\Lambda_{\text{Hybrid}}(z)$ denotes the log likelihood function for B based on $\{r_i\}$ and $\mathbf{P}$. One approach is to find the maxima of the local extrema of the log likelihood function, obtained by equating the gradient to zero. For independent range estimates and power measurements, the gradient of the log likelihood function reads:

$$\nabla\Lambda_{\text{Hybrid}}(z) = \nabla\Lambda_{\text{Power}}(z) + \nabla\Lambda_{\text{Range}}(z), \tag{3.45}$$

where Λ_{Power} and Λ_{Range} are the log likelihood functions of the power measurements and of the range estimates, respectively. The two gradients read [96], [100],

$$\begin{aligned}
\nabla\Lambda_{\text{Power}}(z) &= \sum_{k=1}^{K} \frac{1}{s^2} \frac{M_k - s^2 - \ln\|z - H_k\|}{{d_k}^2} (z - H_k), \\
\nabla\Lambda_{\text{Range}}(z) &= \sum_{i=1}^{2} \frac{1}{\sigma^2_\tau} \frac{r_i - \|z - R_i\|}{r_i} (z - R_i),
\end{aligned} \tag{3.46}$$

with the definitions

$$s = -\frac{\sigma_X \ln 10}{10n_p}, \quad M_k = \frac{(P_0 - P_k)\ln 10}{10n_p} + \ln d_0. \tag{3.47}$$

Due to the non-linear relation (3.46), finding the roots of (3.45) requires global numerical optimization, which is not feasible for most applications. However, an approximate solution can be obtained by initializing a numerical local optimizer with an initial guess, e.g. a weighted least squares (ML-WLS) approach [96].

3.4.4.3 Comparison of Performance

The performances of the three algorithms are compared in term of cumulative density functions (CDF), outlier rates and root mean square errors (RMSE). From the empirical CDFs shown in Figure 3.16 it appears that for a low number of helping nodes, the performance of the proposed method outperforms ML-WLS and is close to that of ML. For high number of helping nodes, the proposed method and ML-WLS has similar performances, except in a large errors regime, where the proposed method prevails.

These large errors are observed to be less frequent when the number of helping nodes is high. To inspect this difference, the occurrence of outliers is considered. An outlier is defined as follows: if $B \in \mathscr{C}_i$, the estimate of B is called an outlier if it lies in the complement of $\mathscr{C}_i$. Note that for the proposed method, an outlier is equivalent to a decision error in (3.43). On Figure 3.17a it can be observed that the outlier rate decreases with the number of helping nodes increases. Not surprisingly, the ML estimator yields the lowest outlier rate of the three methods. It also appears that the proposed method consistently outperforms the ML-WLS in terms of outlier rate. This is most significant when the number of helping nodes is less than four. These differences of performance are also reflected in the RMSEs reported in Figure 3.17b. In particular, for four or less helping nodes it can be observed that proposed method is close to the ML curve, compared to ML-WLS curve.

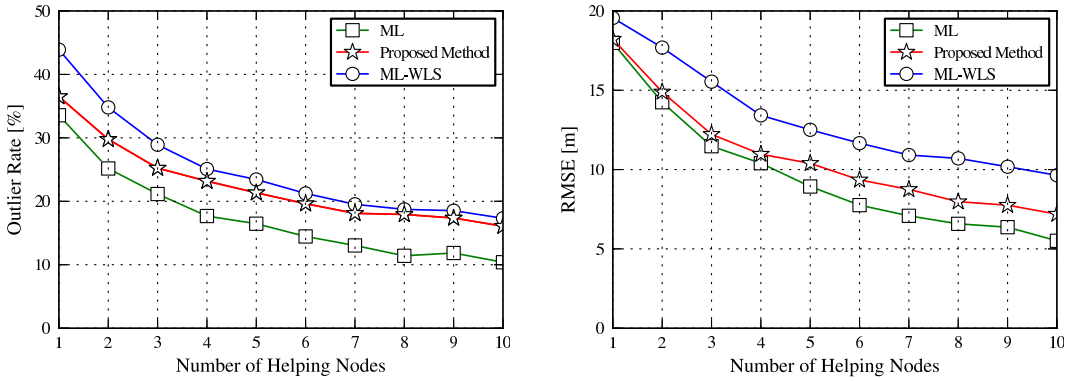

(a) Outlier rate vs. number of helping nodes

(b) RMSE vs. number of helping nodes

Fig. 3.17: Evaluation of the influence of the number of helping node on the (a) Outlier rate and (b) RMSE.

The above observations suggest that the RMSE for the proposed method approach can be attributed to two types of errors: large errors outliers due to decision error in (3.43), and small errors resulting from the approximation in (3.39). The small errors occur since the centroids C_1 or C_2 are used to estimate the position of the blind node. Thus, it is conjectured that the effect of these small errors can be reduced by improving this approximation, considering additional knowledge of the probability model for the range error δ_i. This information could be included directly as a weighting function in the computation of centroids. Alternatively, the proposed method could be used to provide an initial guess for a numerical optimization of the likelihood function. It is further conjectured that the outlier rate, which is equivalent to the rate of false decision in (3.43), could be also reduced by improving the approximation (3.39).

3.4.5 Hypothesis Testing Method vs Existing Methods

This section proposes an evaluation of the hypothesis testing method on a canonical problem of message passing (described in[101]). For that purpose, the scenario illus-

trated in Figure 3.18 is considered. In that given scenario, 4 anchors are available and 2 blind nodes try to estimate their positions. Each blind node is in visibility with only 2 anchors nodes, different for each blind node.

In that situation, the position estimation of each blind node leads to an ambiguity. Indeed, processing two radio observables are not sufficient to obtain a unique solution. However, by considering that a communication channel exists between the two blind nodes, an extra observable could be obtain by both nodes, resolving this ambiguity.

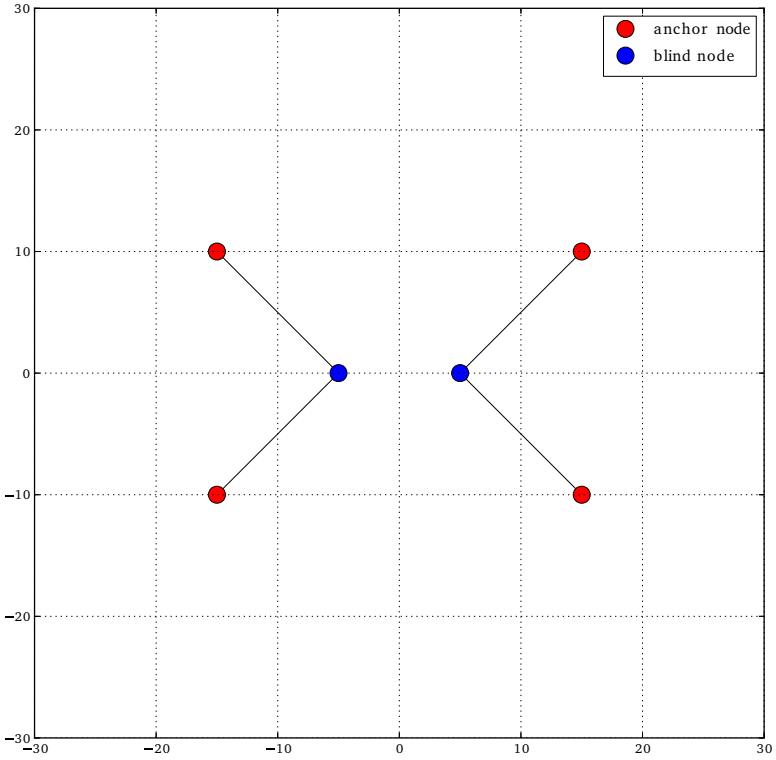

Fig. 3.18: The two blue dots represent the blind nodes. The red dots represent the anchors. The lines determine the anchors and blind nodes connection.

Using a maximum likelihood estimator to solve that under defined problem would lead either to an error in the worst case, or to a position estimated between the both range anchors in the best case. Using the RGPA method proposed in section 3.3, the two possible solutions are proposed. Figure 3.19 shows that situation.

Without extra communication the ambiguity remains for both blind nodes. A solution would be to use a to method proposed in 3.4, where the RSS information is used to decide between in its 2 concurrent estimated positions of each blind nodes.

3.4.5.1 Using Communication to Resolve the Ambiguity

The radio observables are created using a path loss shadowing model (as described in (3.21)) with the following parameters:

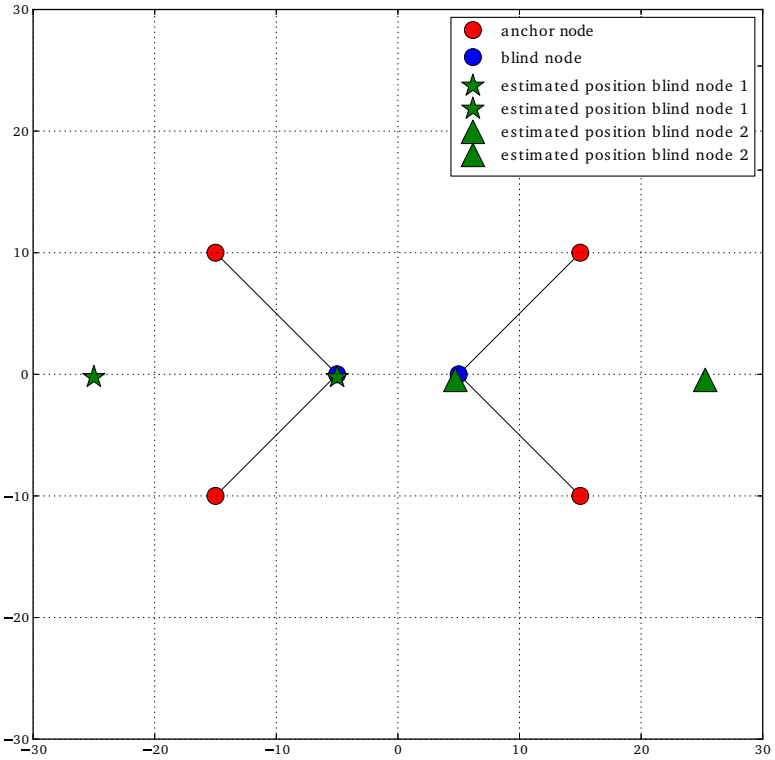

Fig. 3.19: results of RGPA processing on the scenario. The RGPA processing leads to the estimation of 2 possible positions for each blind node.

- Variance of the additive noise $\sigma_X = 4dB$
- Pathloss exponent $n_p = 3$
- $P_0 = -40dB$

First, the distance between the 2 blind nodes is computed, and the received power is deduced from the model with the given parameters.

Assuming that during the communication, each blind node share both a power information and one of their estimated positions, Figure 3.20 shows the resulting localization estimation. The ML estimated position is obtained by using an heterogeneous localization algorithm, based on a maximization of the likelihood function using a numerical local optimizer [64].

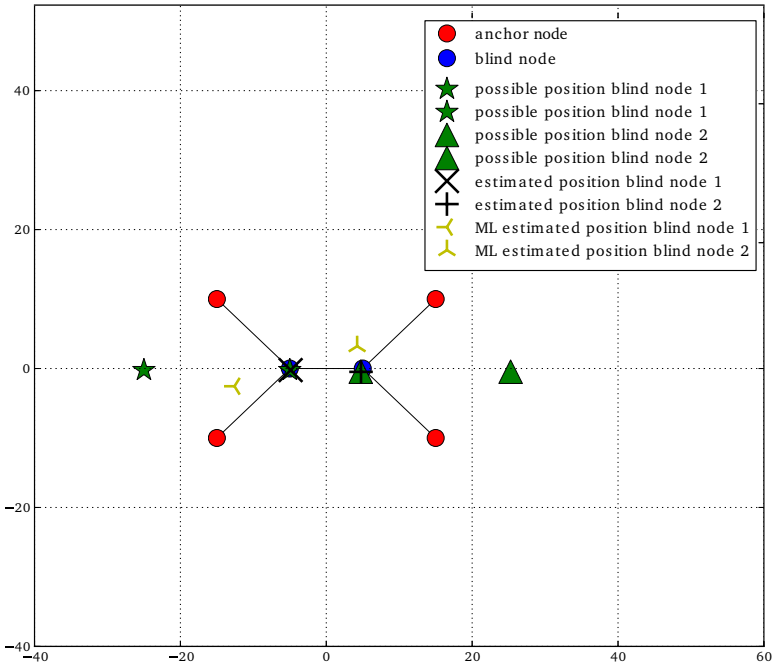

Fig. 3.20: Comparison of the position estimated with the RGPA and the hypothesis testing method to a ML. In this situation, the proposed method reduce the error.

3.4.5.2 Comparison of Performances

The comparison of performances of the proposed approach and ML is performed through a Monte Calro simulation with 500 noise realizations using the communication scenario with the parameters described in table 3.5.

Figure 3.21 compares the error between the estimated position and the ground truth position for the proposed method based on hypothesis testing and ML using either the mean position obtained from the 2 ToAs, or one of the both.

For the proposed method, it can be observed that 95% of the blind node positions are estimated with an error lower than 2 meters, whereas 5% of the estimated position

Table 3.5: Parameters settings

Parameter	Value
range variance σ_r	0.5m
power variance σ_X	4dB
path loss exponent n_p	3,
path loss at 1 meter PL_0	4dB

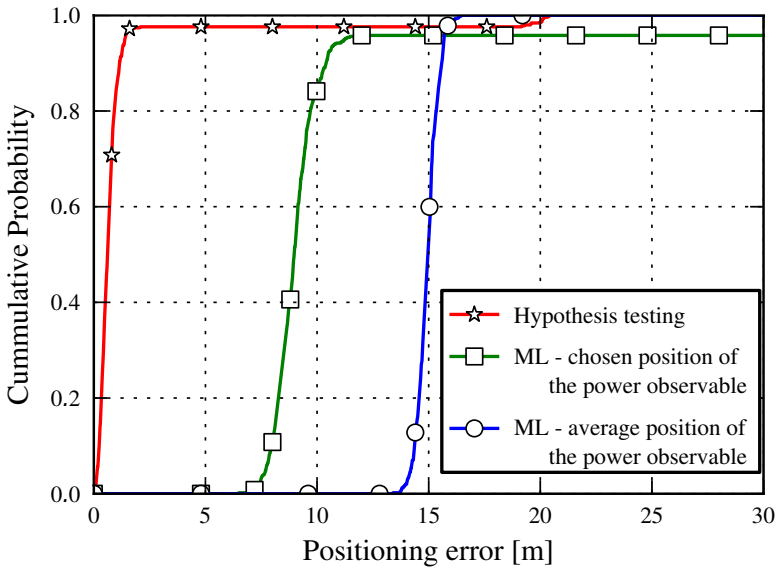

Fig. 3.21: CDF of positioning error using the proposed hypothesis testing approach, a ML using either the mean position obtained from the 2 ToAs an a ML using one of the both position obtained from the 2 ToAs.

are over 20 meters. By construction the hypothesis testing method chose between 2 concurrents estimated positions: one close to the ground truth position, and an image far from the ground truth. As long as the decision is correct, the error on the position estimation is only due to the error on the range observables. When the decision test fails, the wrong position estimation is chosen, and the error is in the order of magnitude of the range observable.

In case of the maximum likelihood estimator, the position estimation is perturbed by 2 factors:

- First, the position of the node which gives the power observation is not exactly known.
- The accuracy of the range observables is degraded by the poor accuracy of the power observable.

For that purpose, 2 strategies have been envisaged. First, one of the two possible solutions given by the range observables is used as the center position of the second blind node (this strategy is equivalent to those adopted for the hypothesis testing method). Second, the mean position of the two possible solutions given by the range observables is used as the center position of the second blind node. The two strategies have inverted advantages and drawbacks. The first strategy reduces the low regime error but also add very large errors. Contrarily, the second strategy limits those large errors but do not achieve to position with an error less than 15m.

Whatever the strategy, the proposed hypothesis testing method prevails on the ML method. A possible explanation of the superiority of the hypothesis testing approach is based on the difference of accuracy between ranges and power observables. It is stated that the possible achievable position estimation accuracy from range observables is generally higher than the one from a power observables. From that statement, it can be envisaged to use both information differently.

That precise problem can also be solved using message passing techniques, as proposed in [101]. Then, each blind node exchanges its belief function with the other one (where the belief function can be assimilated to a power density function). Practically, the exchange of a belief function requires to send a large vector which potentially generate an overhead in the communication channel. By using the hypothesis testing method, the exchange information is limited to an estimated position. Indeed the power received value is not taken into account in the communication because it is measured by the blind node and do not require any communication.

3.5 Conclusion

This chapter has begun with an overview of localization techniques and their associated algorithms. In a second part, a novel heterogeneous localization algorithm based on geometric approach RGPA has been presented. Then simulations have shown that the method outperformed ML approaches in different hybrid scenarios. One of the advantage of the algorithm is its ability to return multiple estimated positions in case of lack of observables. That advantage has been used in a third part to build a location

method on a hypothesis testing. In case of under determined problems where 2 ToAs can lead to multi modal solutions, the method proposes to use the RSS observables to decide between those different solutions. The method has been evaluated with Monte Carlo simulations and tested on a canonical message passing scenario.

Chapter 4

A Dynamic Platform: Handling Propagation, Communication and Agent Mobility in the Network

4.1 Introduction

In order to provide a simulator able to address the indoor dynamic localization problems, building an accurate electromagnetic wave propagation and dedicated localization algorithms is mandatory, but not completely sufficient. First assuming a dynamic simulation, a realistic description of the agent mobility has to be taken into account to ensure producing the radio traces comparable to a realistic situations. Second, with the increasing number of radio standards available on single mobile devices, it would be an asset to simulate a global vision of all the available RATs, to elaborate high level strategies (distributed computation or vertical handover [102]) and ensure a better use of the information available in those networks. Third, supposing that the post 4G networks would increase quality of the network by promoting the synergy of the communication and the localization, the simulation of a communication channel would ensure to be compliant with all the upcoming evolutions. This chapter aims to build a complete framework allowing the simulation of the indoor dynamic localization problems. For that purpose, in addition to the methods presented in the previous chapters, 3 important aspects of the dynamic platform are developed:

- the dynamic mobility of the agent,
- the radio network low level monitoring,
- the inter agents communication.

The first section 4.2 provides a state of the art of both most used mobility modeling, and how this mobility is taken into account in simulators is provided. The second section 4.3 presents the chosen actual implementation of the mobility of the agents into the dynamic platform. The agent mobility is based on a Discrete Event Simulator (DES) allowing each agent to move independently from each other. The mobility is described both at a large scale using a graph description, and at a small scale using

the steering behavior method. The third section 4.4 describes how the electromagnetic simulation and the LDPs are monitored into the dynamic platform. In particular, the representation of the radio network using graphs is detailed. Finally, taking advantage of the graph organization of both the network description and the DES simulation, the last section 4.5 describes the inter agents communication capabilities of the dynamic platform. The last section 4.6 presents different simulation scenarios to illustrate the dynamic platform potential. A first dynamic simulation involving a single agent is run, where LDPs and CIR are obtained for different positions using both the multi-wall model and the RT tool. A dedicated simulation involving two nodes is presented to demonstrate the inter agents communication feature.

4.2 State of the Art on Mobility and Network Simulators

The question of the realistic simulation of the mobility is a problem which has been explored in many different fields using many different approaches. For the problem at hand, it appears that building a wireless propagation simulator able to take into account the mobility should be focused on the choice of the correct mobility model [103]. For that purpose, this section starts with an overview of the existing solutions for modeling the mobility in 4.2.1. Then, the advantages of Discrete Event Simulator (DES) in the considered context are detailed in 4.2.2. Finally, some pre-existing solutions combining mobility and network simulation are exposed in 4.2.3.

4.2.1 Types of Mobility models

According to [104], mobility models can be categorized in three types:
- Random models
- Models with geographic restriction
- Models with spatio-temporal dependency

Random models are widely used in Monte-Carlo simulations where the purpose is to introduce a realistic fluctuation of the channel allowing the design and test of communications algorithms or PHY/MAC design. If those solutions are very easy to implement, the resulting motion is generally not very realistic with respect to a given spatial ground truth. Among those random models, one find those based on Brownian motion [105] or random way point [106]. Some of those models also add a temporal dependency and make depend the actual velocity on the previous computed velocities. One of the most used model, due to its relative statistical coherence with a real human mobility is the Levy Flight random walk model [107]. In the Lévy flight model, the steps are defined in terms of the step-lengths, which have a certain probability distribution (the directions of the steps being isotropic and random). Typically, the steps assume a specific Pareto distribution [108]. Those random models are very convenient to take into consideration the global behavior of an agent movement, but by nature, they are not suited for addressing site-specific situations (even if some works have tried to introduce the environment [109]). New approaches have to be considered to fit with deterministic simulation of the channel propagation.

For such simulations, it is mandatory that the simulated agent positions be bounded in space. That is the aim of models with geographic restriction which limits the movement of the agents into a restricted simulation field. In indoor situation, it meant that a building floor plan would bound the position of the agents and limit their movement to possible way paths (crossing the doors). Graph based models belong to this category, by constraining the movement of an agent on the graph nodes [110]. As well, the Manhattan Mobility model [111] which limits the movement of the nodes to roads between buildings. Those geographically restricted models are very convenient to describe the movement of a agents, but they fail to take into account inter-agent interactions which require a synchronization-like behavior mechanism.

For that purpose, spatio-temporal dependent models are introduced. Those models take care of the *material* environment and the *human* environment. Thus behaviors like, inter-agent avoidance or group mobility to a common target can be envisaged, drastically increasing the realism of the simulation [112]. That level of realism is actually the lowest level required to build a satisfying simulation of the mobility in radio context. Indeed, considering simulation in cases of cooperative networks, the number of cooperative agents in a given area is directly a parameter on the achievable position accuracy of a given algorithm [113].

Another important aspect for producing a correct simulation is the habits of the agents. Indeed, Human motion are led by habits [114], which can be directly translated into the mobility model of the agents. Habits can be modeled e.g. from the propensity of an agent to be in a specific room of a building or to be under the influence of another agent.

Finally, a satisfying agent mobility description would be site-specific and include smart interactions of the agents with both with their environment and with the other agents. A convenient solution to achieve a such deterministic mobility description is to use a Discrete Event Simulator (DES).

4.2.2 Discrete Event Simulator (DES)

From the previous section, it has been seen that the mobility is intrinsically a space-time process in interaction with the environment. Practically, the simulation of such a phenomena can be quite complicated to address because it involves random variables (possible positions into the layout, transitions probabilities,...), which have to be dynamically modified by external events (other agents arrival,...). Those particular kind of problems can be advantageously managed by DESs which are designed for both stochastic and dynamic problems, allowing the discrete evolution of variables [115]. The choice of DES has already been made by other mobility simulators oriented on Urban mobility [116, 117, 118]. For the problem at hand, assuming a full Python implementation in this manuscript, the SimPy framework has been used [119]. SimPy is a DES allowing the simulation of active components.

Another interesting aspect of using DES is the possibility to define autonomous entities. Practically it means that all the decisions of an agent is based only on its own observation of the environment. That autonomy can be limited by rules defined by an

user e.g. avoiding certain rooms of the environment. That precise implementation has been originally created for video games and the simulation of artificial intelligence. One implementation of those type of solution is based on the *steering behaviors* principles [120]. Steering behaviors allowing the computer description of human behavior e.g. "follow a leader", "detect and avoid" or "path following". Based on these principles, a library called Personal Rapid Transit Simulation [121] has been enhanced to fit with the indoor localization problematics. A more precise description will be provided in section 4.3.2.

4.2.3 The Network Simulation in Mobility

Although it exists commercial tools specialized in the pedestrian mobility to improve passenger flow efficiency in existing buildings or evacuation and traffic management [122, 123, 124], there is no such dedicated tools in the wireless communication field. Moreover, in commercial propagation tools mentioned in section 2.2.1.1, the mobility is generally not taken into account. That lack could also be mentioned considering upper layers of the OSI standards (MAC,IP,..), where the mobility parameters is rarely part of simulators [125, 126, 127]. Although most of commercial tools taken into account the mobility, it exists some research tools which integrate it into the network performances evaluation. For that purpose, and considering indoor situation, two models are generally used:

- cellular automata models, which are based on model with geographic constraints
- agent based models, which are either spatio-temporal dependency models or DES based model.

A large number of those studies about the influence of the mobility on the network use cellular automata models [128, 129]. This method consists in the discretization the agent position on a grid. At each time step, each agent can move to a finite number of possible positions on that grid. Due to the ease of the method, the use of a grid for modeling the movement of the agent is often considered as a mobility model [130]. In order to be more site-specific, some positions on the grid can be forbidden, preventing agents to stand behind an open door for instance [131].

A more sophisticated approach is the agent based model, which intends to reproduce a real pedestrian activity constraint by the environment. In that case, the use of DES based mobility model allows to retrieve in simulation phenomena which cannot be detected with a simple random walk or cellular automata model [132]. Despite of their potentialities, only few simulators use that method in the considered context of radio simulations [118]. Moreover, the question of the communication for distributed computation including the mobility seems to be lacking.

4.3 Simulation of the Agents Mobility

The proposed simulation of the agent mobility is based on DES. The movement of the agents description is divided into two modes. First the large scale mobility, which represents the *motivation* of the agent (choosing a destination room) is described

in 4.3.1. Second, the small scale mobility, which constraints the agent to move and interact with the environment and the other agents is described in 4.3.2.

4.3.1 Large Scale Mobility : A Graph Aided Description

At large scale, the agents mobility can be seen as a stochastic succession of two different states :

- a state (SS) where the agent is static
- a state (MS) where the agent is mobile

Most of the time, in indoor environment, mobile agents are static, thus the static state can be fully considered as part of the overall mobility description. The large scale mobility consists in both defining a target for the agent and determining a path to reach that target.

4.3.1.1 The Graph of Room $\mathcal{G}_r$ and the Graph of Way Path $\mathcal{G}_w$

In order to determine the different targets of the agents, the graph of room $\mathcal{G}_r$ is introduced.

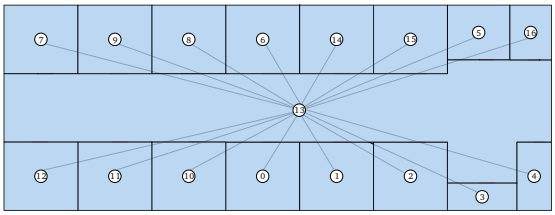

Fig. 4.1: An example of Graph of rooms $\mathcal{G}_r$

The graph of rooms $\mathcal{G}_r$, represented in Figure 4.1, is a simplified version topological graph $\mathcal{G}_t$ described in 2.3.2.2, especially design for the mobility purpose. The nodes of the $\mathcal{G}_r$ represent rooms. For this purpose, the nodes of $\mathcal{G}_r$ are the nodes of $\mathcal{G}_t$ limited to cycles ($\mathcal{G}_t$'s nodes) with a door. In addition, each edge of $\mathcal{G}_r$ interconnects rooms sharing a door. With such a description, each node can determine a target by choosing a room in the nodes of $\mathcal{G}_r$. Both the target and the path are determined with the help of graphs. For a more realistic movement, the graph of way path $\mathcal{G}_w$ representing all the possible transitions between rooms is introduced.

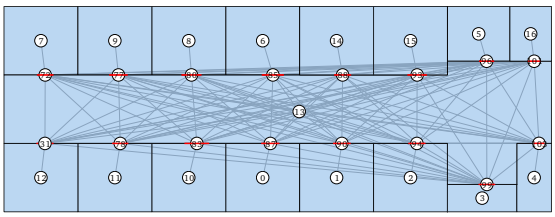

Fig. 4.2: An example of Graph of way path $\mathcal{G}_w$, associated to the graph of room.

The graph $\mathcal{G}_w$, represented in Figure 4.2, has the same "room" nodes than $\mathcal{G}_r$, plus extra nodes associated to each doors. Those nodes are added to encourage the agent both to cross the doors and to avoid unreal trajectory e.g. going to the center of a corridor instead of directly reaching the opposite room. Nodes are connected using two rules :

- All room nodes are connected to a door node
- The doors of two rooms are connected together if the 2 rooms are connected in $\mathcal{G}_r$.

4.3.1.2 Determination of a Target Using the Graphs.

Practically, the graph $\mathcal{G}_r$ allows the agent to randomly choose a target (a.k.a a destination room), and the graph $\mathcal{G}_w$ allows to find a path to this target. That path is a succession of $\mathcal{G}_w$ nodes.

Lets suppose a situation where an agent in room i chooses a *targeted* room t with the help of graph $\mathcal{G}_r$. Rooms i and t correspond respectively to nodes v_r^i and v_r^t of $\mathcal{G}_r$. Then, the path from the room i to the room t is obtained by processing a Djikstra [133] shortest path algorithm $\mathcal{D}$ on nodes $v_w^i$and v_w^t of the graph $\mathcal{G}_w$:

$$\mathcal{V}_p = \mathcal{D}(v_w^i, v_w^t). \tag{4.1}$$

The obtained ordered set of nodes $\mathcal{V}_p$ describes the shortest path between v_w^i and v_w^t. To achieve the whole trajectory from i to t, the agent has to successively go through all the rooms and/or doors corresponding to the nodes of $\mathcal{V}_p$. Each time a node of $\mathcal{V}_p$ is reached, the next one becomes an intermediate target *it*, until the node v_r^t is reached.

In Figure 4.2, an agent in room $i = 12$ with a target in room $t = 15$, corresponds to returned path $\mathcal{V}_p = \{12, 31, 93, 15\}$. Thus, the agent first moves from room 12 to its intermediate target 31 and so on until it moves to its final target in room 7.

4.3.2 Small Scale Mobility : Steering Forces

Once their targets are known and their paths have been determined, agents can start moving in the environment, avoiding walls and going through doors. This particular ability is defined as the small scale description of the mobility and is described with the help of steering behaviors.

Steering behaviors have been introduced in [120] to describe interactions of agents with their environment. Agents are simply described by their mass m and two limiting parameters: their maximum acceleration a_{max} and their maximum velocity v_{max}. This description allow the agents to be driven by several steering forces applied on their center of mass. The different steering forces are described in sections 4.3.2.1 to 4.3.2.3.

The computation of acceleration, velocity and position of agents is ensured by Euler integration [134]. At each time step the agent's acceleration $\mathbf{a}$ is re-evaluated in regards with the resulting steering force applied on it. The true steering forces value is truncated in regard of the maximum acceleration parameter of the agent a_{max}. The steering force $\mathbf{F}$ actually applied on the agent is defined by:

$$\mathbf{F} := \max\left(||\mathbf{F}||, ma_{max}\right)\hat{\mathbf{F}} \tag{4.2}$$

where $\hat{\mathbf{F}}$ is the unitary vector obtained from normalization of $\mathbf{F}$, and m is the mass of the agent. Then, the applied acceleration vector a_n at time step n is given by :

$$\mathbf{a}_n = \frac{\mathbf{F}}{m} \tag{4.3}$$

As well, the true velocity $\mathbf{v}_n$ at time step n is approximated by the Euler integration as the sum of the old velocity and the product of the current acceleration vector with $\delta\tau$, the time between $n-1$ and n:

$$\mathbf{v}_n = \mathbf{v}_{n-1} + \mathbf{a}_n\delta\tau \tag{4.4}$$

Then, the applied velocity $\mathbf{v}_n$ is truncated by the maximum velocity parameter of the agent v_{max}:

$$\mathbf{v}_n := \max\left(||\mathbf{v}_n||, v_{max}\right)\hat{\mathbf{v}}_n \tag{4.5}$$

where $\hat{\mathbf{v}}_n$ is the normalization of $\mathbf{v}_n$.

The position $\mathbf{p}_n$ at time step n is obtained by the Euler integration as the sum of the previous position $\mathbf{p}_{n-1}$ and the current applied velocity :

$$\mathbf{p}_n = \mathbf{p}_{n-1} + \mathbf{v}_n\delta\tau \tag{4.6}$$

The steering forces applied on the agent correspond to human like behaviors. In the following, only three types of steering forces are considered : the seek behavior, the obstacle avoidance behavior and the agent avoidance behavior.

4.3.2.1 Seek Behavior

The seek behavior aims to produce a steering force which attract the agent to a target. In the considered scenario, those targets are succession of intermediate targets as defined in section 4.3.1. The steering force direction depends on the distance vector $\mathbf{d}_n$ between the target $\mathbf{t}_n$ and the actual position of the agent $\mathbf{p}_n$. Then, it is possible to determine a velocity vector $\mathbf{v}_n^d$ defined with :

$$\mathbf{d}_n = \mathbf{t}_n - \mathbf{p}_n \tag{4.7}$$

$$\mathbf{v}_n^d = \max\left(\frac{||\mathbf{d}_n||}{\delta\tau}, v_{max}\right)\hat{\mathbf{d}}_\mathbf{n} \tag{4.8}$$

$$\tag{4.9}$$

where $\mathbf{v}_n$ and $\mathbf{v}_n^d$ are the current velocity vector and the desired velocity vector directed respectively; and $\hat{\mathbf{d}}_n$ is the normalization of $\mathbf{d}_n$

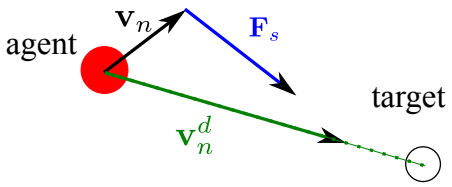

Fig. 4.3: Seek behavior: The steering $\mathbf{F}_s$ vector results from the current velocity vector of the agent $\mathbf{v}_n$ and the desired velocity vector $\mathbf{v}_n^d$ directed to the target.

Thus, the velocity difference $\mathbf{w}_n$ between the actual velocity $\mathbf{v}_n$ and the desire velocity $\mathbf{v}_n^d$, allows to compute the seeking force $\mathbf{F}_s$ to be applied on the agent.

$$\mathbf{w}_n = \mathbf{v}_n^d - \mathbf{v}_n \tag{4.10}$$

$$\mathbf{F}_s = m\frac{\mathbf{w}_n}{\delta\tau}\hat{\mathbf{w}}_n \tag{4.11}$$

where $\hat{\mathbf{w}}_n$ is the normalization of $\mathbf{w}_n$, and m the mass of the agent. This situation is represented in Figure 4.3.

4.3.2.2 Obstacle Avoidance Behavior

The obstacle avoidance behavior aims to produce a steering force avoiding the agent penetrating a wall or any part of the layout. The associated steering force $\mathbf{F}_o$ is given by:

$$\mathbf{F}_o(\mathbf{d}_{k,w}) = \frac{m}{\delta\tau}\left((\mathbf{v}_{n-1} - \mathbf{v}_n)\frac{\alpha}{|\mathbf{d}_{k,w}|}\hat{\mathbf{n}}\right), \tag{4.12}$$

with $\mathbf{d}_{k,w}$ the distance vector from the agent k to a wall w, α a parameter properly chosen for avoiding the agent from grazing the wall and $\hat{\mathbf{n}}$ a normalized vector orthogonal to the obstacle .

4.3.2.3 Agent avoidance

In [135], it is stated that it exists an inter-persons distance boundary. This boundary can be modeled with a circle of a radius r around the agent k [136][22]. While another agent l penetrates inside that circle, an avoidance force F_a proportional to the distance vector between the agents $\mathbf{d}_{k,l}$ is applied. That force can be modeled using the previously defined obstacle avoidance force, regarding the 2 modifications:

1. The distance between the agent and the obstacle is replaced by the distances between the two agents,
2. A rotation matrix has to be introduced in order that the force be applied orthogonally to the velocity vector, and thus creating an avoidance of both agents.

Thus, the agent avoidance force F_a can be written:

$$\mathbf{F}_a(\mathbf{d}_{k,l}) = \begin{cases} \mathbf{H}\mathbf{F}_o(\mathbf{d}_{k,l}) & ,||\mathbf{d}_{k,l}|| \leq \mathrm{r} \\ \vec{0} & ,||\mathbf{d}_{k,l}|| > \mathrm{r} \end{cases} \tag{4.13}$$

with $\mathbf{H}$ a rotation matrix:

$$\mathbf{H} = \begin{pmatrix} 0 & -1 \\ 1 & 0 \end{pmatrix} \tag{4.14}$$

4.3.2.4 Resulting Force

An agent k is under the influence of different steering forces : a seek force which pull the agent to its intermediate target node v_{it} as seen in 4.3.1 and several repulsive forces to avoid obstacles or other agents. The resulting steering force $\mathbf{F}$ is written as the sum of all the steering forces applied on agent k:

$$\mathbf{F} = \mathbf{F}_s + \sum_{w}^{W} \mathbf{F}_o(\mathbf{d}_{k,w}) + \sum_{l \neq k}^{K} \mathbf{F}_a(\mathbf{d}_{k,l}), \tag{4.15}$$

where W and K are respectively the number of walls and agents in the vicinity of the agent k, which is determined with a simple distance threshold. The use of that threshold avoids the useless computation of forces from all the walls of the entire layout.

4.4 Simulation of the Radio Network Organization

Another requirement for building an efficient dynamic platform for localization is to simulate the network organization of radio devices. Among other, it requires to be able:

- to determine the radio observables values with respect to the agent position,
- to assign the correct observables values to the corresponding radio links,
- to simulate the refresh time of those observables.

Similarly to the mobility, the choice of a DES has been made to be able to update all the parameter values of any agent either independently or with a specified refresh time. Once again, an obvious choice to describe this network organization is to take advantage of graphs. For that purpose, the network graph $\mathcal{G}_n$ is introduced. The graph notation used in that part is compliant with the notation introduced in subsection 2.3.1. An example of network graph is given in Figure 4.4.

4.4.1 Network Graph Organization

The network graph $\mathcal{G}_n$ is a Multi-Directed-Graph. Multi-graph means that two nodes can be connected together with more than a single edge. The use of multiple edges allows to represent the possible multiple RATs linking the radio devices. The available RATs of the simulation are $R = \{\rho_1, \ldots, \rho_{N_r-1}\}$, where ρ_r is a given RAT. As well, the graph is built as an oriented graph, which means that the information on the edge linking two nodes A and B is not necessarily the same as that on the edge linking B to A. Indeed, if the transmission channel is reciprocal, it is required to take into consideration the different emission power and sensitivity of each nodes.

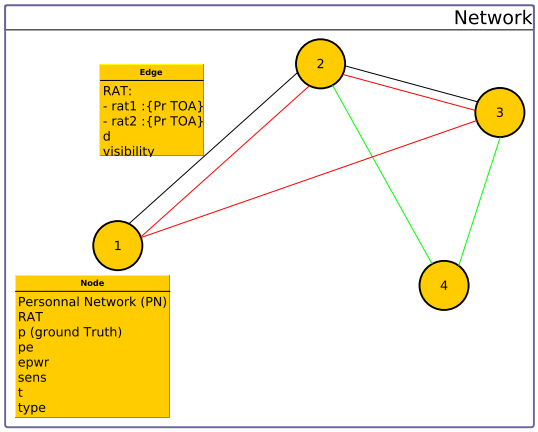

Fig. 4.4: Example of network graph $\mathcal{G}_n$ with 4 nodes on 3 different RATs. The 2 yellow title blocks display extra information associated to the graph edges and nodes.

4.4.1.1 Nodes of $\mathcal{G}_n$

The nodes of $\mathcal{G}_n$, written $\mathcal{V}_n$, are designated by the *id* of their referring agent. They contain information about their radio capabilities. Assuming the high level graph data structure described in 2.3.1, each node has eight attributes:

- Type
  The type attribute indicates if the node is an agent or a base station. By convention, a base station is a radio access point which is static, whereas an agent is a radio access point which can move.
- RATs
  The RATs attribute R^k is a subset of R which gather all the available RAT of the device k: $R^k \subset R$
- Emitted power
  This attribute describes the emitted power and can be eventually be different for each RAT. For this purpose, the emitted power attribute is a dictionary where the keys are RATs selected among one of those available on the device, and the value the emitted power of the associated RAT in dBm.
- Sensitivity
  Similarly to emitted power, sensitivity can be different for each agent. Then, the sensitivity attribute is also described with a dictionary where the keys are RATs selected from those available on the device, and the value the sensitivity of the associated RAT in dBm.
- Ground truth position
  The ground truth position is obtained from the mobility part described in 4.3.
- Estimated position
  The estimated position is obtained using localization algorithms described in section 3.3.
- Personnal network

The personal network is a graph built from the agent vision of the network. More details are given in section 4.4.3.
- Time stamp
  The time stamp indicates when all the parameter values have been refreshed relatively to the beginning of the simulation.

4.4.1.2 Edges of $\mathcal{G}_n$

On the edges $\mathcal{E}_n$ of $\mathcal{G}_n$, are stored information about nodes connectivity. On each edges three attributes are available:
- LDP dictionary
- Ground truth distance
- Visibility

As mentioned before, $\mathcal{G}_n$ is a multiple graph, where each parallel edge represents a single RAT. The keys of the LDP dictionary are the LDPs available by the agent. The values of those LDPs are computed with the help of the multi-wall model described in 2.7. In the future, that evaluation would advantageously be performed by the RT tool. The visibility parameter is a boolean value determined by comparing the sensitivity value to the computed LDP.

4.4.2 Sub-Networks

For computational efficiency, it is convenient to gather nodes sharing the same RAT into a specific network so called sub-network. The sub-networks are then built from the global $\mathcal{G}_n$ multi-graph, by creating as many graphs as $\mathcal{G}_n$ has RAT. Practically, a sub-network is defined as a dictionary with ρ as a key and the subgraph of $\mathcal{G}_n(\rho)$ as a value. A subgraph $\mathcal{G}_n(\rho)$ is $\mathcal{G}_n$ restricted to its nodes $v_n^k(R^k)$ when the RAT ρ is in R^k and can be written :

$$\mathcal{G}_n(\rho) = \mathcal{G}_n - \bigcup_{\substack{k \\ \rho \notin R^k}}^{K} v_n^k(R^k) \tag{4.16}$$

4.4.3 Personal Network $\mathcal{G}_p$

In order to be able to address distributed or cooperative localization schemes, nodes of a network should have their own vision of the network. For that reason, the concept of personal networks is introduced. A personal network is the representation of $\mathcal{G}_n$ from a node point view. Contrary to the network graph, which own an idealistic and complete access to all the position and LDPs of all the nodes of the network, a personal network gives a realistic idea of the actual available information possessed by each node. Based on those information, each node can e.g. perform its position estimation uniquely with its own available information. The personal network of a node k is designated by $\mathcal{G}_p^k$. Practically, the personal networks $\mathcal{G}_p^k$ are built as multi-directed-graph. There is

as much personal network than $\mathcal{G}_n$ has nodes. An example of the personal networks associated to a graph $\mathcal{G}_n$, is presented in Figure 4.5.

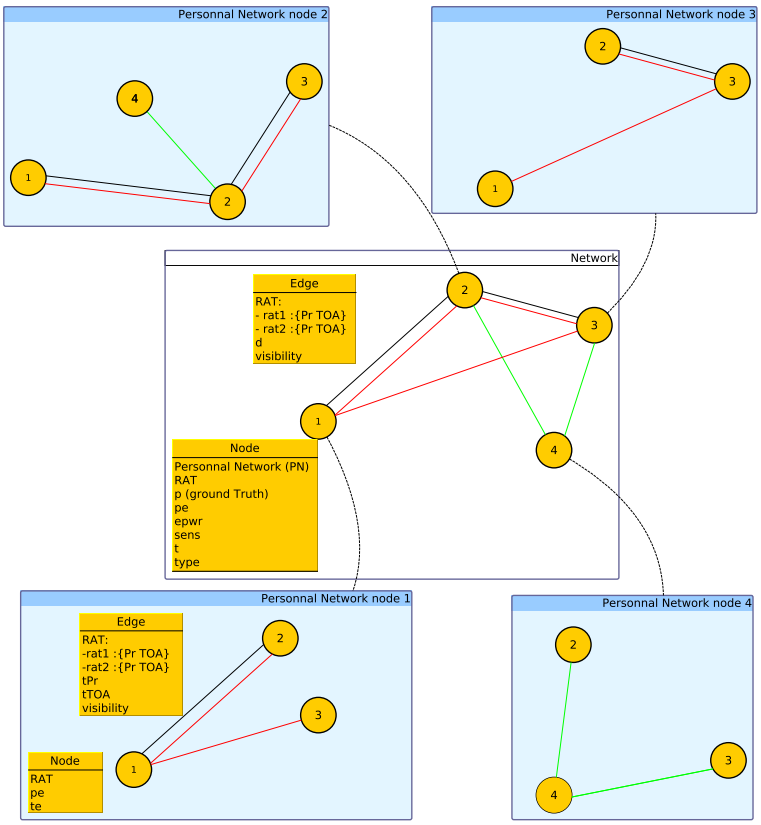

Fig. 4.5: The Network graph $\mathcal{G}_n$ is displayed in the central frame. The associated personal network associated to each node is displayed in frame with a blue background.

4.4.3.1 Building Personal Networks

Always assuming the same notation convention, the set of nodes and the set of edges of $\mathcal{G}_p^k$ are designated by $\mathcal{V}_p^k$ and $\mathcal{E}_p^k$ respectively. By denoting $\mathcal{V}_n(R^k)$ all the nodes of $\mathcal{G}_n$ sharing the same set of RAT R^k, the nodes $\mathcal{V}_n^k$ of a personal network $\mathcal{G}_n^k$ can be written:

$$\mathcal{V}_p^k = \mathcal{V}_n(R^k) \tag{4.17}$$

By construction, a node k of the personal network $\mathcal{G}_p^k$ is linked to all the nodes of its personal network. Similarly to $\mathcal{G}_n$, this link is only a potential connection and do not inform on the actual connectivity of the node with its neighbors (that information is managed by a boolean value on the edge). Taking into consideration that a personal

network is a directional graph, the set of edges can be written :

$$\mathcal{E}_p^k = \left(\bigcup_{\substack{l \subset \mathcal{V}_p^k \\ l \neq k}} e_n^{l,k} \right) \bigcup \left(\bigcup_{\substack{m \subset \mathcal{V}_p^k \\ m \neq k}} e_n^{k,m} \right) \tag{4.18}$$

where $e_n^{l,k}$ and $e_n^{k,m}$ are edges of $\mathcal{G}_n$ linking nodes l, k and k, m respectively.

4.4.3.2 Nodes of Personal Network

In order to perform a realistic simulation, the attributes of the personal networks' nodes are limited to information supposed to be available by the node in a real case:

- RAT
  The RAT attribute of node $\mathcal{V}_p^k$ is obtained from the same node $\mathcal{V}_n^k$ of $\mathcal{G}_n$.
- Estimated position
  The estimated position is obtained from the computation of a localization algorithm either algebraically or geometrically, using for instance the RGPA algorithm described in section 3.3.
- Time stamp of estimated position
  Because of the DES description, the position estimation is asynchronously updated. Each estimation has to be time stamped for the ease of post processing.

4.4.3.3 Edges of Personal Network

Each personal network $\mathcal{G}_p^k$ is a multi-graph where each edge corresponds to a different RAT. Each edge of the personal network contains 3 attributes about the connections of a device k with the other nodes of its neighborhood:

- LDP dictionary
  The values of the LDP dictionary are LDPs available in regard of RAT standards. Those values are directly updated from those available on $\mathcal{G}_n$ edges with a specific refresh time. This procedure aims to increase the realism of the simulation by limiting the amount of information available by each node. The refresh time of each personal networks LDP is requested by the localization stage. This particular process is detailed the next subsection 4.5.
- LDP time stamp
  Due to the DES description, each LDP information is time stamped for the ease of post processing.
- Visibility
  The visibility between two nodes k and l is updated by taking account the sensitivity of node k, the emitted power of node l and the computed received power LDP of those two nodes.

Note that the quantity of information available in both the nodes and the edges of the personal network could be advantageously increased. Here is just the minimal piece of information required for the upcoming communication stage.

4.5 Simulation of the Communication Stage

The LDPs information contained in the edges of the personal network are refreshed at a different rate that those on the edges of the network. Indeed, personal networks edges are refreshed only on the request of the localization stage (when no enough LDP are available). For that purpose, the communication stage is introduced.

4.5.1 Communication Stage Processing

The communication stage links all the nodes of a given personal network. The processing of this stage is independent and unique for each agent. This stage is driven by the localization stage: when the localization stage of a given agent detects that there is a lack of LDP to estimate the position (or that the information are obsolete), a refresh request is sent to the communication stage.

The communication stage of each agent is divided in two processes: a reception process waiting for a request, and a transmission process sending requests to other agents reception processes. The transmission process is triggered by a localization stage with the help of a *refresh request*. Hence, a node k receive a *refresh request*, its transmission stage sends a specific request to the reception stage of all of part of the nodes (depending of the chosen configuration). When the reception process received a request from a transmission stage of a node k, a specific proeccing is performed to update the personal network of the node k with values contains of the personal network of the requested node.

Practically, the requests are generated using SimPy SimEvents [119]. SimEvents allow to activate or interrupt a SimPy process execution with the help of a *signal*. Each signal of the communication stage corresponds to a specific request both from a given node to another one and on a given RAT. For computational convenience, those signals are stored as values of a communication dictionary, where the keys are a simple message (k, l, r) designating the *id* of the requester node, the *id* of the requested node and the RAT of the communication respectively. That dictionary, shared between all nodes of $\mathcal{G}_n$, contains all the possible inter-nodes signals combinations.

Lets consider the particular situation of Figure 4.6, where the localization stage of a node k has not enough LDPs to estimate a position. The localization stage send a refresh request to the communication stage. Then, the transmission process of node k sends a request to the nodes l and m, belonging to its personal network. For that purpose it uses 2 messages of the communication dictionary: (k, l, r) and (k, m, r) to request information of nodes l and m on RAT r. The reception processes of nodes l and m are triggered by the signals associated to the two messages (k, l, r) and (k, m, r) respectively. Finally, receiver processes of l and m update the personal network of node k with the information contained in their personal networks.

4.5.2 Data Update

The communication stage processing allows to update information between nodes of a given personal network to another. In a first approach, that procedure is used to

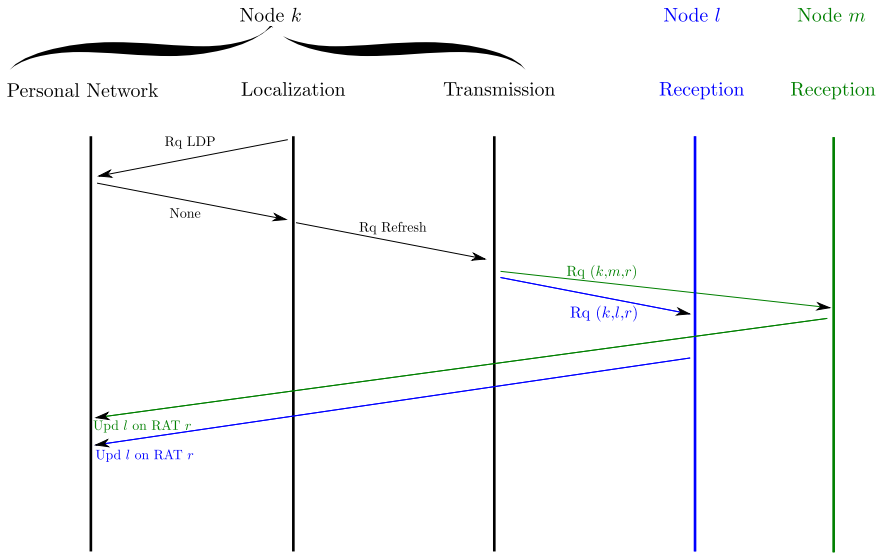

Fig. 4.6: Example of communication process initiated by the localization stage of node k. Because no information are available to estimate its position, the localization stage of node k requests a communication. The transmission stage of node k sends request to node l and m. Both nodes will thus update the personal network of node k.

update radio observables from a node to another. Practically, the implementation of that processing do not actually requires any data exchanges between nodes but only request exchanges. The data update is performed by the node receiving the request using data values from its personal network. Hence, each node is able to share any type of information contained in its personal network among

- its observables LDPs,
- its estimated position,
- its velocity and acceleration vectors,
- its visibility information.

Exchanging the LDPs information helps to simulate a classical data exchange during a communication. The estimated position and the visibility allows to address cooperatives approaches, where the position of other radio devices can be exploited to estimate the node position [113]. The velocity and acceleration vector enables cooperative data fusion algorithm.

As mentioned before, the information contained in the personal network of each node can be easily extended with any type of information. Those extra-information could also be shared by the communication stage. Hence, a node evaluating its position with the help of message passing methods (as described e.g. in [137]), could easily share the PDF information with its peers.

4.5.3 Communication Restriction

Another aspect of the proposed communication stage consists in applying some rules to restrict the data exchanges. In cooperative schemes, this feature allows a node not to provide specific personal network data on a request from one peer. Typically, that feature can be used in cooperative algorithms to test censoring effect on the position estimation [138], or in link selection to estimate the influence of the Global Dilution of Precision (GDOP) e.g. [139]. Hence, an user can setup the communication restriction on criteria of:

- received power,
- distance,
- GDOP,
- ambiguous estimated position (multi-modal solutions provided by RGPA).

Obviously, this list could be extended in the future to address more complex scenarios.

4.6 Example of Use of the Dynamic Platform

This section proposes to illustrate some examples on how the dynamic simulation, the propagation tools and the localization algorithms can be used together.

A first scenario described in 4.6.1 considers an agent moving into the environment, where it is connected to 3 anchors nodes. That scenario is used in 4.6.2 to run the multi-wall algorithm to provide regularly ToA and RSS LDPs between the agent and the anchors nodes. Based on the same simulation data, some CIR are computed using the RT tool in 4.6.3. Finally, a second simulation involving 2 mobile agents is proposed in 4.6.4, to demonstrate the communication stage.

4.6.1 Displaying the Mobility

The example illustrated in Figure 4.7 is considered to evaluate the multi-wall approach and the RT tool. In this example, a single agent is moving into the layout and is in visibility of 3 anchors nodes. The three anchors nodes are represented with triangles. The different ground truth positions of the agent are sampled every second and plotted as red dots. Between each dots, 1 second has elapsed. Every 10 seconds the small dots are replaced by larger dots with an indexed variable t. Those larger dots are *checkpoint positions* and they allow to determine the direction of the agent and to give reference points to easily match the position and the LDP values in the following figures.

From that simulation a log file is saved containing all the positions of each nodes (mobiles and statics) and the radio link between all nodes. Hence, the log file contains:

- The true node positions
- The estimated node positions (if one localization algorithm has been setup)
- The received power and delay for all the links at each timestamp.

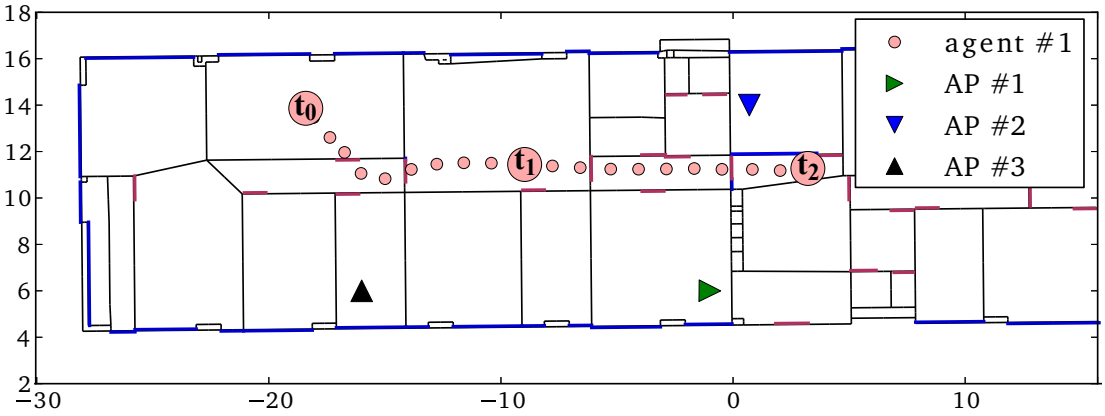

Fig. 4.7: Simulation of a trajectory of a mobile agent with 3 static access points

4.6.2 Exploiting the Location Dependent Parameter (LDP) Using the Multi-Wall Approach

From the trajectory, it is possible to get the evolution of LDPs between all the radio links. Figure 4.8, shows the evolution of both the received power and the excess time of delay along the mobile agent trajectory. The 3 different plots correspond to 3 radio links involving the mobile agent and the 3 static access points respectively. Logically, an increase of the received power value corresponds to a decrease of the delay.

4.6.3 Computing the CIR Using the RT

The incremental evaluation of the CIR during the dynamic simulation has not been fully implemented yet. However, it is already possible to use the simulation log to post process the dynamic simulation with the RT tool ans evaluate the CIR of all the links of the layout.

One of the advantage of the graph based RT is the signature description. As explained in chapter 2.6.2, signatures have been introduced to represent the persistent component of the radio channel. It means that for a given environment, the channel perturbation are caused by some specific signatures which can be directly related to specific pattern into the CIR.

Between 2 rooms, signatures are assumed to be stationary. Practically it means that while the transmitter or the receiver remain in their respective rooms, the same set of signatures can be used. It can be noticed that the signature description is only related to the environment and do not involve the position of neither the receiver nor the transmitter. Consequently, as long as an agent belong to a same room, the same set of signatures can be reused to calculate associated rays.

As an illustration, CIRs of the mobile agent is computed for points of its trajectory belonging to the same room. On the left column of Figure 4.10 are displayed the obtained rays between 6 positions of the agent and an access point. Facing these layout representations, the corresponding obtained CIR are displayed. The 6 set of rays and

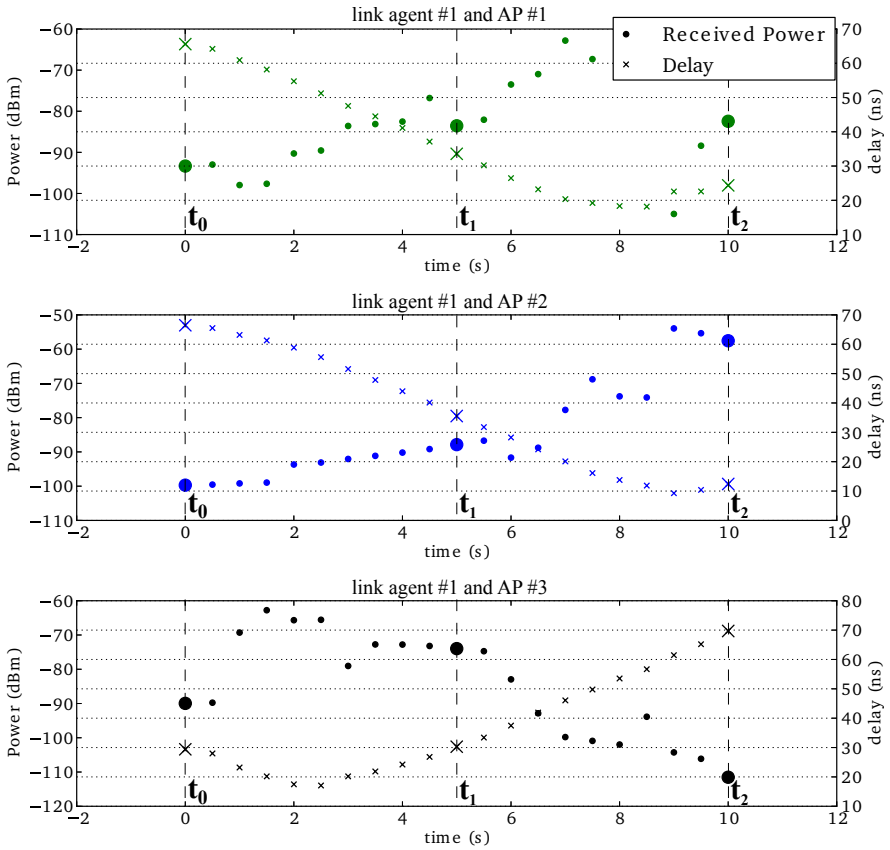

Fig. 4.8: The 3 figures correspond to 3 different radio links. On each figure are plot siulatneously the received power and the estimated delay as a function of the simulation time. Each dot corresponds to an estimation of received power value, whereas each cross correspond to an estimation of the delay .

CIRs have been obtained using the same set of signatures.

For the 6 CIRs obtained in Figure 4.9, Figure 4.10 displays an histogram of the computation time for each of those signatures. As expected, the computation of the first CIR is longer due to the cold start computation of the signatures. However, for the next 5 positions of the mobile agent (which still belong to the same cycle), CIRs are obtained significantly more rapidly.

As an example, Figure 4.11 shows a comparison of a simulated CIR to a measurement obtained during the measurement campaign of the WHERE1 project [97]. For this example, the emission power of the transmitter was known and has been used to scale the RT tool. The simulation does not include the additive noise. Then, it can be observed that the delay of both the first path at 27 ns and another contribution at 36 ns are correctly estimated by the RT tool. However, the simulation depends on the description of the environment. For that simulation, furnitures have not been taken into account. This can be explained why a strong contribution can be observed in simulation at 30 ns and lack into the measured data. On the contrary, several contributors appearing between 32 and 35 ns on measurement and are not retrieved by the RT simulation. This difference can be explained by a limited number of rays researched during the simulation. However, the RT simulator is designed for localization purpose. The aim here is not to get all the channel contributors but the most significant one which are required to provide accurate simulated LDPs and thus feed localization algorithms. More examples of the RT tool are provided in the analyze of the WHERE 2 measurement campaign in chapter 5.

4.6.4 Example of Use of the Communication Stage

The simulation represented in Figure 4.12 is considered to demonstrate the communication stage. Here, 2 moving agents and 4 static anchors are considered. The two mobile agents start from a different side of the layout, move toward each other, cross themselves into a corridor and continue to their destinations. The different trajectories of the agent 1 and the agent 2 are represented by red and white dots respectively. Similarly to the previous simulation, between 2 dots 1 s has elapsed, and checkpoint position is set every 10 seconds. Considering the network organization, 3 different RATs are involved in the simulation: rat_1, rat_2 and rat_3.

The mobile agent 1 embeds rat_1 and rat_3 and the mobile agent 2 embeds rat_2 and rat_3, as well as the two mobile agents can only be connected together on rat_3. The mobile agent 1 is connected on rat_1 to the 2 static anchors represented with the red triangles, whereas the mobile agent 2 is connected on rat_2 to the 2 static anchors represented with the white triangles. Finally, each second, each agent tries to estimate its position with the available ToA of its personal network. If not enough ToA are available, it try to communicate with its neighborhood. The communications stage has been configured to exchange both ToA and estimated positions.

Figure 4.13 represents the positioning error of the mobile agent as a function of the time. First of all, the zero values at the beginning correspond to an initialization value and just mean that the agents haven't yet start to estimate the position. On both

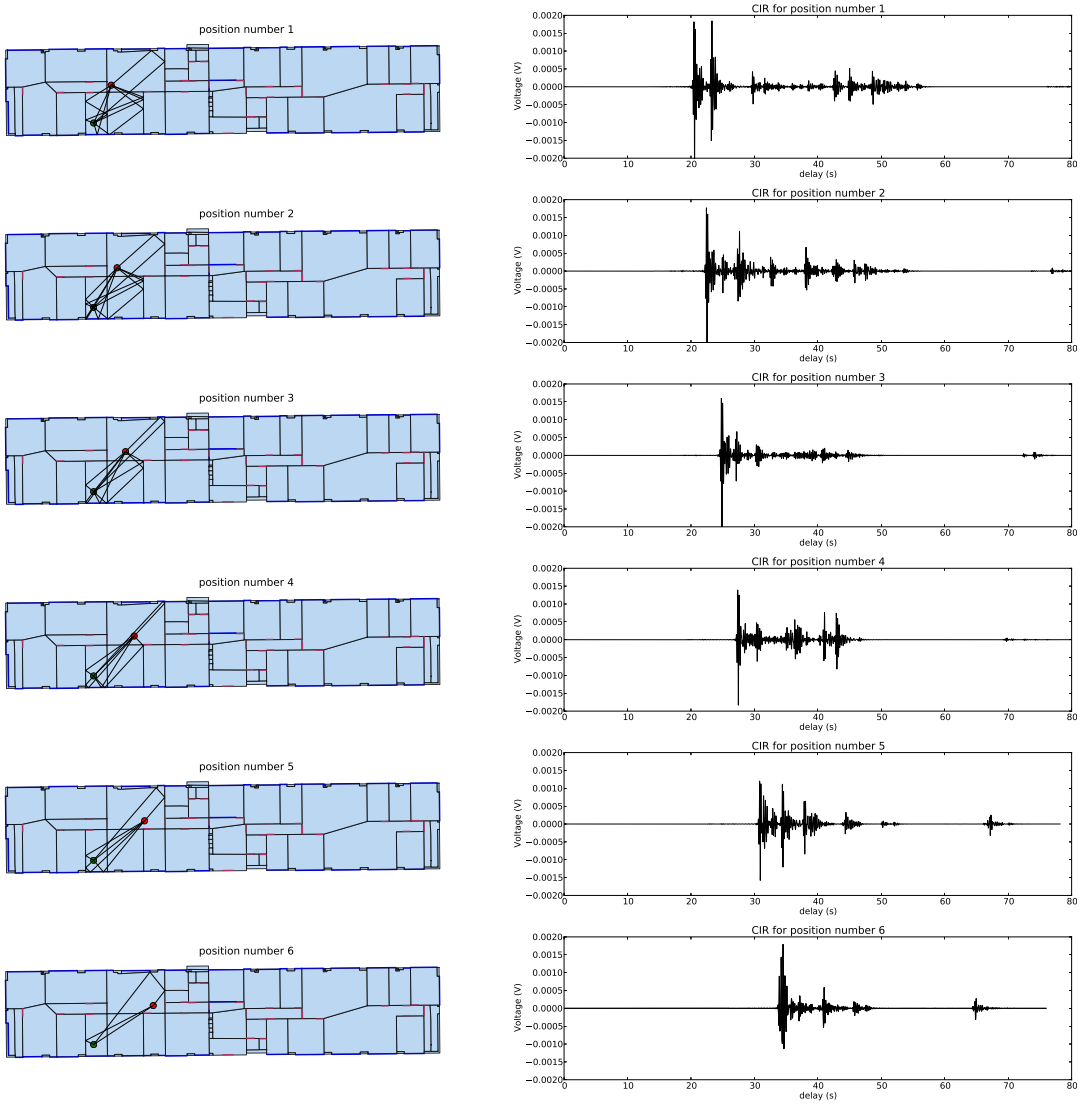

Fig. 4.9: The figures on the left show computed rays between the mobile agent and an access point for different position of the mobile agent along the trajectory. On the right column are displayed the evaluated CIRs corresponding to the situation on the left column.

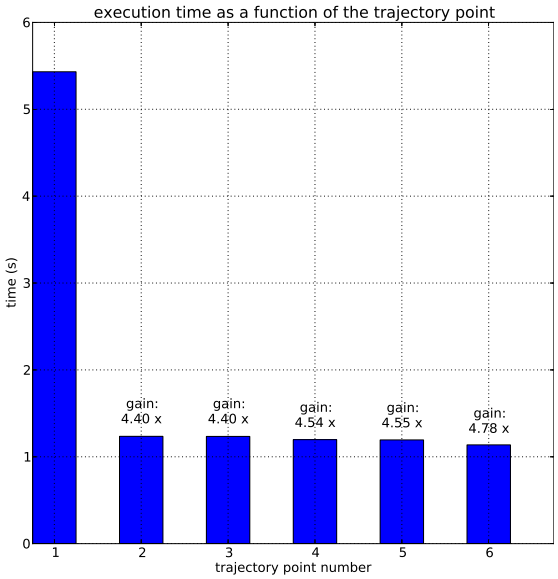

Fig. 4.10: Time required to produce CIR for 6 different positions of the mobile node. The gain indication informs about speed improvement in CIR computation relative to the first cold start requiring signature computation (position 1). The used computer to perform that simulation is an Intel Core I7 with 4Gb of RAM.

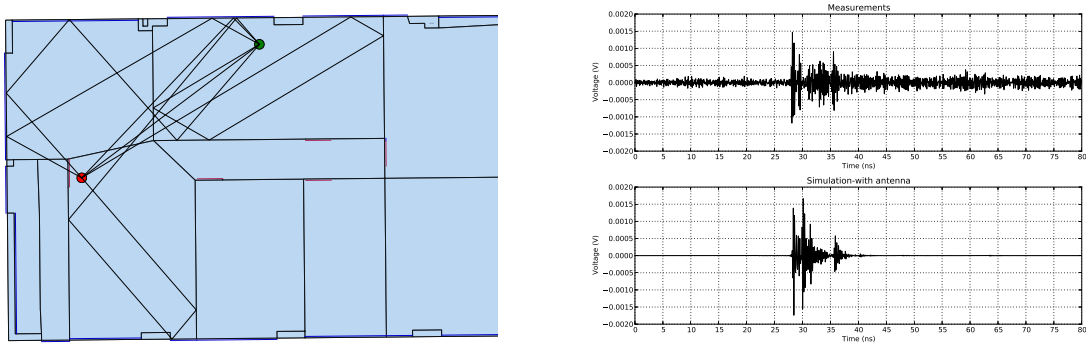

(a) (b)

Fig. 4.11: An example of CIR computation. In (a) is shown the situation of the simulation and the 2D rays generated by the ray tracing computation. In (b), the simulated and measured CIRs of the situation are represented as a function of delay.

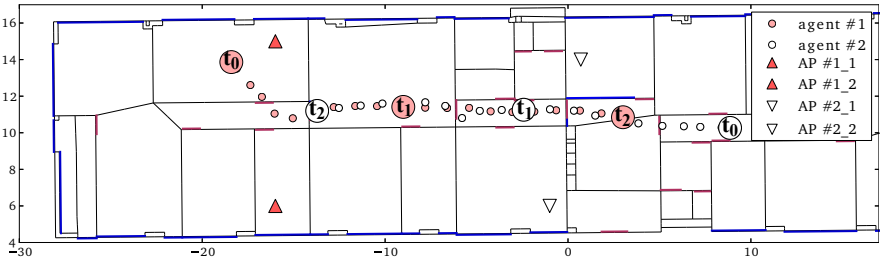

Fig. 4.12: Simulation scenario: ground truth positions of the mobile agent 1 and mobile agent 2 are represented by red and white dots respectively. Anchors nodes of mobile agent 1 and mobile agents 2 are represented by red and white triangles respectively. In addition both mobile agents can be connected together.

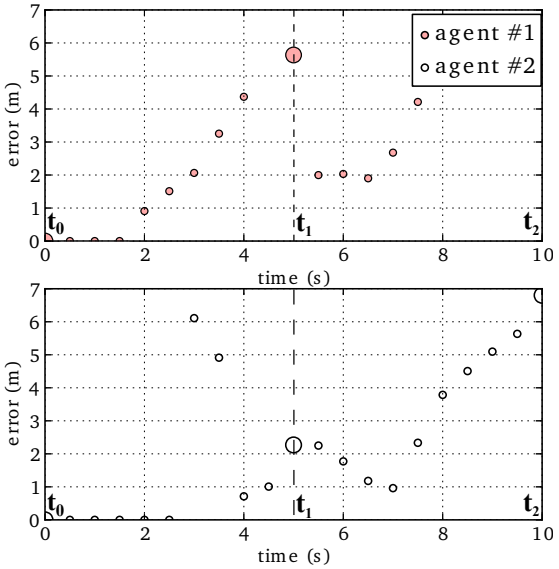

Fig. 4.13: Positioning error of the 2 mobile agents as a function of the time. The proximity of the two agents, enabling the communication process is observable between 4s and 7s.

curves, 2 regimes can be observed. A regime of large positioning error, corresponding to situation where mobile agents have only access to 2 anchors nodes for positioning, and a regime of small positioning error where a third anchor (the other agent) helps to estimate the position.

Indeed, it is noticeable that a discontinuity appears in the positioning error at 5s for agent 1 and 4s for agent 2. Considering the checkpoint values, which corresponds to those represented in Figure 4.12, it appears that the decrease of the positioning error corresponds to a situation where the 2 mobile agents are in visibility. Then, the two agents communicate between each other in order to exchange both their estimated position and a ToA value. As long as they are in visibility, the position error value remains low. At time 7 seconds, both node loose their respective visibility and thus the possibility to exchange information. Then, the position estimation is no longer accurate and the positioning error increases again.

4.7 Conclusion

At the beginning of this chapter, a state of the art on the mobility model and on the network simulator has been provided. The next section have detailed the agent mobility into the proposed dynamic platform. That mobility is animated by a DES, and can be split into two parts: a first part detailing the large scale mobility based on the graph description, a second part detailing the small scale mobility of the agent. This second part based on the steering behavior method has described how an agent can move into a given environment and interact with other agents. The main original part of that work is the adaptation of the steering behavior method to the graph representation.

This chapter has also introduced a description of the adopted graph-oriented network organization. In particular, this section has detailed how the agents could get their LDPs (obtained by the multi-wall method described in the first chapter). A basic communication protocol has also been described allowing the exchange of messages between agents.

Finally, the last section has provided two examples of simulations. The first simulation has shown a single agent moving into a synthetic environment, where LDPs and CIR have been evaluated from its trajectory. The second simulation has demonstrated how the communication stage could be used for addressing cooperative localization problems.

Chapter 5

Evaluation of the Proposed Methods on Measured Data

5.1 Introduction

This chapter proposes the evaluation of the methods presented in the previous chapters based on the data obtained from a measurement campaign realized during European project FP7 WHERE2.

The first section 5.2 describes the heterogeneous platform used to perform the measurement campaign. The different used radio technology are listed, and the different measurement scenarios are detailed. Then, the extraction of channel parameters is performed on a specific scenario of the PTIN site measurement campaign.

The second section 5.3, provides a comparison between measured LDPs and simulated LDPs using the developed simulator. In a first time, a comparison is provided using the site specific multi-wall to evaluate LDPs on all measured points. In a second time, a selected sample of measured CIR are compared to those obtained with the RT tool.

The third section 5.4 is an attempt to evaluate the localization algorithms presented in this thesis based on both scenarios extracted from the PTIN site measurement campaign. Then, the estimated position accuracy is evaluated using the proposed RGPA method and compared to a standard ML approach for all mobile positions of the data set. Finally, the interest of localization method based on hypothesis testing is demonstrated making use of a selection of 2 measured ToAs and 1 complementary measured RSS.

5.2 Description of the Measurement Campaign

This section focuses on the description of the measured data obtained during the FP7 WHERE2 Project. First a global description of the measurement campaign is proposed. Then the channel parameters are extracted from a given scenario.

5.2.1 The FP7 WHERE2 Project

This thesis has been realized all along the European FP7 WHERE2 Project [140]. The WHERE 2 project aims to enhance the efficiency of future wireless communications systems by using both the positioning and communications information. The estimation of the position of mobile terminals will be obtained using heterogeneous localization algorithms using different types of radio observables obtained from different RATs.

5.2.2 Specificities of the PTIN Measurement Campaign

The WHERE2 measurement campaign has been realized during 4 days in April 2013 in the office of PTIN partner in Aveiro Portugal. The results of this measurement campaign are public and can be downloaded from [141]. All the aggregated radio access technologies have been used for the first time jointly, providing a very unique heterogeneous radio dataset for evaluating positioning applications. The platform was composed of :

- 2 short range radios (ZigBee, IR-UWB)
- 1 long range cellular radio (3GPP-LTE OFDM)
- several embedded inertial sensors (accelerometer, magnetometer, gyrometer)

During the measurement campaign, all radio link data associated to each radio technology have been stored into a time stamped data base. A measurement testbed has been embedded on a mobile trolley, which has been moved along the PTIN building.

The measurement testbed is equipped with a device of each type of short and medium range radio platform and inertial sensors. Depending on the scenarios, data from either all or a selected number of devices have been stored in a database for post processing.

The trajectories of the trolley have been pre-determined and are specific for each scenario. Slaves radio devices linked to their coordinators on the trolley have been spread into the measurement area in the PTIN building. Some of those radio devices are mobile whereas most are static access points.

Figure 5.1 shows a representation of the WHERE2 test bed embedded on the trolley and the organization of the devices of all RATs around.

5.2.3 Considered Radio Technologies

This work has been focused on the exploitation of 2 short ranges radio technologies providing 2 types of radio observables:

- Zigbee which provides RSS observables,
- Channel Energy Profile (CEP) from the CEA UWB platform [142] and their associated ToA estimates.

5.2.3.1 Zigbee Nodes

The ZigBee nodes are IEEE 802.15.4 compliant RF transceiver designed for low-power and low-voltage wireless applications. The main specifications of the devices are

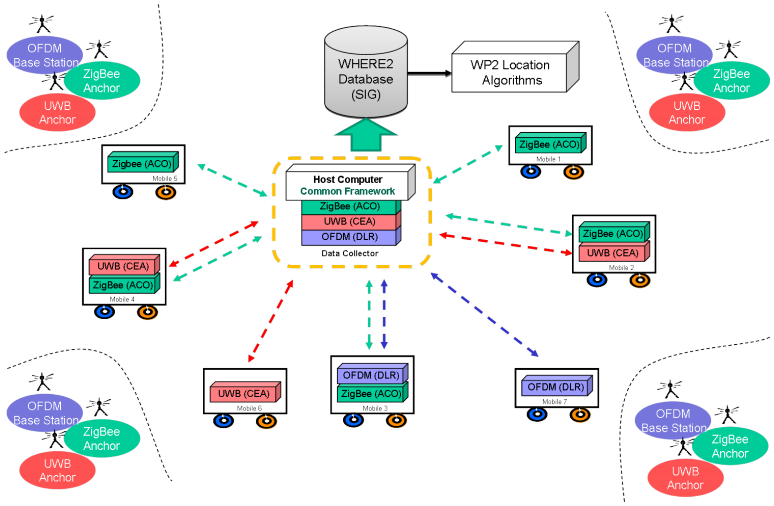

Fig. 5.1: Where 2 measurement platform. Different radio technologies (ZigBee, IR-UWB, OFDM) are embedded on a mobile Trolley

[142] :

- Frequency: 2.4 GHz Band
- Bandwidth: 5 MHz
- Modulation: DSSS(OQPSK)
- Rx sensitivity: -92 dBm

Devices are organized in a centralized topology network, which means that a device has to be configured as a coordinator. Here, the coordinator node has been placed on the measurement trolley.

5.2.3.2 Impulse Response Ultra Wide Band (IR-UWB) Nodes

The IR-UWB nodes generally used for sensor network deployment, are well suited for localization and tracking applications [143]. Through a low data rate (LDR) data transmission, they allow a round trip delay (RTD) measurements between peer-to-peer devices. Devices are also organized in a centralized topology network, and the coordinator has been placed on the measurement trolley. The main specifications of the IR-UWB devices are [142]:

- Frequency: 4.5 GHz ISM Band
- Bandwidth: 500 MHz
- Modulation: Differential Binary Phase Shift Keying (DBPSK)
- Rx sensitivity: -70 dBm between 4 GHz and 4.5 GHz

Among other the Impulse Response Ultra Wide Band (IR-UWB) nodes provide ranging time observables, which can be directly converted to range observables. In addition to those observables, the devices also provide the channel energy profile with a time resolution of 1 ns.

5.2.4 Description of the Selected Scenarios

The PTIN site WHERE2 measurement campaign is very rich and is made of 4 different scenarios, each including several sub scenarios. Each one of those sub scenarios takes into account a large number of situations involving mobile nodes, different RATs, and different visibility situations. In the following only 2 specific scenarios have been selected:

- scenario 2 which gathers data from all RATs where all nodes are static except the moving trolley. This scenario is used for model parameters extraction.
- scenario 4 which gathers data on a fine ground truth point grid (1 point every 0.5m). No pre-defined track for the multi-RAT trolley is used. All mobile nodes are static.

5.2.4.1 Scenario 2 : Model parameters extraction

In scenario 2, a trolley with a ZigBee node coordinator and an IR-UWB node coordinator has been moved on 18 different measurement points in the PTIN building. Those points are figured by the black dot on Figure 5.2. Inside the building are placed 15 IR-UWB devices which provide ranges observables between each other and between the trolley and also 7 ZigBee devices which provide RSS observables between each other including the node placed on the trolley.

5.2.4.2 Scenario 4 : Testing scenario

The scenario 4 is the selected scenario for the platform and algorithm evaluations. In this scenario all the devices except those embedded on the trolley are static. The 15 IR-UWB devices and the 7 Zigbee devices stand at the same position as in scenario 2. Figure 5.3a shows the positions of the ToA anchor and the RSS anchor represented by red dots and green triangles respectively. The different trolley positions (a.k.a measurement points) are represented by the blue dots. Figure 5.3b specifies the id of the measurements points. Each arrow corresponds to a contiguous set of measurements. The number associated to the tail and the head corresponds respectively to the first and the last measurement index of the set.

5.2.5 Deriving Site-Related Models from Scenario 2

In order to be able to feed the localization algorithms, the parameters of the pathloss model for the RSS nodes and the error distance model for the ToA nodes have to be estimated. Model parameters are extracted from scenario 2.

5.2.5.1 Deriving a ZigBee RSS Pathloss Shadowing Model

Figures 5.4a and 5.4b represent respectively the received power and the ground truth distances as a function of the measured points. For a specific measurement point, several power measurements are performed. The red dots represent the mean value of the measurement. It can be observed that the received power is weakly correlated to the

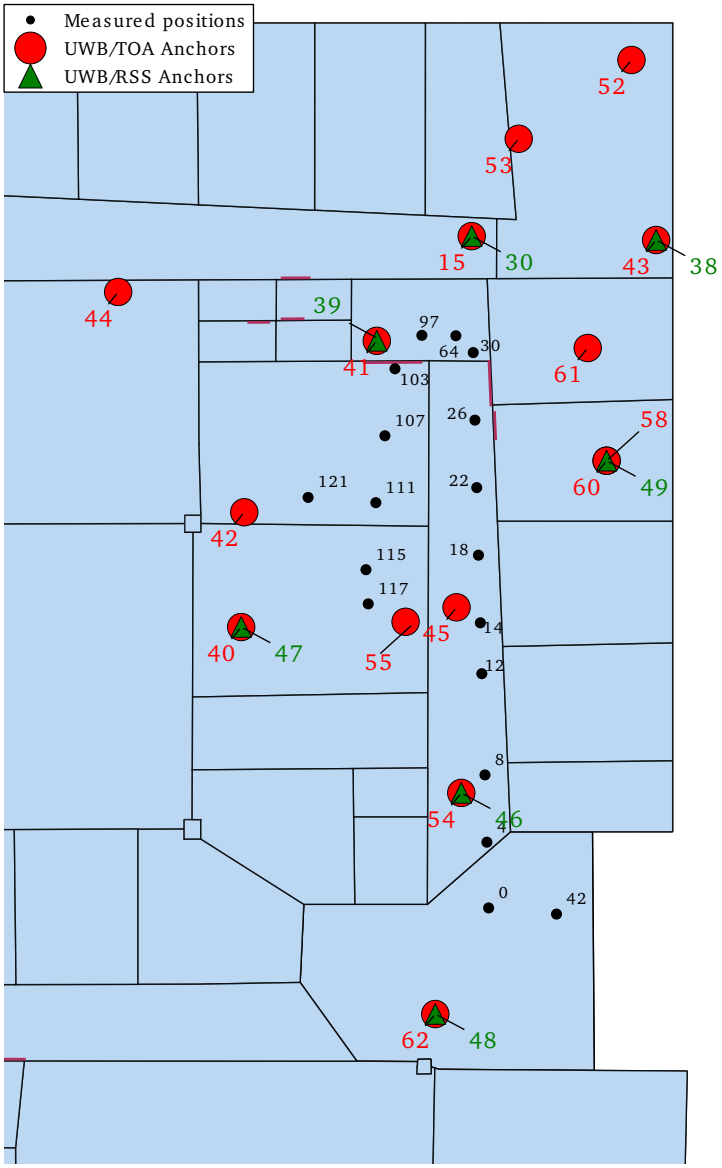

Fig. 5.2: Scenario 2: Measurement points and anchor positions superimposed on the building map of the measurement campaign. The red dots represent the position of the UWB ToA devices, the green triangle represents the position of the ZigBee devices. The black dots and their associated number represent a measurement point.

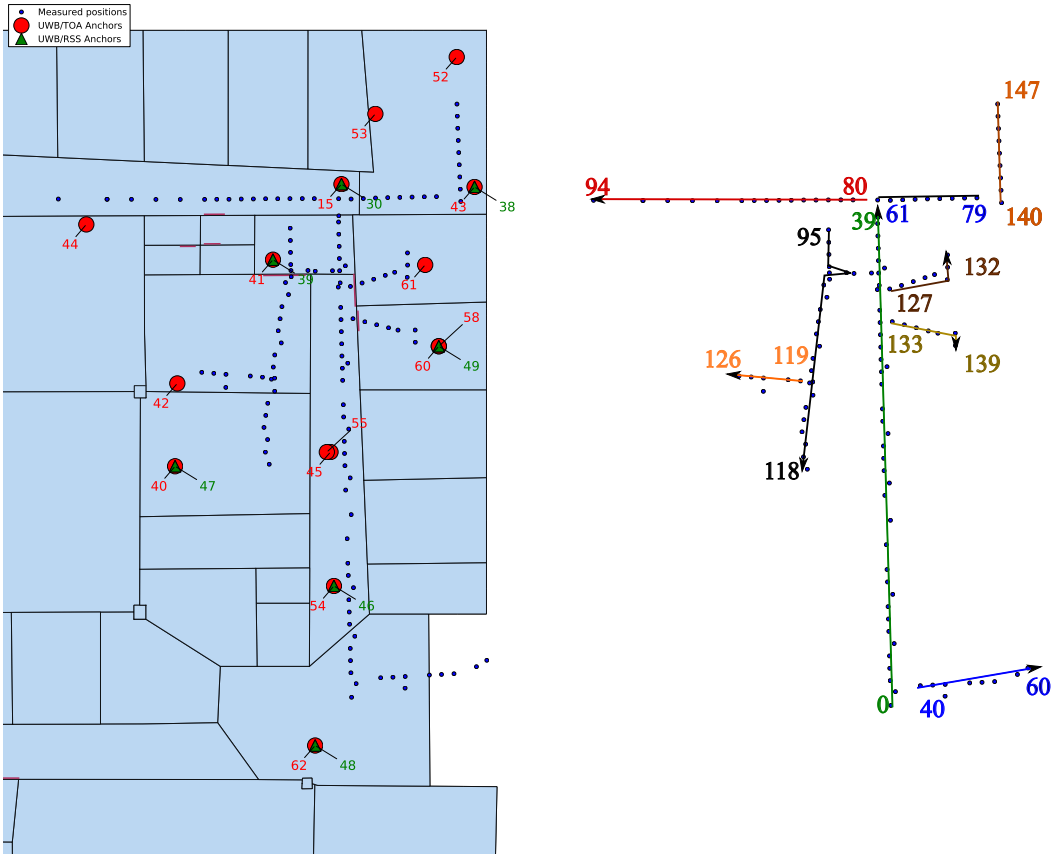

(a) Measurement and anchors positions (b) Indexes of the measured positions

Fig. 5.3: Scenario 4: Both figures represent the Scenario 4 description. In (a) is represented the different trolley positions with blue dots, and the positions and name of ToA and RSS anchor nodes with red dots and green triangles respectively. In (b) is superimposed the measurement indexes of the trolley trajectory. The number associated to the tail and the head corresponds respectively to the first and the last measurement index of the set.

distance. As expected, in case of strong received power the relation to small distance is clear. Regarding the collected data, it appears that there is a significant number of radio link which return the saturated minimal value of $-81dBm$. Actually that value corresponds to the sensitivity of the receiver. This value should be used carefully with respect to its relation to distance. In the following they haven't been considered for the determination of the path loss model parameters.

Using the log-normal shadowing model (equation 5.1), the path loss model parameters for both one-link and multi-link cases are extracted. By denoting RSS the received RSS value, RSS_0 the RSS received at d_0, d the distance, and assuming X_σ as a zero-mean Gaussian random variable representing the shadowing, it can be written:

$$RSS = RSS_0 - 10n_p \log_{10}(\frac{d}{d_0}) + X_\sigma \tag{5.1}$$

By applying a linear regression on the measured data the model parameters can be extracted. The values of the model parameters are reported in Table 5.1, and the result of the regression is provided in Figure 5.5

Table 5.1: Zigbee path loss models extracted for scenario 2.1

Zigbee NodeID	RSS_0 (dB)	n_p	σ (dB)
All	-50.21	2.21	5.73
30	-51.38	1.16	6.85
38	-55.45	2.01	3.20
39	-47.14	2.48	5.93
46	-47.33	3.07	4.56
48	-41.62	2.95	4.98
49	-52.77	2.68	4.56

On those extracted RSS values, it is noticeable that the received power values have a very large variability. This variability has also been observed on the static links. As an example, the received power as a function of the measurement point of 2 static links is given in Figure 5.6. In that static situation the power values can vary in a range of almost 30 dB. The interpretation of those variations calls for making a distinction between static and dynamic shadowing. There exists in the upper region (least attenuation) different relatively static levels which probably correspond to a certain combination of discrete configurations of the building as open or closed doors. In the lower region the observed fluctuations are probably due to other strong dynamic shadowing due to human bodies moving into the channel. As a consequence, it exists some issues about exploiting over simplified path loss model in such complex and variable situations. This point has to be kept in mind in the further method evaluation. More generally, the best use of the received power information is a quite complex problem (n.b. even in fingerprinting approaches), due to its fragile property of being very sensitive to channel modifications. In any case and whatever the used technique, having a tool for understanding and predicting the association of received power and distance or received power and position is an asset.

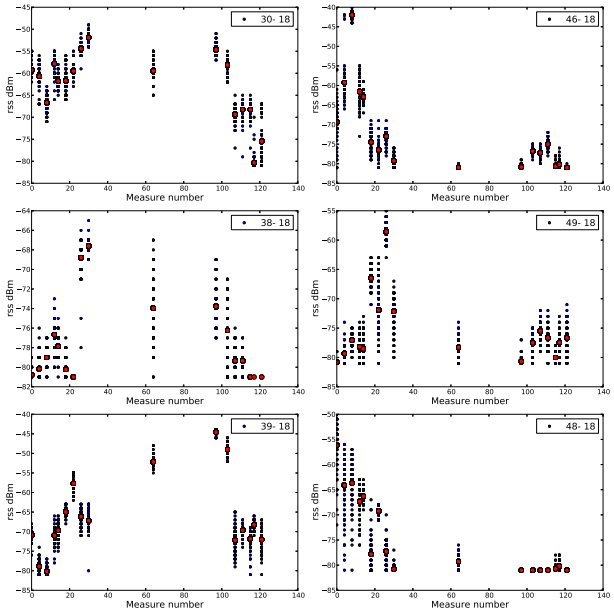

(a) Received power vs measurement id

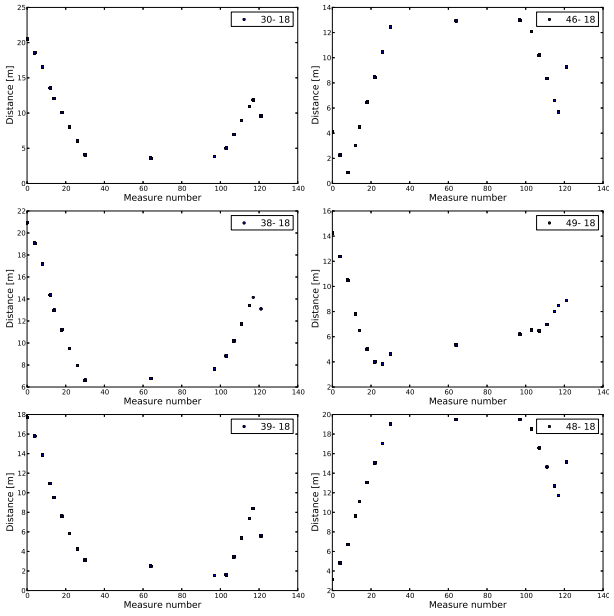

(b) Distance vs measurement id

Fig. 5.4: Scenario 2.1, measured Zigbee RSS : (a) received power as a function of the measured points, (b) ground truth distance as a function of the measured point. The red dots on the received power correspond to the mean values of received power for the given measured positions.

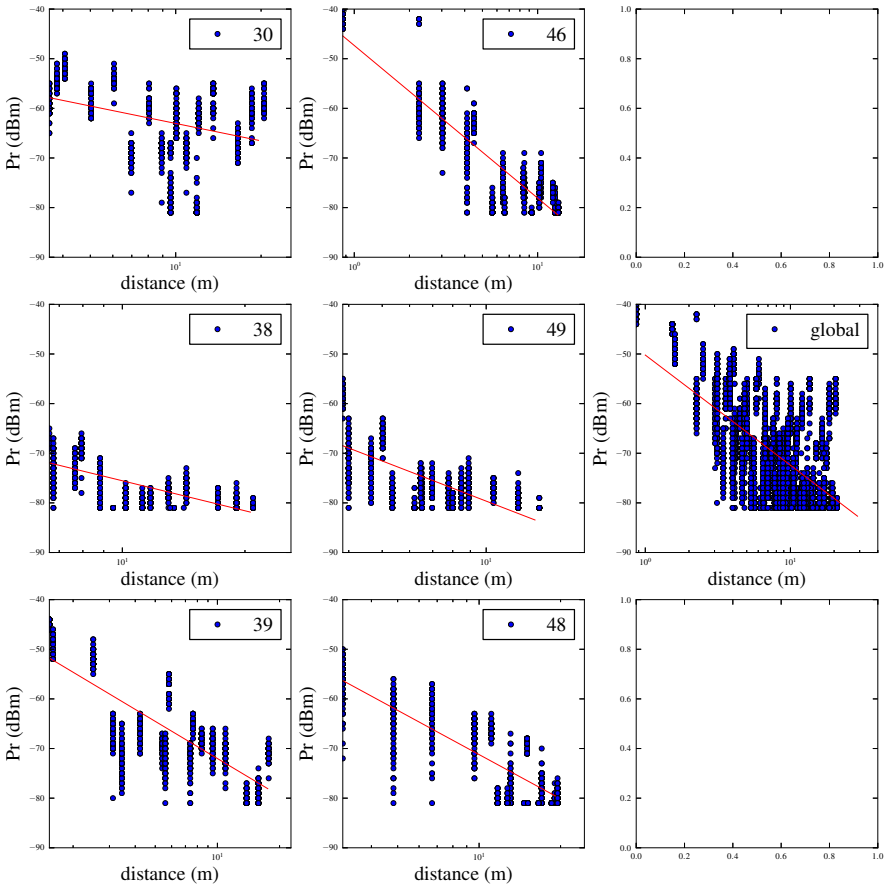

Fig. 5.5: Received power as a function of the distance for the each RSS anchors. The red line correspond to the extracted one slope path loss model.

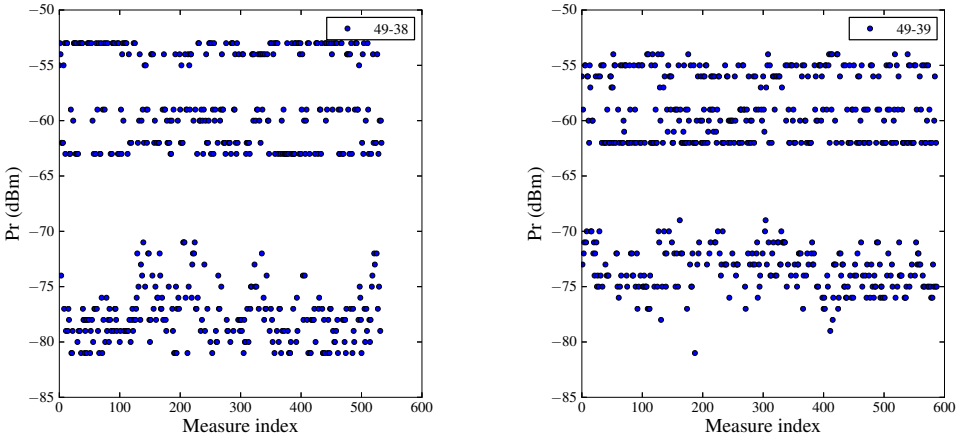

(a) (b)

Fig. 5.6: Example of power measurement between 2 static links (a) between 38 and 49 and (b) between 39 and 49

5.2.5.2 Deriving an IR-UWB Ranging Error Model

Using a similar procedure on the IR-UWB, matching the measured distances to the true distances, and assuming a Gaussian model for the error distribution, it is possible to derive a ranging error model. The obtained values of the model are presented in Table 5.2. It is noticeable that the model parameter values have been obtained by aggregating of all the measured data without any distinction between LOS and NLOS situations. In regard with the theoretical achievable performances of IR-UWB technology, it is very likely that, in LOS situations, both the mean ranging error and the standard deviation would be significantly lower.

Table 5.2: UWB ToA ranging model extracted for scenario 2.1

Scenario	mean ranging error (m)	std (m)
2.1	0.46	2.52

5.3 Comparison between measured and simulated LDPs

This part is dedicated to the evaluation of the methods proposed in the three first chapters. For that purpose the measurement environment has been recreated in a synthetic version. With the help of this environment, the site specific multi-wall approach is used to produce ToA and RSS observables. Those simulated values are compared to the measured one, for all the measured positions. As well, the proposed RT tool produces CIR for specific trolley positions and are compared to the measured ones. Then, the measured ToA and RSS observables are used to feed the RGPA. The positioning performances are evaluated and compared to a ML approach. Finally, the data set is used to evaluate the hypothesis testing method against RGPA and a ML approach.

Table 5.3: RMSE values and variance between measures and simulations for the RSS and ranges observables

Anchor type/ LDP	RMSE	Error Variance
ZigBee / RSS	5.37 dBm	27,5 dBm
IR-UWB / ranges	0.82 m	1.98 m

5.3.1 Evaluation of the Multi-wall Approach on Measured Data

This part compares simulated LDP obtained with the multi-wall approach described in 2.7, with those measured during the WHERE 2 measurement campaign [144].

Comparison between measures and simulations have been performed for all the available anchors along the trolley trajectory. Figures 5.7 and 5.8 show those comparisons between measurement and multi-wall simulation for received powers and ranges respectively. The error is defined as the difference between measures and simulations values and it is represented by the red crosses. The measurements point indexes are related to the indexes presented in Figure 5.3b.

It has to be noticed that the materials parameters of the real measurement environment are not known, and thus have been modeled with standard pre-existing materials from the synthetic platform database. Except for some specific link and positions where the error can be very high, probably due to that lack of knowledge of the environment, it is noticeable that the site specific multi-wall approach provides a good estimation of both the received powers and the range observables. That behavior is also confirmed by the RMSE values and Error variances presented in table 5.3.

5.3.2 Evaluation of the Ray Tracing Approach on Measured Data

In this part, the measured UWB CIR are compared to the simulated one for two positions of the trolley. The two different configurations of trolley/peer node position represented in Figure 5.9 are considered. The first configuration corresponds to a NLOS situation where the trolley is positioned behind a door and the peer node is next to a wall of a room. The second configuration corresponds to a LOS situation where the trolley and the peer node are both positioned into a corridor.

From those 2 configurations, all the computation steps described in 2 are applied in order to obtain 2D rays (Figure 5.10) then 3Drays (Figure 5.11).

In figures 5.12, the generated CIR is compared to the measures obtained from the data collected to the IR-UWB. The measured data are channel energy profile with a time resolution of $1ns$, stored into a circular buffer. As a consequence, the stored energy profiles have been realigned using the measured ranging estimation to be comparable with the simulation. In addition, each measured sample is a $16bit$ integer value proportional to the log received power. For the comparison these integer values have been converted into their respective dBm values. Note that this conversion is an approximation of the actual received values due to the lack of information on both the emission power level and the maximum received power level.

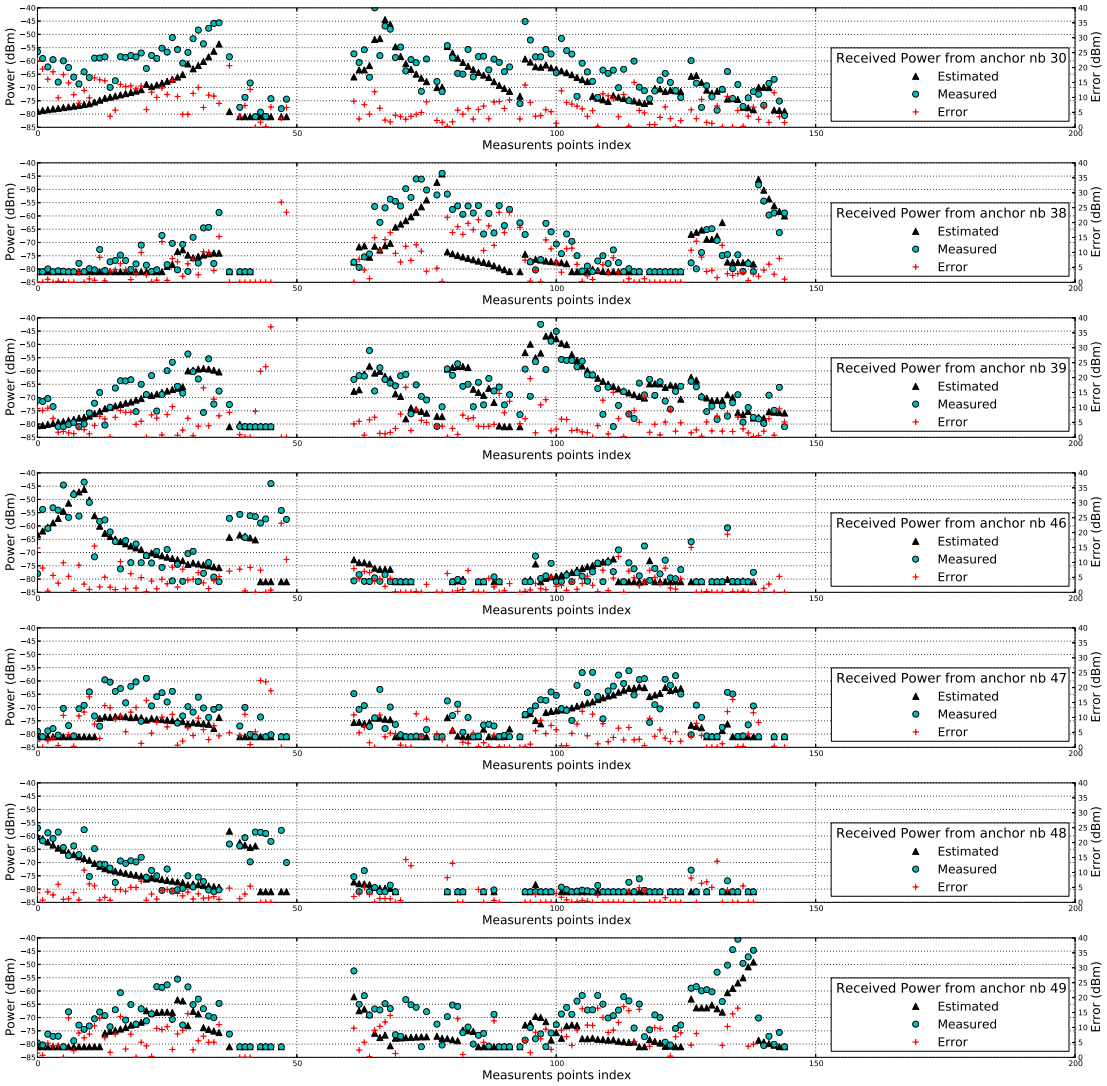

Fig. 5.7: Comparison simulation measures of the received power for 7 ZigBee anchor nodes as a function of different measurement positions. Cyan dots are the measured data, black dots are simulated data, red crosses are the error for each trajectory point.

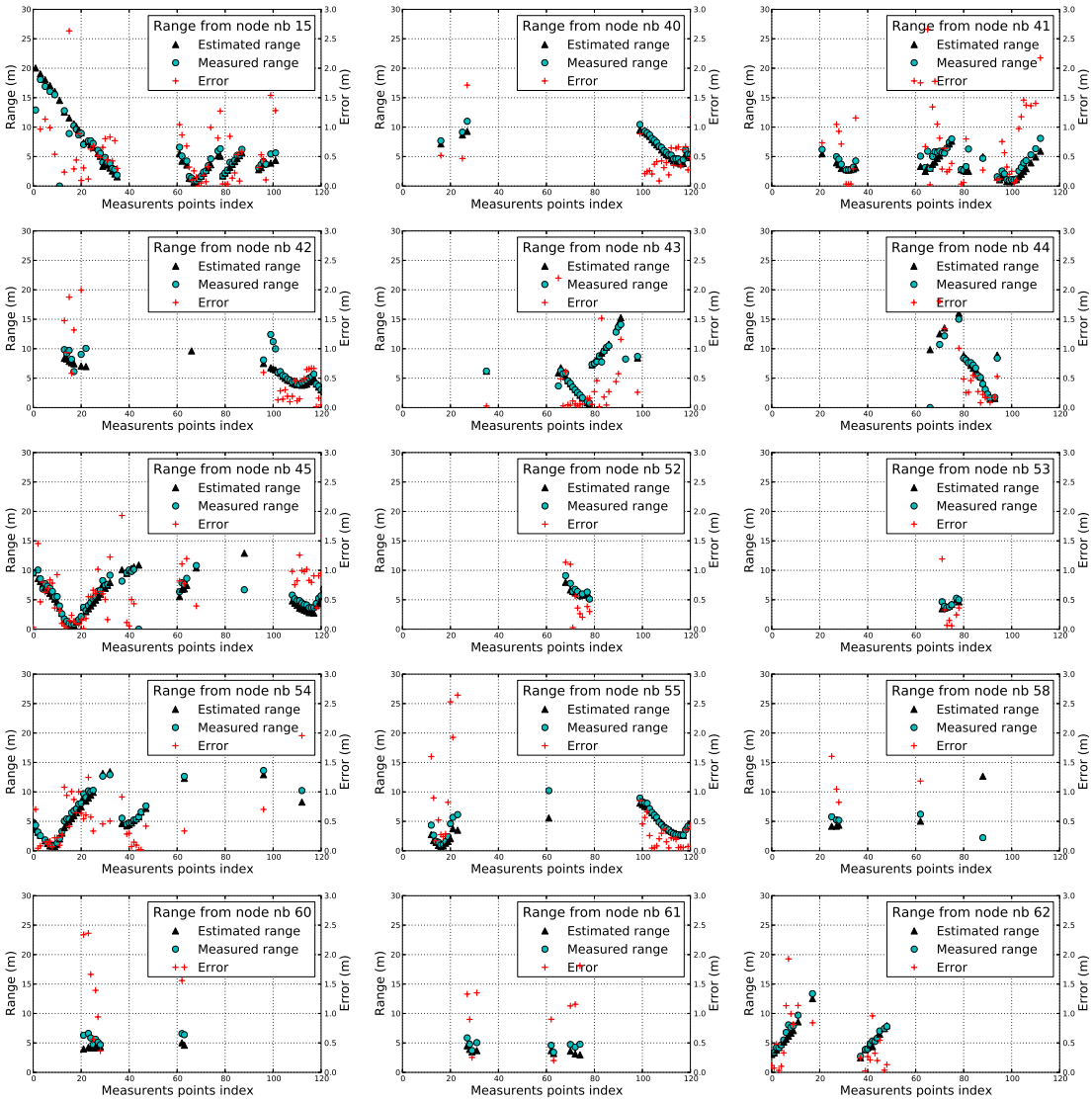

Fig. 5.8: Comparison simulation measures of the ranges for 15 IR-UWB anchors nodes as a function of different measurement position. Cyan dots are the measured data, black dots are simulated data, red crosses are the error for each trajectory point.

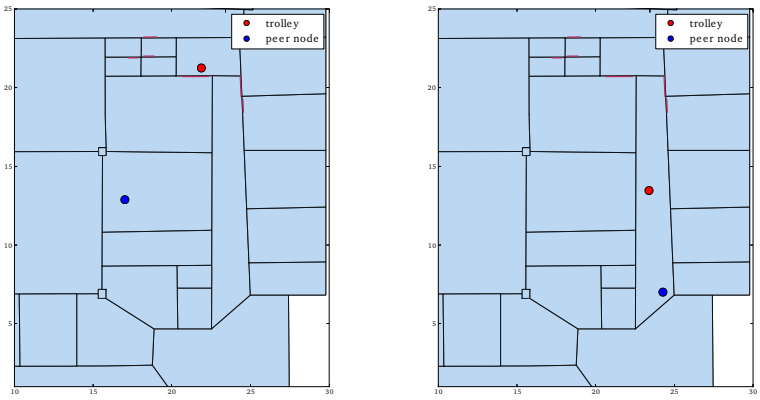

(a) Conf. 1: node positions (b) Conf. 2: node positions

Fig. 5.9: Two position configurations of the Trolley and the peer node used for CIR computation. In (a) configuration 1 is a NLOS situation. In (b) configuration 2 is a NLOS situation

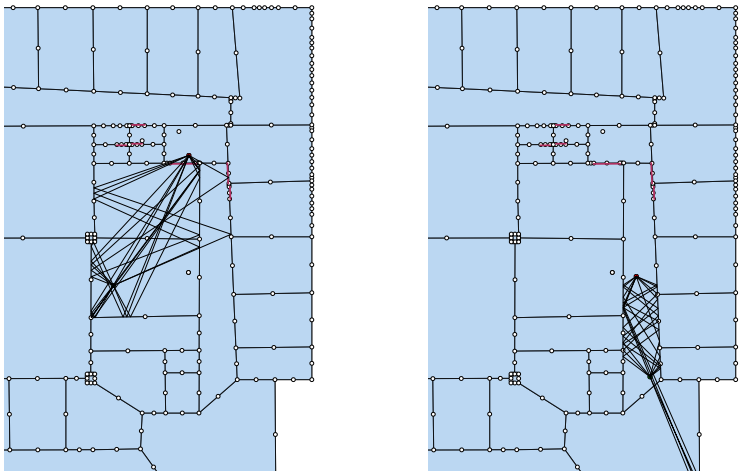

(a) Conf. 1: 2D rays (b) Conf. 2: 2D rays

Fig. 5.10: 2D rays obtained from the RT computation for (a) configuration 1 and (b) configuration 2

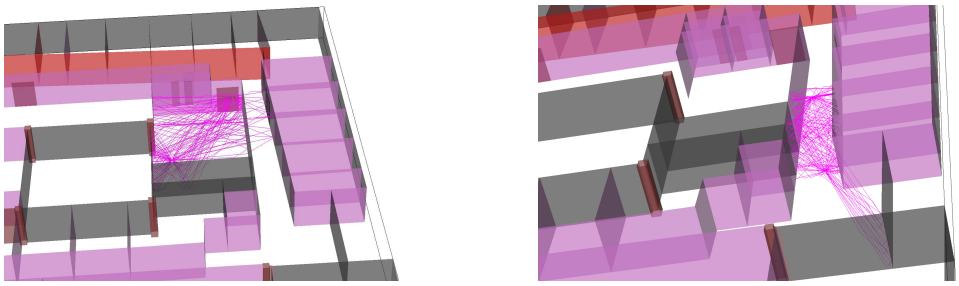

(a) Conf. 1: 3D rays (b) Conf. 2: 3D rays

Fig. 5.11: 3D rays obtained from the RT computation

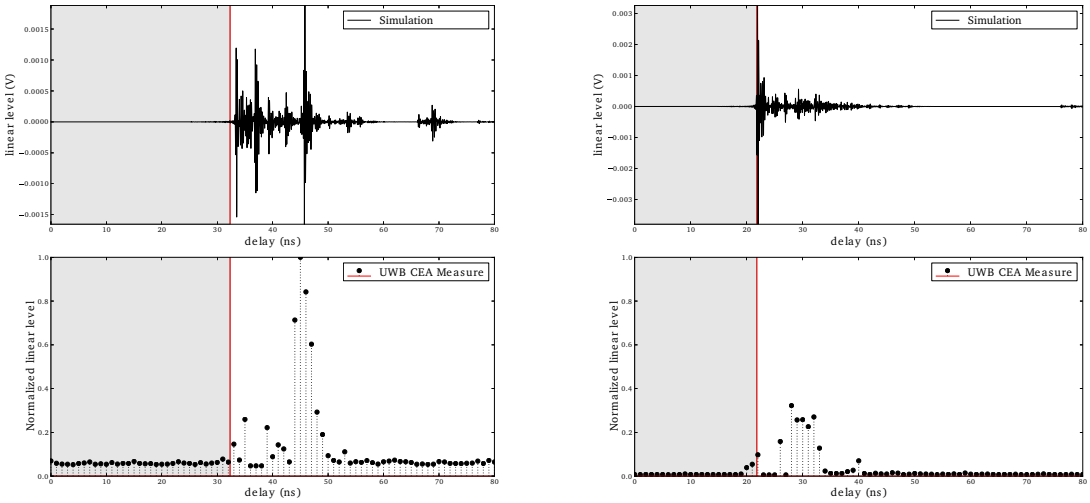

(a) Conf. 1: CIR vs channel energy profile (b) Conf. 2: CIR vs channel energy profile

Fig. 5.12: Channel impulse responses generated using the proposed ray tracing tool compared to the normalized measured channel energy profile. In (a) , the ground truth delay is 32.3 ns whereas the delay corresponding to the measured two way ranging is 32.8 ns. In (b) , the ground truth delay is 21.8 ns whereas the delay corresponding to the measured two way ranging is 22.17 ns. The red line separating the grey part from the white part represent the ground truth delay.

For the ease of the comparison, it would be convenient to observe the corresponding channel energy profile of the simulated data. According to [145], the impulse response h of propagation channel can be written :

$$h(\tau) = \sum_i a_i \delta(\tau - \tau_i). \tag{5.2}$$

where a_i and τ_i are the attenuations and their associated propagation delay respectively. Then it is possible to proceed to the discretization of the channel impulse response using the following formula:

$$h_l = \sum_i a_i \text{sinc}(l - \tau_i W). \tag{5.3}$$

where l and W are a tap index and the band of the system respectively. The lth tap can be interpreted as the sample l/Wth of the low-pass filtered baseband channel response $h_b(\tau)$ convolved with $\text{sinc}(W\tau)$.

Observing that h is the expression of the transmission channel for a given frequency proposed in (2.144), it is possible to discretize the simulated propagation channel to obtain the associated channel energy profile.

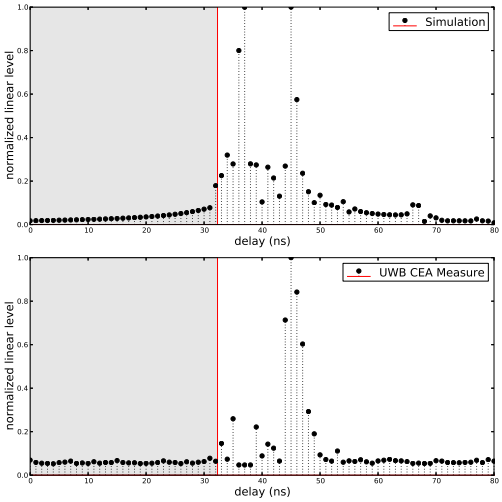

(a) Conf. 1: Channel Energy Profile Comparison

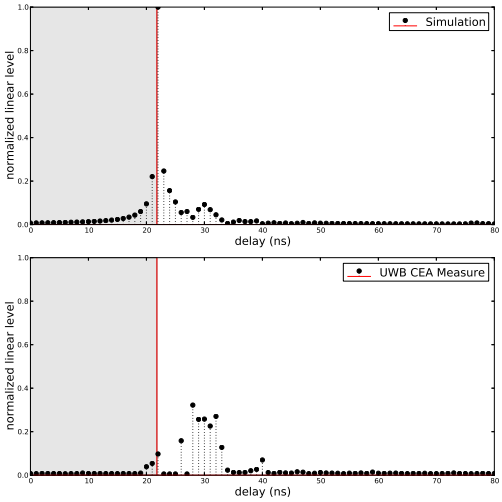

(b) Conf. 2: Channel Energy Profile Comparison

Fig. 5.13: Channel energy profile of simulations and measure. In (a) , the ground truth delay is 32.3 ns whereas the delay corresponding to the measured two way ranging is 32.8 ns. In (b) , the ground truth delay is 21.8 ns whereas the delay corresponding to the measured two way ranging is 22.17 ns. The red line separating the grey part from the white part represent the ground truth delay.

The simulated and measured channel energy profile of both situations are compared in figures 5.13a and 5.13b, with normalized power level. The normalized power level representation has been chosen due both to the uncertainty on integer-dBm conversion

and to the missing emission power level. The lack of those information prevents to obtain the correct received power in simulation. That inaccuracy is also enforced by the unknown of the transmitter and receiver antenna orientations and radiation patterns. However, as explained previously, the aim here is not so much to provide a strictly faithfull simulation of the channel, but to retrieve the main contributors of the CIR and the position of the clusters (in the sens of the Saleh-Valenzuela model [38]), both required for localization purpose.

Considering Figure 5.13a corresponding to a NLOS situation, it can be observed that the first path used to estimate the delay at 32.8ns is correctly retrieved in terms of delay in simulation. As well a second strong contribution at about 45 ns is observable on both simulation and measure. At 35 ns a strong contribution is observed on the RT simulation missing on the measurement. It is probably caused by an obstacle non described in the synthetic environment occulting that contribution. For instance, no furnitures have been taken into account in the RT simulation whereas the room involved in that configuration is a open space with several desk and computers [144]. Considering Figure 5.13b corresponding to a LOS situation, a contribution corresponding to the direct path is observed both in simulation and measurement at 21.8 ns. The level of that contribution is higher in simulation than in measurement. Contrarily, around 30 ns a second contribution is observable with a higher level in measurement than in simulation. The most probable explanation of this difference is the antenna orientation. In simulation, the main lobes of each antenna facing each other explaining the strong contribution at the exact ground truth delay. In measurement, it is likely that the main lobes of both antennas are not facing each other explaining that the direct path contribution has a lower level than the later arrived one.

5.4 Evaluation of proposed localization algorithms

This section focuses on the evaluation of the localization algorithms on the real data set. First, RGPA is evaluated for non-hybrid and hybrid cases on the whole data set. Second, the hypothesis testing method is evaluated by restricting the number of observables ToA and RSS to be compliant with the method.

5.4.1 Evaluation of the Performances of RGPA

In this section, the RGPA localization algorithm is applied on the measured data and compared to an heterogeneous ML approximation algorithm initialized with a random value [146, 96]. For that purpose, the models extracted in subsection 5.2.5 and the dataset from scenario 4.1 5.2.4.2 are considered.

Both ML and RGPA algorithms are compared with the help of Cumulative Density Functions (CDFs) of positioning error using 3 different configurations:

- Zigbee RSS (Figure 5.15b)
- IR-UWB ToA (Figure 5.15a)
- Zigbee RSS and IR-UWB ToA (Figure 5.15c)

For each of this 3 configurations, the number of observable depends on the position of the trolley. However, each available observable of a given LDP at a given position is used to perform the position estimation. Figure 5.14 shows the percentage of measures involving a given number of LDP. For instance, 30% of the estimated position have been estimated using only 4 ToAs.

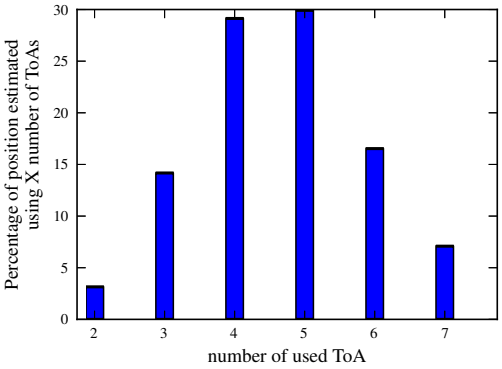

(a) Percentage of the number of ToA used

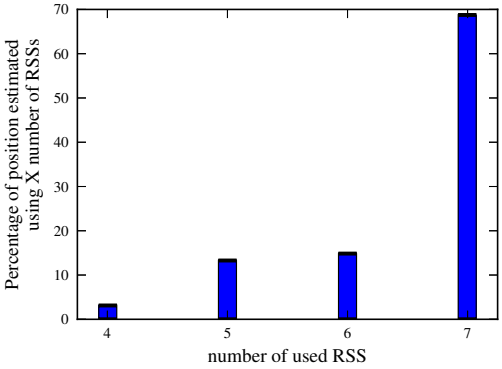

(b) Percentage of the number of RSS used

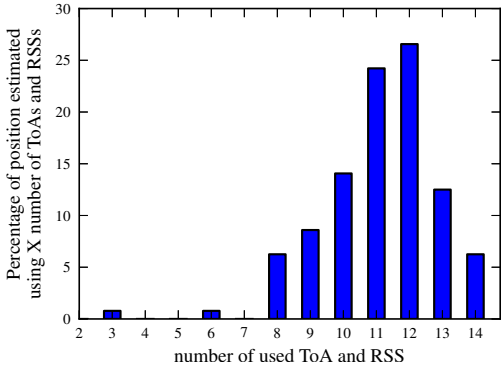

(c) Percentage of the number of ToA and RSS used

Fig. 5.14: Histograms to represent the number of LDPs used per evaluated position. for the 3 configuration involving : (a) only the ToA, (b) only the RSS or (c) the ToA and RSS. For instance, simulation involving only RSS LDPs, 15% of estimated position have been realized with 5 RSS.

Figure 5.15a represents the CDFs of positioning error for both RGPA and ML using only ToA observables. It can be observed that RGPA outperforms the ML in the regime of low errors. Thus, 90% of the positions are estimated with an error less than 3 meters using RGPA whereas the ML achieves an error less than 4 meters in that situation. However, for few estimated positions with a large error, the ML prevails on the RGPA.

On contrary, considering the comparison of CDFs of positioning error using only RSS observables on Figure 5.15b, the ML outperforms the RGPA approach. This result can be partly explained by the difficulties of RGPA to bound a RSS constraint. Indeed

as exaplained in section 3.3, the RSS constraint is built with the help of a model. That model converts a received power information into a distance which helps to limit a space region. Typically, when several RSS constraints are used, the box resulting of the merge of all RSS geometric boxes 9, bounds a large area. As a consequence, the estimation of the position can be less accurate than with a ML solution.

That trend is also confirmed in heterogeneous case where RSS are used in addition to ToA observable, as it can be observed in Figure 5.15c. If the RGPA globally outperforms the ML algorithm, it seems that it don't really take advantage of the extra RSS information. That result is confirmed by considering the summarized performances in terms of Root Mean Square Error (RMSE) and standard deviation presented in Table 5.4. It can be observed that the RGPA algorithm performs as well with or without RSS LDPs in terms of RMSE. That behavior can be explained by difficulties of RGPA to box the RSS constraints. Hence, the constraint box of the RSS observables don't help to restrict the area where the position is estimated.

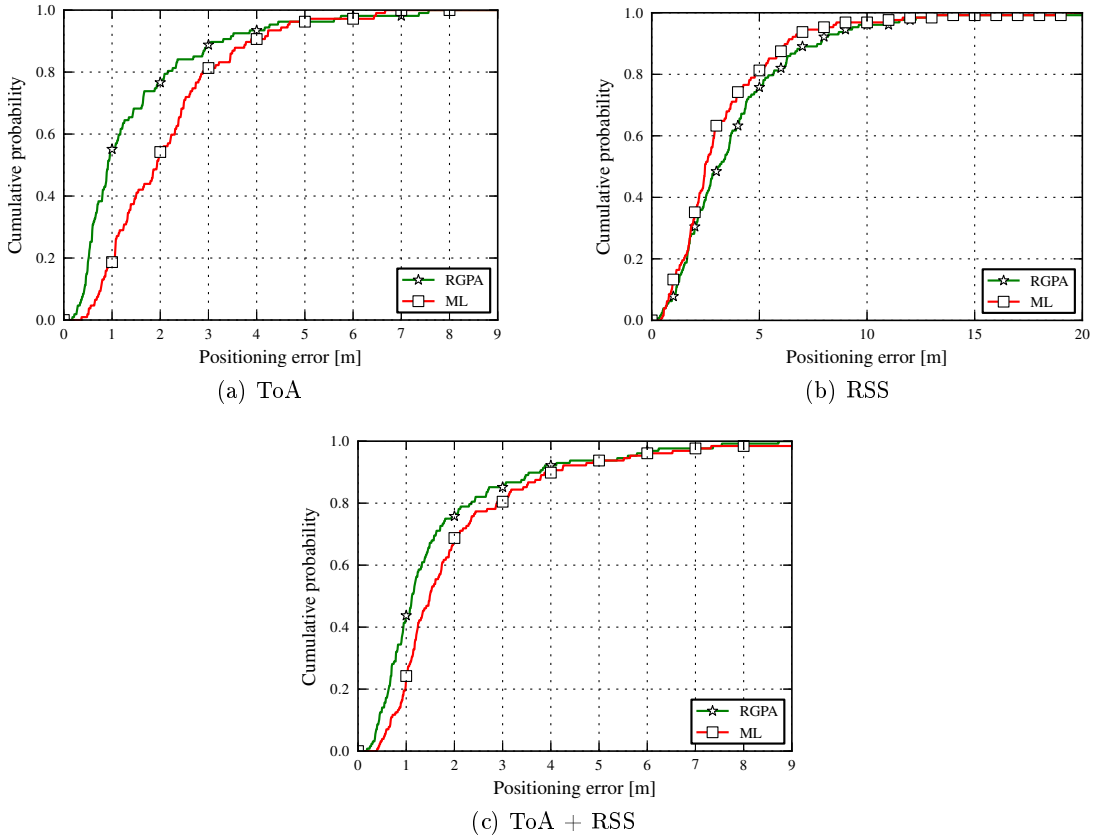

(a) ToA (b) RSS

(c) ToA + RSS

Fig. 5.15: CDFs of positioning error comparison between ML and RGPA algorithms using (a) IR-UWB ToA LDP and (b) Zigbee RSS LDP, (c) fusion of ToA and RSS LDPs.

Figure 5.16 shows the positioning error of both RGPA and ML for each position

Table 5.4: Statistical positioning error for scenario 4.1

LDPs algorithms	mean positioning error [m] ML	mean positioning error [m] RGPA	std of positioning error [m] ML	std of positioning error [m] RGPA
Zigbee RSS	3.27	4.01	2.63	2.96
UWB ToA	2.13	1.64	1.31	1.43
Zigbee RSS + UWB ToA	1.93	1.64	1.56	1.52

indexes, for the 3 considered scenarios. Both Figure 5.16a and Figure 5.16c corroborate the observation of the CDF. RGPA globally out performs the ML method, except on some points. It is noticeable that for those points RGPA commits large errors explaining the lower performances in the regime of large errors of the CDF. A further work should be required to completely determine the origin of that problem. An hypothesis would be that those large errors correspond to multimodal situation and then the position estimation would be performed on the wrong possible solution.

5.4.2 Localization based on hypothesis testing

In this section, the localization based on the hypothesis testing method presented in 3.4 is applied on the data from measurement campaign. One of the difficulties encountered in this method rely on the questionable reliability of the path loss shadowing model used for the RSS. Indeed, it has been seen, that the power information is used to decide between multi modal solutions. The quality of this decision is directly related to the quality of the model used for the power information. As mentioned before in 5.2.5.1, obtaining the parameters of a pathloss shadowing model is not an easy task due to different kind of observable variability. In those conditions, the method based on hypothesis testing has shown their limits, and has performed worst that the classic RGPA. Hence, in this section, the parameters of the path loss shadowing model have been extracted on the same scenario 4 instead of scenario 2. Assuming that point that we are now relying on a very specific and thus favorable model, the concept of the method is proven in the following.

Figure 5.17 shows a comparison between the ML method, the RGPA method and the RGPA used with the hypothesis testing method (RGPA HT). The simulation has been run on the 150 measurement points of scenario 4 using 2 ToA observables with the best GDOP and choosing the RSS observable with the highest value. All algorithms are fed with the same observables' parameters. First of all, it is noticeable that both RGPA and RGPA HT prevail on ML for positioning errors under 2 mİn that region, the RGPA HT method starts to differentiate to the RGPA from 1 mof positioning error. Indeed, it is very likely that estimated positions obtained with a precision of 1 mare obtained with the help of 2 very precise ToAs in situations where no multi modal solutions appear. For positioning error above 3 m, ML prevail or performs as well that RGPA or RGPA HT. However, RGPA HT reduces the amount of large errors compared to RGPA. That limitation of large error is also observable on Figure 5.18 comparing the positioning errors of RGPA and RGPA HT for each measurement points. The cases

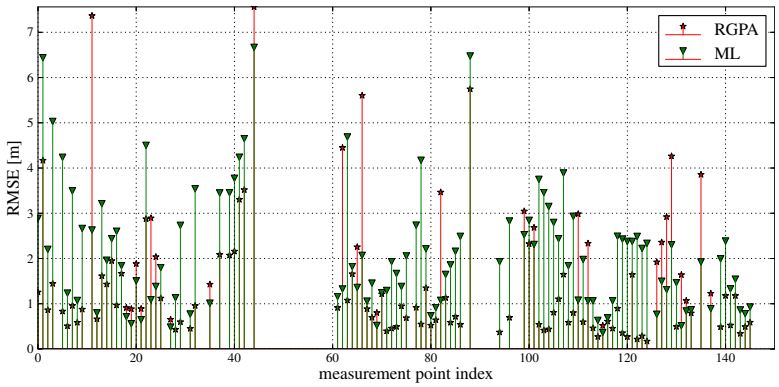

(a) ToA

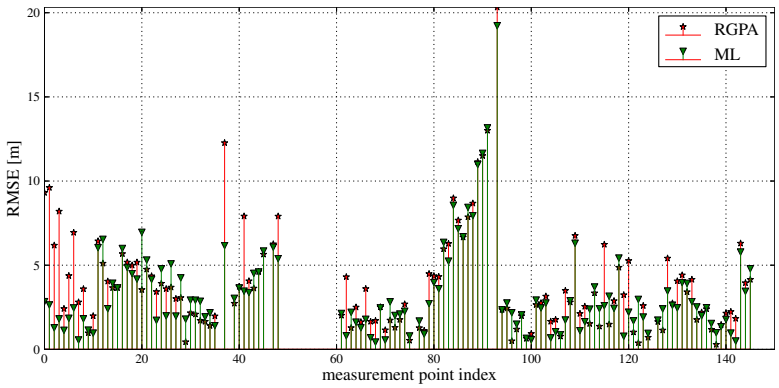

(b) RSS

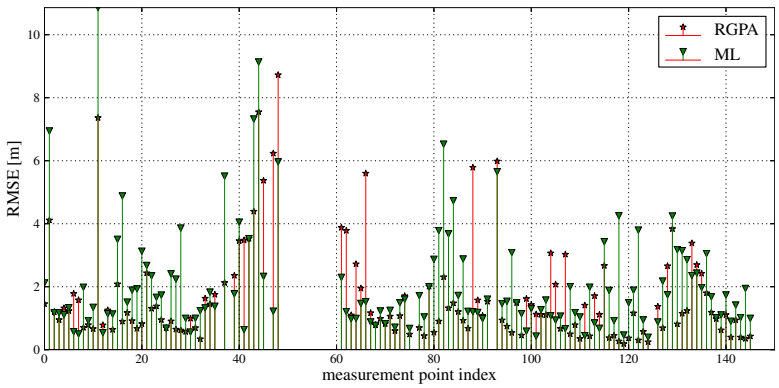

(c) ToA + RSS

Fig. 5.16: Error of positioning using RGPA or ML as a function of the measurement points for (a) IR-UWB ToA LDP and (b) Zigbee RSS LDP, (c) fusion of ToA and RSS LDPs.

where the positioning errors of RGPA HT are higher than those of RGPA correspond to a false decision on the ToA area. As it can be observed in table 5.5, the RGPA HT benefits of the ToA accuracy, providing the lower mean error of positioning compared to both RGPA and ML. It is noticeable that RGPA HT has a higher standard deviation than the positioning error than ML. This can be explained by the method itself. An error using RGPA HT corresponds to a false detection which is equivalent to select the wrong region. That wrong region can be distant from the ground truth positions and thus cause a relative high error.

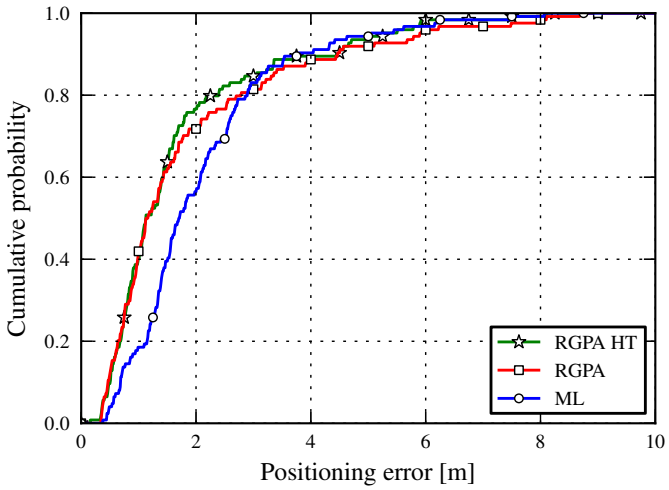

Fig. 5.17: Comparison of position estimation between ML, RGPA and RGPA with the hypothesis testing for 2 ToAs and 1 RSS. Both the ML and RGPA use the same 3 observables to perform the position estimation. RGPA with the hypothesis testing uses the RSS observable to choose between the 2 multi modal solutions that might appear.

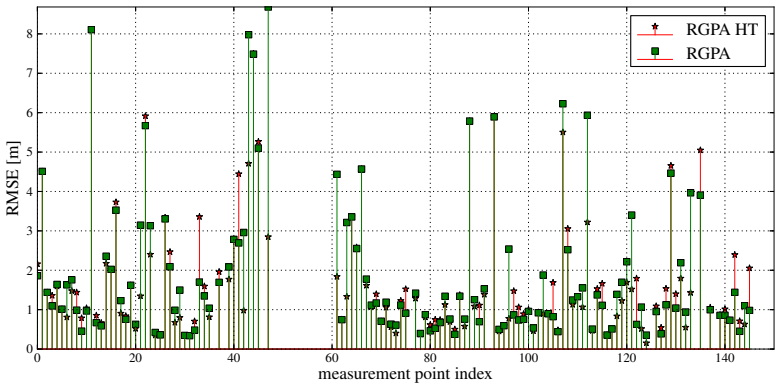

Fig. 5.18: Error of positioning using RGPA or RGPA with the hypothesis testing as a function of the measurement point.

Table 5.5: Statistical positioning error RGPA vs RGPA HT

Method	RMSE [m]	std of positioning error [m]
ML	2.10	1.98
RGPA	1.85	3.14
RGPA HT	1.70	2.36

5.5 Conclusion

This chapter has focused on the exploitation of the FP7 WHERE2 project measurement campaign. First, an accurate description of the measurement campaign has been provided including the used devices, technologies and a description of the 2 selected scenarios. A specific section has been dedicated to the radio channel parameters extraction from one of those 2 scenarios. Then, the evaluation of the multi-wall approach has been performed on the whole data set, and a comparison simulation / measurements of the ToA and RSS has been provided. Simulation have shown very promising results in regard of the incomplete knowledge of the constitutive materials used in the environment. The CIR obtained from the RT tool have also been compared to those obtained by measure. Especially, the results have shown that the RT was able to predict quite accurately the influence of multi-path contributors. Then, the RGPA has been tested on the measured data set to evaluate the accuracy in term of position estimation. In cases of RSS observables, RGPA approach has provide results little less accurate than a ML solution. This result was expected due to the actual difficulty of RGPA to manage RSS observables. In the other cases RGPA has outperformed the ML based solution. Finally, the hypothesis method has been applied on a situation where 2 ToA observable and a single RSS was available. In that situation, the method has shown its interest against a ML approach, by reducing the positioning RMSE.

Chapter 6

Conclusion

The aim of this thesis is to address the problem of the dynamic simulation of electromagnetic wave propagation in indoor environments for localization purpose. The focus has been mainly made on three aspects of the simulation: the radio wave propagation, the localization algorithms and the design of the dynamic platform. The obtained results and the reached conclusions are summarized, and future research ideas are proposed.

6.1 Conclusions

- The concept of signature has been introduced to describe the observable path persistency effect in case of differential move of transmitter or/and receiver position. A signature is a sequence of interaction and related slabs relying only on the environment topology and not on specific positions in that environment. Hence, a single signature can be used to produce multiple rays for different transmitter and receiver positions. For this reason, signatures are a natural candidate for incremental processing.
- A multiple graph description has been introduced as a core of the RT to describe both the synthetic environment and to model the relation between possible electromagnetic interactions. The graph description provides a natural framework both for the signature and for the mobility. Indeed, the specific sequence of interactions describing the signature is a specific path into a graph of interaction. As well, the different room visited by an agent in mobility are a sequence of a specific graph's nodes.
- A vectorized approach of the RT tool has been proposed to resolve the antagonist needs of speed and large bandwidth required by the simulation of mobility and UWB respectively. The proposed solution has taken advantage of the Multi Dimensional Array (MDA) structures. MDAs are extensions of matrices in high dimensions optimized for computer processing. Hence, the interactions coefficients and the entire channel can be computed for an entire frequency range in the same time. The description of those operation in high dimensions has required to introduce an adapted mathematical formalism.

- A site specific multi-wall approach has been presented taking advantage of the vectorized slab description used in the RT tool. The deterministic description of the environment is used to produce ToA and RSS observables depending on the wave polarization and incidence angle. Hence the method can be considered as a RT computation limited to the direct path ray. In addition of a very limited computation speed, the method has shown good performances in comparison with real measurements.
- RGPA, an heterogeneous localization algorithm based on interval analysis approach has been proposed. The algorithm uses the LDP values to delimit regions of Euclidean space. The intersection of those regions where lie the sought position is assimilated to the enclosing box for computational efficiency. A recursive bisection process on that box is proceed to delimit a restricted area where the position can be estimated. That restricted area can be directly related to a quality indicator of the position estimation and/or to the error variance of the estimation. In simulation and in most real cases, RGPA has outperformed a ML estimator in terms of position accuracy.
- An original method to resolve the localization in situations where only 2 accurate range observables and several power observables are available. The proposed solution use the power observables not to be part of the global localization procedure, but only to decide between the 2 potential solutions created by the 2 range observables. One advantage of the method is to conserve the high accuracy of the range observable position estimation and avoid its degradation by the less accurate power observables. The method exploit advantageously the RGPA algorithm and its intrinsic ability to determine muti modal solutions. Applied on measured data, the method has shown its interest only in the limit case where 2 range observables and a unique 1 power observable was available, reducing the mean value of positioning error compared to a ML approach.
- A dynamic platform has been introduced including 3 important aspects for the simulation of dynamic, heterogeneous and cooperative scenarios. First the realistic mobility of the agent is simulated using a discrete event simulator. The agent mobility is described at a large scale and at a small scale for determining the path to reach a destination and navigating and avoiding obstacle of the environment respectively. Second, radio parameters of each agents and the organization of the radio network is monitored by a *network graph*. A such description allow the simulation of both heterogeneous and distributed networks by managing multiple RAT per agent and by giving to each agent a restricted and self-centered vision of the global network through the so called personal network.Third, a minimal communication protocol enabling the simulation of cooperative localization schemes has been implemented. These three features have been demonstrated into a synthetic environment for an heterogeneous and cooperative localization scenario.
- The description of the dynamic platform has shown how nodes mobility can be implemented in a propagation tools and how it can be used for localization. As well, the network organization has shown how propagation tools and discrete event simulation of mobility can be linked to provide accurate LDPs. In addition, the

simple communication protocol which have been implemented allow to evaluate the performances of distributed localization algorithms. Finally, all the work presented in this thesis has been implemented, and is the core of the open source project *PyLayers* [147]. The proposed RT tool, the mobility, network and communication model and the localization algorithm described in different chapter can be use for free on the website.

6.2 Perspectives and Future Work

- The proposed vectorized RT don't benefit yet of the entire potentialities of the signature description. To access to a full incremental RT, it would be necessary to determine an algorithm to update signatures. Indeed, when the transmitter and/or the receiver move(s), several signatures remain and some disappear. There is then an interest in finding the best procedure to replace the vanished signatures by new valid ones. It requires to introduce a definition of distance between signatures.
- The current version of the vectorized RT tool do not take into account the diffraction interactions. However, all the required stages of the RT from the signature determination to the interaction evaluations are already ready to integrate the diffractions. This feature will be integrated very shortly. As well, the integration additional furnitures into synthetic environment is also considered.
- The vectorization efforts performed on the RT have allowed very satisfying speed improvement, but the vectorized approach enable naturally parallelize processing. Similarly, the bisection process of the RGPA the algorithm could also benefit of a parallelized version.
- The RGPA algorithm could advantageously be moved into a distributed an cooperative algorithm. From the distributed approach, it could be envisaged that a node computes its own position but also those of its neighbors, in order to detect potential error or bias. Open question for a cooperative approach would be on the nature of exchanged information between 2 nodes. Should the node share their boxes estimation or only their LDP and how this choice impact on the position estimation.
- The localization algorithm based on the hypothesis testing could be generalized both for situation where more that 2 multi-modal solutions appear. as well, the hypothesis test should be determined for different error model of received power or ranges.
- The mobility stage of the dynamic platform could be switched from a agent representation to a body representation, in order to address BAN problematics. In addition, a such representation would allow the influence of the position of the antenna on the body, and the influence of the body on the propagation channel. With such an evolution, the dynamic platform could become a candidate for a dynamic through-the-wall detection simulator.
- The actual slab model could be advantageously used as a stand alone application

for blind material characterization. Indeed, by coupling to real measurements and learning algorithms it should be possible to determine the different parameters of a given slab.

– Finally, the basic communication procedure implemented would benefit from taking into consideration real MAC Layer exchange protocols, notably, by interfacing with the dedicated pre-existing WSNET tool [127].

Chapter 7

Résumé en Français

7.1 Introduction

Depuis ces 10 dernières années le monde des communications sans fil rencontre de nombreux défis. Parmi eux, l'un des plus importants est de trouver des solutions permettant d'assumer une croissance exponentielle de la demande en terme de données tout en réduisant la consommation énergétique. Afin de résoudre ces deux demandes antagonistes, les différentes pistes envisagées tendent à rendre les réseaux sans fil plus adaptatifs à leurs environnements et aux ressources spectrales disponibles, en particulier avec les techniques de radio intelligentes ou de réseaux auto organisés. Pour y parvenir, l'une des conditions nécessaires est la connaissance de la position des terminaux.

En effet, l'information de position, qui a longtemps été une valeur ajoutée à destination des utilisateurs, pourrait devenir un atout pour les opérateurs téléphoniques. Ainsi la connaissance de la position des terminaux permettrait à l'opérateur d'optimiser son réseau en terme de débit et de consommation énergétique. Cette utilisation de la position dans le domaine des télécommunications fait d'ailleurs l'objet de nombreuses recherches, notamment au niveau Européen avec les projets FP7 WHERE1 (2007-2010) et FP7 WHERE2 (2010-2013). Au regard de ces différentes recherches, il apparaît entre autres que l'actuelle organisation centralisée des réseaux de communication pourrait être remise en question. En effet, la multiplication du nombre de terminaux mobiles, du nombre de standards disponibles sur un même terminal et la connaissance des informations de localisations ouvrent la voie aux réseaux distribués.

Présumant que les futurs réseaux sans fils seront basés sur une architecture distribuée et hétérogène (regroupant différents standards), et que l'information de position sera probablement une des clés pour cette évolution, il est nécessaire dès maintenant d'envisager les méthodes et les algorithmes optimisés pour ces évolutions. À défaut de pouvoir valider ces méthodes sur des systèmes réels, il est nécessaire de construire les simulateurs permettant d'adresser ces nouvelles problématiques. Pour ce faire, il est nécessaire d'accomplir plusieurs tâches simultanément. Tout d'abord, afin d'être compatible avec les futurs standards dont les fréquences et la largeur de la bande sont en perpétuelles augmentations, un tel simulateur doit permettre de réaliser des simulations

pour des systèmes ultra large bande afin d'accompagner leurs évolutions prévisibles. Ensuite, la multiplication des terminaux sans fil est principalement liée à leur aspect mobile. Ainsi, la mobilité est une variable importante à prendre en compte dans un simulateur. Cet aspect de la simulation pose toutefois deux défis majeurs: créer un modèle de mobilité réaliste afin de produire des observables simulés en rapport avec la réalité, intégrer la mobilité comme un paramètre à part entière de la simulation. Finalement, la constitution des réseaux distribués est conditionnée par la capacité qu'ont les nœuds de ce réseau à pouvoir communiquer entre eux. La difficulté ici n'est pas tant la communication en tant que telle mais les stratégies à mettre en place pour que cette communication soit optimisée. Or cette question n'étant pas encore tranchée par la communauté scientifique, il est nécessaire de créer un simulateur permettant d'explorer et d'évaluer les différentes options possibles.

L'un des objectifs principaux de cette thèse est de construire une plate-forme de simulation permettant de répondre à toutes ces interrogations. La construction d'une telle plate-forme de simulation nécessite de s'intéresser à la modélisation de la propagation, à l'analyse des déplacement des humains dans un environnement intérieur, et aux problématiques de localisation. Cette thèse propose ainsi de relier la propagation et la mobilité, la mobilité aux algorithmes et les algorithmes à la propagation par l'intermédiaire d'un unique outil de simulation.

Plan du document

Ce document est divisé en 4 chapitres. Les 3 premiers chapitres 7.2,7.3 et 7.4 adressent un point spécifique de la plate-forme de simulation (propagation, localisation, simulation dynamique). Chacun de ces 3 chapitres contient une description du point abordé ainsi qu'une partie validation. La dernière section 7.5 est dédiée à la validation des différentes méthodes sur des données réelles issues d'une campagne de mesure.

Le premier chapitre 7.2 présente un outil de tracé de rayon vectorisé, basé sur une description de l'environnement à l'aide graphe. Tout d'abord, les différents graphes utilisés pour la modélisation de l'environnement sont présentés. Ces graphes sont à l'origine de l'introduction du concept de signature, permettant la description des composantes statiques du canal. De ces signatures les rayons 2D puis 3D sont obtenus. Une fois les rayons obtenus l'obtention du canal de propagation et de transmission à partir des rayons est décrite à l'aide d'un formalisme vectorisé s'appuyant sur des structures de Multi Dimensional Arrays (MDAs). Cette vectorisation permet également l'introduction d'un modèle multiwall en dernière partie de ce chapitre.

Le second chapitre 7.3 propose 2 algorithmes de localisation en milieu intérieur. Tout d'abord, une méthode de localisation basée sur des méthodes de calcul d'analyse d'intervalles est décrite. Cette méthode appelée RGPA est ensuite validée en simulation et comparée à d'autres approches de type ML. Dans une seconde partie, l'algorithme de RGPA est mis à profit pour exploiter une méthode de localisation basée sur un test d'hypothèse. Cette méthode est également validée en simulation.

La troisième section 7.4 adresse 3 différents aspects de la plateforme dynamique : la mobilité, l'organisation du réseau et les communications entre nœuds. La mobilité des

agents est simulée tout d'abord à grande échelle, en utilisant les graphes pour définir les objectifs et les trajectoires des agents, puis à petite échelle en utilisant un modèle de *steering behaviors*, pour gérer le déplacement et l'évitement d'obstacles. L'organisation du réseau est modélisée à l'aide d'un graphe pour surveiller les potentiels échanges entre agents. Finalement un protocole de communication entre agents minimal est introduit. Ces trois aspects sont ensuite testés dans une partie simulation.

La dernière section 7.5 s'intéresse à la validation des algorithmes en utilisant des données issues d'une campagne de mesure du projet FP7 WHERE2. Les observables radio issus du multiwall et les CIR obtenus par RT sont confrontées aux mesures. De même, la précision de l'estimation de position des deux algorithmes de localisation est évaluée en utilisant les données mesurées.

7.2 Modélisation déterministe de la propagation: Une approche vectorisée basée sur les graphs

Afin de pouvoir adresser les problématiques des réseaux émergents dont la bande s'élargit à chaque montée en fréquence et dont la multiplication des terminaux n'a d'égale que leurs propensions à être mobiles, il devient nécessaire de créer des outils de simulation rapides et optimisés.

Cette partie présente un outil de tracé de rayon (Ray-Tracing (RT)) basé sur les graphes et sur une approche vectorisée du calcul de la réponse impulsionnelle du canal (Channel Impulse Response (CIR)). L'utilisation des graphes devrait permettre de répondre aux problématiques de mobilité, notamment avec l'introduction du concept de signature, qui permet de re générer rapidement des rayons dès lors que l'émetteur et/ou le récepteur ne se sont que peu déplacés. L'approche vectorisée permet quant à elle d'optimiser l'évaluation de la CIR pour une très large bande de fréquence. Enfin, la vectorisation permet également le développement d'un modèle de multiwall spécifique permettant d'accéder rapidement à des LDPs.

7.2.1 De l'utilisation des graphes dans l'outil de RT

Cette partie s'intéresse à la description de l'environnement de l'outil de RT à l'aide de graphes.

7.2.1.1 La description de l'environnement par les graphes

Afin de décrire l'environnement de simulation, 2 graphes sont nécessaires. Le graphe de structure $\mathcal{G}_s(\mathcal{V}_s, \mathcal{E}_s)$, et le graphe de topologie $\mathcal{G}_t(\mathcal{V}_t, \mathcal{E}_t)$. Le graphe de structure $\mathcal{G}_s$, dont un exemple de représentation est donné en figure 7.1a permet de modéliser les différentes parties d'un plan de bâtiments. Ainsi ses nœuds décrivent à la fois les segments et arêtes des éléments du plan. Le graphe de topologie $\mathcal{G}_t$, représenté en figure 7.1b, est construit à base des cycles de $\mathcal{G}_s$. Un cycle est défini par un chemin fermé partant et finissant d'un même nœud et qui n'emprunte qu'une seule fois les nœuds

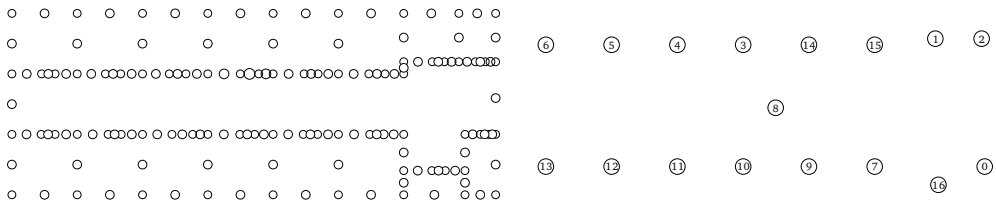

(a) Graphe de structure (b) Graphe de topologie

Fig. 7.1: Pour un même environnement, un exemple de (a) graphe de structure $\mathcal{G}_s$ et de (b) graphe de topologie $\mathcal{G}_t$.

et les liens dans le chemin. Cette représentation en cycle permet une accélération du traitement et la création d'autres graphes utiles pour la propagation.

7.2.1.2 Les Graphes pour déterminer les signatures de rayons

L'outil de RT proposé, basé sur l'optique géométrique et la théorie uniforme de la diffraction GO/UTD, repose également sur une description des graphes pour décrire la propagation des ondes électromagnétiques. Pour cela, deux nouveaux graphes sont introduits.

Le graphe de visibilité $\mathcal{G}_v$

Le graphe de visibilité $\mathcal{G}_v$ permet de décrire la visibilité optique entre les points et les arêtes du plan d'un bâtiment. Les nœuds de $\mathcal{G}_v$ sont identiques à ceux de $\mathcal{G}_s$. Les liens de $\mathcal{G}_v$ relient les nœuds (points ou segments) en visibilité optique. La figure 7.2 représente un graphe de visibilité.

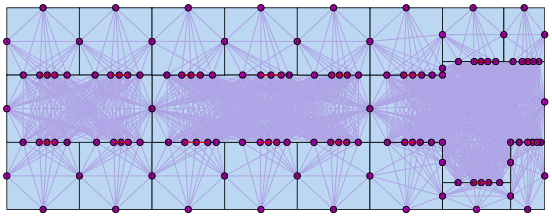

Fig. 7.2: Graphe de Visibilité $\mathcal{G}_v$

Ce graphe de visibilité est une étape intermédiaire pour déterminer un graphe d'interactions. En effet, ce graphe n'est pas suffisant d'un point de vue électromagnétique. Il n'est par exemple pas possible avec ce seul graphe de faire la distinction entre une réflexion et une transmission. Ainsi le graphe $\mathcal{G}_i$ est introduit pour lever cette ambiguïté.

Le Graphe d' interactions G_i

Le graphe d'interactions $\mathcal{G}_i$ est un graphe orienté qui rassemble toutes les interactions possibles entre les nœuds $\mathcal{V}_s$ de chaque cycle de $\mathcal{G}_t$. En pratique une interaction de $\mathcal{G}_v$ peut générer 4 interactions dans $\mathcal{G}_i$: La réflexion d'un coté et de l'autre d'un slab, et/ou la transmission dans un sens et dans l'autre d'un slab. Finalement, on considère 3 types d'interactions: la transmission (T), la réflexion (R), et la diffraction (D). La figure 7.3 illustre les différentes relations entre ces interactions du graphe $\mathcal{G}_i$.

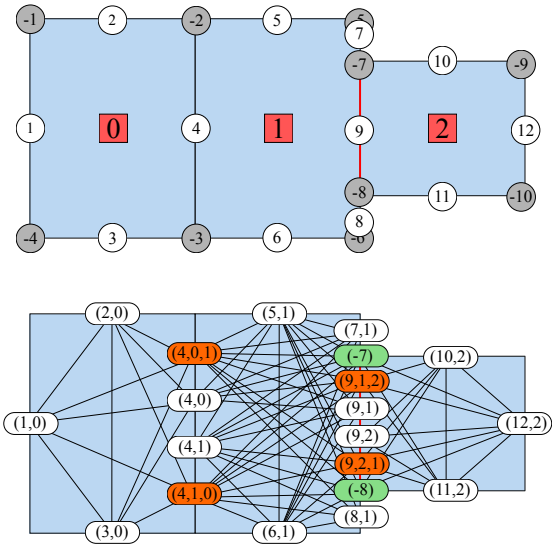

Fig. 7.3: A

u-dessus sont représentés les nœuds de $\mathcal{G}_s$ et les numéros de cycles (dans les carrés rouges) de $\mathcal{G}_t$. En dessous est représenté le graphe d'interaction $\mathcal{G}_i$ associé. Les nœuds correspondants à une réflexion sont en blancs, à une transmission sont en oranges, et à une diffraction sont en vert.

7.2.2 Des graphes aux signatures de rayons

L'introduction du concept de signature est motivée par plusieurs points. Tout d'abord, l'observation des réponses impulsionnelles de canal CIR montre qu'il existe des chemins persistants [43]. En clair, lorsqu'un terminal effectue un petit déplacement dans l'espace, les contributeurs de la réponse impulsionnelle sont globalement les mêmes qu'avant le déplacement. De plus, ces contributeurs sont influencés par la topologie de l'environnement et par sa composition (matériaux utilisés). Une signature représente un contributeur individuel de la CIR. Par extension, la partie stationnaire de la CIR est obtenue en agrégeant les différentes signatures. D'autre part, il a été montré que la modélisation stochastique du canal et plus particulièrement l'influence de la réverbération sur la CIR pouvait être modélisée à l'aide de graphes [44]. Par extension, il est conjecturé ici qu'il est possible de représenter le (ou les) contributeur(s) important(s) du canal en utilisant les graphes.

Definition 13 (Rayon 2D) *Un rayon 2D est une poly ligne dont chaque segment est délimité par une interaction ou un point dans un repère* $(O, \hat{\mathbf{x}}, \hat{\mathbf{y}})$*.Un rayon 2D* $\tilde{\mathbf{r}}$ *avec* L_h *points d'interactions est une liste ordonnée de* $L_h + 2$ *points, en considérant* $\tilde{\mathbf{p}}_{-1}$ *et* $\tilde{\mathbf{p}}_{L_h}$*, que ces points extrémaux de la liste qui représentent l'émetteur et le récepteur.*

$$\tilde{\mathbf{r}} = [\tilde{\mathbf{p}}_{-1}, \tilde{\mathbf{p}}_0, \ldots, \tilde{\mathbf{p}}_{L_h-1}, \tilde{\mathbf{p}}_{L_h}] \tag{7.1}$$

Definition 14 (Signature) *Une signature de rayon 2D (ou signature)* $\mathbf{s} = \mathcal{S}(\tilde{\mathbf{r}})$ *avec* L_h *interactions est associée à 2 séquences ordonnées de longueurs* L_h*. La première séquence est une liste indiquant le type d'interaction (R,T,D), la seconde séquence est une liste indiquant la nature de slab associé à l'interaction. Une signature peut être obtenue à partir du graphe* $\mathcal{G}_i$ *ou dérivée à partir d'un rayon.*

$$\mathbf{s} = \begin{bmatrix} n_0 & \ldots & n_l & \ldots & n_{L_h-1} \\ t_0 & \ldots & t_l & \ldots & t_{L_h-1} \end{bmatrix} \tag{7.2}$$

Les signatures sont obtenues à partir des nœuds de $\mathcal{G}_i$ en 2 étapes. Tout d'abord, on recherche les 2 cycles de départ et d'arrivée dans lesquels se trouvent respectivement l'émetteur et le récepteur. De ces 2 cycles, tous les nœuds du cycle de départ et du cycle d'arrivée sont extraits. Enfin, une recherche des chemins reliant les nœuds du cycle de départ à ceux du cycle d'arrivée est effectuée. Ces chemins sont une succession de nœuds de $\mathcal{G}_i$, où pour chacun d'entre eux il est possible d'associer un type d'interaction et la nature du slab rencontré. On obtient ainsi un ensemble de signatures, qui vont servir à l'obtention des rayons 2D.

7.2.3 Des signatures aux rayons 3D

Afin d'obtenir des rayons 3D à partir des signatures, comme illustré en figure 7.4a, 3 étapes sont nécessaires. Tout d'abord rechercher les signatures donnant des rayons 2D valides dans le plan $(O, \hat{\mathbf{x}}, \hat{\mathbf{y}})$. En effet, les signatures sont définies d'un cycle à un autre. Aussi, en fonction de la position de l'émetteur et du récepteur dans leurs pièces respectives, il est possible que certaines signatures ne génèrent pas de rayons valides. Pour déterminer ces rayons 2D une méthode à base d'images de la source et de rétro propagation de rayon est appliquée. Cette méthode consiste à vérifier que l'extrémité de la poly ligne constituant le rayon 2D ainsi que le slab associé à l'interaction s'intersectent. Tous les rayons remplissant cette condition sont considérés comme valides et sont conservés pour une étape ultérieure. La figure 7.4b illustre cette étape. Ensuite, il convient de retrouver les rayons réfléchis au sol et au plafond. Cette recherche est indépendante de la recherche précédente de rayons valides et s'effectue dans un plan virtuel $(O, \hat{\mathbf{s}}, \hat{\mathbf{y}})$ représenté en figure 7.4c. En utilisant de nouveau un procédé d'image de la source, il est possible en théorie de générer une infinité de rayons réfléchis sol et plafond. La dernière étape consiste à réconcilier les 2 ensembles de rayons trouvés dans $(O, \hat{\mathbf{x}}, \hat{\mathbf{y}})$ et dans $(O, \hat{\mathbf{s}}, \hat{\mathbf{y}})$. Pour cela, il faut déterminer dans un premier temps l'ordre d'apparition des différentes interactions (murs, sol, plafond) puis déterminer les coordonnées manquantes

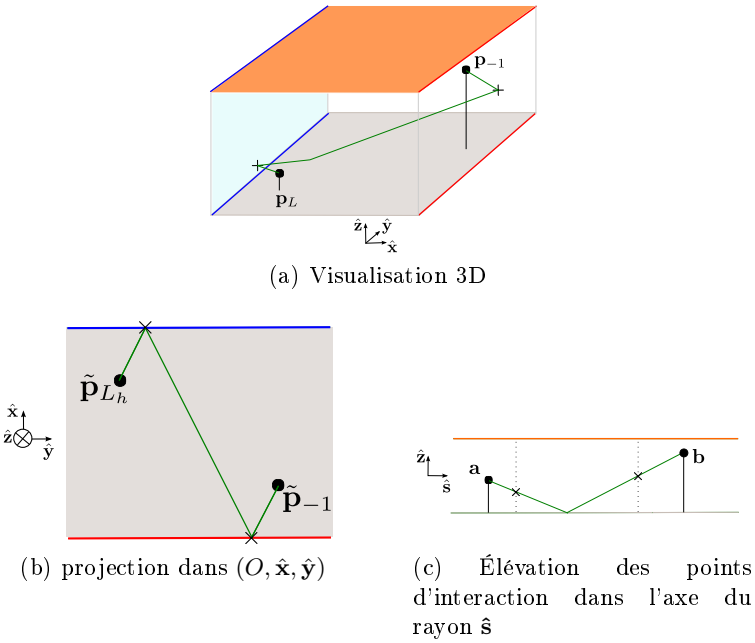

(a) Visualisation 3D

(b) projection dans $(O, \hat{\mathbf{x}}, \hat{\mathbf{y}})$

(c) Élévation des points d'interaction dans l'axe du rayon $\hat{\mathbf{s}}$

Fig. 7.4: 3 représentations du même rayon dans 3 axes différents.

de chacune d'entre elles dans $(O, \hat{\mathbf{x}}, \hat{\mathbf{y}}, \hat{\mathbf{z}})$. Pour ce faire, il est nécessaire d'utiliser une paramétrisation sur chacun des deux groupes de rayons. En effet, en paramétrant les interactions d'un rayon entre 0 et 1 dans le plan $(O, \hat{\mathbf{x}}, \hat{\mathbf{y}})$ et dans le plan $(O, \hat{\mathbf{s}}, \hat{\mathbf{y}})$, il apparaît que les deux paramétrisations générées sont comparables. Ainsi l'ordre des interactions dans $(O, \hat{\mathbf{x}}, \hat{\mathbf{y}}, \hat{\mathbf{z}})$, peux être obtenu simplement en assemblant et en classant par ordre croissant les éléments des deux paramétrisations. Une fois cet ordre retrouvé, il suffit d'appliquer de simples règles de géométrie (théorème de Thalès) afin d'obtenir les coordonnées manquantes. Finalement, on obtient un rayon 3D r définit par :

$$\mathbf{r}_r = [\mathbf{p}_{r,-1}, ..., \mathbf{p}_{r,l}, ..., \mathbf{p}_{r,L}] \tag{7.3}$$

avec les points interactions $\mathbf{p}_{r,l} = [x_{r,l}, y_{r,l}, z_{r,l}]^T$.

Extension des rayons 3D

La description d'un rayon 3D est une suite de points d'interactions. À ces différents points d'interactions, il est possible d'associer des informations supplémentaires, qui sont nécessaires pour l'évaluation future du canal de propagation. On définit tout d'abord les matrices de slab $\mathbf{M}_r$ et d'interactions $\mathbf{N}_r$, qui regroupent respectivement des informations sur la nature du slab et le type d'interaction. De même, comme illustré sur la figure 7.5, il est possible de déterminer :

– le plan d'onde incident avec ses coordonnées $\left(\hat{\mathbf{e}}_{r,l}^{i,\perp}, \hat{\mathbf{e}}_{r,l}^{i,\parallel}\right)$, arrivant sur l'interaction $\mathbf{p}_{r,l}$ transverse à $\hat{\mathbf{s}}_{r,l-1}$

– le plan d'onde sortant avec ses coordonnées $\left(\hat{\mathbf{e}}_{r,l}^{o,\perp}, \hat{\mathbf{e}}_{r,l}^{o,\parallel}\right)$ partant de $\mathbf{p}_{r,l}$ transverse à $\hat{\mathbf{s}}_{r,l}$

Ainsi, pour un rayon comptant $L+1$ interactions (où les interactions -1 et $L+1$ représentent l'émetteur et le récepteur), il est possible de créer les matrices des plans d'incidence:

$$\mathbf{B}_r^i = \left[\hat{\mathbf{e}}_{r,-1}^{i,\perp}, \hat{\mathbf{e}}_{r,-1}^{i,\parallel}, \ldots, \hat{\mathbf{e}}_{r,L-1}^{i,\perp}, \hat{\mathbf{e}}_{r,L-1}^{i,\parallel}\right] \tag{7.4}$$

de dimension $(3 \times 2L)$, et les matrices $\mathbf{B}_r^o$ des plans de sortie:

$$\mathbf{B}_r^o = \left[\hat{\mathbf{e}}_{r,0}^{o,\perp}, \hat{\mathbf{e}}_{r,0}^{o,\parallel}, \ldots, \hat{\mathbf{e}}_{r,L}^{o,\perp}, \hat{\mathbf{e}}_{r,L}^{o,\parallel}\right] \tag{7.5}$$

de dimension $(3 \times 2L)$.

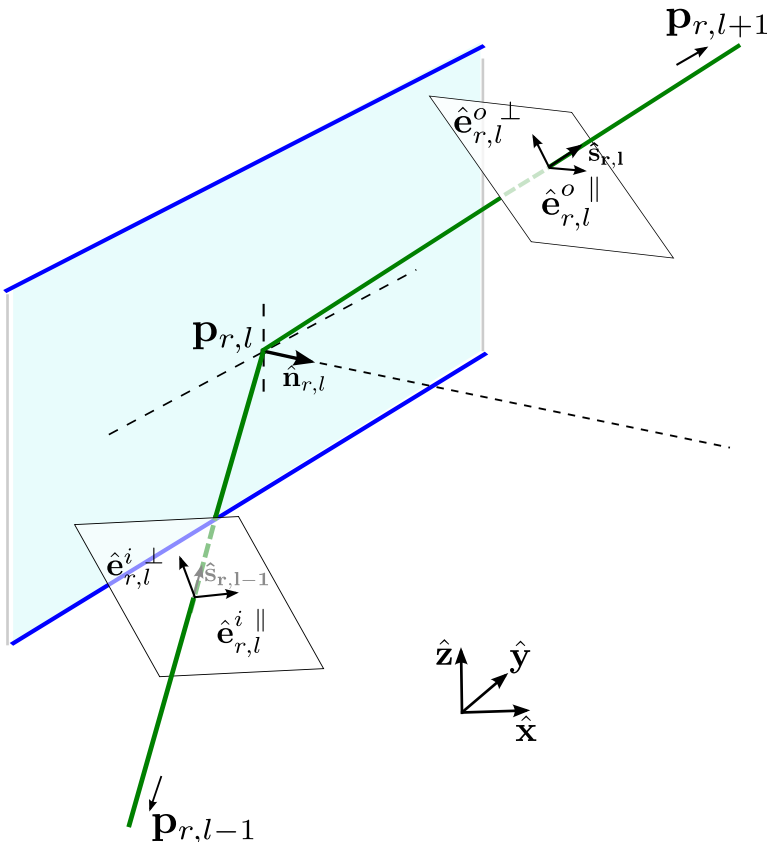

Fig. 7.5: Plan d'onde d'incidence et de sortie pour l'interaction l

7.2.4 Calcul du canal de transmission

Le calcul du canal de propagation va être effectué à l'aide de Multi Dimensional Arrays (MDAs). Les MDAs sont des structures de données multidimensionnelles permettant un calcul par ordinateur très efficace et potentiellement hautement parallélisable.

En pratique, ces MDA sont équivalentes aux `numpy ndarrays` de la librairie Numpy de Python [46]. Pour le problème du calcul du canal de transmission, les opérations vont être effectuées avec des MDA à 5 dimensions (aussi appelé axes):

- fréquence (f),
- rayon (r),
- interaction (l),
- polarisation 1 (p),
- polarisation 2 (q).

Avec de tels objets, les interactions pourront être évaluées de manière vectorielle à bas niveau pour toutes les fréquences simultanément, en évitant un bouclage de haut niveau qui serait chronophage. Les conventions de notation et les opérations sur les MDAs sont décrites dans l'annexe A.

7.2.4.1 Organisation vectorielle des données.

Pour pouvoir utiliser les MDAs il est nécessaire que les données sur les axes d'une MDA soient homogènes. Or ici, tous les rayons ont des nombres d'interactions différents, ce qui les empêchent d'être stockés directement dans des MDAs. Pour pallier ce problème, la solution retenue est d'organiser les différents rayons par nombre d'interactions. Ainsi, un rayon 3D, qui n'est autre qu'une liste de L_n interactions, est stocké dans un bloc d'interactions $\mathbf{L}_n$. Il est alors possible d'écrire une séquence $(\mathbf{L}_0, .., \mathbf{L}_n, ., \mathbf{L}_{N_{i-1}})$ de N_i blocs de rayons. Le bloc $\mathbf{L}_n$ est alors un bloc contenant R_n rayons de L_n interactions. Cette organisation des données est illustrée par un exemple figure 7.6.

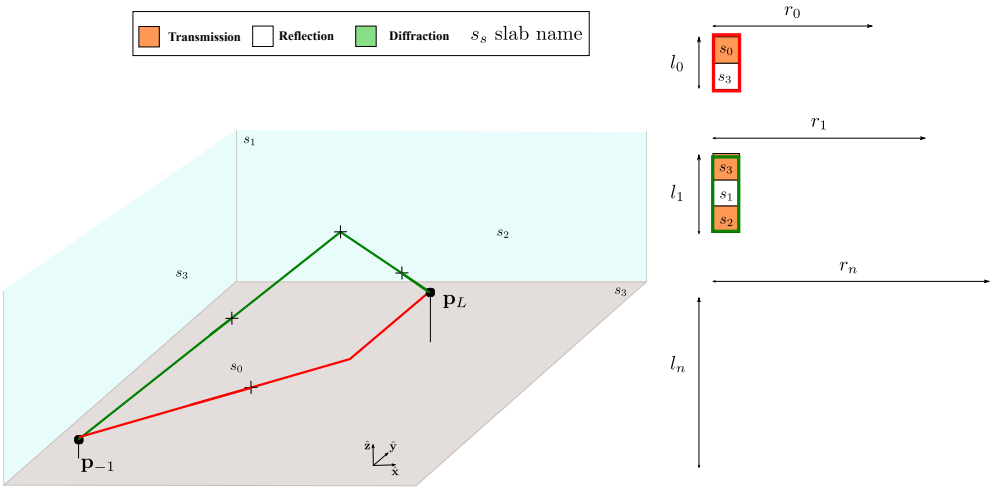

Fig. 7.6: Exemple d'organisation des données pour 2 rayons : le rayon rouge compte 2 interactions stockées dans le $\mathbf{L}_n$ bloc numéro 0. Le rayon vert compte 3 interactions et est stocké dans le $\mathbf{L}_n$ bloc numéro 1. Les autres données stockées dans les différents $\mathbf{L}_n$ blocs correspondent à des rayons non représentés sur la figure.

7.2.4.2 Évolution des matrices en MDA

Dans la partie 7.2.3, il a été vu que différents types d'informations pouvaient être extraits à partir d'un rayon 3D. En utilisant le formalisme des MDA il est tout d'abord possible d'exprimer les matrices de bases pour un $\mathbf{L}_n$ bloc n, pour tous les rayons, toutes les interactions ainsi:

$$ {}^{i}_{n}\mathbf{B}_{r,l,p,x} = \underset{(r,l,p,x)}{\text{reshape}} \left({}^{i}_{n}\mathbf{B}_{r,lp,x} \right) \tag{7.6} $$

$$ {}^{o}_{n}\mathbf{B}_{r,l,p,x} = \underset{(r,l,p,x)}{\text{reshape}} \left({}^{o}_{n}\mathbf{B}_{r,lp,x} \right) \tag{7.7} $$

. où x est un axe spatial. Ainsi, on peut également définir une MDA unitaire liant les bases d'entrée et de sortie tel que :

$$ {}_{n}\mathbf{B}_{r,l,p,q} = {}^{o}_{n}\mathbf{B}^{x,p}_{r,l} \; {}^{i}_{n}\mathbf{B}^{x,p}_{r,l} \tag{7.8} $$

De même, les matrices $\mathbf{N}_r$ et $\mathbf{M}_r$ contenant les informations de nature des slabs et de type d'interactions peuvent s'exprimer à l'aide de MDA et être ainsi écrites:

- ${}_{n}\mathbf{N}_{r,l}$,
- ${}_{n}\mathbf{M}_{r,l}$.

Ces deux dernières MDA permettent ainsi de créer une MDA d'interaction globale notée:

$$ {}_{n,i,s,a}\mathbf{A}_{r,l} \tag{7.9} $$

où i, s et a sont des paramètres de type d'interaction, de nature du slab et d'angle d'incidence liés à chacune des interactions.

7.2.4.3 Évaluation des interactions

Une première étape consiste à regrouper toutes les interactions de même type et de même nature de slabs. Pour cela, autant de MDAs que de type d'interaction et de nature de slab sont créées à partir de la MDA d'interactions complète ${}_{n,i,s,a}\mathbf{A}_{r,l}$. Cette étape, illustrée par la figure 7.7 est nécessaire, car le traitement pour chaque type d'interaction et de slab est spécifique et ne peux être effectué sur la matrice d'interactions complète.

Une fois cette répartition effectuée, chacune de ces MDAs est évaluée individuellement permettant d'obtenir les coefficients de transmissions ou de réflexions pour toutes les fréquences considérées. Toutes les MDAs ainsi évaluées sont recombinées pour recréer une MDA d'interaction complète et évaluée ${}_{n}\mathbf{A}_{f,r,l,p,q}$, comme illustré sur la figure 7.8

7.2.4.4 Canal de propagation et canal de transmission

L'évaluation des interactions ainsi faite, il est possible d'exprimer le canal de propagation proposé dans [47] à l'aide de MDA. Ainsi, le canal de propagation entre 2 points

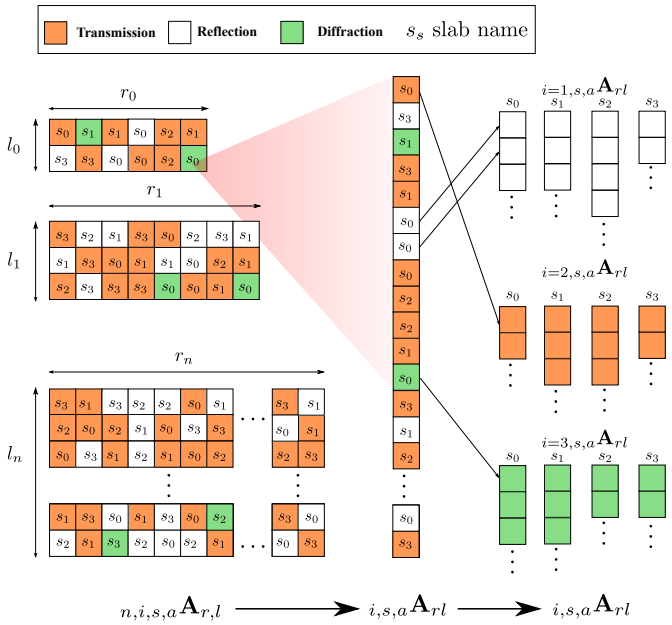

Fig. 7.7: Traitement sur la MDA d'interactions. La MDA organisée en $\mathbf{L}_n$ blocs est ensuite concaténée et réorganisée. Enfin chaque interaction est rangée par type et nature de slab.

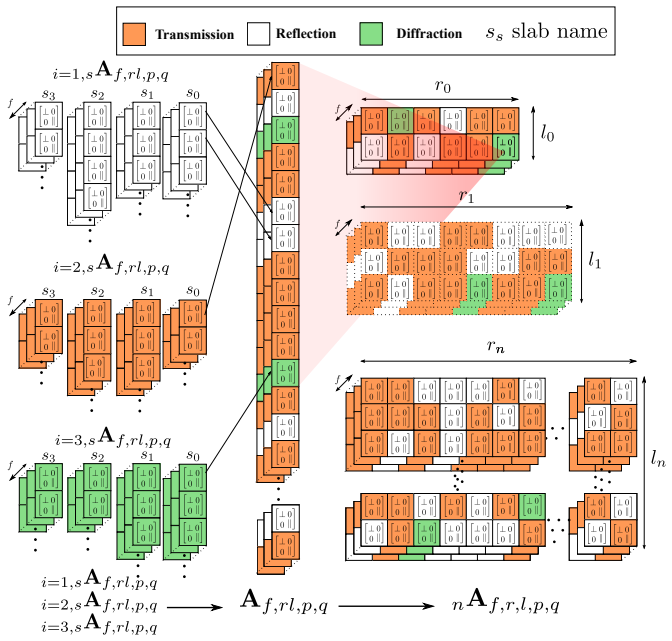

Fig. 7.8: Une fois évaluées pour chaque type et nature de slab, les MDA sont regroupées et réorganisées dans leurs formes initiales.

a et b pour un $\mathbf{L}_n$ bloc donné peut s'écrire:

$$ {}^{ab}_{n}\tilde{\mathbf{C}}_{f,r,p,q} = {}_{n}\mathbf{B}^{p,\underline{q}}_{\star,r,l[L_n]} \left[\prod_{u=l_{n-1}}^{0} {}_{n}\mathbf{A}^{p,\underline{q}}_{f,r,l[u]} \; {}_{n}\mathbf{B}^{\underline{p},q}_{\star,r,l[u]} \right] \tag{7.10} $$

Pour obtenir le canal de propagation complet ${}^{ab}\tilde{\mathbf{C}}_{f,r,p,q}$, il suffit de concaténer les $\mathbf{L}_n$ blocs le long de l'axe des r:

$$ {}^{ab}\tilde{\mathbf{C}}_{f,r,p,q} = \overset{\mid}{r}_{\mid n=0}^{N-1} \; {}^{ab}_{n}\tilde{\mathbf{C}}_{f,r,p,q} \tag{7.11} $$

Ainsi la dimension de r est $dim(r) = \sum_{n=0}^{N} n \times R_n$. Ces étapes sont illustrées par la figure 7.9

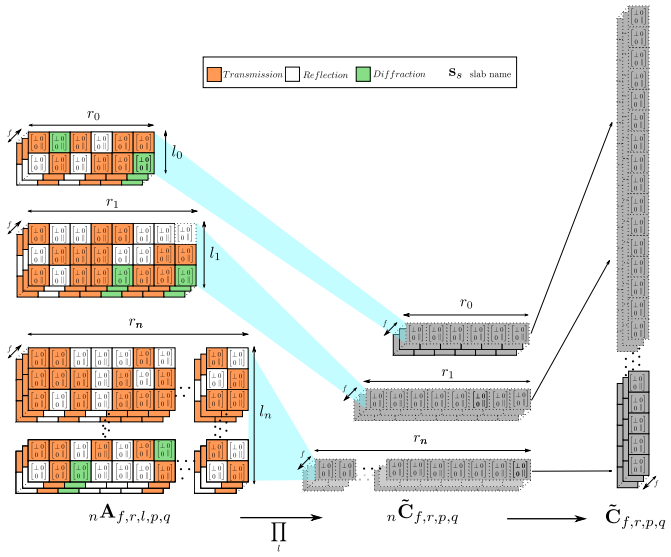

Fig. 7.9: Diagramme expliquant comment obtenir le canal de propagation ${}^{ab}\tilde{\mathbf{C}}_{f,r,p,q}$ pour toutes les fréquences des MDAs d'interactions complètes et évaluées classées en $\mathbf{L}_n$ blocs.

Le canal de transmission complet peut être obtenue grâce à

$$ {}^{ab}\mathbf{H}_{f,p,q} = {}^{ab}\boldsymbol{\gamma}_{f,p,q} \; {}^{ab}\boldsymbol{\alpha}^{\underline{r}}_{f,\star,\star} exp(-2j\pi \mathbf{f}_{f,\star,\star} \boldsymbol{\tau}^{\underline{r}}) \tag{7.12} $$

avec

$$ {}^{ab}\boldsymbol{\gamma}_{f,r,p,q} = \frac{-jc}{4\pi \mathbf{f}_{f,\star}} \left(1 - {}^{b}\mathbf{S}^{p,\underline{q}}_{f,\underline{r}}\right) \left(1 - {}^{a}\mathbf{S}^{\underline{p},q}_{\underline{f},r}\right) \tag{7.13} $$

$$ {}^{ab}\boldsymbol{\alpha}_{f,r} = {}^{b}\mathbf{F}^{\underline{p},1}_{f,r} \; ({}^{ab\ell}\tilde{\mathbf{C}}^{p,\underline{q}}_{f,r} \; {}^{a}\mathbf{F}^{p,1}_{\underline{f},r})^{\underline{p},1}_{f,r} \tag{7.14} $$

où ${}^{a}\mathbf{S}_{f,r,p,q}$ et ${}^{b}\mathbf{S}_{f,r,p,q}$ sont les paramètres S des antennes de a et b, et ${}^{a}\mathbf{F}_{f,r,p}$ et ${}^{b}\mathbf{F}_{f,r,p}$ sont des paramètres relatifs à leurs polarisations et à leurs gains.

7.2.5 Modèle MultiWall spécifique

L'utilisation de l'outil de RT permet d'obtenir des CIRs très précises pour en extraire des paramètres topo dépendants LDP. Toutefois, en fonction des applications, le calcul de la réponse impulsionnelle complète n'est pas forcément nécessaire et une estimation plus sommaire de la valeur des LDPs peut suffire. Dans ce cas, une solution est d'utiliser le modèle "multiwall" spécifique.

Le modèle "multiwall" spécifique peut être considéré comme un lancé de rayons réduit au simple trajet direct entre l'émetteur et le récepteur. Ainsi en tirant profit de la méthode d'évaluation des interactions de 7.2.4.3, il est possible d'estimer les pertes sur le trajet direct liées à la traversé des obstacles de l'environnement $\mathbf{P}_{f,p,q}$ avec :

$$\mathbf{P}_{f,p,q} = -20\log_{10} |\ {}^{e}\mathbf{A}_{f,p,q}\ | \tag{7.15}$$

où ${}^{e}\mathbf{A}_{f,p,q}$ est la matrice d'interactions complète et évaluée de toutes les interactions du trajet direct.

De même, il est possible d'évaluer l'excès de retard $\tau_c(f_f, o)$ introduit par la traversée des différents matériaux, pour une rampe de fréquence f et pour une polarisation de l'onde o:

$$\tau_c(f_f, o) = \begin{cases} \arg(\ {}^{c}\mathbf{A}_{f[f_f],p[0],q[0]}\ ), & \text{for an orthogonal polarization} \\ \arg(\ {}^{c}\mathbf{A}_{f[f_f],p[1],q[1]}\ ), & \text{for an perpendicular polarization} \end{cases} \tag{7.16}$$

avec

$${}^{c}\mathbf{A}_{f,p,q} = \prod_{l=L_i-1}^{0}{}_{i=1,s=M_l,a=\theta_l} \mathbf{A}^{l,\underline{1}}_{f,p,q}\ \exp^{(j\mathbf{d}^{l,1}_{\star,\star,\star})} \tag{7.17}$$

où M_l et θ_l sont les slabs et angles d'incidence associés à l'interaction l.

Ainsi le retard global sur trajet direct $\tau(f, o)$ est obtenu par:

$$\tau(f, o) = \tau_{LOS} + \tau_c(f, o) \tag{7.18}$$

où τ_{LOS} est le temps de propagation entre l'émetteur et le récepteur en espace libre.

7.2.6 Conclusion

Cette partie a décrit un outil de RT basé sur les graphes. En particulier, il a été introduit le concept de signature de rayon. Ce concept permet de modéliser la stationnarité de certaines composantes de la réponse impulsionnelle liées à l'environnement de simulation. Il ouvre la porte au concept de RT incrémental en évitant le recalcul intégral des rayons entre deux positions proches. Des signatures, les rayons 2D puis 3D ont été construits. Une organisation originale de ces rayons par blocs d'interactions de mêmes longueurs a permis un traitement vectorisé. En particulier, la notion de Multi Dimensional Array (MDA) a été introduite ainsi qu'une notation spécifique permettant la vectorisation complète des calculs. Utilisée à la fois pour l'évaluation des interactions et l'estimation du canal de propagation et de transmission, cette écriture permet un calcul efficace et rapide même pour une très large gamme de fréquences. Tirant toujours

avantage de cette description vectorielle, un modèle "multiwall" spécifique a été décrit pour permettre une évaluation rapide des LDP.

7.3 Localisation en milieu intérieur: Des approches robustes et hétérogènes

Le chapitre précédent a présenté un outil de RT permettant d'adresser des problèmes complexes, notamment en contexte mobilité. Une des utilisations envisagées de ce type d'outils est la validation d'algorithmes de localisation. Une première partie de ce chapitre va présenter une méthode de localisation hétérogène basée sur des techniques ensemblistes par bissections. Puis, tirant parti des possibilités offertes par de telles méthodes, et notamment la possibilité d'obtenir des solutions en cas de carence d'observables, une technique de localisation basée sur un test d'hypothèses sera présentée. Chacun des algorithmes sera validé en simulation .

7.3.1 Description de l'algorithme Robust Geometric Positioning Algorithm (RGPA)

Cette partie propose la description de l'algorithme de localisation basé sur les méthodes d'analyse d'intervalles ainsi que sa validation en simulation.

7.3.1.1 Description des contraintes géométriques

Tout comme les algorithmes de localisation algébrique classiques, tel que ceux basés sur le ML, l'algorithme de localisation géométrique RGPA utilise les différents observables radio (Time of Arrival (ToA), Time Difference of Arrival (TDoA) et Received Signal Strength (RSS)) pour estimer la position d'un terminal. Toutefois, contrairement à des algorithmes algébriques, RGPA va résoudre géométriquement le problème de localisation en limitant des zones de l'espace à l'aide des observables radios.

En assumant le fait que chaque LDP peut être associé à la fois à un nœud ancre (dont la position est connue) et à un modèle d'erreur dont les paramètres peuvent être grossièrement connus, il est possible de délimiter des régions de l'espace spécifiques pour chacun des LDPs.

Dans le cadre d'un observable de type distance r évalué entre un nœud ancre à la position $\mathbf{a} = [x_a, y_a, z_a]$ et le nœud à positionner à la position $\mathbf{b} = [x_b, y_b, z_b]$ on peut écrire:

$$r = \|\mathbf{a} - \mathbf{b}\| + \delta_r, \tag{7.19}$$

où δ_r est un terme de bruit additionnel.

Dans le cadre d'un observable de type TDoA Δ, provenant de deux nœuds ancres aux positions $\mathbf{a}$, $\mathbf{a}^{'}$ on peut écrire:

$$\Delta = \|\mathbf{a} - \mathbf{b}\| - \|\mathbf{a}^{'} - \mathbf{b}\| + \delta_\Delta, \tag{7.20}$$

où δ_Δ est un terme de bruit additionnel. Enfin, dans le cadre d'un observable de type RSS, le logarithme de la puissance reçue peut être exprimé grâce au modèle de pathloss suivant:

$$P(d) = P_0 - 10n_p \log_{10}(d), \tag{7.21}$$

où P_0 est la puissance reçue à 1 mètre et n_p est l'exposant d'affaiblissement.

D'après [94], la distance d peut être reliée à la puissance P d'une ancre à la position $\mathbf{a}$ par l'estimation suivante:

$$d = \exp(M - S^2) + \delta_P \tag{7.22}$$

avec

$$M = \frac{\log(10)(P_0 - P)}{10n_p} \tag{7.23}$$

$$S = -\frac{\log(10)\sigma_X}{10n_p} \tag{7.24}$$

où σ_X^2 est la variance de l'erreur sur la puissance reçue. Ainsi, le terme d'erreur de distance associé δ_P peut être estimé avec :

$$\delta_P = \sqrt{(1 - \exp(-S^2))\,(\exp(2M - 2S^2))} \tag{7.25}$$

En supposant que les termes d'erreurs δ_r, δ_Δ et δ_P sont Gaussiens, centrés et de variances respectives σ_r^2, σ_Δ^2 et σ_P^2, il est possible de construire les intervalles de contrainte $[I_r]$, $[I_\Delta]$ et $[I_P]$ définis par:

$$[I_r] = [r - \gamma\sigma_r, r + \gamma\sigma_r] \tag{7.26}$$

$$[I_\Delta] = [\Delta - \gamma\sigma_\Delta, \Delta + \gamma\sigma_\Delta] \tag{7.27}$$

$$[I_P] = [P(d) - \gamma\sigma_P, P(d) + \gamma\sigma_P] \tag{7.28}$$

$$\tag{7.29}$$

où γ, est un facteur d'ajustement qui, sans informations préalables, sera choisit à $\gamma = 3$ pour obtenir un intervalle de confiance de 99% .

Ainsi, chacun des LDPs donne lieu à des limitations géométriques de l'espace particulières, qui prennent la forme:

- d'un anneau en 2D (une sphère en 3D) centré sur $\mathbf{a}$ pour la contrainte de distance, et pour la contrainte de puissance RSS,
- de deux hyperboles en 2D (ou 2 hyperboloïdes de révolution en 3D) pour une contrainte TDoA.

7.3.1.2 Description de l'algorithme géométrique

L'algorithme RGPA permet d'obtenir la position d'un terminal en 5 étapes résumées dans le tableau 7.1.

Table 7.1: Description des étapes nécessaires à l'estimation de la position

1. La construction des contraintes géométriques,
2. La création de boîtes de contraintes,
3. La fusion des boîtes de contraintes,
4. L'approximation par algorithme de Kd-Tree de la région approximée,
5. L'estimation de la position dans la région approximée.

Table 7.2: Paramètres de simulation

Paramètres	Valeurs	
$\mathcal{H}_P$	$[-1,1]\times[-1,1]$	km^2
$\mathcal{H}_D$	$[-100,100]\times[-100,100]$	m^2
$\mathcal{H}_R$	$[-10,10]\times[-10,10]$	m^2
σ_r	2.97	m
σ_Δ	3.55	m
σ_X	4.34	dB
n_p	2.64	
P_0	-40	dB

La construction de contrainte géométrique a été décrite en section 7.3.1. La création de boîtes de contrainte consiste à trouver la boîte englobante associée à la contrainte géométrique. Une fois ces boîtes obtenues, on recherche leur intersection. L'intersection de ces boîtes délimite une région de l'espace contenant la position du nœud à positionner. À l'intérieur de cette région, on applique un algorithme de bissection de type Kd-Tree [95]: La région est découpée en 4 sous-régions. Les arêtes de chacune des 4 sous-régions sont testées avec chacune des contraintes géométriques. Il s'agit d'un test d'inclusion de chacune des arêtes des boîtes avec la zone de confiance de la contrainte. Si toutes les arêtes sont à l'extérieure de toutes les zones de confiances, la boîte est rejetée, si elles sont contenues par toutes les zones de confiances, la boîte est désignée comme étant englobée. Dans les autres cas, la boîte est désignée comme étant ambiguë. Le processus de bissection est répété itérativement sur les boîtes ambiguës avec un critère d'arrêt sur le nombre de boîtes ou la taille des boîtes. Finalement, l'estimation de la position est effectuée en cherchant le barycentre des boîtes.

7.3.1.3 Évaluation de l'algorithme géométrique

L'algorithme géométrique est évalué à l'aide de la méthode de Monte-Carlo. Le scénario considéré est donné en figure 7.10 et les paramètres de simulation sont donnés dans le tableau 7.2. Les différentes positions du nœud à positionner sont aléatoirement choisies dans $\mathcal{H}_R$. Ainsi, sur les Figures 7.11 (a-d), on peut observer que dans les différentes configurations, RGPA prévaut sur la méthode de ML. Toutefois, le gain apporté est plus limité avec l'utilisation d'observables de puissances, du fait de la complexité à déterminer la boîte englobante d'une contrainte RSS.

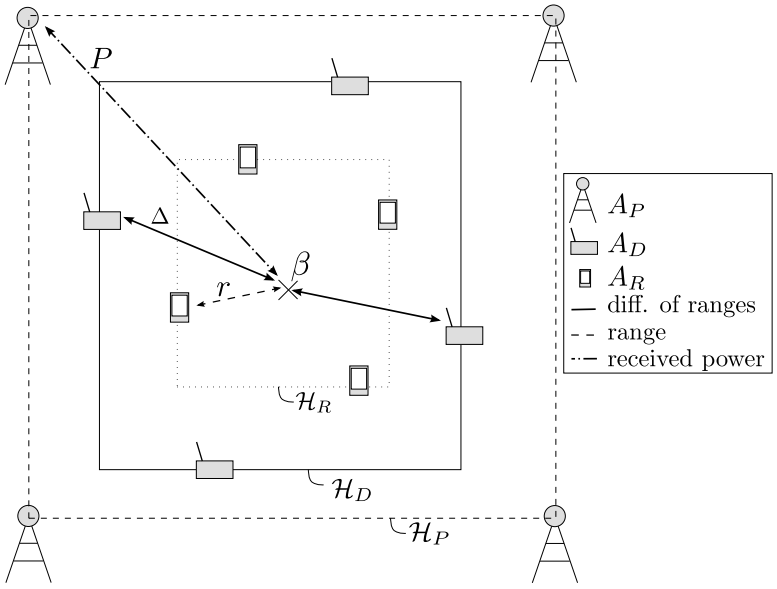

Fig. 7.10: Le nœud à positionner en position β a accès: à des observations de distances $\{r\}$ provenant des ancres aux positions $\{A_R\}$, à des TDoA $\{\Delta\}$ provenant des ancres aux positions $\{A_D\}$ et des RSS $\{P\}$ provenant des ancres aux positions $\{A_P\}$.

7.3.2 Localisation hétérogène basée sur le teste d'hypothèses

Le RGPA permet de résoudre le problème de localisation géométriquement en limitant des régions dans le plan en 2D ou dans l'espace en 3D. L'un des avantages de cette méthode de résolution est sa capacité à délimiter spatialement ces régions. De plus, quand le nombre d'observables radios est insuffisant, l'emplacement du nœud à positionner peut être ambigu. En l'occurrence, plusieurs régions discontinues aussi vraisemblables les unes que les autres peuvent apparaître. Le RGPA offre la possibilité de délimiter spatialement toutes ces régions.

D'autre part, on remarque généralement que la position estimée à partir d'observables de distances est généralement plus précise que celle obtenue par des informations de puissances. À ce titre, il est conjecturé que ces deux informations, dans le cadre de la localisation hétérogène, ne peuvent être utilisées de la même manière. La méthode basée sur le test d'hypothèse propose de tenir compte de cette dissymétrie de qualité d'information.

7.3.2.1 Description de la méthode

Le scénario de localisation hétérogène considéré est composé de 2 observables de distance et d'un certain nombre d'observables de puissances fournis par des *nœuds aidants*, comme représenté en figure 7.12. Plutôt que d'utiliser toutes ces informations sur le même plan, il est proposé une méthode de localisation en 2 étapes. Tout d'abord, obtenir 2 régions distinctes en appliquant RGPA avec les observables de distances. Puis,

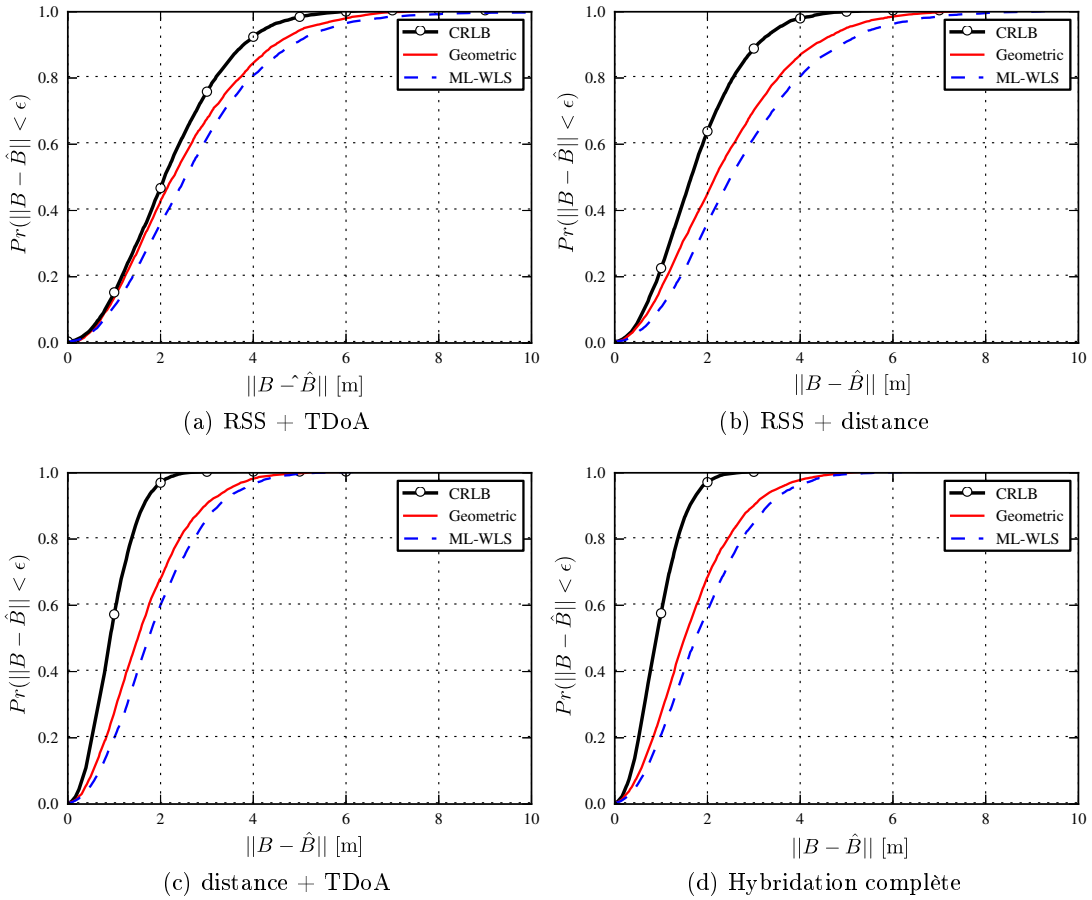

(a) RSS + TDoA (b) RSS + distance

(c) distance + TDoA (d) Hybridation complète

Fig. 7.11: CDFs d'erreur de positionnement comparant RGPA à des algorithmes de ML et de WLS.

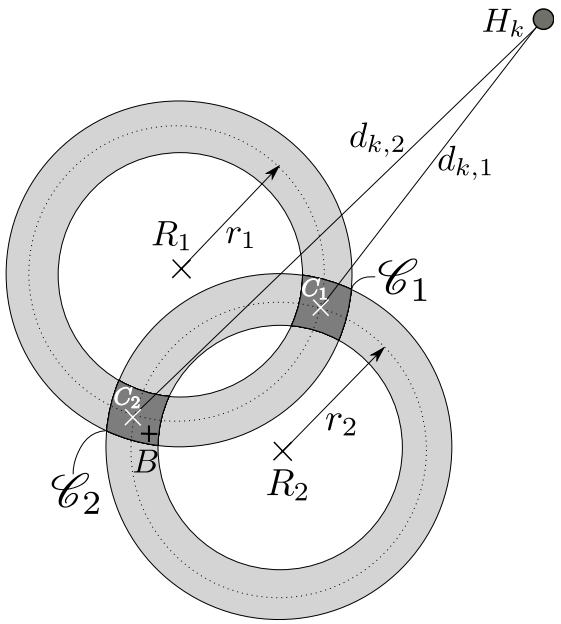

Fig. 7.12: Le nœud à positionner en position B reçoit deux observables de distances r_1 et r_2 des 2 ancres aux positions R_1 et R_2. L'erreur commise sur ces distances est modélisée par deux anneaux de confiances centrés sur R_1 et R_2. L'intersection de ces 2 anneaux génère les 2 régions grisées $\mathscr{C}_1$ et $\mathscr{C}_2$, avec leurs barycentres C_1 et C_2. De plus, le nœud à positionner reçoit des informations de log puissance des nœuds d'aide aux positions H_k. On note $d_{k,i}$ la distance entre H_k et C_i.

choisir entre ces deux régions à l'aide des observables de puissances.

En modélisant l'information de log puissance du nœud aidant k par :

$$P_k = \mu(d_k) + X_k, \tag{7.30}$$

où X_k est une variable aléatoire Gaussienne centrée et de variance σ_k, il est possible de décider entre les deux zones créées par les 2 observables de distances avec la règle de décision suivante :

$$\sum_{k=1}^{K} \frac{1}{2\sigma_k^2} \left[\mu_{k,2}^2 - \mu_{k,1}^2\right] \underset{\mathscr{C}_2}{\overset{\mathscr{C}_1}{\lessgtr}} \sum_{k=1}^{K} \frac{1}{\sigma_k} P_k(\mu_{k,1} - \mu_{k,2}). \tag{7.31}$$

7.3.2.2 Résultat de simulation

En utilisant les paramètres de simulation donnés par le tableau 7.3 et deux nœuds aidants, on obtient la CDF présentée en figure 7.13. On voit que la méthode rivalise avec un algorithme de ML dans ce cas. L'évolution du RMSE en fonction du nombre de nœuds aidants, présentés en figure 7.14, montre que la méthode à un intérêt principalement quand le nombre d'observables de puissances est limité.

Table 7.3: Paramètres de simulation

Paramètres	Valeurs	
$\mathcal{S}$	$[-20, 20] \times [-20, 20]$	m^2
$\mathcal{L}$	$[-80, 80] \times [-80, 80]$	m^2
σ_δ	0.9	m
σ_X	4	dB
n_p	3	
P_0	-40	dB

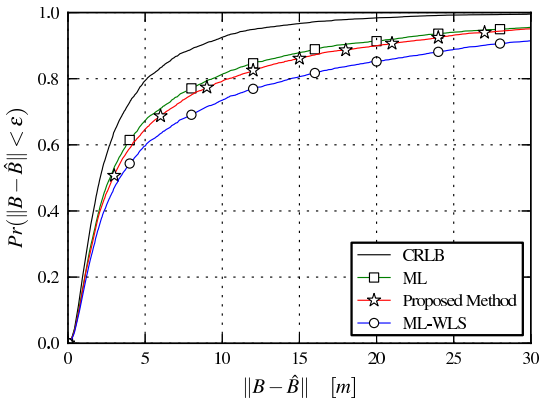

Fig. 7.13: CDF d'erreur de position avec 2 nœuds aidants.

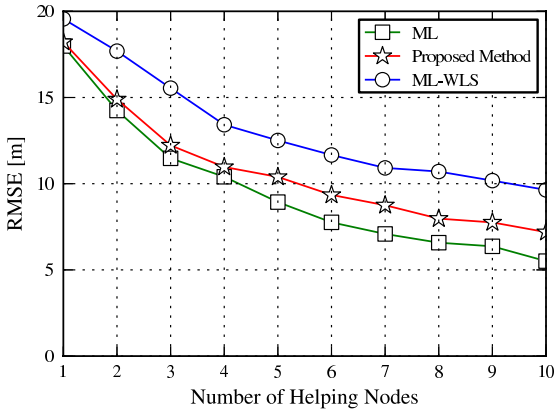

Fig. 7.14: RMSE en fonction du nombre de nœuds aidants.

7.3.3 Conclusion

Cette partie a présenté deux algorithmes de localisation: une technique de localisation hétérogène basée sur des méthodes ensemblistes (RGPA) et une méthode basée sur le test d'hypothèses. RGPA permet entre autres de délimiter spatialement des régions de l'espace satisfaisants les observables radios. La méthode a montré son intérêt en comparaison à des techniques de ML en simulation. Un des avantages de RGPA, est sa capacité à délimiter plusieurs régions disjointes notamment dans des cas de carence d'observables. Cette propriété a été mise à profit pour élaborer un algorithme basé sur un test d'hypothèses. En effet, dans un cas où, seuls deux observables de distances sont disponibles, RGPA permet l'identification des deux régions candidates contenant potentiellement le nœud à positionner. La méthode de test d'hypothèses consiste alors à choisir entre ces deux régions à l'aide d'observables de puissances. Alors qu'une approche classique, pourrait dégrader la précision apportée par les observables de distances en les fusionnant avec des observables de puissances, l'approche proposée ici la conserve. La méthode a montré qu'elle pouvait rivaliser avec un ML dans des cas ou peu d'observables de puissance sont disponibles.

7.4 La plateforme dynamique: Gérer la propagation, la communication et la mobilité des agents dans le réseau

Afin de proposer un outil de simulation pour la localisation en intérieur complet, il convient d'ajouter à la simulation de la propagation la mobilité des agents et leur capacité à communiquer entre eux. Cette section va décrire trois aspects de la plateforme de simulation: la mobilité, l'organisation des réseaux et la communication entre nœuds. Une dernière partie démontrera l'intérêt de la plateforme à travers 2 simulations: L'une axée sur l'extraction des LDPs et de la CIR, l'autre illustrant un scénario de localisation coopératif.

7.4.1 Mobilité des agents

La mobilité des agents de la plateforme dynamique est assurée par un simulateur événementiel discret. À ce titre, chaque agent gère lui même sa mobilité indépendamment des autres. La mobilité des agents est décrite en 2 étapes. Une première étape large échelle, qui s'appuie sur les graphes afin que l'agent choisisse une destination et détermine le chemin pour l'atteindre et une seconde étape petite échelle, où l'agent se déplace jusqu'à sa destination en interaction avec l'environnement.

7.4.1.1 Mobilité large échelle basée sur les graphes

Afin que les agents puissent choisir une destination et trouver un chemin pour s'y rendre, les graphes de pièces $\mathcal{G}_r$ et de chemins $\mathcal{G}_w$ sont introduits. Comme représenté sur la figure 7.15a, les nœuds du graphe $\mathcal{G}_r$ sont des pièces et si deux pièces sont adjacentes un lien est créé entre les deux nœuds respectifs. Ce graphe de pièces permet de construire

le graphe de chemin représenté en figure 7.15b. Ce graphe utilise les nœuds du graphe de pièces auxquels sont ajoutés des nœuds correspondant au centre des couloirs et des portes. Ces nœuds supplémentaires permettent de définir des objectifs intermédiaires aux agents et ainsi suivre une trajectoire plus réaliste. Les liens de ce graphe sont construits suivant deux règles:

- les nœuds associés à une pièce sont reliés aux nœuds associés aux portes de cette même pièce,
- deux nœuds associés à des portes sont reliés entre eux si les deux pièces auxquels ils appartiennent sont adjacentes.

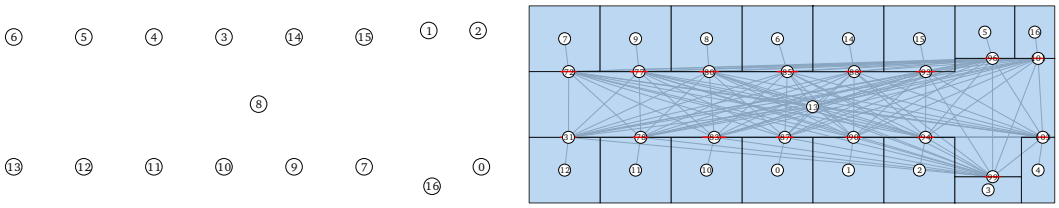

(a) (b)

Fig. 7.15: Illustration des (a) Graphe de pièces $\mathcal{G}_r$, (b) Graphe de chemins $\mathcal{G}_w$.

Pour déterminer son trajet, l'agent détermine tout d'abord la pièce dans laquelle il se trouve puis la pièce où il souhaite se rendre. Ces deux pièces correspondent à deux nœuds de $\mathcal{G}_r$. le trajet est alors obtenu en utilisant un algorithme de plus court chemin, de type Djikstra [133], entre les deux nœuds. L'algorithme retourne un ensemble de nœuds de $\mathcal{G}_w$ constituant des objectifs intermédiaires pour atteindre sa destination. Tous les objectifs intermédiaires sont parcourus itérativement par l'agent à l'aide du modèle de forces virtuelles basé sur les *steering behaviors*.

7.4.1.2 Mobilité petite échelle basée sur les *steering behaviors*

Le principe de *steering behaviors* a été introduit dans [120] afin de décrire les interactions d'agents avec leur environnement. Les agents sont alors assimilés à leurs centres de masses et on uniquement un attribut de poids. Le principe est de mettre en mouvement chaque agent en appliquant différentes forces sur leurs centres de masses respectifs. Ainsi, pour un agent, les différentes forces appliquées à son centre de masse sont :

- Une force qui attire l'agent vers son prochain objectif intermédiaire (déterminé en section 7.4.1.1),
- Des forces de répulsions liées à l'environnement qui éloigne l'agent des murs,
- Des forces de répulsions liées aux autres agents, pour éviter que deux agents s'entre-chocs.

La résultante de ces forces est une force qui déplace l'agent vers son objectif tout en évitant les différents obstacles. À chaque pas de temps mécanique, les valeurs des différentes forces et donc la résultante sont mises à jour afin d'assurer un mouvement réaliste.

7.4.2 L'organisation du réseau en graphe

En plus de la mobilité, il est nécessaire de simuler les connectivités potentielles entre les différents agents. Pour ce faire, un graphe de réseaux $\mathcal{G}_n$ est introduit.

$\mathcal{G}_n$ est un multigraphe orienté. Un multigraphe indique que deux nœuds peuvent être reliés par plus d'un unique lien. Ici, ces multiples liens permettent d'obtenir des informations de LDP différentes en fonction des RAT. L'utilisation d'un graphe orienté permet de rendre compte de la dissymétrie de liaison qui peut apparaître lorsqu'on considère une puissance d'émission et/ou une sensibilité de réception différente pour chacun des terminaux. Les nœuds du graphe de réseau contiennent des informations spécifiant leurs RATs, leurs puissances d'émission, ou leurs sensibilités radio. Sur les liens de $\mathcal{G}_n$ sont stockés les valeurs LDPs échangées entre les différents agents. Les valeurs des LDPs sont pour le moment calculées à l'aide du modèle multiwall décrit dans 7.2.5, et pourront l'être prochainement avec l'outil de RT.

Afin de pouvoir adresser des problèmes de localisations distribuées, le concept de réseaux personnels est introduit. Un réseau personnel est un graphe stocké dans un nœud du graphe $\mathcal{G}_n$. Il représente la vision qu'à un nœud du réseau. Ainsi il peut être vu comme une restriction du graphe $\mathcal{G}_n$ centré sur un nœud k et limité aux voisins de k partageant les mêmes RATs. La figure 7.16 illustre un réseau $\mathcal{G}_n$ ainsi que les réseaux personnels associés à chacun des nœuds.

Cette description des réseaux personnels permet de créer un espace de réservé pour chaque nœud, où il est possible de maîtriser les informations dont le nœud dispose et les informations que le nœud peut recueillir chez ses voisins. Ce dernier point est géré par l'étage de communication entre nœuds.

7.4.3 Mécanisme de communication entre les agents

Chaque agent dispose de 2 voies de communication gérées par 2 mécanismes distincts. Un mécanisme de réception, qui attend qu'une requête lui parvienne. Un mécanisme d'émission, commandé par l'étage de localisation afin d'envoyer des requêtes. Lorsqu'un agent cherche à se positionner et qu'il est en carence d'information, l'étage de localisation envoie une requête à la partie transmission de l'étage de communication. Ce dernier interroge alors le réseau personnel du nœud pour connaître les nœuds qui sont en visibilités. En fonction de la configuration définie par l'utilisateur, une requête est alors envoyée à tout ou partie des nœuds du réseau personnel. La partie réception de chacun des nœuds concernés met à jour le réseau personnel du nœud ayant effectué la demande. Le type d'informations mises à jour sont configurées par l'utilisateur du simulateur parmi, entre autres, les différents LDPs et/ou une position estimée.

7.4.4 Exemple d'utilisation du simulateur dynamique

Cette partie démontre l'utilité de la plateforme dynamique au travers de 2 exemples. Le premier s'intéresse à la production dynamique de LDPs et de CIR, le second à la localisation distribuée.

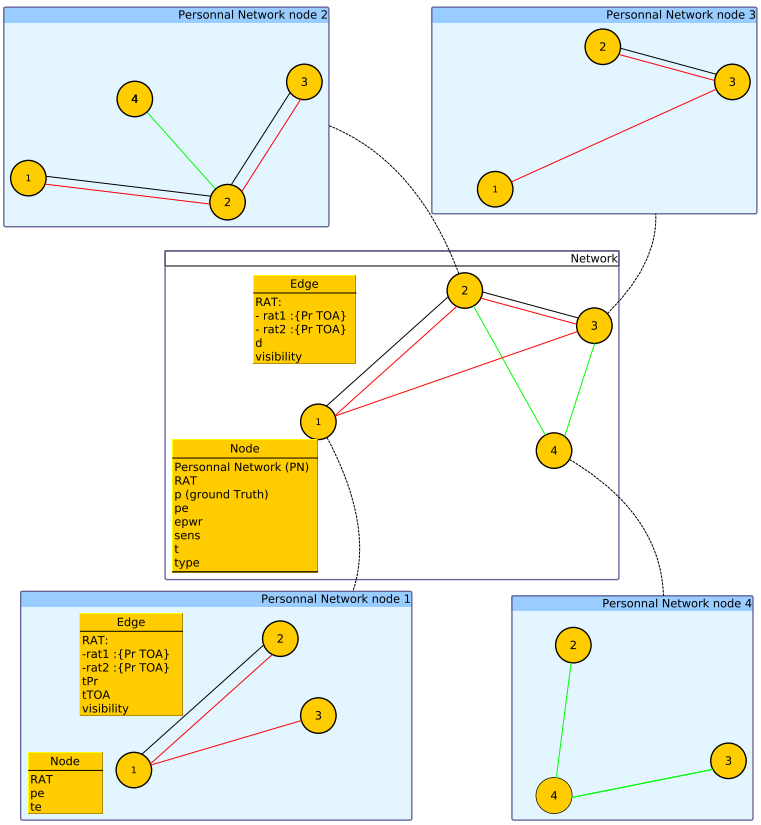

Fig. 7.16: Le graphe $\mathcal{G}_n$ et les réseaux personnels associés à chaque nœud.

7.4.4.1 Obtention des LDPs sur une trajectoire synthétique

On considère le scénario illustré en figure 7.17 où un agent se déplace dans un environnement et est en connexion potentielle avec 3 points d'accès, représentés par les triangles. La trajectoire de l'agent est représentée par les différents points rouges. Chaque point rouge correspond à un échantillon de la positon à un instant t et est séparé de 1s de son voisin. Les points rouges incluant des nombres sont des repères permettant de se figurer la direction de déplacement.

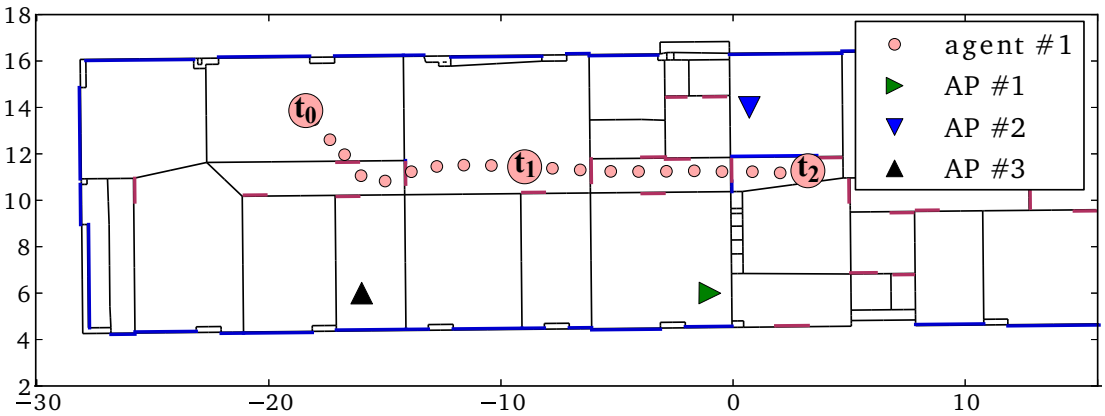

Fig. 7.17: Trajectoire d'un agent mobile en présence de 3 points d'accès statiques.

La figure 7.18, représente les différentes valeurs de ToA et RSS calculées à l'aide du modèle multiwall pour les différentes positions échantillonnées de l'agent. Les 3 graphiques représentent les différents liens entre l'agent mobile et les 3 points d'accès.

7.4.4.2 Obtention de la CIR à partir d'un trajectoire synthétique

L'implémentation de l'outil de RT ne permettant pas encore la simulation temps réel de la CIR, les données suivantes sont post-traitées. Sur la partie gauche de la figure 7.19 on observe les rayons 2D obtenus pour 6 positions différentes. Sur la partie droite sont affichées les CIRs correspondantes. L'agent se déplaçant dans la même pièce, les signatures permettant d'obtenir les rayons de la première CIR sont réutilisées pour calculer les 5 autres CIR.

7.4.4.3 Démonstration de la communication entre agents

Pour démontrer l'intérêt de la simulation de la communication entre agents, on s'intéresse au scénario illustré par la figure 7.20, où 2 agents se croisent dans un couloir. Chacun des agents, dont les différentes positions sont représentées par les points rouges et verts, peuvent communiquer sur 2 RATs, et n'ont qu'une RAT en commun. Leur seconde RAT ne leur permet de communiquer qu'avec 2 ancres (représenter par les deux triangles rouges pour le premier agent, et par les deux triangles verts pour le second agent). Chacun des nœuds essaye de se positionner à chaque rafraîchissement de la position.

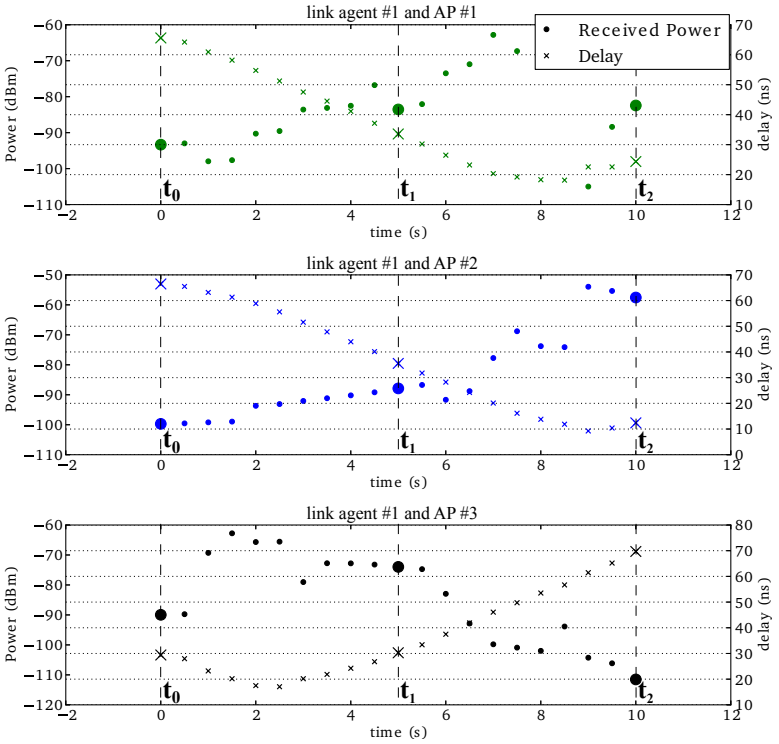

Fig. 7.18: Évolution des valeurs de puissance reçue et de ToA simulées entre l'agent mobile 3 ancres statiques. L'évaluation des LDPs est effectuée en temps réel grâce au modèle multiwall.

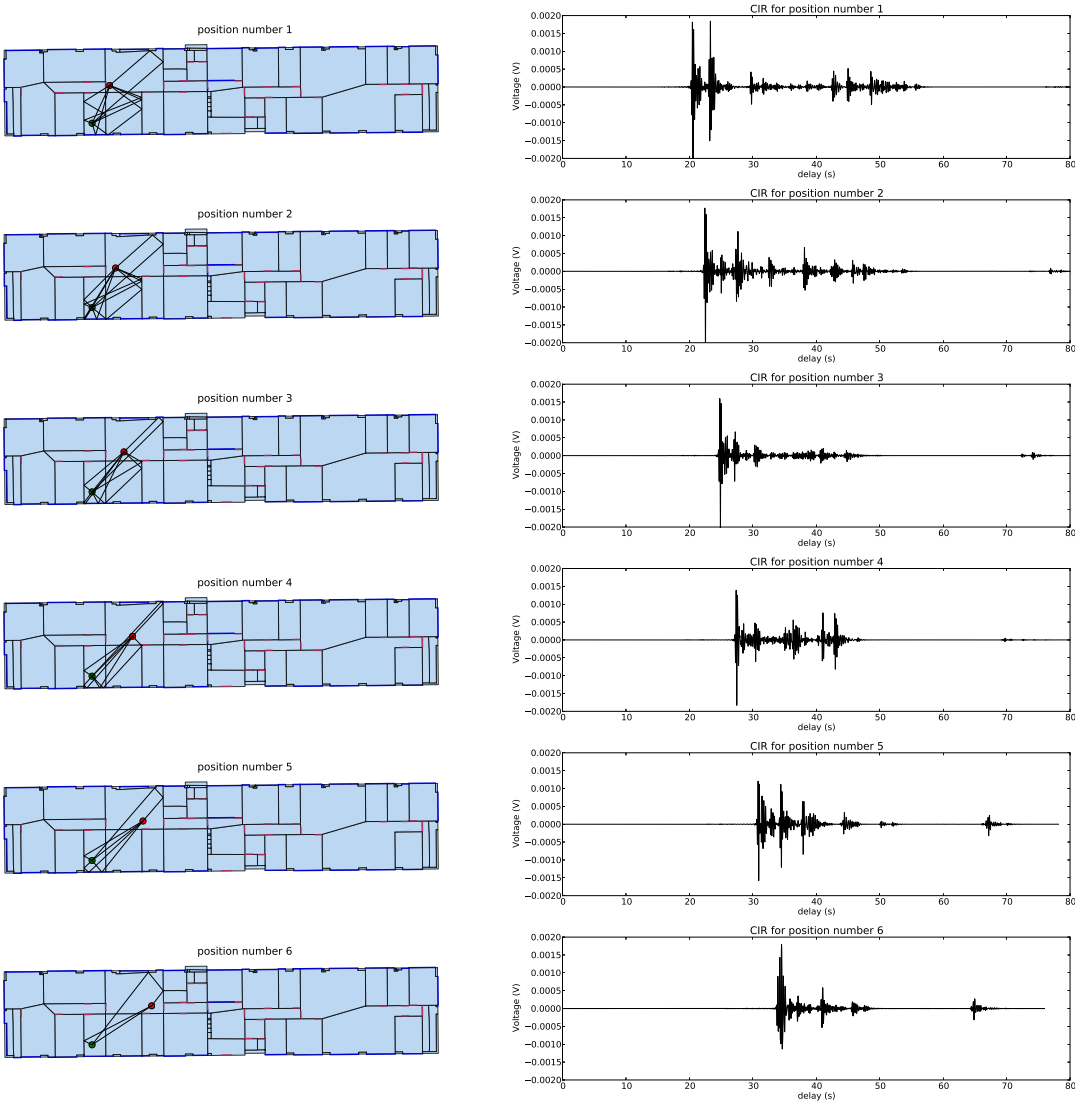

Fig. 7.19: Exemple d'obtention de CIR pour 6 positions d'agent différentes

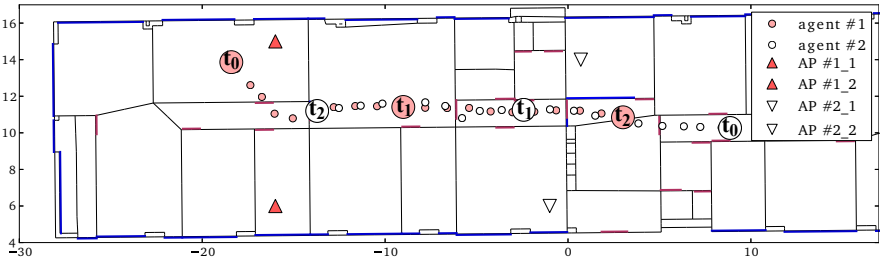

Fig. 7.20: Scenario de simulation pour illustrer l'intérêt de la communication entre agents. L'agent 1 représenté par le rond rouge ne peut se connecter qu'aux ancres représentées par les triangles rouges. L'agent 2 représenté par le rond rouge ne peut se connecter qu'aux ancres représentées par les triangles verts. Les deux agents peuvent également communiquer entre eux s'ils sont en visibilité

L'erreur de position des agents en fonction du temps de simulation est présentée en figure 7.21. Il apparaît que l'erreur de positionnement croit pour les deux agents jusqu'à 4s ou 5s, puis décroit brutalement à cet instant. Cet instant indiqué par le repère numéro 1 pour l'agent rouge, corresponds au moment où les deux agents sont en visibilités. Ils se sont alors échangé leurs estimations de positions et un ToA qui leur a permis de se positionner. Dès lors qu'ils s'éloignent l'un de l'autre, ils ne sont plus en visibilité et ne peuvent donc plus échanger d'information. L'erreur de position croit de nouveau.

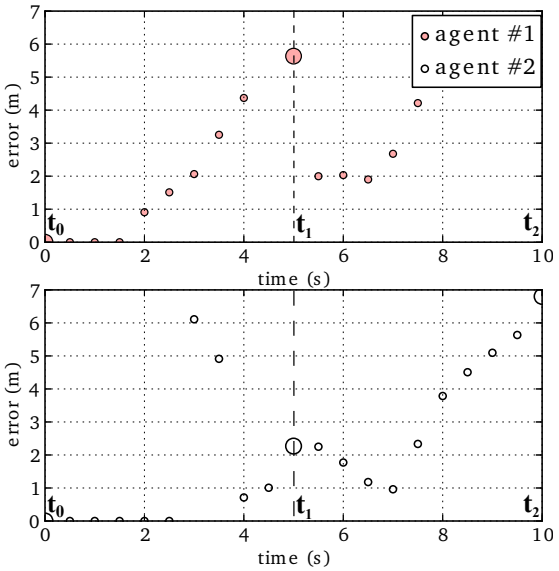

Fig. 7.21: Erreur d'estimation de la position pour les 2 agents en fonction du temps.

7.4.5 Conclusion

Cette partie s'est focalisée sur 3 différents aspects de la plateforme de simulation dynamique. Tout d'abord, la mobilité des agents a été abordée, en proposant une description de la mobilité des agents basée à la fois sur les graphes et les *steering behavior*. Ensuite, la modélisation de l'organisation des réseaux a été présentée à l'aide du graphe de réseau. Notamment, la notion de graphe personnel, simulant la vision qu'un nœud peut avoir du réseau a été introduite pour permettre des simulations de scénarios distribués. L'intérêt de cette fonctionnalité est renforcé par l'introduction d'un mécanisme de communication entre les nœuds permettant de simuler des échanges d'informations tels que des LDPs. Enfin, une dernière partie a proposé deux exemples d'utilisation de la plateforme dynamique. Un premier exemple où les LDPs d'un agent sont calculés au cours de la simulation et où des CIR sont évaluées en post-traitement. Une seconde simulation a illustré un mécanisme de positionnement coopératif, rendu possible par l'étage de communication.

7.5 Evaluation des méthodes proposées à l'aide de données mesurées

Ce chapitre propose l'évaluation des différents outils décrits précédemment en utilisant des données réelles obtenues par une campagne de mesure menée lors du projet européen FP7 WHERE2 [140].

7.5.1 Exploitation des données de mesure WHERE2

La campagne de mesure qui a été réalisée dans le cadre du projet européen FP7 WHERE2 est la première campagne de mesure publique de localisation hétérogène incluant des technologies ultra large bandes [144]. Parmi les différents scénarios réalisés au cours de cette campagne, 2 ont été retenus ici, l'un pour extraire les paramètres des modèles de LDPs, l'autre pour évaluer les algorithmes.

7.5.1.1 Extraction des paramètres de simulation

Le tableau 7.4 résume les différentes valeurs des paramètres du modèle de pathloss shadowing pour les LDP de puissance. De même, assumant un modèle Gaussien pour l'erreur des ToAs, les paramètres extraits sont donnés dans le tableau 7.5.

7.5.1.2 Comparaison des mesures avec la simulation multiwall.

Les figures 7.22 et 7.23 comparent les valeurs des RSS et ToA pour tous les points mesurés lors de la campagne de mesure aux valeurs obtenues à l'aide de la simulation multiwall. Une bonne correspondance simulation mesures peut y être observée.

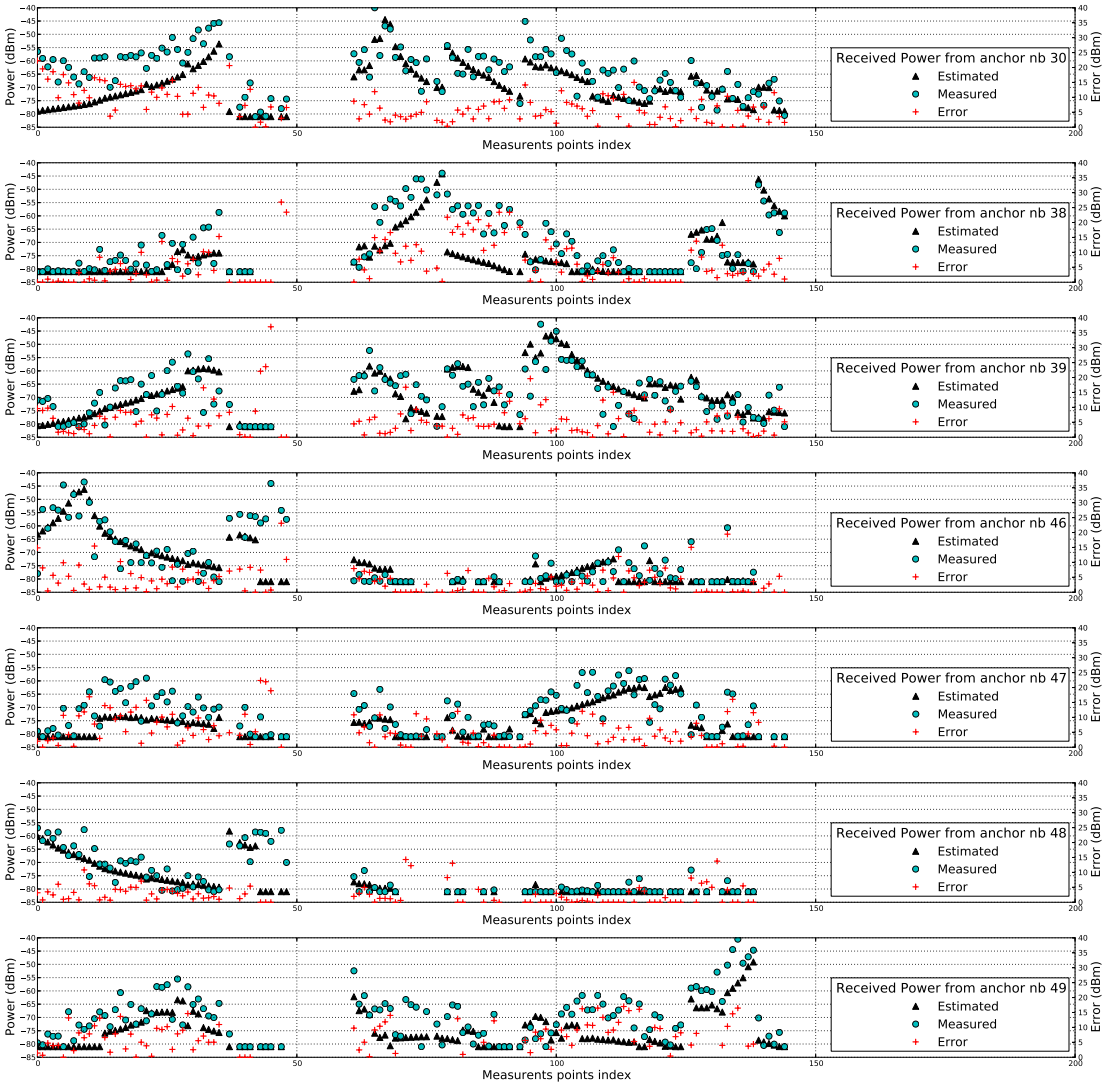

Fig. 7.22: Comparaison mesures simulations de la puissance reçue pour 7 ancres fournissant des observables RSS en fonction des différents points de mesures. Les points bleus représentent les données mesurées, les points noirs représentent les données simulées avec le multiwall, et les croix rouges représentent l'erreur.

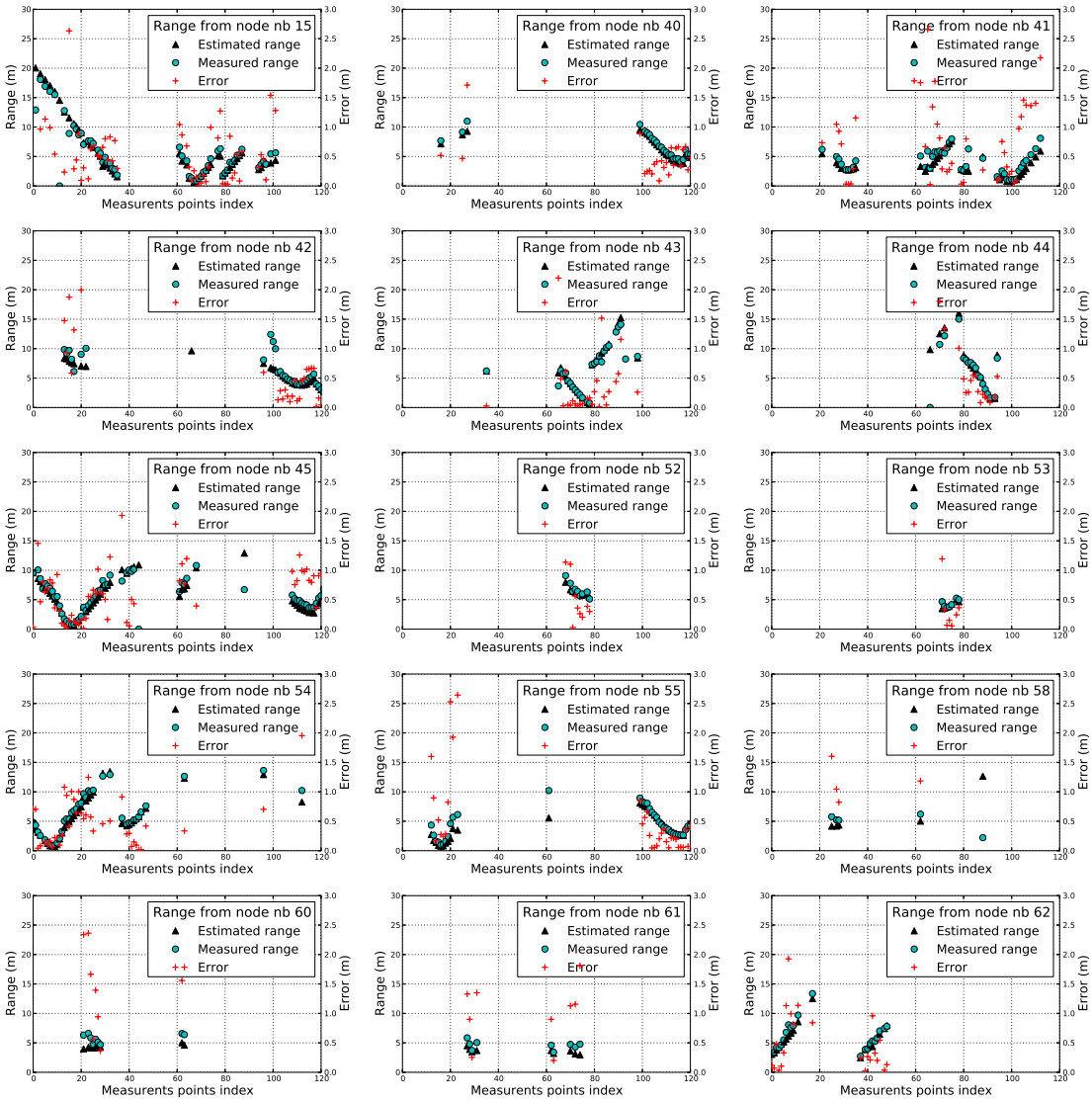

Fig. 7.23: Comparaison mesure simulation de la puissance reçue pour 15 ancres fournissant des observables ToA en fonction des différents points de mesures. Les points bleus représentent les données mesurées, les points noirs représentent les données simulées avec le multiwall, et les croix rouges représentent l'erreur.

Table 7.4: Paramètres du modèle de pathloss extrait du scenario 2.1

Numéro de nœud	RSS_0 dB	n_p	σ dB
Tous	-50.21	2.21	5.73
30	-51.38	1.16	6.85
38	-55.45	2.01	3.20
39	-47.14	2.48	5.93
46	-47.33	3.07	4.56
48	-41.62	2.95	4.98
49	-52.77	2.68	4.56

Table 7.5: Paramètres du modèle d'erreur de distance UWB extrait du scenario 2.1

Scenario	erreur de distance (m)	variance (m)
2.1	0.46	2.52

7.5.1.3 Comparaison de CIR mesurées et produites avec l'outil de RT

La figure 7.24 compare les CIRs mesurées et simulées par l'outil de RT. La comparaison montre que l'outil de RT permet de retrouver le premier trajet ainsi que les contributeurs principaux de la CIR. On observe aussi que certains trajets retrouvés par la simulation sont absents de la mesure. Cet effet est probablement dû à des occultations liées à un obstacle non représenté dans l'environnement de simulation.

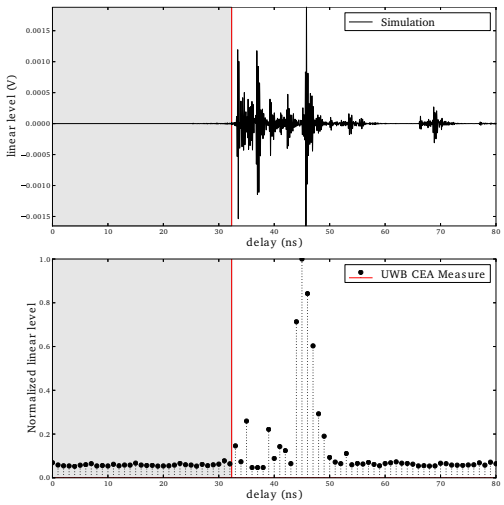

Fig. 7.24: Comparaison d'une CIR obtenue par la mesure et simulée avec l'outil de RT. Le retard réel de 21.8 ns et la valeur mesurée est de 22.17 ns. La ligne rouge représente le retard réel.

7.5.2 Évaluation des performances de l'algorithme RGPA

L'évaluation du RGPA sur les données mesurées montre que la méthode prévaut sur le ML lorsque sont utilisés des observables ToAs seuls ou associés à des observables de puissances. La méthode fournit de moins bons résultats que le ML lorsqu'on utilise uniquement des observables de puissances. Ce comportement est imputable à la complexité d'utilisation des observables RSS avec la méthode RGPA.

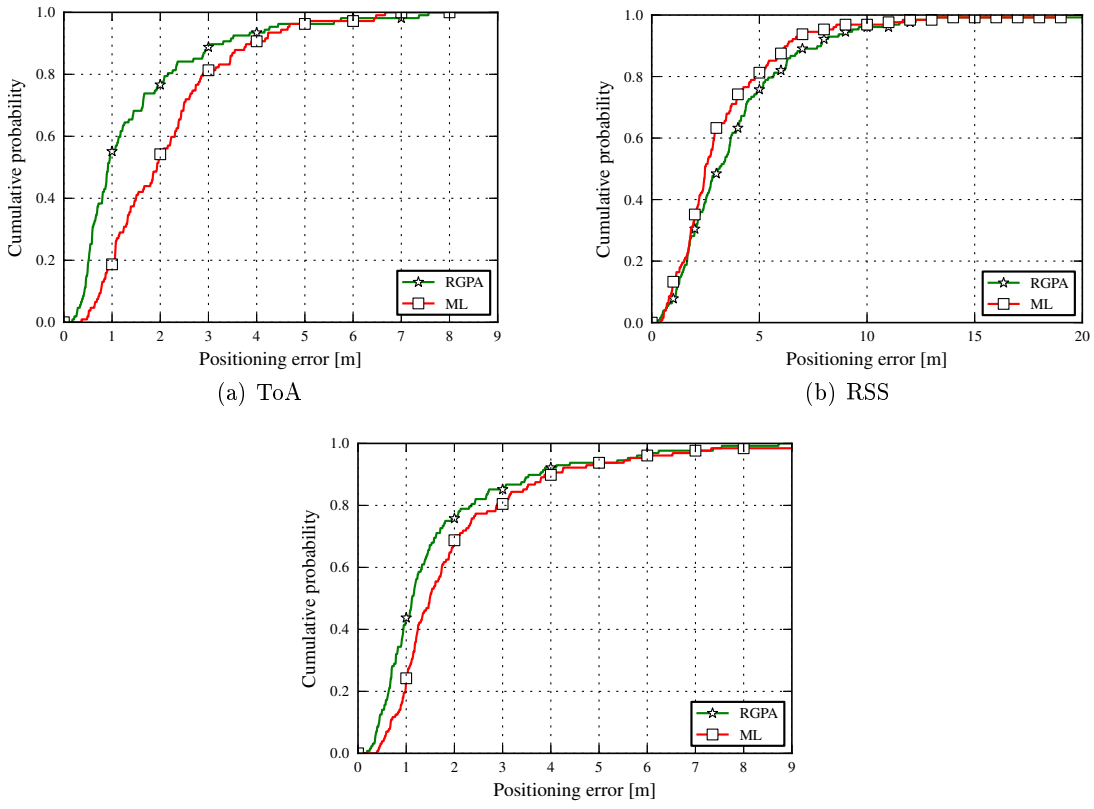

(a) ToA

(b) RSS

(c) ToA + RSS

Fig. 7.25: CDFs d'erreur de positionnement comparant RGPA au ML.

7.5.3 Évaluation de l'algorithme de localisation de test d'hypothèses

La méthode de test d'hypothèse, RGPA et une méthode de ML ont été appliquées sur un scénario comptant 2 ToA et un RSS. Les différentes valeurs de RMSE et de variances obtenues sont reportées dans le tableau 7.6. Ces résultats montrent que la méthode de test d'hypothèse permet de réduire l'erreur moyenne de positionnement. Toutefois, la variance de l'erreur obtenue avec la méthode proposée est plus importante qu'en utilisant un ML. Ceci peut s'expliquer par la nature du test de décision. Une erreur de décision correspond à un choix erroné de la zone parmi les deux délimitées

par les ToAs. Ainsi, la position choisie peut être très éloignée de la position réelle, entraînant ainsi une erreur importante.

Table 7.6: Erreur quadratique moyenne de positionnement de ML, RGPA et RGPA HT

Méthode	RMSE erreur de position [m]	variance de l'erreur de positon [m]
ML	2.10	1.98
RGPA	1.85	3.14
RGPA HT	1.70	2.36

7.5.4 Conclusion

Ce chapitre a permis de valider les différentes méthodes proposées dans les chapitres précédents avec des données issues d'une campagne de mesure. Le multiwall et l'outil de RT ont montré leurs capacités à prédire les valeurs de LDPs et à retrouver les principaux contributeurs de la CIR. Les bonnes performances de positionnement de l'algorithme RGPA observées en simulation ont été retrouvées en utilisant les données mesurées. Finalement, la méthode de localisation basée sur le test d'hypothèses a montré qu'elle pouvait réduire l'erreur quadratique moyenne de positionnement comparée à une approche de type ML.

7.6 Conclusion générale

Cette thèse avait pour but d'adresser le problème de la simulation dynamique de la propagation d'ondes électromagnétiques en intérieur, notamment pour des problématiques de localisation. Trois principaux aspects ont été abordés: la propagation des ondes, les algorithmes de localisation, et la définition d'une plateforme de simulation dynamique. Ce chapitre résume les principaux résultats obtenus et les optiques de recherches futures.

7.6.1 Conclusions

- Le concept de signature de rayon a été introduit pour décrire l'effet de persistance de chemin observable dans les CIR lors de légères variations de positions de l'émetteur ou du récepteur. La signature, définie comme une séquence d'interactions et de matériaux associés, est spécifique à la topologie de l'environnement.
- Une description sous forme de graphe de l'outil de RT a permis de modéliser l'environnement, mais également les relations entre les interactions électromagnétiques. Une telle représentation a facilité l'utilisation des signatures et la description de la mobilité.
- L'accélération engendrée par le formalisme vectorisé de l'outil de RT a permis de réaliser des simulations ultra large bande en mobilité. Ce formalisme repose sur un description en MDA.

- L'outil de multiwall a également profité de cette vectorisation et a permis d'obtenir rapidement des observables radios simulés acceptant la comparaison avec ceux obtenus en mesures.
- La méthode de localisation hétérogène RGPA a montré de très bonnes performances en simulation et sur des données mesurées comparativement à un algorithme de ML.
- Une méthode basée sur un test d'hypothèses utilisant des observables de puissance pour décider entre deux positions estimées concurrentes a été proposée. Comparée à un ML, l'utilisation de la méthode a permis de réduire l'erreur quadratique moyenne de positionnement sur des données mesurées, lorsque peu d'observables de puissances sont disponibles.
- Trois aspects de la plateforme dynamique ont été introduits: la mobilité, l'organisation du réseau et la communication entre noeuds, permettant la simulation de scénarios dynamiques, hétérogènes et coopératifs.
- Le travail de cette thèse sert de support à un projet open source *PyLayers* [147]. Ainsi, les différents outils de RT, multiwall, la plateforme dynamique et les méthodes de localisation présentés dans les différentes sections sont téléchargeables et utilisables gratuitement sur le site web.

7.6.2 Axes de recherche future

- Pour accéder à un raytracing incrémental, un algorithme permettant la mise à jour des signatures serait nécessaire. En effet, en cas de mouvement, certaines signatures sont amenées à disparaître. Un procédé permettant de remplacer les signatures disparues par de nouvelles reste à déterminer.
- La version actuelle de l'outil de raytracing vectorisé ne prend pas en compte l'évaluation des interactions de type diffraction. Toutefois ce type d'interaction devrait être très prochainement ajouté à l'évaluation du canal, puisque les différents étages de simulation sont déjà compatibles.
- Une des améliorations rendues possibles par la vectorisation de l'outil de raytracing est la possibilité d'utiliser des techniques de calcul distribué pour évaluer les différents rayons. Cette amélioration mériterait d'être implémentée afin de réduire une nouvelle fois temps de traitement de l'outil.
- RGPA pourrait être envisagé dans des scénarios de localisation coopératifs et distribués. Pour cela, la nature des données échangées reste à déterminer.
- L'algorithme de test d'hypothèses pourrait être généralisé à des situations multimodales impliquant plus de deux zones, et également être exprimé pour différents modèles d'erreurs de puissances reçues.
- Concernant la plateforme dynamique, la représentation des agents pourrait évoluer vers une représentation corporelle, afin d'adresser les problématiques de réseaux BAN. Une telle représentation permettrait l'étude poussée de l'influence du corps humain dans le canal.
- Le protocole de communication basique proposé pourrait s'enrichir notamment en implémentant des mécanismes de couche MAC. En particulier, cet étage de communication pourrait intégrer l'outil de simulation WSNET [127].

Appendix A

Multi Dimensional Array (MDA)

An MDAs is an extension of the matrix in high dimensions. This concept of MDAs is convenient to describe algebraic operations involving a large number of dimensions. Traditional mathematical notations hardly allow to express what has been implemented computationally. For that reason, this appendix introduces various notation and operations convention referring to MDA used throughout this work.

MDA is a data structure. As every data structure, it is discrete. MDAs dimensions are named axes and have a finite length. In the following the word axis is taken as a synonymous of dimension. Each new dimension is associated with a new axis. An MDA can also be shown as a `numpy.array` structure [46]. Besides, `Numpy` is a python library which provides methods for manipulating MDAs very close from mathematical tensor calculus. `Numpy` is very concise and efficient for dealing with such abstracted objects where the geometrical intuition is weak. When comes the time to write mathematically what is coded with `Numpy` surprisingly, we have observed that the tensor calculus convention as Einstein sum for example was not able to express such operation as broadcasting. The purpose of the following is to provide a concise, unambiguous, mathematical set of notations able to express what has been effectively computationally implemented.

A.1 General notation convention

In the following, a notation inspired by the Einstein notation [148] is introduced. In Einstein notation the sum operator is omitted and both superscript and lower script are used to indicate indices of coordinates to be multiplied. The superscript indices refer to column indexes whereas the lower script indices refer to row indexes. This notation is very convenient and per-formative but for operations in high dimension it would be convenient to keep track on the involved axes during the multiplication. Moreover, that notation introduces anonymous indexes as $i, j, k, ...$ which can increase the reading complexity in case of high dimensions.

For that purpose, we propose an evolution of the notation in accordance with the following rules:

1. the sum operator is implicit,
2. the right lower scripts indicate the axis names (or in case of operation the axes not directly involved in the calculus),
3. the right superscripts are used to specify the axes directly involved in operation,
4. underlined axes of the right superscript indicate the axes to be multiplied together (in replacement of Einstein anonymous variables),
5. the axis variable and the axis name share the same variable name, and explicitly indicate the nature of the axis.
6. the shape of an axis (number of elements in the given axis) does not appear in the notation and has to be pointed out elsewhere,
7. the shape of MDA is a tuple of integers which contains the length of each axis.
8. the left superscript is optionally used to discriminate MDAs,
9. the left lower script is optionally used to specify dependent parameters of the MDA

Despite right lower scripts indicate the axis names, it is possible to address a specific u^{th} element on axis j for all element on axis i of a MDA $\mathbf{A}_{i,j}$ axis with this notation:

$$\mathbf{A}_{i,j[u]} \tag{A.1}$$

A.2 Operation rules

Classically, the dot product $\mathbf{C}$ of 2 matrices $\mathbf{A}$ and $\mathbf{B}$ with dimension (I, J) and (J, K), sharing a common axis of length J, can be written as the simple sum of products:

$$c_{i,k} = \sum_{j=0}^{J-1} a_{i,j} b_{j,k} \tag{A.2}$$

where $a_{i,j}$ and $b_{j,k}$ are the elements of $\mathbf{A}$ and $\mathbf{B}$ and $c_{i,k}$ the elements of the resulting matrix product $\mathbf{C}$.

In higher dimensions, matrices are replaced by MDAs and this simple operation can be reproduced, under the condition of conformability [45]. Conformability means that 2 MDAs involved into a calculus can only have 1 axis each with a different dimension. Hence if $\mathbf{A}$ and $\mathbf{B}$ are two 5-axis MDAs with dimensions (I, V, K, L, M) and (V, J, K, L, M) respectively; it is possible to write a particular dot product relatively to compatible axis v (in position 1 and 0 respectively):

$$c_{i,j,k,l,m} = \sum_{v=0}^{V-1} a_{i,v,k,l,m} b_{v,j,k,l,m} \tag{A.3}$$

where $a_{i,v,k,l,m}$ and $b_{v,j,k,l,m}$ are the elements of $\mathbf{A}$ and $\mathbf{B}$ respectively and $c_{i,k}$ the elements of the resulting MDA product $\mathbf{C}$. Unfortunately, when a large number of compatible dimensions exists, it is possible to give a meaning to several different dot products. Then, it becomes necessary to find a way to make explicit on which axis the summation is going to be applied.

Using the convention rules described in A.1, equation (A.3) can be written:

$$\mathbf{C}_{i,j,k,l,m} = \mathbf{A}^{i,\underline{v}}_{k,l,m}\mathbf{B}^{\underline{v},j}_{k,l,m} \tag{A.4}$$

Since the axes order of $\mathbf{A}$ MDA is known, it is possible to simplify the notation by omitting the axes not involved in the calculus. Then , (A.4) becomes:

$$\mathbf{C}_{i,j,k,l,m} = \mathbf{A}^{i,\underline{v}}\mathbf{B}^{\underline{v},j} \tag{A.5}$$

Thus the MDA dot product can be read as a classical dot product between 2 matrices of dimension (I, V) and (V, J), where the operation would propagate along all the remaining axes k, l, and m. Using this notation, the dot product of a matrix and its transpose can be performed on a MDA by simply summing on the common axis:

$$\mathbf{A}_{k,l,m}\mathbf{A}^{T}_{k,l,m} = \mathbf{A}^{i,\underline{v}}_{k,l,m}\mathbf{A}^{i,\underline{v}}_{k,l,m} \tag{A.6}$$

$$\mathbf{A}^{T}_{k,l,m}\mathbf{A}_{k,l,m} = \mathbf{A}^{\underline{i},v}_{k,l,m}\mathbf{A}^{\underline{i},v}_{k,l,m} \tag{A.7}$$

In case of column or row vector, the transposition is denoted by expliciting an unitary axis. The shape of a column vector $\mathbf{A}_i$ is $(i, 1)$. The outer product of $\mathbf{A}_i$:

$$\mathbf{C}_{i,i,k,l,m} = \mathbf{A}^{i,\underline{1}}_{k,l,m}\ \mathbf{A}^{i,\underline{1}}_{k,l,m} \tag{A.8}$$

The inner product (scalar product) is

$$\mathbf{C}_{k,l,m} = \mathbf{A}^{\underline{i},1}_{k,l,m}\ \mathbf{A}^{\underline{i},1}_{k,l,m} \tag{A.9}$$

A.3 Specific Notations and Operators

A.3.1 Broadcasting

Another aspect of MDAs directly derived from Numpy Python's library [149] [46] is the broadcasting. Broadcasting allows to compute 2 MDAs who share at least one axis with the same shape.

As shown on Figure A.1, the missing axes are built from the repetition of existing axes to allow operation. Considering $\mathbf{A}_{i,j,k,l}$ and $\mathbf{B}_{j,k,l}$, it is possible to perform the dot product on axes k and l while at the same time broadcasting axis i with:

$$\mathbf{C}_{i,j,k,l} = \mathbf{A}^{k,\underline{l}}_{i,j}\ \mathbf{B}^{\underline{k},l}_{\star,j} \tag{A.10}$$

The upper script is the place where a summation is done. This notation allows to handle objects which have not the same number of axis.

The $\star$ symbol is used to indicate which axis has been broadcasted.

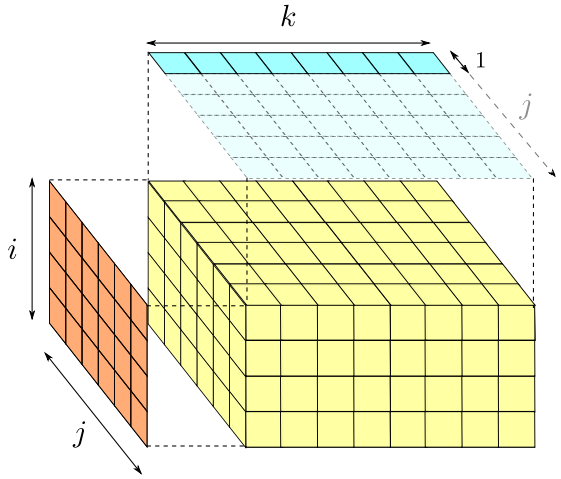

Fig. A.1: Broadcasting of 2 MDAs with shape (I, J) and $(1, K)$ respectively. Column values of the second MDA are repeated to the axis j to fit with the first MDA allowing multiplication. The shape of the resulting MDA is (I, J, K).

A.3.2 Concatenate

As well, we introduce the concatenation operator on an axis u $\Big|_u$. The concatenation is the operation consisting in stacking MDAs along a given axis. The dimension of the resulting MDA along this axis is the sum of the two others:

$$\mathbf{C}_{i,k,l,m} = \mathbf{A}_{i,k,l,m} \Big|_l \mathbf{B}_{i,k,l,m} \tag{A.11}$$

Hence if the dimension of axis l of both $\mathbf{A}_{i,k,l,m}$ and $\mathbf{B}_{i,k,l,m}$ is $dim(l) = L$, the resulting dimension on axis l of $\mathbf{C}_{i,k,l,m}$ is $dim(l) = 2L$. By extension it is possible to write:

$$\mathbf{C}_{i,k,l,m} = \Big|_{0}^{M-1} \mathbf{A}_{i,k,l,m} \tag{A.12}$$

where the resulting dimension on axis l of $\mathbf{C}_{i,k,l,m}$ is $dim(l) = M \times L$.

A.3.3 Union

The union operator $\bigcup$ allows to gather elements of a MDA together. For instance:

$$\mathbf{C}_{i,k,l,m} = \bigcup_{u=0}^{L-1} \mathbf{C}_{i,k,l[u],m} \tag{A.13}$$

if $dim(l) = L$

A.3.4 Reshape

The reshaping operator allows change the number of axis of an MDA by reallocating some dimensions:

$$\mathbf{C}_{i,k,lm} = \underset{(i,k,lm)}{\text{reshape}}\left(\mathbf{C}_{i,k,l,m}\right) \tag{A.14}$$

where the axis lm size is $\dim(lm) = \dim(l) \times \dim(m)$. By convention the reshaped axe name is a concatenation of the original axes.

A.3.5 Relation Between Matrices and MDAs for Classical Dot Product

Let's suppose 2 MDA $\mathbf{A}$,$\mathbf{B}$ with dimension (I, J),(K, L). Under the condition that the given axes are compatible, the 6 potential different permutations and their associated Python/Numpy equivalent are given by :

$$\mathbf{A}^T\mathbf{B} = \mathbf{C}_{j,l} = \mathbf{A}^{\underline{i},j}\mathbf{B}^{\underline{k},l} \tag{A.15}$$
$$\mathbf{B}^T\mathbf{A} = \mathbf{C}_{l,j} = \mathbf{B}^{\underline{k},l}\mathbf{A}^{\underline{i},j} \tag{A.16}$$
$$\iff \texttt{np.einsum('ij,ik} \rightarrow \texttt{jk',AB)} \tag{A.17}$$
$$\iff \texttt{np.sum(A[:,:,newaxis]*B[:,newaxis,:],axis=0)} \tag{A.18}$$

$$\mathbf{AB} = \mathbf{C}_{i,l} = \mathbf{A}^{i,\underline{j}}\mathbf{B}^{\underline{k},l} \tag{A.19}$$
$$\mathbf{BA} = \mathbf{C}_{k,j} = \mathbf{B}^{k,\underline{l}}\mathbf{A}^{\underline{i},j} \tag{A.20}$$
$$\iff \texttt{np.einsum('ij,jk} \rightarrow \texttt{ik',AB)} \tag{A.21}$$
$$\iff \texttt{np.sum(A[:,:,newaxis]*B[newaxis,:,:],axis=1)} \tag{A.22}$$

$$\mathbf{AB}^T = \mathbf{C}_{i,k} = \mathbf{A}^{i,\underline{j}}\mathbf{B}^{k,\underline{l}} \tag{A.23}$$
$$\mathbf{BA}^T = \mathbf{C}_{k,i} = \mathbf{B}^{k,\underline{l}}\mathbf{A}^{i,\underline{j}} \tag{A.24}$$
$$\iff \texttt{np.einsum('ik,jk} \rightarrow \text{ij',AB)} \tag{A.25}$$
$$\iff \texttt{np.sum(A[:,newaxis,:]*B[newaxis,:,:],axis=2)} \tag{A.26}$$

List of Figures

List of Tables

List of Acronyms

BAN Body Area Networks
CDF Cumulative Density Function
CIR Channel Impulse Response
CRLB Cramer-Rao Lower Bound
DES Discrete Event Simulator
FDTD Finite Difference Time Domain
GDOP Global Dilution of Precision
GO Geometrical Optics
IR-UWB Impulse Response Ultra Wide Band
LDP Location Dependent Parameter
LOS Line of Sight
MDA Multi Dimensional Array
ML Maximum Likelihood
MoM Method of Moments
MWF Multi Wall and Floor
NLOS Non Line of Sight
PDF Power Density Function
RAT Radio Access Technology
RGPA Robust Geometric Positioning Algorithm
RMSE Root Mean Square Error
RSS Received Signal Strength
RT Ray-Tracing
TDoA Time Difference of Arrival
ToA Time of Arrival
UTD Uniform Theory of Diffraction
UWB Ultra Wide Band
WLS Weighted Least Square

List of the Publications Associated with this Work

[ALU12] N. Amiot, M. Laaraiedh, and B. Uguen. Evaluation of a geometric positioning algorithm for hybrid wireless networks. *Software, Telecommunications and Computer Networks (SoftCOM), 2012 20th International Conference on*, pages 1–5, sept. 2012.

[ALU13] N. Amiot, M. Laaraiedh, and B. Uguen. PyLayers: An Open Source Dynamic Simulator for Indoor Propagation and Localization. *International Conference on Communications (ICC), IEEE*, may 2013.

[APLU12] N. Amiot, T. Pedersen, M. Laaraiedh, and B. Uguen. A Hybrid Positioning Method Based on Hypothesis Testing. *Wireless Communications Letters, IEEE*, PP(99):1–4, 2012.

[DRF+13] Benoit Denis, Ronald Raulefs, Bernard Henri Fleury, Bernard Uguen, Nicolas Amiot, Lorena De Celis, Jacobo Dominguez, Michael Koldsgaard, Mohamed Laaraiedh, Hadi Noureddine, Emanuel Staudinger, and Gerhard Steinboeck. Cooperative and Heterogeneous Indoor Localization Experiments. In *IEEE International Conference on Communications 2013: IEEE ICC'13 - Workshop on Advances in Network Localization and Navigation (ANLN) (ICC'13 - IEEE ICC'13 - Workshop ANLN)*, Budapest, Hungary, June 2013.

[LAAU11] M. Laaraiedh, N. Amiot, S. Avrillon, and B. Uguen. Theoretical performances assessment of hybrid localization techniques. *Statistical Signal Processing Workshop (SSP), 2011 IEEE*, pages 185–188, june 2011.

[NAM13] Jimmy Jessen Nielsen, Nicolas Amiot, and Tatiana K. Madsen. Directional Hidden Markov Model for Indoor Tracking of Mobile Users and Realistic Case Study. pages 1–6, 2013.

[UAL12] B. Uguen, N. Amiot, and M. Laaraiedh. Exploiting the graph description of indoor layout for ray persistency modeling in moving channel. pages 30–34, march 2012.

Bibliography

[1] Kane S. Yee. Numerical solution of initial boundary value problems involving maxwells equations in isotropic media. *IEEE Trans. Antennas and Propagation*, pages 302–307, 1966.

[2] M. Porebska, T. Kayser, and Werner Wiesbeck. Verification of a Hybrid Ray-Tracing/FDTD Model for Indoor Ultra-Wideband Channels. In *European Conference on Antenna and Propagation*, pages 169–172, 8-10 Oct. 2007.

[3] Roger F. Harrington. *Field Computation by Moment Methods*. Wiley-IEEE.

[4] Boau-Cheng W. Chang-Fa Yang. A ray-tracing method for modeling indoor wave propagation and penetration. *Antennas and Propagation, IEEE Transactions on*, 46(6):907—-919, June 1998.

[5] Zi-Liang Liu, Juan Yang, and Chang-Hong Liang. The hybrid higher-order mom-utd formulation for electromagnetic radiation problems. In *Electromagnetic Compatibility and 19th International Zurich Symposium on Electromagnetic Compatibility, 2008. APEMC 2008. Asia-Pacific Symposium on*, pages 718–721, 2008.

[6] R.G. Kouyoumjian and P.H. Pathak. A uniform geometrical theory of diffraction for an edge in a perfectly conducting surface. *Proceedings of the IEEE*, 62(11):1448–1461, Nov. 1974.

[7] J. Walfisch and Henry L. Bertoni. A theoretical model of UHF propagation in urban environments. *Antennas and Propagation, IEEE Transactions on*, 36(12):1788–1796, 1988.

[8] J-P Rossi, J.-C. Bic, A.J. Levy, Y. Gabillett, and M. Rosen. A ray launching method for radio-mobile propagation in urban area. In *Antennas and Propagation Society International Symposium, 1991. AP-S. Digest*, pages 1540–1543 vol.3, 1991.

[9] Vauzelle Rodolphe. *Un modèle de diffraction en 3D dans le premier ellipsoïde de Fresnel* . PhD thesis, Université de Poitiers, January 1994.

[10] J.F Legendre. *Etude de modèles de propagation basée sur la théorie de la diffraction.* PhD thesis, Insa de Rennes, January 1995.

[11] Seong-Cheol Kim, B.J. Jr. Guarino, T. III Willis, V. Erceg, S.J. Fortune, R.A. Valenzuela, L.W. Thomas, J. Ling, and J.D. Moore. Radio propagation measurements and prediction using three-dimensional ray tracing in urban environ-

ments at 908 MHz and 1.9 GHz. *Vehicular Technology, IEEE Transactions on*, 48(3):931–946, 1999.

[12] Gerd Wölfle, Reiner Hoppe, and Friedrich M Landstorfer. A fast and enhanced ray optical propagation model for indoor and urban scenarios, based on an intelligent preprocessing of the database. In *Proceedings of the 10th IEEE International Symposium on Personal, Indoor and Mobile Radio Communications (PIMRC)*. Citeseer, 1999.

[13] S.Y. Seidel and T.S. Rappaport. Site-specific propagation prediction for wireless in-building personal communication system design. *Vehicular Technology, IEEE Transactions on*, 43(4):879–891, Nov 1994.

[14] Chang-Fa Yang, Boau-Cheng Wu, and Chuen-Jyi Ko. A ray-tracing method for modeling indoor wave propagation and penetration. *Antennas and Propagation, IEEE Transactions on*, 46(6):907–919, 1998.

[15] E. Damosso, L.M. Correia, Information Market European Commission. DGX III Telecommunications, and of Research. *COST Action 231: Digital Mobile Radio Towards Future Generation Systems : Final Report*. EUR (series). European Commission, 1999.

[16] Volcano : Radio propagation model software. `http://www.siradel.com/1/volcano-software-suite.aspx`. Accessed: 2013-08-30.

[17] WinProp Software Suite : Wave Propagation and Radio Network Planning. `http://www.awe-communications.com/Products/`. Accessed: 2013-08-30.

[18] http://www.remcom.com/wireless-insite.

[19] Sigint Solutions : 3DTruEM. `http://www.sigintsolutions.com`. Accessed: 2013-08-30.

[20] FeritOzan Akgul and Kaveh Pahlavan. A model for spatial behavior of multipath components pertinent to indoor geolocation using ray optics. *International Journal of Wireless Information Networks*, pages 1–18, 2013.

[21] M. Heidari and Kaveh Pahlavan. Performance evaluation of indoor geolocation systems using PROPSim hardware and ray tracing software. In *Wireless Ad-Hoc Networks, 2004 International Workshop on*, pages 351–355, 31 May-3 June 2004.

[22] Kardi Teknomo. *Microscopic Pedestrian Flow Characteristics: Development of an Image Processing Data Collection and Simulation Model*. PhD thesis, Tohoku University, Japan, Sendai, 2002.

[23] S. Gezici, Z. Tian, G. B. Giannakis, H. Kobayashi, A. F. Molisch, H. V. Poor, and Z. Sahinoglu. Localization via ultra-wideband radios: a look at positioning aspects for future sensor networks. *IEEE Signal Processing Magazine*, 22(4):70–84, 2005.

[24] Paul Meissner and Klaus Witrisal. Multipath-assisted single-anchor indoor localization in an office environment. In *Systems, Signals and Image Processing (IWSSIP), 2012 19th International Conference on*, pages 22–25. IEEE, 2012.

[25] Paul Meissner, Mingming Gan, Francesco Mani, Erik Leitinger, M Froehle, C Oestges, T Zemen, and K Witrisal. On the use of ray tracing for performance

prediction of uwb indoor localization systems. In *IEEE ICC 2013 Workshop on Advances in Network Localization and Navigation (ANLN), Budapest, Hungary*, 2013.

[26] Christophe Liebe, Pierre Combeau, Alain Gaugue, Yannis Pousset, Lilian Aveneau, Rodolphe Vauzelle, and Jean-Marc Ogier. Ultra-Wideband Indoor Channel Modelling Using Ray-Tracing Software for through-the-Wall Imaging Radar. *International Journal of Antennas and Propagation*, 2010:Article ID 934602, 14 pages, June 2010.

[27] A. Toccafondi, S.M. Canta, and D. Erricolo. Recent advances in the incremental theory of diffraction for complex source point illumination. In *General Assembly and Scientific Symposium, 2011 XXXth URSI*, pages 1–4, 2011.

[28] IEEE standard for information technology - telecommunications and information exchange between systems - local and metropolitan area networks - specific requirement part 15.4: Wireless medium access control (mac) and physical layer (phy) specifications for low-rate wireless personal area networks (wpans). *IEEE 802.15.4a-2007*, October 2007.

[29] E. Karapistoli, F-N Pavlidou, I. Gragopoulos, and I. Tsetsinas. An overview of the ieee 802.15.4a standard. *Communications Magazine, IEEE*, 48(1):47–53, 2010.

[30] BeSpoon and Leti Establish World Record Distance Measurement on a Single Chip. `http://bespoon.com/tag/world-record-uwb-standalone-long-range/`. Accessed: 2013-07-16.

[31] decaWave : thinking outside the band. `http://www.decawave.com/`. Accessed: 2013-07-16.

[32] IEEE standard for local and metropolitan area networks - part 15.6: Wireless body area networks. *IEEE Std 802.15.6-2012*, February 2012.

[33] Giovanni Bellusci, G J M Janssen, Junlin Yan, and Christian C.J.M. Tiberius. A New Approach to Low Complexity UWB Indoor LOS Range Estimation. In *PIMRC 2008*, 2008.

[34] A. Goldsmith. *Wireless Communications*. Cambridge University Press, August 2005.

[35] T. S. Rappaport. *Wireless Communications: Principles and practice*. Prentice Hall, January 2002.

[36] Homayoun Hashemi. Impulse response modeling of indoor radio propagation channels. *IEEE Journal on Selected Areas in Communications*, 11(7):967–978, 1993.

[37] J.R. Foerster. The effects of multipath interference on the performance of uwb systems in an indoor wireless channel. In *Vehicular Technology Conference, 2001. VTC 2001 Spring. IEEE VTS 53rd*, volume 2, pages 1176–1180 vol.2, 2001.

[38] A. Saleh and R. Valenzuela. A statistical model for indoor multipath propagation. *IEEE J.Sel. A. Commun.*, 5(2):128–137, September 2006.

[39] Sophocles J. Orfanidis. *Electromagnetic Waves and Antennas*, chapter 8. Rutgers University, 2003.

[40] OpenStreetMap. `http://www.openstreetmap.org`. Accessed: 2013-08.

[41] R. Diestel. *Graph Theory*. Electronic library of mathematics. Springer-Verlag, 2000.

[42] Keith Paton. An algorithm for finding a fundamental set of cycles of a graph. *Commun. ACM*, 12(9):514–518, September 1969.

[43] Chia-Chin Chong, Chor-Min Tan, D.I. Laurenson, S. McLaughlin, M.A. Beach, and A.R. Nix. A novel wideband dynamic directional indoor channel model based on a Markov process. *Wireless Communications, IEEE Transactions on*, 4(4):1539–1552, 2005.

[44] T. Pedersen and B. H. Fleury. Radio Channel Modelling Using Stochastic Propagation Graphs. In *Communications, 2007. ICC '07. IEEE International Conference on*, pages 2733–2738, 24-28 June 2007.

[45] Ashu M. G. Solo. Multidimensional Matrix Algebra and Multidimensional Matrix Calculus (5 Parts). In *CSC*, pages 353–381. CSREA Press, July 2010.

[46] NumPy. `http://www.numpy.org/`. Accessed: 2013-07-16.

[47] Louis-Marie Aubert, Bernard Uguen, and Friedman Tchoffo-Talom. Deterministic simulation of MIMO-UWB transmission channel. *C. R. Physique*, 7(7), Sept. 2006.

[48] R. Burghelea, S. Avrillon, and B. Uguen. Vector spherical harmonics antenna description for ir-uwb ray tracing simulator. In *Electromagnetics in Advanced Applications, 2009. ICEAA '09. International Conference on*, pages 303–306, 2009.

[49] Lei Yu, Mohamed Laaraiedh, Stéphane Avrillon, Bernard Uguen, Julien Keignart, and Julien Stephan. Performance evaluation of threshold-based toa estimation techniques using IR-UWB indoor measurements. In *EW*, 2012.

[50] J.M Keenan and A.J Motley. Radio Coverage in Buildings. *British Telecom technology journal*, (8(1)):19–24, 1990.

[51] L. M. Correia, editor. *Wireless Flexible Personalized Communications - COST 259: European Co-operation in Mobile Radio Research*. John Wiley & Sons, 2001. COST Action 259—Final Report.

[52] M. Lott and I. Forkel. A multi-wall-and-floor model for indoor radio propagation. volume 0, Rhode Island, Greece, May 2001.

[53] Guillaume Tesserault. *Modélisation multi-fréquences du canal de propagation*. PhD thesis, University of Poitiers, December 2008.

[54] Amitangshu Pal. Localization algorithms in wireless sensor networks: Current approaches and future challenges. *Network Protocols and Algorithms*, 2(1):45–73, 2010.

[55] Federal Communications Commission. Guidelines for Testing and Verifying the Accuracy of Wireless E911 Location Systems. *FCC Reports and Carrier Data*, April 2000.

[56] ICT-217033 WHERE Project. Deliverable 3.4: Location based optimisation for PHY algorithms/protocols, May 2010.

[57] Neal Patwari, Joshua N Ash, Spyros Kyperountas, Alfred O Hero III, Randolph L Moses, and Neiyer S Correal. Locating the nodes: cooperative localization in wireless sensor networks. *Signal Processing Magazine, IEEE*, 22(4):54–69, 2005.

[58] M. Triki, D. T. M. Slock, V. Rigal, and P. Francois. Mobile terminal positioning via power delay profile fingerprinting: Reproducible validation simulations. *Proceedings of the IEEE Vehicular Technology Conference (VTC-Fall 2006)*, pages 1–5, September 2006.

[59] H. Laitinen, J. Lahteenmaki, and T. Nordstrom. Database Correlation Method for GSM Location. *Proceedings of the IEEE Vehicular Technology Conference (VTC-Spring 2001)*, 4:2504–2508, May 2001.

[60] A.J. Weiss. On the Accuracy of a Cellular Location System Based on RSS Measurements. *IEEE transactions on vehicular technology*, 52(6):1508–1518, 2003.

[61] S. Sorour, Y. Lostanlen, and S. Valaee. Rss based indoor localization with limited deployment load. In *Global Communications Conference (GLOBECOM), 2012 IEEE*, pages 303–308, 2012.

[62] S. Gezici. A survey on wireless position estimation. *Wireless Personal Communications (Springer Netherlands)*, 44(3):263–282, February 2008.

[63] C. Mannweiler, R. Raulefs, J. Schneider, B. Denis, A. Klein, B. Uguen, M. Laaraiedh, and H. Schotten. A Robust Management Platform for Multi-Sensor Location Data Interpretation. *Proceedings of ICT mobile summit*, June 2010.

[64] Mohamed Laaraiedh, Lei Yu, Stephane Avrillon, and Bernard Uguen. Comparison of Hybrid Localization Schemes using RSSI, TOA, and TDOA. *Wireless Conference 2011 - Sustainable Wireless Technologies (European Wireless), 11th European*, pages 1–5, april 2011.

[65] L. Doherty, L. E. Ghaoui, and K. Pister. Convex position estimation in wireless sensor networks. *Proceedings of IEEE INFOCOM 2001*, 3:1655–1663, 2001.

[66] C. Savarese, J. M. Rabaey, and J. Beutel. Locationing in Distributed Ad-Hoc Wireless Sensor Networks. *Proceedings of IEEE International Conference on Acoustics, Speech and Signal Processing*, 4:2037–2040, 2001.

[67] Koen Langendoen and Niels Reijers. Distributed localization in wireless sensor networks: a quantitative comparison. *Comput. Netw.*, 43(4):499–518, November 2003.

[68] Christos Politis, Toshikane Oda, Sudhir Dixit, Andreas Schieder, Hong-Yon Lach, Michael I Smimov, Sami Uskela, and Rahim Tafazolli. Cooperative Networks for the Future Wireless World. *IEEE Communications Magazine*, 42(9):70–79, September 2004.

[69] Stefano Severi, Giuseppe Abreu, Giuseppe Destino, and Davide Dardari. Multihop versus message-passing: A complexity and accuracy comparison for distributed localization. In *WPNC*, pages 45–50. IEEE, 2011.

[70] Frank R. Kschischang, Brendan J. Frey, and Hans-Andrea Loeliger. Factor graphs and the sum-product algorithm. *IEEE TRANSACTIONS ON INFORMATION THEORY*, 47:498–519, 1998.

[71] U. Ferner, H. Wymeersch, and M.Z. Win. Cooperative anchor-less localization for large dynamic networks. In *Ultra-Wideband, 2008. ICUWB 2008. IEEE International Conference on*, volume 2, pages 181–185, 2008.

[72] Y. Bar-Shalom and X. R. Li. *Estimation and Tracking:: Principles, Techniques, and Software*. Ybs Publishing, Ringbound edition, February 1998.

[73] M. Laaraiedh. *Contribution on Hybrid Localization Techniques For Heterogeneous Wireless Networks*. PhD thesis, University of Rennes 1, December 2010.

[74] M. Laaraiedh, S. Avrillon, and B. Uguen. Overcoming Singularities In TDoA Based Location Estimation Using Total Least Square. *Proceedings of the International Conference on Signals, Circuits and Systems (SCS09)*, pages 1–4, November 2009.

[75] T.K. Moon. The expectation-maximization algorithm. *Signal Processing Magazine, IEEE*, 13(6):47–60, 1996.

[76] J. Shao. *Mathematical Statistics, 2nd edition*. Springer, October 2007.

[77] Ramon E. Moore. *Interval analysis*. 1966.

[78] Eldon Hansen. Interval arithmetic in matrix computations, part I. 2(2):308–320, 1965.

[79] Martine Ceberio, Vladik Kreinovich, and Lev Ginzburg. On the use of intervals in scientific computing: What is the best transition from linear to quadratic approximation?. In Jack Dongarra, Kaj Madsen, and Jerzy Wasniewski, editors, *PARA*, volume 3732 of *Lecture Notes in Computer Science*, pages 75–82. Springer, 2004.

[80] S. Salcedo-Sanz, M. Claramunt-bielsa, J.L. Vilar-zann, and A. Heras. *Statistical and Soft Computing Approaches in Insurance Problems*. Computational Mathematics and Analysis. Nova Science Publishers, Incorporated, 2013.

[81] M. W. M. Gamini Dissanayake, Paul Newman, Steven Clark, Hugh F. Durrant-whyte, and M. Csorba. A solution to the simultaneous localization and map building (slam) problem. *IEEE Transactions on Robotics and Automation*, 17:229–241, 2001.

[82] T. RaiSsi, N. Ramdani, and Y. Candau. Set membership state and parameter estimation for systems described by nonlinear differential equations. *Automatica*, 40(10):1771–1777, October 2004.

[83] Amadou Gning and Philippe Bonnifait. Constraints propagation techniques on intervals for a guaranteed localization using redundant data. *Automatica*, 42(7):1167–1175, 2006.

[84] Fabrice Le Bars. *Analyse par intervalles pour la localisation et la cartographie simultanées; Application à la robotique sous-marine*. These, Université de Bretagne occidentale - Brest, October 2011.

[85] V. Drevelle and Ph. Bonnifait. High integrity GNSS location zone characterization using interval analysis. *ION GNSSSavannah, GA : United States*, 2009.

[86] V. Drevelle and P. Bonnifait. Global positioning in urban areas with 3-D maps. In *Intelligent Vehicles Symposium (IV), 2011 IEEE*, pages 764–769, june 2011.

[87] L. Jaulin O. Reynet and G. Chabert. Robust tdoa passive location using interval analysis and contractor programming. In *Radar*, Bordeaux, France, 2009.

[88] Farah Mourad, Hichem Snoussi, Fahed Abdallah, and Cédric Richard. Guaranteed Boxed Localization in MANETs by Interval Analysis and Constraints Propagation Techniques. In *Global Telecommunications Conference, IEEE, GLOBECOM*, 2008.

[89] F. Mourad, H. Snoussi, F. Abdallah, and C. Richard. A Robust Localization Algorithm for Mobile Sensors Using Belief Functions. *Vehicular Technology, IEEE Transactions on*, 60(4):1799–1811, may 2011.

[90] Jean-Benoist Leger and Michel Kieffer. Guaranteed robust distributed estimation in a network of sensors. In *ICASSP*, pages 3378–3381. IEEE, 2010.

[91] L. Jaulin, M. Kieffer, O.Didrit, and E. Walter. *Applied interval Analysis*. Springer, September 2001.

[92] Gilles Chabert. *Techniques d'intervalles pour la résolution de systèmes d'équations*. PhD thesis, Nice, Sophia Antipolis, 2007. Thèse de doctorat : Informatique.

[93] V. Drevelle and P. Bonnifait. Reliable positioning domain computation for urban navigation. *Intelligent Transportation Systems Magazine, IEEE*, 5(3):21–29, 2013.

[94] M. Laaraiedh, S. Avrillon, and B. Uguen. Hybrid Data Fusion techniques for localization in UWB networks. In *Positioning, Navigation and Communication, 2009. WPNC 2009. 6th Workshop on*, pages 51–57, march 2009.

[95] Andrew W. Moore. An intoductory tutorial on kd-trees, 1991.

[96] M. Laaraiedh, S. Avrillon, and Bernard Uguen. Enhancing positioning accuracy through direct position estimators based on hybrid RSS data fusion. In *Proc. VTC Spring*, pages 1–5, Barcelona, Spain, 2009.

[97] ICT-217033 WHERE Project. Deliverable 4.1: Measurements of location-dependent channel features, October 2008.

[98] S.M. Kay. *Fundamentals of Statistical Signal Processing: Detection theory*. Prentice-Hall PTR, NJ, 1998.

[99] K. Papakonstantinou and D. Slock. Cramer-Rao bounds for hybrid localization methods in LoS and NLoS environments. pages 213–217, sept. 2010.

[100] M. Laaraiedh, S. Avrillon, and B. Uguen. A Maximum Likelihood ToA Based Estimator For Localization in Heterogeneous Networks. *International Journal on Communication, Network and System Sciences (IJCNS)*, 3(1):38–42, January 2010.

[101] Hadi NOUREDDINE AL MOUSSAWI. *Some Signal Processing Techniques for Wireless Cooperative Localization and Tracking*. These, Télécom Bretagne, Université de Bretagne Occidentale, November 2012. 12956 12956.

[102] Jacques Palicot, Joseph Mitola III, Zander Lei, and Friedrich Jondral. Special issue on 10 years of cognitive radio: state-of-the-art and perspectives. *EURASIP J. Wireless Comm. and Networking*, 2012:214, 2012.

[103] H Andrés Lagar-Cavilla, Gerard Baron, Thomas E Hart, Lionel Litty, and Eyal De Lara. On the Robustness of Simple Indoor MANET Simulation Models. *Ad hoc & sensor wireless networks*, 4(4), 2007.

[104] A. Helmy W. Hsu, F. Bai. *Mobility Modeling for Vehicular Networks*. Chapman & Hall CRC, 2012.

[105] Eitan Altman, Robin Groenevelt, and Philippe Nain. Relaying in Mobile Ad Hoc Networks: The Brownian Motion Mobility Model. Technical Report RR-5311, INRIA, September 2004.

[106] S. Mao. *Fundamentals of wireless networks*, chapter 8, pages 201–234. Elsevier Inc., Amsterdam, The Netherlands, 2009.

[107] Injong Rhee, Minsu Shin, Seongik Hong, Kyunghan Lee, Seong Joon Kim, and Song Chong. On the levy-walk nature of human mobility. *IEEE/ACM Trans. Netw.*, 19(3):630–643, June 2011.

[108] M. E. J. Newman. Power laws, pareto distributions and zipf's law. *Contemporary Physics*, 46:323–351, December 2005.

[109] Yacine Benchaïb and Claude Chaudet. Using virmanel and silumod to study protocol for mobile multihop networks. In *SECON*, pages 76–78. IEEE, 2012.

[110] J. Tian, J. Hähner, C. Becker, I. Stepanov, and K. Rothermel. Graph-based mobility model for mobile ad hoc network simulation. In *Simulation Symposium, 2002. Proceedings. 35th Annual*, pages 337–344, 2002.

[111] Fan Bai, Narayanan Sadagopan, and Ahmed Helmy. IMPORTANT: A framework to systematically analyze the Impact of Mobility on Performance of RouTing protocols for Adhoc NeTworks. In *INFOCOM 2003. Twenty-Second Annual Joint Conference of the IEEE Computer and Communications. IEEE Societies*, volume 2, pages 825–835. IEEE, 2003.

[112] Amit Jardosh, Elizabeth M. Belding-Royer, Kevin C. Almeroth, and Subhash Suri. Towards realistic mobility models for mobile ad hoc networks. In *Proceedings of the 9th annual international conference on Mobile computing and networking*, MobiCom '03, pages 217–229, New York, NY, USA, 2003. ACM.

[113] H. Wymeersch, J. Lien, and M.Z. Win. Cooperative Localization in Wireless Networks. *Proceedings of the IEEE*, 97(2):427–450, 2009.

[114] Marta C Gonzalez, Cesar A Hidalgo, and Albert-Laszlo Barabasi. Understanding individual human mobility patterns. *Nature*, 453(7196):779–782, 2008.

[115] Lawrence M Leemis and Stephen Keith Park. *Discrete-event simulation: A first course*. Pearson Prentice Hall Upper Saddle River, NJ, 2006.

[116] Daniel Krajzewicz, Jakob Erdmann, Michael Behrisch, and Laura Bieker. Recent development and applications of SUMO - Simulation of Urban MObility. *International Journal On Advances in Systems and Measurements*, 5(3&4):128–138, December 2012.

[117] Franco Tecchia, Céline Loscos, R Conroy-Dalton, and YL Chrysanthou. Agent behaviour simulator (abs): A platform for urban behaviour development. 2001.

[118] MobiReal : A realistic network simulator. `http://www.mobireal.net/`. Accessed: 2013-07-16.

[119] SimPy Simulation Package. `http://simpy.sourceforge.net`. Accessed: 2013-07-16.

[120] Craig W Reynolds. Steering behaviors for autonomous characters. In *Game Developers Conference*, volume 1999, pages 763–782, 1999.

[121] Personal Rapid Transit Simulation. `http://sourceforge.net/projects/prt/`. Accessed: 2013-07-16.

[122] SimWalk: Pedestrian Simulation for Transport, Aviation and Architecture. `http://www.simwalk.com/`. Accessed: 2013-06-13.

[123] PTV Viswalk. `http://vision-traffic.ptvgroup.com/en-us/products/ptv-viswalk/`. Accessed: 2013-05-26.

[124] Legion Pedestrian Software. `http://www.legion.com/`. Accessed: 2013-05-26.

[125] The Network Simulator -ns2-. `http://www.isi.edu/nsnam/ns/`. Accessed: 2013-05-26.

[126] Gustavo Carneiro, Helder Fontes, and Manuel Ricardo. Fast prototyping of network protocols through ns-3 simulation model reuse. *Simulation Modelling Practice and Theory*, 19(9):2063 – 2075, 2011.

[127] WSNet / Worldsens simulator. `http://wsnet.gforge.inria.fr/`. Accessed: 2013-08-30.

[128] Victor J. Blue and Jeffrey L. Adler. Cellular automata microsimulation for modeling bi-directional pedestrian walkways. *Transportation Research Part B: Methodological*, 35(3):293–312, March 2001.

[129] Jan Dijkstra, Harry J. P. Timmermans, and Joran Jessurun. A multi-agent cellular automata system for visualising simulated pedestrian activity. In Stefania Bandini and Thomas Worsch, editors, *ACRI*, pages 29–36. Springer, 2000.

[130] Yacine Benchaïb and Claude Chaudet. SILUMOD: A Simulation Language for User Mobility Models Definition in Multihop Networks. In *First Asia-Pacific Programming Languages and Compilers Workshop (APPLC 2012)*, page 1, Beijing, Chine, June 2012.

[131] D.M. Rose, T. Jansen, S. Hahn, and T. Kurner. Impact of realistic indoor mobility modelling in the context of propagation modelling on the user and network experience. In *Antennas and Propagation (EuCAP), 2013 7th European Conference on*, pages 3979–3983, 2013.

[132] Kumiko Maeda, Akira Uchiyama, Takaaki Umedu, Hirozumi Yamaguchi, Keiichi Yasumoto, and Teruo Higashino. Urban pedestrian mobility for mobile wireless network simulation. *Ad Hoc Networks*, 7(1):153–170, 2009.

[133] E.W. Dijkstra. *A Short Introduction to the Art of Programming.* Holland, 1971.

[134] L. Euler. *Introductio in analysin infinitorum.* Introductio in analysin infinitorum. apud Marcum-Michaelem Bousquet & socios, 1748.

[135] E.T. Hall. *The Hidden Dimension.* Doubleday, 1966.

[136] Microscopic Pedestrian Simulation Model to Evaluate 'Lane-like Segregation'of Pedestrian Crossing. In *Proceedings of Infrastructure Planning Conference. Kouchi, Japan.*

[137] Claus Pedersen, Troels Pedersen, and Bernard H. Fleury. Exploiting Network Topology Information to Mitigate Ambiguities in VMP Localization. In *4th IEEE International Workshop on Computational Advances in Multi-Sensor Adaptive Processing (CAMSAP 2011)*, pages 57–60, San Juan, Puerto Rico, December 2011.

[138] K. Das and H. Wymeersch. Censoring for Bayesian Cooperative Positioning in Dense Wireless Networks. *Selected Areas in Communications, IEEE Journal on*, 30(9):1835–1842, 2012.

[139] S. Zirari and B. Denis. Comparison of links selection criteria for mobile terminal positioning in cooperative heterogeneous networks. In *Software, Telecommunications and Computer Networks (SoftCOM), 2012 20th International Conference on.*

[140] WHERE2 : Wireless Hybrid Enhanced Mobile Radio Estimators - Phase 2. `http://www.kn-s.dlr.de/where2/`. Accessed: 2013-07-16.

[141] Post process csv files. `https://bscw.eurecom.fr/bscw/bscw.cgi/443383`. Accessed: 2013-07-16.

[142] Interoperability framework requirements and main specifications. FP7-ICT-2009-4 WHERE2 Deliverable D4.1, October 2011.

[143] M. Pezzin and D. Lachartre. A low power, low data rate impulse radio ultra wide band transceiver. In *Future Network and Mobile Summit, 2010*, pages 1–10, 2010.

[144] Test and evaluation of the integrated system under real scenario conditions. FP7-ICT-2009-4 WHERE2 Deliverable D4.5, October 2013.

[145] David Tse and Pramod Viswanath. *Fundamentals of Wireless Communication.* Cambridge University Press, June.

[146] M. Laaraiedh, N. Amiot, S. Avrillon, and B. Uguen. Theoretical performances assessment of hybrid localization techniques. *Statistical Signal Processing Workshop (SSP), 2011 IEEE*, pages 185–188, june 2011.

[147] PyLaters. `http://www.pylayers.org`. Accessed: 2013-07-16.

[148] Albert Einstein. The foundation of the general theory of relativity. *Annalen der Physik*, 49(7):769–822, 1916.

[149] Python Programming Language. `http://www.python.org`. Accessed: 2013-07-16.

Abstract

This thesis focuses on the development of tools and methods dedicated for ultra wide band (UWB) localization systems in indoor environment. The thesis work was conducted within the European FP7 project Where2, about the cooperative localization in cellular networks. Data from a measurement campaign conduct during the project are used to validate the proposed algorithms. This thesis is divided in four parts:

The first part is focused on the description of an original raytraing tool based on a graph description. In order to be compliant with the requirement of a mobile simulation, a new concept of rays signature enabling incremental computation, and a vectorized formalism for processing rays are described and implemented. The second part is focused on the indoor localization techniques, where a novel technique based on interval analysis approaches is presented and compared to alternative techniques. Advantageously using this approach, a specific processing based on an hypothesis testing method using received power observations to resolve ambiguities appearing in under determined localization problems is described. A third part describes different aspects of the dynamic platform. In particular a realistic mobility model based on «steering behaviors», a graph description of the network scene and an inter agents communication protocol are detailed. The fourth section uses measured data obtained from an heterogeneous measurement campaign to validate both the developed software platform and the proposed localization algorithms.

Résumé

Cette thèse porte sur le développement d'outils et de méthodes pour l'étude des systèmes de localisation Ultra Large Bande en milieu intérieur. Le travail de thèse a été mené pour partie dans le cadre du projet européen FP7 WHERE2, portant sur la localisation coopérative dans les réseaux cellulaires. La thèse utilise pour sa partie validation des données obtenues dans le cadre de ce projet. La thèse comporte 4 grandes parties.

Une première partie présente un outil de raytracing basé sur une description à base de graphes. Afin de pouvoir adresser les problématiques de simulation de la mobilité, l'outil introduit le concept nouveau de signature ainsi qu'un formalisme vectorisé permettant l'accélération du calcul du champ sur les rayons obtenus. Une seconde partie concerne les techniques de localisation utilisées en intérieur et propose une méthode originale basée sur des approches ensemblistes. Cette méthode est évaluée et comparée à des techniques alternatives comme le des moindres carrés pondérés ou le maximum de vraisemblance. Tirant parti des spécificités de la méthode précédente, une méthode basée sur un test d'hypothèse est décrite. Cette dernière propose d'exploiter les données de puissance reçue (largement disponible en pratique) pour lever les ambiguïtés multimodales dans les cas de carence d'observables précis. Une troisième partie présente 3 aspects de la plateforme dynamique. Tout d'abord une simulation de la mobilité réaliste basée sur les «steering behaviors», puis la description sous forme de graphe du réseau sans fil et enfin un protocole simplifié de communication inter agents. La quatrième partie exploite des données radio obtenues lors d'une campagne de mesure pour valider les différents étages de la plateforme et les algorithmes de localisation proposés.